Search for exotic long-lived particles using disappearing tracks with the CMS experiment in proton-proton collisions at $\sqrt{s} = 13$ TeV

DISSERTATION
ZUR ERLANGUNG DES DOKTORGRADES
AN DER FAKULTÄT FÜR MATHEMATIK, INFORMATIK UND
NATURWISSENSCHAFTEN
FACHBEREICH PHYSIK
DER UNIVERSITÄT HAMBURG

VORGELEGT VON

VIKTOR GERHARD KUTZNER

HAMBURG

2023

Universität Hamburg
DER FORSCHUNG | DER LEHRE | DER BILDUNG

Gutachter/innen der Dissertation:	Prof. Dr. Peter Schleper
	Dr. Isabell Melzer-Pellmann
Zusammensetzung der Prüfungskommission:	Prof. Dr. Dieter Horns
	Prof. Dr. Peter Schleper
	Dr. Isabell Melzer-Pellmann
	Prof. Dr. Gudrid Moortgat-Pick
	Prof. Dr. Elisabetta Gallo
Vorsitzender der Prüfungskommission:	Prof. Dr. Dieter Horns
Datum der Disputation:	29.6.2023
Vorsitzender Fach-Promotionsausschuss:	Prof. Dr. Günter Sigl
Leiter des Fachbereichs Physik:	Prof. Dr. Wolfgang Parak
Dekan der Fakultät MIN:	Prof. Dr.-Ing. Norbert Ritter

Abstract

A search for heavy charged long-lived particles is presented in the context of theories beyond the Standard Model (BSM) with a small mass splitting between the two lightest newly proposed particles. Such BSM models can be targeted using the signature of a track that disappears in the inner tracking detector. The lightest particle in the final state of the long-lived particle decay presents a candidate for dark matter, whose existence is strongly hinted at by astrophysical evidence.

A small mass splitting between the two lightest new particles can for example occur between the chargino and a neutralino in the context of the minimal supersymmetric Standard Model. Given a sufficiently small mass splitting in the range of $m_\pi \lesssim \Delta m \lesssim 200$ MeV, the chargino is expected to decay in the CMS tracker volume into soft leptons, which are not reconstructed, or hadrons and a lightest supersymmetric particle, leaving a short track that then seems to disappear. The signature is a reconstructed track with missing hits in the outer layers of the tracker, with little or no energy deposited in the calorimeter in the neighborhood of the track's trajectory.

Events are selected with one or more disappearing tracks in final states with at least one jet as well as with and without leptons. The leptonic channel serves to target top and bottom squark production, for which leptons can arise due to leptonic top quark decays. For both event topologies, the analysis is binned in terms of number of jets, missing transverse momentum, and the number of b-quark-tagged jets in order to provide sensitivity to the chargino production mechanism. A further binning in terms of the energy loss dE/dx provides sensitivity to the chargino mass, as the chargino is assumed to be highly ionizing.

Data-driven methods are used to determine the Standard Model backgrounds, which can arise either as the result from mal-reconstructed leptons, or from tracks reconstructed from random combination of hits. Results are presented using 137 fb^{-1} of proton-proton collision data at $\sqrt{s} = 13$ TeV collected with the CMS experiment during Run 2, with mass exclusion limits reaching up to squark masses and dark matter masses of $m_{\tilde{b}} \approx 1.575$ TeV and $m_{\chi_1^0} \approx 1.15$ TeV, as well as of $m_{\tilde{t}} \approx 1.6$ TeV and $m_{\chi_1^0} \approx 1.2$ TeV. Mass exclusion limits for the gluino mass and dark matter mass reach up to $m_{\tilde{g}} \approx 2.25$ TeV and $m_{\chi_1^0} \approx 1.7$ TeV.

Zusammenfassung

Im Rahmen von Theorien jenseits des Standardmodells (BSM) mit einer kleinen Massendifferenz zwischen den beiden leichtesten postulierten Teilchen wird eine Suche nach schweren geladenen langlebigen Teilchen vorgestellt. Solche BSM-Modelle können anhand der Signatur einer Spur, die im inneren Spurdetektor verschwindet, aufgespürt werden. Das leichteste Teilchen im Endzustand des langlebigen Teilchenzerfalls ist ein Kandidat für dunkle Materie, deren Existenz aufgrund astrophysikalischer Hinweise vermutet wird.

Eine kleine Massendifferenz zwischen den beiden leichtesten neuen Teilchen kann beispielsweise zwischen dem Chargino und einem Neutralino im Rahmen des minimalen supersymmetrischen Standardmodells auftreten. Bei einer hinreichend kleinen Massendifferenz im Bereich von $m_\pi \lesssim \Delta m \lesssim 200$ MeV wird erwartet, dass das Chargino im CMS-Trackervolumen in niederenergetische Leptonen, die nicht rekonstruiert werden, oder Hadronen und ein leichtestes supersymmetrisches Teilchen zerfällt und eine kurze Spur hinterlässt, die dann zu verschwinden scheint. Die Signatur ist eine rekonstruierte Spur mit fehlenden Treffern in den äußeren Schichten des Trackers, wobei wenig oder gar keine Energie im Kalorimeter in der Nähe der Spur deponiert wird.

Es werden Ereignisse mit einer oder mehreren verschwindenden Spuren in Endzuständen mit mindestens einem Jet sowie mit und ohne Leptonen ausgewählt. Der leptonische Kanal dient der Produktion von Top- und Bottom-Squarks, bei denen Leptonen durch leptonische Top-Quark-Zerfälle entstehen können. Für beide Ereignistopologien wird die Analyse hinsichtlich der Anzahl der Jets, des fehlenden transversalen Impulses und der Anzahl von b-Jets gebinnt, um eine Sensitivität für den Chargino-Produktionsmechanismus zu erreichen. Eine weitere Unterteilung in Bezug auf den Energieverlust dE/dx bietet Sensitivität für die Chargino-Masse, da angenommen wird, dass das Chargino stark ionisierend ist.

Die dominanten Standardmodell-Untergründe von prompten Leptonen und nicht-echten Spuren werden mit Daten-getriebenen Untergrundbestimmungsmethoden quantifiziert. Die Ergebnisse werden auf Grundlage von 137 fb^{-1} von Proton-Proton-Kollisionen bei $\sqrt{s} = 13$ TeV, die während Run 2 aufgezeichnet worden sind, vorgestellt. Ausschlusslimits auf die Bottom- und Top-Squarkmassen und Masse des Dunkle-Materie-Teilchens wurden bis $m_{\tilde{b}} \approx 1.575$ TeV und $m_{\chi_1^0} \approx 1.15$ TeV, sowie $m_{\tilde{t}} \approx 1.6$ TeV und $m_{\chi_1^0} \approx 1.2$ TeV bestimmt. Ausschlusslimits auf die Masse des Gluinos und Masse des Dunkle-Materie-Teilchens wurden bis $m_{\tilde{g}} \approx 2.25$ TeV und $m_{\chi_1^0} \approx 1.7$ TeV bestimmt.

The results shown in this thesis have been reviewed within the CMS collaboration and the analysis has been carried out in a blinded fashion. The results have been unblinded within the CMS collaboration, and the publication process is ongoing.

Contents

Chapter 1

Introduction

Since the acclaimed discovery of the last undetected elementary particle of the Standard Model (SM), the Higgs boson, at the Large Hadron Collider (LHC) in 2012 [1, 2], further data has been collected at about twice the centre-of-mass energy at a value of $\sqrt{s} = 13$ TeV and about a factor ≈ 13 more luminosity. This discovery and the new data ushered in a new era in particle physics, in which many open, but few constrained, questions can be addressed regarding the smallest scales. The search for new physics presented here complements a rich program of past searches as well as precision measurements carried out with the Compact Muon Solenoid (CMS) experiment at the LHC in an effort to answer parts of these open questions.

The increasing amount of available proton-proton collision data for physics analyses, with simultaneously larger excluded regions of phase space, has lead to the rise of so-called signature-based approaches, as analyses investigate more rare particle decays with striking signatures.

Most BSM searches target promptly decaying particles with a decay length much smaller than 0.1 mm. Specially designed searches for exotic long-lived particles (LLPs) on the other hand could potentially uncover a hidden sector of physics. Many BSM theories predict such exotic LLPs, e.g. supersymmetry (SUSY) with split, anomaly-mediated, or gauge-mediated SUSY-breaking. In this case, the production and decay of new particles happen at a distance greater than 0.1 mm from the interaction point. Targeting decays of particles with longer lifetimes requires going beyond standard collider event reconstruction techniques and making use of non-standard approaches, such as dedicated triggers, customized track reconstruction, or measuring the time-of-flight of particles undergoing energy loss via ionization. One such search with a signature referred to as a disappearing track has been studied recently and has been found to have a profound impact on the viable phase space of a broad class of physics models beyond the SM (BSM). Non-standard reconstruction approaches for LLP signatures typically require a data-driven method to estimate the corresponding background as well, since Monte-Carlo (MC) simulation is not expected to necessarily account for such approaches accurately enough. The goal of this thesis is therefore to search for disappearing tracks of heavy charged particles in association with high transverse momentum jets from decays of heavy colored particles and missing transverse momentum from dark matter candidates.

In Ch. 2 of this thesis, the Standard Model of particle physics is introduced, followed by a discussion of the questions it leaves open. Evidence from astrophysical observations establishing the presence of dark matter is laid out in Ch. 3, with a survey of dark matter candidate particles and the possible methods to detect them. Hypothetical exotic long-lived particles, which have the possibility to decay into dark matter are also introduced, and their production and detection mechanisms in collider experiments are discussed. Ch. 4 presents an overview of the LHC and the CMS experiment, as well as the event reconstruction. Compressed supersymmetric models with a small mass splitting between the two lightest supersymmetric particles are considered as a production mechanism for the signature of a disappearing track, for which the analysis strategy and its implementation is presented in Ch. 5.

The results and interpretation in terms of compressed supersymmetric models are presented in Ch. 6. The findings are placed into a broader context, which provides a comparison with respect to other searches at the LHC, from both the CMS and ATLAS experiments.

Chapter 2

The Standard Model

This chapter gives an introduction to the fundamentals of the Standard Model (SM) of particle physics, which has been validated in a longstanding series of experiments, the latest being the discovery of the Higgs boson predicted within this framework [1,2]. The following discussion is based on [3–5].

2.1 Elementary particles

The SM provides a comprehensive description of elementary particles and their interactions with each other. The SM is foremost a quantum field theory (QFT), whose underlying local gauge symmetries are SU(3) for quantum chromodynamics and SU(2)×U(1) for the unified electroweak interaction. These symmetries define the SM in terms of particles and the interacting forces. The SU(2)×U(1) gauge symmetry is spontaneously broken via the Higgs mechanism, which gives rise to the non-zero mass of most particles and the Higgs boson [3]. The elementary particles are grouped into quarks, leptons and gauge bosons, of which the gauge bosons act as force carriers. Figure 2.1 shows the elementary particles described by the SM.

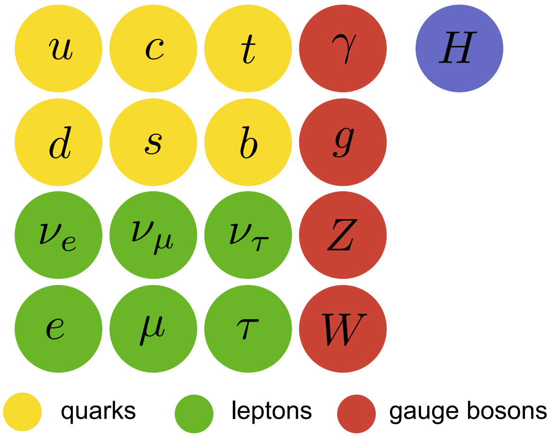

Figure 2.1: Elementary particles described by the SM. Shown are the three families of quarks and leptons as well as the gauge bosons and the Higgs boson. Figure from [5].

Quarks and leptons are fermionic particles with a spin of $\frac{1}{2}$, and are described as matter fields. Depending on the helicity of a fermion, *left-handed* particles belong to weak iso-doublets, and *right-handed* belong to weak iso-singlets [3].

Fermions are grouped in three *generations*, with increasing particle masses for each generation excluding neutrinos. The three generations of charged leptons are composed of the electron, muon, and tauon, which differ in their respective mass $m_\tau > m_\mu > m_e$. Each lepton generation is accompanied by a light neutrino with zero charge. For quarks, the three generations are consisting of the *up* and *down* quarks, *charm* and *strange* quarks as well as *top* and *bottom* quarks, with increasing masses per generation. Each generation is composed of two quarks with electric charge $q = +\frac{2}{3}e$ (the *up, charm* or *top* quarks) and $q = -\frac{1}{3}e$ (the *down, strange* and *bottom* quarks). Quarks have an additional color charge of *red, green* and *blue*, while antiquarks have an anticolor charge.

Forces are mediated through spin-1 gauge bosons coupling to the matter fields. While photons γ, Z, and W bosons are carriers of the electroweak force, gluons g are the carrier of the strong force. Force carriers can be electrically charged in the case of $W^\pm$ bosons, color charged in the case of the gluon, or carry no charge of any kind as in the case of the photon.

In the following sections, the components of the SM Lagrangian $\mathcal{L}_{\text{SM}}$ are constructed.

2.2 Quantum electrodynamics

Quantum electrodynamics (QED) describes the electromagnetic interaction, in which the electromagnetic force is mediated via photon exchange. QED is described by a U(1) local gauge symmetry, for which the Lagrangian is given by

$$\mathcal{L}_{\text{QED}} = \bar{\psi}(x)(i\not{D} - m)\psi(x) - \frac{1}{4}F_{\mu\nu}(x)F^{\mu\nu}(x), \tag{2.2.1}$$

with a Dirac field $\psi(x)$ describing leptons with masses m, and the kinetic term $F_{\mu\nu}(x) = \partial_\mu A_\nu - \partial_\nu A_\mu$ to allow for the propagation of the photon field $A_\mu(x)$ [4]. $\not{D}$ is referred to as the covariant derivative, and is defined by

$$\not{D} = \gamma^\mu D_\mu = \gamma^\mu(\partial_\mu - ieQA_\mu), \tag{2.2.2}$$

with $D_\mu = \partial_\mu - iqA_\mu$, the gamma matrices γ^μ and electric charge eQ.

2.3 Quantum chromodynamics

The strong interaction is described by quantum chromodynamics (QCD), whereby the strong force is mediated via color-charged vector bosons, the gluons. Quarks with mass m_q enter the Lagrangian via quark fields q_i as

$$\mathcal{L}_{\text{QCD}} = \sum_q \bar{q}(x)(i\not{D} - m_q)q(x) - \frac{1}{4}F^\alpha_{\mu\nu}(x)F^{\mu\nu}_\alpha(x), \tag{2.3.1}$$

with the gluon field strength $F^\alpha_{\mu\nu}(x) = \partial_\mu A^\alpha_\nu(x) - \partial_\nu A^\alpha_\mu + g_s f^{\alpha\beta\gamma} A_{\mu\beta} A_{\nu\gamma}$. Here, A^α_μ are the eight gluon fields which give rise to the color-charged gluons, g_s the strong coupling constant, and structure constants are the $f^{\alpha\beta\gamma}$ [4].

2.4 Electroweak interactions

Electroweak interactions are described for a fermion field f by the weak isospin SU(2) group [3], here the force carriers are the $W^{\pm}$ and the Z boson. The Lagrangian is given as

$$\mathcal{L}_{\mathrm{EW}} = \sum_{f=l,q} (\bar{f} i \not{D} f) - \frac{1}{4} W^{i}_{\mu\nu} W^{\mu\nu}_{i} - \frac{1}{4} B_{\mu\nu} B^{\mu\nu}, \tag{2.4.1}$$

with field strength tensors $W^{i}_{\mu\nu}$ and $B_{\mu\nu}$ [4]. The electroweak interaction eigenstates derived from a superposition of the field strength tensor components yield the $W^{\pm}$, Z, and γ gauge bosons. $\not{D}$ differs for the left- and right-handed fermion fields because the SU(2)$_{\mathrm{L}}$ gauge fields couple only to left-handed fields and because the U(1)$_{\mathrm{Y}}$ hypercharge differs as well.

2.5 Higgs mechanism

Introducing the Higgs boson field in the Lagrangian allows for the generation of vector boson masses in a gauge-invariant way [3]. The kinetic and interaction terms for the Higgs sector are written in terms of a spontaneous symmetry breaking (SSB) term and a Yukawa coupling term,

$$\mathcal{L}_{\mathrm{H}} = \mathcal{L}_{\mathrm{H}}^{\mathrm{SSB}} + \mathcal{L}_{\mathrm{H}}^{\mathrm{Yukawa}}. \tag{2.5.1}$$

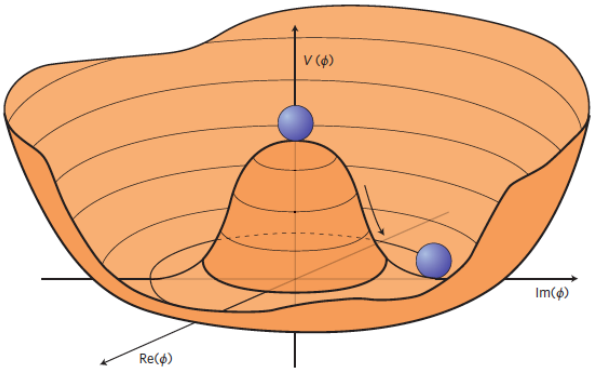

Figure 2.2: Illustration of the Higgs potential $V(\phi)$, for which $V(\phi) = \mu^2(\phi) + \lambda(\phi)^2$ is assumed. Shown is the case $\mu^2 < 0$, $\lambda > 0$. Symmetry breaking occurs once a point in the circular minimum is chosen. Taken from [6].

The spontaneous symmetry breaking term is given by

$$\mathcal{L}_{\mathrm{H}}^{\mathrm{SSB}} = (D_{\mu}\phi)^{\dagger}(D^{\mu}\phi) - V(\phi), \tag{2.5.2}$$

with a field ϕ and a renormalizable potential $V(\phi)$ [4]. Assuming an effective potential,

$$V(\phi) = \mu^2(\phi) + \lambda(\phi)^2, \tag{2.5.3}$$

the Lagrangian $\mathcal{L}_{\mathrm{H}}^{\mathrm{SSB}}$ is shown to be invariant under global $U(1)$ phase transformations $\phi \rightarrow e^{i\alpha}\phi$ [6]. Spontaneous symmetry breaking is introduced by choosing $\mu^2 < 0$ and $\lambda > 0$, as the minimized potential $V(\phi)$ yields a non-zero vacuum expectation value,

$$|\phi|^2 = -\frac{\mu^2}{2\lambda}, \tag{2.5.4}$$

as depicted as the minimum in Fig. 2.2. Choosing a point in the minimum spontaneously breaks rotational U(1) symmetry [6].

The interaction term is given by

$$\begin{aligned} \mathcal{L}_{\mathrm{H}}^{\mathrm{kinetic}} = -\frac{M_H^2}{2v}H^3 - \frac{M_H^2}{8v^2}H^4 - \frac{m_f}{v}\bar{f}Hf + M_W^2 W_\mu^+ W^{\mu-}\left(1+\frac{2}{v}H+\frac{1}{v^2}H^2\right) + \\ + \frac{1}{2}M_Z^2 Z_\mu Z^\mu \left(1+\frac{2}{v}H+\frac{1}{v^2}H^2\right), \end{aligned} \tag{2.5.5}$$

and contains the masses of the SM particles M_H, M_f, M_W, and M_Z as constraining parameters.

2.6 Standard Model Lagrangian

The final SM Lagrangian is the sum of the individual Lagrangian terms introduced above,

$$\mathcal{L}_{\mathrm{SM}} = \mathcal{L}_{\mathrm{QED}} + \mathcal{L}_{\mathrm{QCD}} + \mathcal{L}_{\mathrm{EW}} + \mathcal{L}_{\mathrm{H}}. \tag{2.6.1}$$

It allows for highly precise predictions of the fine-structure constant α, the Fermi constant G_F, and the Weinberg angle $\sin^2\theta_\omega$ of the electroweak interaction, as well as the relationship between the W and Z boson masses [4].

2.7 Physics beyond the Standard Model

While the SM is able to provide a consistent theoretical description of nearly all discoveries in particle physics up to this point, many questions remain unanswered. On the theoretical side, the fundamental force of gravity is not accounted for in the model, and the large discrepancy between the electroweak and gravitational energy scales presents a real puzzle. The gauge hierarchy problem concerns quantum corrections to the Higgs mass parameter, implying a ratio of the Higgs and Planck mass of $m_H^2(m_{\mathrm{Planck}})/m_{\mathrm{Planck}}^2 \approx 10^{-36}$, with the Higgs mass m_H given at the Planck scale [7]. The SM does not provide an explanation for the fact that there is a large difference. On its own this is not a problem, but the issue is the non-zero average Higgs field being highly sensitive to the scale where new physics replaces the SM at the Planck scale, and this sensitivity implies the two scales should be within an order of magnitude of each other. The lack of unification of the electroweak and strong interactions for large energies poses another problem, as does the origin of the number of the fermion generations.

A small number of experimental observations are also not accurately accounted for by the SM. The discovery of non-zero neutrino mass, for which experimental bounds have been placed by experimental measurements, is not accounted for in the original version of the SM. Neutrino oscillations, which showed that neutrinos in fact have mass, were first observed by measuring fewer electron neutrinos in the flux of solar neutrinos, indicating a linear superposition of neutrino mass eigenstates for each neutrino. Possibly the $g-2$ anomaly is also not described in the SM [8, 9]. Astrophysical observations indicating the presence of dark matter, which is discussed in the following chapter, can also not be explained as any particle in the SM.

Numerous extensions to the SM have been proposed to address one or many issues discussed above. One of the more well-motivated and well studied, namely, supersymmetric extensions, are central to this work. Supersymmetric scenarios involving long-lived massive charged particles in particular are explored in this work.

Chapter 3

Dark matter and exotic long-lived particle particles

This chapter describes the motivation for dark matter (DM) through astrophysical observations and cosmological arguments. A potential candidate for a DM particle is introduced and different detection methods are discussed. A possible production of DM through the decay of an exotic long-lived particle is considered. The chapter concludes with an overview of detection signatures of long-lived particles. The following introduction of DM is based on [10,11] and [5].

3.1 Dark matter

3.1.1 Astrophysical evidence

Astrophysical observations indicate the presence of non-luminous and electrically inert DM in the universe. Measurements of galaxy rotation curves yield too large values for the rotational velocity, which for a stable Keplerian orbit is given by

$$v(r) = \sqrt{\frac{G \cdot m(r)}{r}}, \tag{3.1.1}$$

where G is the gravitational constant, $m(r)$ is the total mass contained within r, and r is the radius from the galactic central point [10]. At large distances r from the galactic center, the velocity of luminous objects is expected to decrease with $v(r) \propto \sqrt{1/r}$. Measurements as shown in Fig. 3.1-left however yield approximately constant velocities for the most distant galactic objects, indicating the presence of a dark halo. The measurements indicate that DM is only weakly-interacting, leading to a lower bound on the DM density of at least $\Omega_{DM} \gtrsim 0.1$, described further below.

An indication of the particle-like nature of DM is given by the *bullet cluster* (1E0657-558), a collision between two galaxy clusters. While the hot gas clouds containing most of the baryonic matter interacted during the collision and subsequently increased in temperature and decelerated, gravitational lensing showed that the majority of the total mass continued to move on its original trajectory [12].

Massive compact halo objects causing gravitational microlensing may contribute to baryonic DM, a form of DM which is expected only to interact gravitationally. However, the low number of such identified objects and further results from big bang nucleosynthesis and the cosmic microwave background radiation disfavor the assumption of baryonic DM [10].

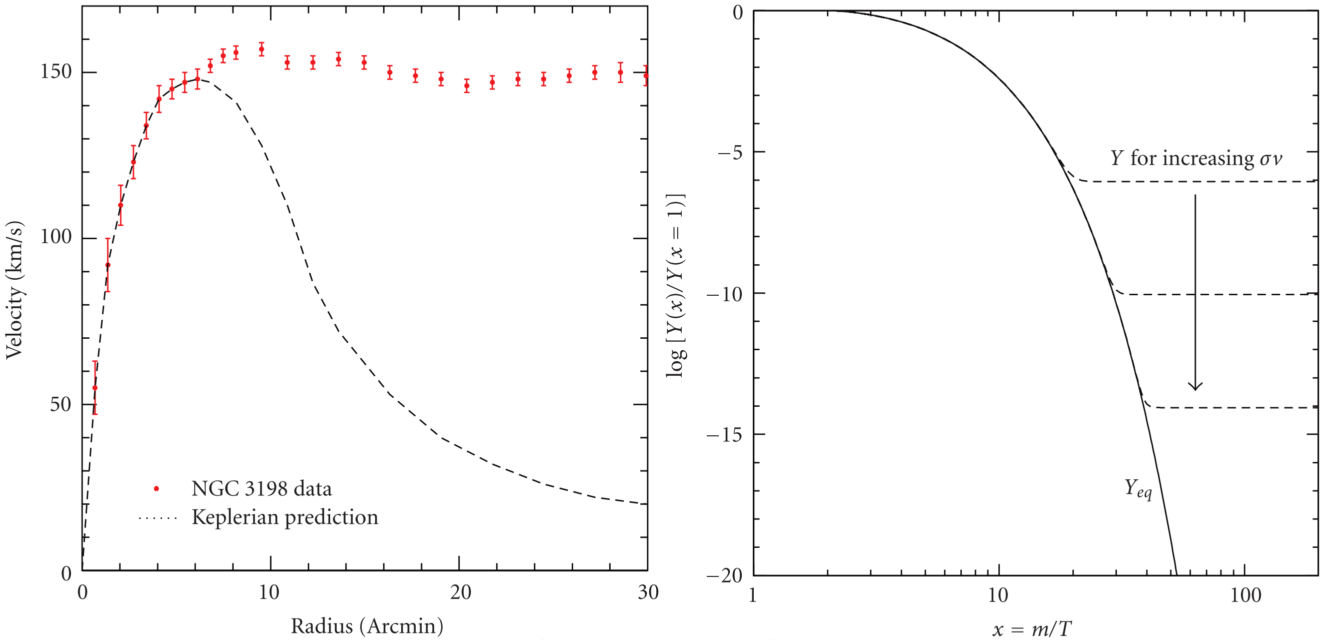

Figure 3.1: Left: Rotation velocity of luminous objects from galaxy NGC 3198 depending on the radius compared to the Keplerian prediction. The measured data indicates an approximately constant velocity for large radii, indicating the presence of a *dark halo*. Right: Relative WIMP abundance $Y(x)/Y(x = 1\ m/T)$ in the early universe depending on the inverse temperature showing the WIMP freeze-out for an increasing WIMP-SM annihilation rate $\sigma \times v$, with the annihilation cross section σ, WIMP velocity v and WIMP mass m. Figure taken from [10].

The observation of anisotropies in the cosmic microwave background radiation measured by the Planck observatory allows the determination of the thermal relic density of cold, non-baryonic matter. It is determined from global fits of cosmological parameters to multiple observations, also including the spatial distribution of galaxies [11, 13],

$$\Omega_{\text{nbm}} h^2 = 0.1186 \pm 0.0020. \tag{3.1.2}$$

Here, h denotes the reduced Hubble constant $h = H/100\ \text{km sec}^{-1}\text{Mpc}^{-1}$. The resulting density is significantly larger than the baryonic matter density $\Omega_{\text{b}} h^2$ alone,

$$\Omega_{\text{b}} h^2 = 0.02226 \pm 0.00023, \tag{3.1.3}$$

which is a fraction of ≈ 19 % of the cold, non-baryonic matter density. The baryonic matter density is determined by the ratio of ^{2}H (deuterium) and ^{4}He, the deuterium having been mainly produced through the big bang nucleosynthesis.

3.1.2 Particle candidates for dark matter

A viable candidate for non-baryonic DM is required to be stable, electrically neutral, and possibly weakly interacting. It should also account for the right relic density and must not exceed $\Omega_{\text{nbm}} h^2$. These requirements can be satisfied by primordial black holes, axion-like particles, sterile neutrinos, or weakly interacting massive particles (WIMPs). WIMPs can, in principle, be detected in collider searches in TeV-scale collisions, and are thus investigated in dedicated searches [11], including this search.

The most promising candidate in collider searches is an electrically neutral WIMP DM χ with a mass m_{DM} in the range of 10 GeV to $\mathcal{O}(\text{TeV})$ [11]. In the ΛCDM[1] model, WIMPs can yield the correct relic density $\Omega_{\text{nbm}}h^2$ [14].

A thermal and chemical equilibrium of WIMPs and SM particles is assumed after inflation in the early universe. At decreased temperatures $T < m_{DM}$, the WIMP density is exponentially suppressed as indicated by the solid line in Fig. 3.1-right. Here, the relative WIMP abundance depending on the inverse temperature is shown, in which the abundance corresponds to the relic density. The rate of annihilation between WIMPs and SM particles is given by the cross section multiplied by the WIMP velocity. Once the annihilation rate is below the Hubble expansion rate of the universe, the WIMPs no longer annihilate, which is referred to as "freeze-out" [11]. The resulting constant relative abundance for increasing rates of annihilation is visible in Fig. 3.1-right as dashed lines. Larger annihilation rates lead to a smaller relic density. In the case of WIMPs, the corresponding cross section is on the order of the electroweak scale $\mathcal{O}(\text{pb})$.

The Standard Model does not provide a viable WIMP candidate, even though the neutrino interacts weakly and is electrically neutral. Measurements by the predecessor of the Planck observatory, the Wilkinson Microwave Anisotropy Probe (WMAP), constrain the neutrino mass to $m_\nu < 0.23$ eV, which can only account for a cosmological density of $\Omega_\nu h^2 < 0.0072$ [10, 15].

3.1.3 WIMP dark matter detection methods

WIMP DM may be detected through different types of interactions, shown in Fig. 3.2. The annihilation of SM particles to DM is the most relevant for collider searches. In this case, initial or final state radiation is required in order to tag the event in which DM is produced. Indirect detection searches are sensitive to DM annihilation resulting in SM particles. In direct detection experiments, DM recoils off detector nuclei. This interaction can be either spin-dependent or spin-independent, referring to the spin of the DM particle. The detection principles of the relevant experiments are discussed in the following.

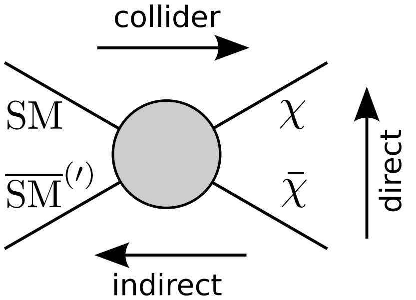

Figure 3.2: DM detection schemes. DM may be detected using either SM or DM annihilation processes or in direct-detection searches, in which the DM recoils off detector nuclei. Figure from [5].

Direct-detection searches

WIMPs are expected to interact with target nuclei through elastic scattering, following the assumption that WIMPs are gravitationally trapped inside galaxies with non-relativistic velocities in order to account for the observed rotational curves. Measured nuclear recoil energies range from $\mathcal{O}(10\text{eV})$ to $\mathcal{O}(100\text{keV})$, corresponding to WIMP masses of $\mathcal{O}(1\text{ GeV})$ up

---

[1] Λ cold DM model

to $\mathcal{O}(10\,\text{TeV})$. Recoils due to WIMPs are expected to show an exponential energy spectrum, which is determined by the convolution of the WIMP velocity distribution and the angular scattering distribution. The differential recoil spectrum is given by [16]:

$$\frac{dR}{dE}(E,t) = \frac{\rho_0}{m_{DM} m_\text{n}} \cdot \int v \cdot f(v,t) \frac{d\sigma}{dE}(E,v) d^3 v. \tag{3.1.4}$$

Here ρ_0 indicates the local DM density, m_n the mass of the target nucleus, v the WIMP velocity and $\frac{d\sigma}{dE}(E,v)$ the differential scattering cross section. The time-dependent velocity distribution $f(v,t)$ accounts for the change in WIMP velocity revolution of the earth around the sun. The differential recoil spectrum can be approximated by [16, 17]

$$\frac{dR}{dE}(E) \approx \left(\frac{dR}{dE}\right)_0 F^2(E) \exp\left(-\frac{E}{E_c}\right), \tag{3.1.5}$$

in which $\left(\frac{dR}{dE}\right)_0$ is the event rate at zero momentum transfer, and E_c denotes the characteristic energy scale depending on m_{DM} and m_n. $F^2(E)$ is a form-factor correction depending on spin-dependent or spin-independent nuclear interactions, in which direct-detection experiments are subdivided and probe different coupling mechanisms [16]. Vector and scalar DM would lead to spin-independent interactions, for which the cross section is proportional to the square of the mass of the nucleus. Axial-vector DM on the other hand would lead to spin-dependent interactions, which yield separate bounds for the DM-proton and DM-neutron interaction cross sections. As the expected interaction rate is at most one event per day and kilogram of detector material, direct-detection experiments require intense efforts to suppress background contributions [11].

Considering spin-independent interactions, the most sensitive experiments are dual-phase Xenon experiments, which include the LUX[2] DM experiment as well as XENON1T[3]. Here, two types of detection are used simultaneously to increase sensitivity and to reduce background contributions. Nuclear interactions in the Xenon target generate scintillating light which is detected by photomultiplier tubes. A strong electric field further allows the detector to be used as a time-projection chamber, which detects free electrons from the nuclear interaction. The electrons drift to the surface of the liquid xenon and are extracted with an anode, producing a signal [18]. The LUX-ZEPLIN experiment, a successor to the LUX experiment, is a direct-detection, underground, and low-background experiment, which relies on time projection chamber measurements with a large array of 494 photomultiplier tubes. They detect either vacuum ultraviolet scintillation photons (photons with a wavelength between 100-200 nm [19]) or secondary scintillation photons from ionizing electrons [20].

For lower WIMP masses below $m_{DM} < 10$ GeV the SuperCDMS[4] and CRESST-II[5] experiments are most sensitive [21]. The CDMS experiment detects phonons produced by the interactions with a cryogenic Germanium detector operated at low temperatures of $\mathcal{O}$(10mK) and at a high bias voltage [22]. In CRESST-II, a scintillating CaWO_4 crystal is used, allowing the detection of both scintillating light and phonons due to the temperature increase followed by a nuclear interaction [23].

The PICO-2L experiment at SNOLAB[6] uses a two-litre bubble chamber filled with a super-

---

[2] Large Underground Xenon DM experiment

[3] predecessor: XENON100

[4] Cryogenic DM Search

[5] Cryogenic Rare Event Search with Superconducting Thermometers

[6] Sudbury Neutrino Observatory Laboratory. The PICO collaboration is the merger of the PICASSO and COUPP groups.

heated liquid C_3F_8. Charged particles deposit energy through ionization, which creates the characteristic track signatures. The PICO experiment offers a good electron-recoil and alpha decay rejection. It provides the most stringent constraints on the spin-dependent DM-proton scattering cross section in the lower mass range of $m_{DM} < 50$ GeV [21]. For spin-independent interactions, the LUX-ZEPLIN experiment currently provides the best constraints in the same mass range.

A hard limitation for direction-insensitive direct detection experiments are neutrinos from astrophysical sources, commonly referred to as the neutrino background. The astrophysical sources include solar, atmospheric, and diffuse supernova neutrinos [24], and may produce the same signature as a WIMP signal. Collider searches on the other hand are independent of the neutrino background limit.

Indirect detection

Indirect DM searches are sensitive to WIMP annihilation products such as high-energy neutrinos of the order $\mathcal{O}(\text{ GeV})$, gamma rays, positrons, antiprotons, and antinuclei [11,25]. Experiments such as Super-Kamiokande, IceCube and AMANDA[7] are sensitive to a possible signal coming from the sun or from the center of the earth, as the WIMP density and thus the annihilation probability is potentially increased for WIMPs that are slowed down by massive objects. The experiments include large arrays of photomultipliers to detect a possible WIMP annihilation signal. Other experiments such as the H.E.S.S. Cherenkov telescope and Fermi-LAT probe the strong TeV point source at the center of the galaxy, which is expected to contain a high DM density. The PAMELA and AMS detectors, installed on a satellite and the International Space Station (ISS), respectively, as well as the BESS polar balloon mission are sensitive to antiparticles, which may originate from WIMP annihilations. Differences in the high-energy positron and electron fluxes are measured by the PAMELA and AMS02 experiments. They showed a rise of the positron fraction between 10 and 200 GeV, which might be caused by DM annihilation [11].

Cross section bounds are determined depending on the WIMP mass m_{DM}. Lower bounds on the cross section competitive to direct-detection searches are derived from annihilation signals coming from the direction of the sun, which are spin-dependent bounds on the DM-proton cross section. In this case, the Super-Kamiokande experiment (using $\chi\chi \to b\bar{b}$) and the IceCube experiment (using $\chi\chi \to t\bar{t}$) yield the lowest bounds depending on the mass range of m_{DM}.

Figure 3.3 shows the best current bounds on the DM-neutron cross section for spin-independent and on the DM-proton cross section for spin-dependent interactions, with the LUX-ZEPLIN dark matter experiment providing the most stringent constraints placed on spin-independent interactions. For spin-dependent interactions, the PICO collaboration provides the most stringent constraints.

Collider searches

In collider searches, the annihilation of SM particles into a pair of DM does not leave a signal which can be distinguished from other SM processes. Therefore, an additional component of initial state radiation X is required, which is produced along with the DM particle(s):

$$pp \to \chi\bar{\chi} + \mathrm{X}. \tag{3.1.6}$$

---

[7] Antarctic Muon And Neutrino Detector Array

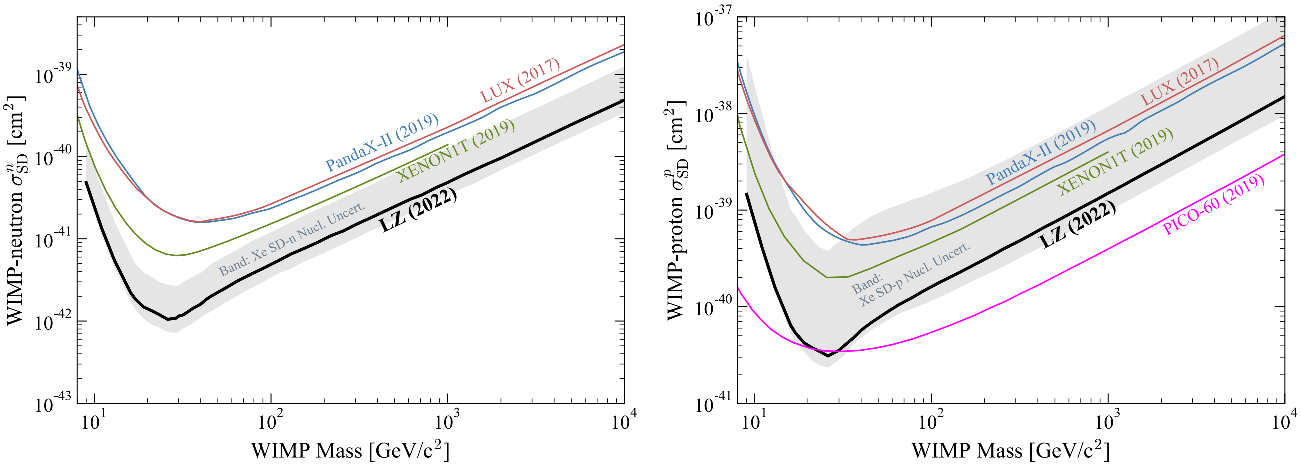

Figure 3.3: Best current bounds on the DM-nucleon cross section for direct and indirect DM detection experiments depending on m_{DM}, shown for the DM-neutron cross section for spin-independent (left) and on the DM-proton cross section for spin-dependent interactions (right). Figure from [20].

Some DM collider searches focus on their initial state radiation signature. This includes, among others, mono-jet, mono-γ, mono-Z or mono-W searches. Alternative strategies focus on the production of other exotic BSM particles, which themselves decay into DM particles. This analysis targets both approaches, as will be discussed in detail in Ch. 5.

3.2 Supersymmetry

3.2.1 Introduction

Supersymmetry (SUSY) is an extension of the SM that postulates a symmetry between bosons and fermions. Fermions with half-integer spin and bosons with integer spin are associated with their superpartners, with integer spin sfermions and half-integer spin bosinos [10]. Figure 3.4 shows the additional considered particles including squarks and sleptons, the superpartners to quarks and leptons, as well as the superpartners to the gauge bosons for the most simple implementation of SUSY, given by the Minimal Supersymmetric Standard Model (MSSM). The model also introduces a WIMP candidate, the lightest supersymmetric partner (LSP), in case R-parity is conserved. R-parity is defined as

$$R = (-1)^{3B+L+2S}, \tag{3.2.1}$$

with baryon number B, lepton number L, and spin S. The baryon number is defined as the number of hadrons consisting of three quark constituents. The conservation of R-parity has direct implications for the dark matter particle in particular, as it ensures the absolute stability of the LSP. In SUSY models, the LSP is the lightest neutralino, which is a massive particle and a superposition of the neutral superpartners of the Higgs and electroweak gauge bosons [11]. Thus, the LSP χ^0_1 can be either bino-, wino-, or higgsino-like.

Due to electroweak symmetry breaking, higgsinos and electroweak gauginos mix with each other [26]. The neutralinos are Majorana mass eigenstates emerging from the diagonalization of the neutralino mass matrix of four electrically and color-neutral SUSY states from neutral higgsinos (H_u^0, H_d^0) and neutral electroweak gauginos ($\tilde{B}$, $\tilde{W}^0$), given by

$$\mathbf{M}_\chi = \begin{bmatrix} M_1 & 0 & -\frac{g' v_d}{\sqrt{2}} & \frac{g' v_u}{\sqrt{2}} \\ 0 & M_2 & \frac{g v_d}{\sqrt{2}} & -\frac{g v_u}{\sqrt{2}} \\ -\frac{g' v_d}{\sqrt{2}} & \frac{g v_d}{\sqrt{2}} & 0 & -\mu \\ \frac{g' v_u}{\sqrt{2}} & -\frac{g v_u}{\sqrt{2}} & -\mu & 0 \end{bmatrix}, \tag{3.2.2}$$

in which M_1 and M_2 are the soft SUSY-breaking bare masses of the bino and wino, g and $g\prime$ the SM SU(2) and U(1) gauge couplings, v_u and v_d the vacuum expectation values of the scalar Higgs doublet neutral components, and μ the mass parameter of the Higgs doublet superfields [27]. The lightest Majorana neutralino $\tilde{\chi}_1^0$, referred to as the LSP, emerges as the dark matter candidate in the context of SUSY.

Similarly, charginos $\tilde{\chi}_1^\pm$ are Dirac mass eigenstates resulting from the mixing between charged higgsinos (H_u^+, H_d^-) and winos ($\tilde{W}^+$, $\tilde{W}^-$) [26].

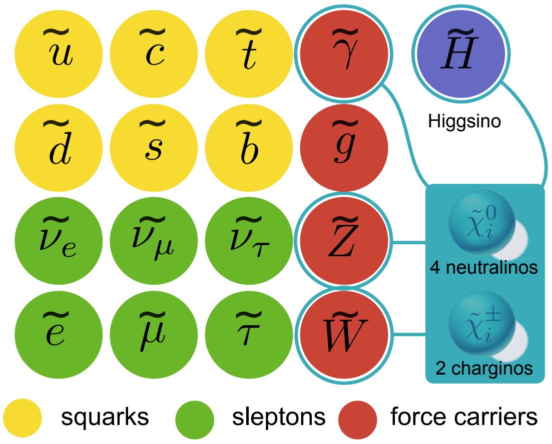

Figure 3.4: The Minimal Supersymmetric Standard Model (MSSM). SM fermions (bosons) are associated with a bosonic (fermionic) superpartner shown in the figure. The superposition of the neutral superpartners of the Higgs and gauge bosons yields four additional neutralinos $\tilde{\chi}_i^0$ and two charginos $\tilde{\chi}_i^\pm$. Figure from [5].

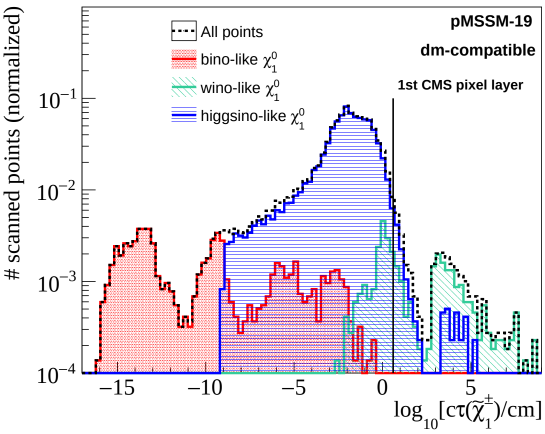

Figure 3.5: Scan over model points in the phenomenological Minimal Supersymmetric Standard Model in which LHC exclusion constraints have been applied. Shown is the number of surviving model points depending on the decay length. The first layer of the pixel detector is marked as a lower bound on the detection capability of the CMS detector with regards to long-lived particles contained in the model points. Figure from [30].

3.2.2 The phenomenological Minimal Supersymmetric Standard Model

The complete description of SUSY by the MSSM introduces over 100 free parameters [26]. By making a number of general assumptions, a more compact version of the model with minimal impact on its phenomenology can be obtained. This new model, the phenomenological Minimal Supersymmetric Standard Model (pMSSM), makes the assumptions of the absence of tree-level flavor changing neutral currents, the absence of CP violation, mass degenerate first and second generation particles, the presence of trilinear couplings only in the third generation, and the assumption of the lightest neutralino being the LSP [28]. In total, the number of free parameters is reduced to 19 parameters defined at the TeV scale. Thus, the pMSSM can be used to study the MSSM as a proxy [29].

The preliminary results of a systematic scan of pMSSM model points provide a further motivation for the search for exotic long-lived particles [30]. Figure 3.5 shows the abundance of model points in the pMSSM depending on the chargino proper decay length, after dark matter constraints imposed by LHC results have been applied. A significant portion of model points with wino-like and higgsino-like dark matter include long-lived charginos with a decay length greater than the first pixel layer of CMS, which potentially can be detected using tracks reconstructed in the CMS tracking detector.

3.3 Exotic long-lived particles

3.3.1 Particle lifetime

The probability of a particle decaying after time t is described by Poisson statistics, and is given by

$$P(t) = \exp\left(-\frac{t}{\gamma\tau}\right), \tag{3.3.1}$$

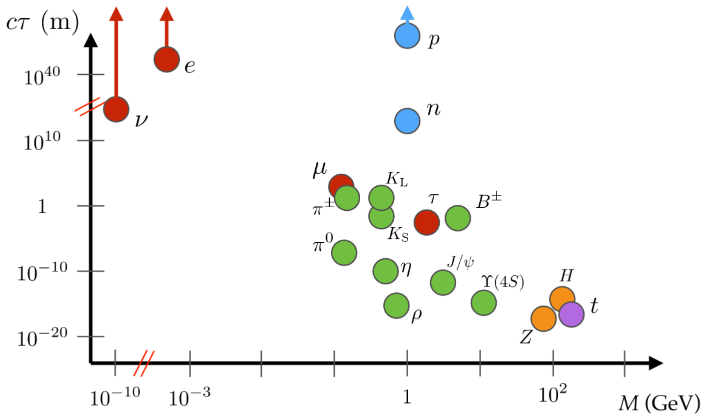

Figure 3.6: Decay length of particles in the Standard Model. Figure from [32]

with the Lorentz boost of the particle given by γ and its proper lifetime τ. The lifetime of a particle τ is the inverse of the decay width,

$$\tau = \frac{1}{\Gamma}. \tag{3.3.2}$$

Particles with both short and long lifetimes exist in the Standard Model, as illustrated by the lifetime of the Z boson $\tau \propto 10^{-25}$ s and the lower bound of the proton lifetime of $\tau \geq 10^{34}$ years, the latter having been established by the Super-Kamiokande experiment [31]. Figure 3.6 shows the wide spectrum of different decay lengths proportional to the lifetime of particles in the Standard Model dependent on their respective mass.

3.3.2 Production mechanisms

Free particles exhibit a long lifetime if their decay is suppressed, which can happen as a result of near mass degeneracies in electroweak supersymmetry, or due to small symmetry-breaking parameters [32]. For example, in a pion decay,

$$\pi^+ \to W^+ \to \mu^+ \nu_\mu, \tag{3.3.3}$$

the quark flavor is not conserved in the electroweak decay, where the decay is thus highly off-shell,

$$\Gamma_{\pi^+} \sim g_W^2 \left(\frac{m_\pi}{m_W}\right)^4 m_{\pi^+}, \tag{3.3.4}$$

with the coupling for the weak interaction of g_W, the pion mass m_π, and the W mass m_W. This highly off-shell decay in turn leads to a longer lifetime of $\tau_{\pi^\pm} = 26.033$ ns for a charged pion compared to a neutral pion, $\tau_{\pi^0} = 8.5$ as, where quark flavor-conserving decays are allowed. Even longer lifetimes can be observed in, for example, the neutron decay,

$$n \to p + W, W \to e^- \bar{\nu}_e, \tag{3.3.5}$$

in which the neutron and proton mass m_n and m_p are nearly mass degenerate due to isospin invariance. The small mass difference implies a small phase space and therefore a long lifetime.

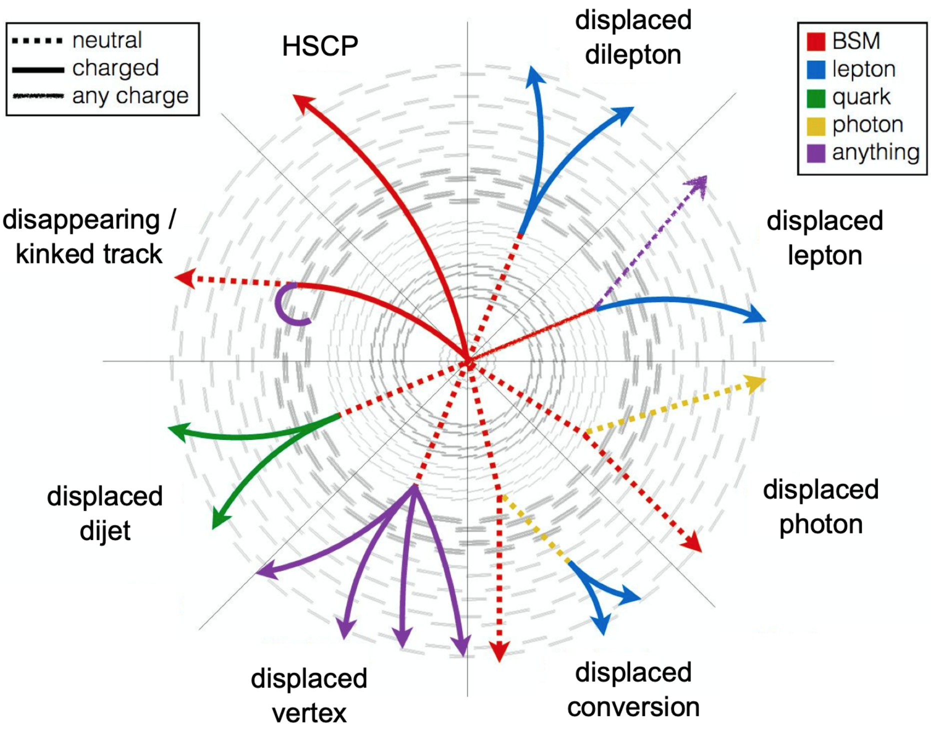

Figure 3.7: Different LLP detection methods in collider searches, including the signature of disappearing tracks. The color of the particles refers to Standard Model particles, such as leptons, quarks or photons as well as BSM particles. Figure taken from [35].

The mediating particle of the decay, the W boson, is thus off-shell as well, and the decay width of the neutron Γ_n is given by

$$\Gamma_n \sim g_W^2 \left(\frac{m_n - m_p}{m_W} \right)^4 (m_n - m_p) \,. \tag{3.3.6}$$

This mechanism leads to a mean lifetime of the free neutron of $\tau_n = 880.2$ s.

The same principle also applies to other scenarios with a small mass splitting between the parent and one of the daughter particles, leading to a compressed phase space and thus to an increased lifetime of the parent particle.

3.3.3 Detection signatures of exotic long-lived particles

In the following, an overview of the different detection signatures of exotic long-lived particles (LLPs) at colliders is given. Specific signatures correspond to different ranges of targetable lifetime, or decay products, and therefore constitute a choice of the targeted phase space. Efforts to compare LLP searches at the LHC are summarized in [33], and recent CMS results are summarized in [34]. Figure 3.7 illustrates the LLP signatures of current LHC searches, which are highlighted counterclockwise. Non-SM particles are depicted in red, with solid curves indicating charged particles, and dashed curves neutral particles.

Heavy stable charged particles (HSCP) are slow-moving particles with $\beta = v/c \lesssim 0.9$, and thus are expected to have a higher rate of energy loss via ionization (dE/dx) and a longer time-of-flight (TOF) [36]. Both aspects are investigated in the search to identify different kinds of

HSCPs, one of which are strongly-interacting HSCPs forming R-hadrons in the context of split SUSY. Other possibilities are HSCPs that behave like leptons as in the minimal gauge-mediated supersymmetry-breaking model (mGMSB), or HSCPs which behave like long-lived lepton-like fermions in a modified Drell-Yan production. For the dE/dx measurement, a discriminator I_{as} is used to distinguish SM particles from HSCP candidates. For the time-of-flight measurements, information from the muon drift tubes (DT) and cathode strip chambers (CSC) is used.

Disappearing tracks may be produced in models with a small mass splitting between a charged massive mother particle and one of its invisible neutral daughter particles, with a non-reconstructed SM daughter particle, and are characterized by missing hits in the outer tracker layers as well as an insignificant deposited energy in the calorimeters. They are the focus of this work and are discussed in detail in Ch. 5.

Kinked tracks are a slightly modified signature, for which the SM particle is reconstructed, usually as a low-momentum curled track.

Displaced dijets and displaced vertices can be both analyzed in a search targeting multijet events [37]. On the one hand, displaced dijets can arise from e.g. a long-lived virtual top squark which decays to a pair of quarks. On the other hand, long-lived neutralino or gluino decaying into a pair of a quark and a squark can create the signature of displaced vertices. For both signatures, the long-lived particle itself remains invisible. The separation between the vertices d_{VV} can be used to discriminate between signal and background, with signal events having two well-separated displaced vertices from two LLPs emitted approximately back-to-back, and background events which are dominated by only one displaced vertex.

LLPs from displaced conversions produce the signature of two leptons originating from a photon decay, which is radiated off a long-lived neutral particle. A displaced photon targets the same production model, but aims to select events based on the displaced photon alone. The displaced lepton and displaced dilepton signatures target a charged (neutral) long-lived particle decaying into one lepton and an additional particle, or two leptons.

Not shown in Fi. 3.7 is the highly unusual signature of stopped exotic, long-lived particles. While the search for HSCPs aims to detect the LLP itself, the complimentary search for stopped particles searches for the decay products of the LLP instead [38]. The slow-moving ($\beta = v/c \lesssim 0.5$) LLPs in question would come to rest in the CMS detector and either their hadronic or muonic decay can be reconstructed during the time between proton-proton collisions. Here, cosmic rays, beam-halo particles, and detector noise are considered as background. To suppress the dominant background of beam-halo particles, events which are at least two bunch crossings away from proton bunches are selected.

3.4 Summary

In conclusion, dark matter has been motivated through astrophysical observations and cosmological arguments, and an electrically neutral WIMP dark matter candidate $\tilde{\chi}_1^0$ has been identified. Supersymmetry provides a consistent theoretical model which includes such a candidate. Following this approach, dark matter $\tilde{\chi}_1^0$ may arise as a decay product in the decay of charginos $\tilde{\chi}_1^\pm$. Given a sufficiently small mass splitting between the chargino and the LSP candidate, $\Delta m(\tilde{\chi}_1^\pm, \tilde{\chi}_1^0)$, the phase space for the decay can be highly compressed, which leads to an increased lifetime of the chargino. In turn, this can lead to the signature of a disappearing track, which has been compared to other signatures of LLP searches at the LHC. The signature is discussed in detail in Ch. 5.

Chapter 4

The Compact Muon Solenoid experiment at the Large Hadron Collider

The collider search for dark matter is performed with the Compact Muon Solenoid (CMS) experiment hosted at the Large Hadron Collider (LHC). The Large Hadron Collider is located at CERN near Geneva in the border region of Switzerland and France. It is a circular collider with a circumference of 27 km. Figure 4.1 shows the location and general layout of the collider, as well as the major LHC experiments including the CMS experiment.

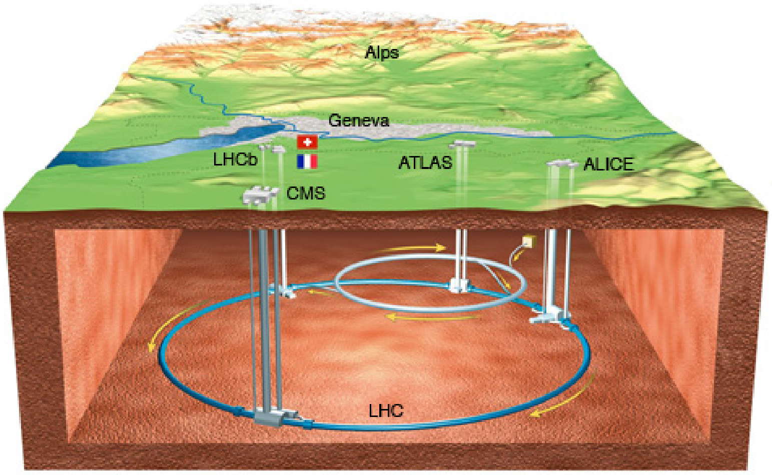

Figure 4.1: The Large Hadron Collider (LHC) with the accompanied main experiments ATLAS, ALICE, CMS and LHCb. Figure from [39].

The following description is based on the CMS documentation [40]. The CMS detector is designed to study collisions at a centre-of-mass energy of up to $\sqrt{s}$ =14 TeV. Figure 4.2 shows a transverse cross section of the general layout of the detector. The inner detector components are surrounded by a superconducting solenoid that creates a magnetic field of $B = 3.8$ T. The innermost layer of the detector encompasses the silicon tracker, which allows for precision measurement of the momentum of charged particles in the magnetic field. The crystal electromagnetic and a sampling hadron calorimeter follow. Outwards, the iron return yoke interspersed with the muon chambers is located. Exemplary particle tracks are indicated in Fig. 4.2 for charged particles including leptons and hadrons, as well as neutral hadrons and a

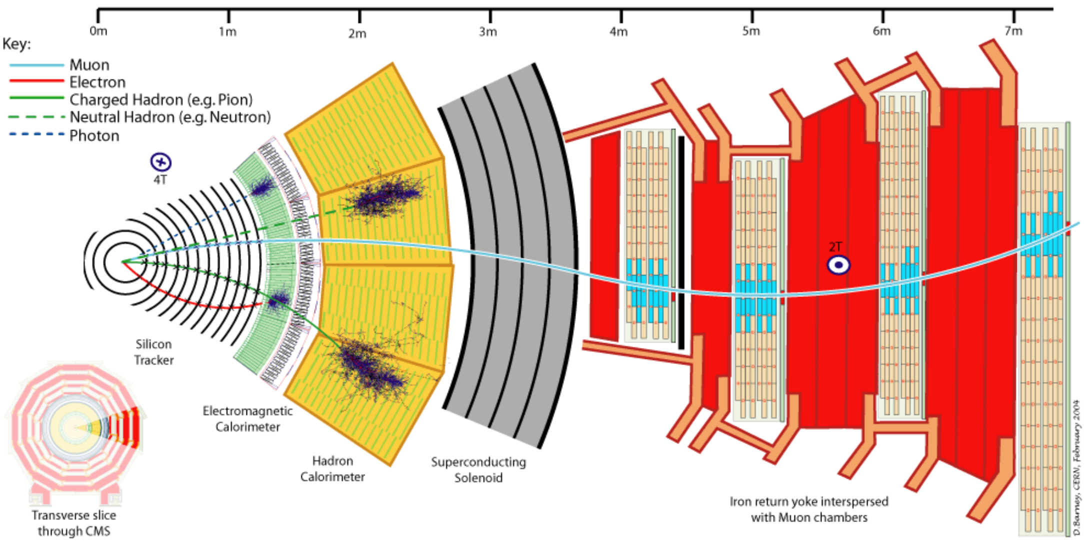

Figure 4.2: Transverse cross section through the Compact Muon Solenoid (CMS) detector. Depicted are the silicon tracker, the electromagnetic and hadron calorimeter, the superconducting solenoid and the muon chambers with exemplary tracks of five different particles. Figure from [41].

photon. Electrons and charged hadrons are shown as bended tracks in the silicon tracker with their energy deposited in the electromagnetic and hadron calorimeter, respectively. Neutral particles such as neutrons or photons only deposit energies in the respective calorimeters most often without leading to tracks in the silicon tracker. Muons are minimum-ionizing particles (MIP) and reach the muon chambers located outwards from the electromagnetic and hadron calorimeter.

In order to describe the different angular regions of the detector, the quantity of pseudorapidity is used, as defined by

$$\eta = -\ln \tan \frac{\theta}{2},$$

where the polar angle θ is 0 or π for the beam directions. In the following, pseudorapidity is used in particular to distinguish between the barrel region ($|\eta| < 1.2$) and the endcap region ($1.2 < |\eta| < 2.4$) of the detector.

4.1 CMS detector components

4.1.1 Tracking detector

The inner tracking system consists of a silicon pixel detector containing 1440 pixel modules in three barrel layers and a silicon strip tracker containing 15148 strip detector modules in 10 barrel detection layers. Charged particles create electron-hole pairs in the silicon material, which is characterized by the presence of a band gap. Electrons can thus be excited from the valence band to the conduction band. The resulting electric current is proportional to the energy of the particle. The number of electron-hole pairs is then measured, and the track of a charged particle can be recorded.

Between data-taking in 2016 and 2017, the pixel detector was upgraded in order to increase tracking efficiency and to mitigate accumulated radiation damage during Run 1 and the be-

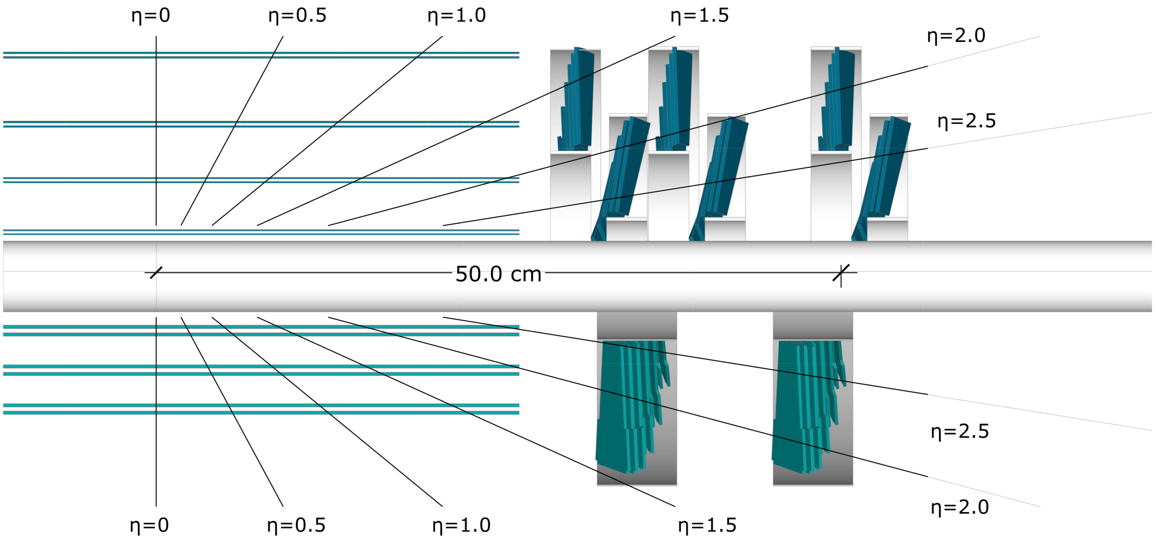

Figure 4.3: CMS inner tracking detector before (bottom) and after (top) the upgrade installed between data-taking in 2016 and 2017. The upgraded detector features an additional silicon pixel layer, as well as the innermost layer located closer to the beam pipe, for BPIX (barrel region of the pixel detector) and an additional endcap disk for FPIX (forward region of the pixel detector). Taken from [42].

ginning of Run 2 in 2016 [42]. The upgrade furthermore served as a preparation for high-luminosity data-taking in the following runs. Figure 4.3 shows a depiction of the inner pixel tracking detector before and after the upgrade. During the upgrade, an additional pixel barrel layer was added, increasing the total number of pixel barrel layers to four with a total of 1184 pixel modules. This, as well as the installation of the innermost pixel barrel layer 10 mm closer to the beam pipe, leads to an improved vertex resolution [43]. In the following, detector conditions before the upgrade are referred to as *Phase 0*, and after the upgrade as *Phase 1*.

The layout of the upgraded tracking detector, depicting the pixel layers in green, is shown in Fig. 4.4 in the $\eta - r$ plane.

The tracking detector also measures the energy loss dE/dx of heavy, charged particles, which

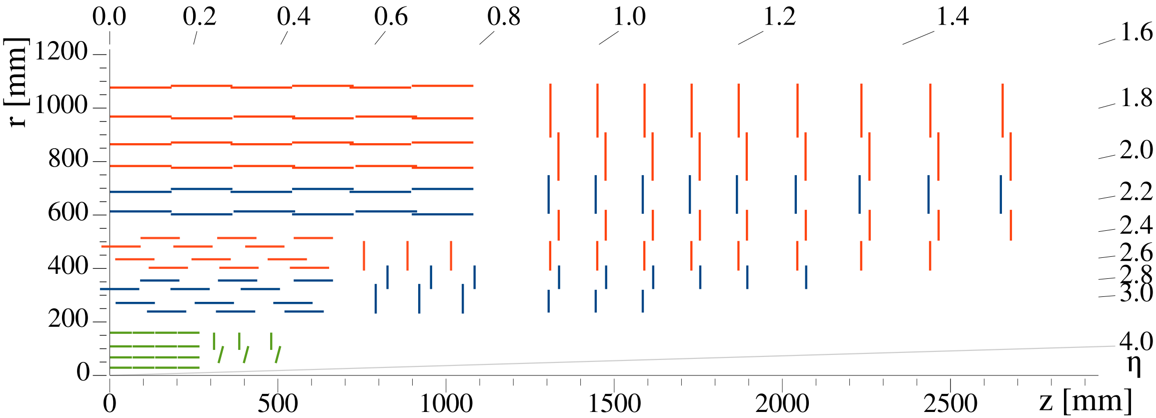

Figure 4.4: Diagram of the Phase 1 tracking detector after the upgrade of the pixel detector, shown in the $r - \eta$ plane. Tracking layers are depicted in the barrel ($|\eta| < 1.479$) and endcap region ($|\eta| > 1.479$). Taken from [44].

is relevant to this search. The *Bethe-Bloch* equation describes the mean rate of the deposited energy loss, and for moderately relativistic charged heavy particles is given by

$$\left\langle \frac{dE}{dx} \right\rangle \propto \frac{Z}{A}\frac{1}{\beta^2}\left[\frac{1}{2}\ln\left(\frac{m_e\beta^2\gamma^2 W_{\max}(m)}{I^2}\right)\right], \tag{4.1.1}$$

with atomic number Z and atomic mass A of the absorber, in this case the silicon tracker material, the electron mass m_e, the mass m of the investigated particle, the ratio $\beta = \frac{v}{c}$, the Lorentz factor γ, the maximum possible energy transfer to an electron $W_{\max}$, and the mean excitation energy I [11]. For this analysis, a dedicated calibration is performed for the measured value of dE/dx, as described in Sec. 5.8.

4.1.2 Electromagnetic calorimeter

The electromagnetic calorimeter is used to measure the energy of charged particles as well as photons and is comprised of individual scintillating lead tungstate ($PbWO_4$) crystals. The calorimeter is structured into a barrel volume with a radius of 129 cm and two endcaps. 61200 crystals are located in the barrel region and 7324 crystals are located in each endcap. An overall high granularity limits the effects of high pile-up [45]. The scintillation of the crystal triggered by electrons and photons is detected with avalanche photodiodes in the barrel and vacuum phototriodes in the endcaps [40].

4.1.3 Hadronic calorimeter

The sampling hadron calorimeter is comprised of an alternating absorber and active scintillation material, structured into a barrel volume and two endcaps as well as an outer calorimeter volume. It is designed to measure the energy of hadrons. The determination of possible missing transverse energy is of special importance. For the absorber material, brass plates are used, with the exception of stainless steel in the inner- and outermost regions. The active material consists of trays of plastic scintillators connected to wavelength shifting fibers. The scintillators are optically connected to hybrid photodiodes.

4.1.4 Muon chambers

Muons are detected through three different types of gaseous detectors depending on the radiation environment for the given muon chamber [46]. Drift tubes (DT) are used in the low-radiation barrel region ($|\eta| < 1.2$). In the endcap region ($|\eta| < 2.4$), cathode strip chambers are used. In order to provide high-precision timing for the trigger information, resistive plate chambers are used in both regions up to $|\eta| < 2.1$ [45].

4.1.5 High-level trigger

As the LHC provides proton-proton collisions at a high rate of 40 MHz, the CMS experiment utilizes a sophisticated trigger system in order to select the events which are to be stored. The reduction of available data is necessary as not all detected events can be recorded and processed due to the high amount of events, which is further increased by multiple interactions from the same bunch crossing referred to as pile-up. The trigger system consists of the hardware-based Level-1 (L1) and the software-based high-level trigger (HLT). The L1 trigger

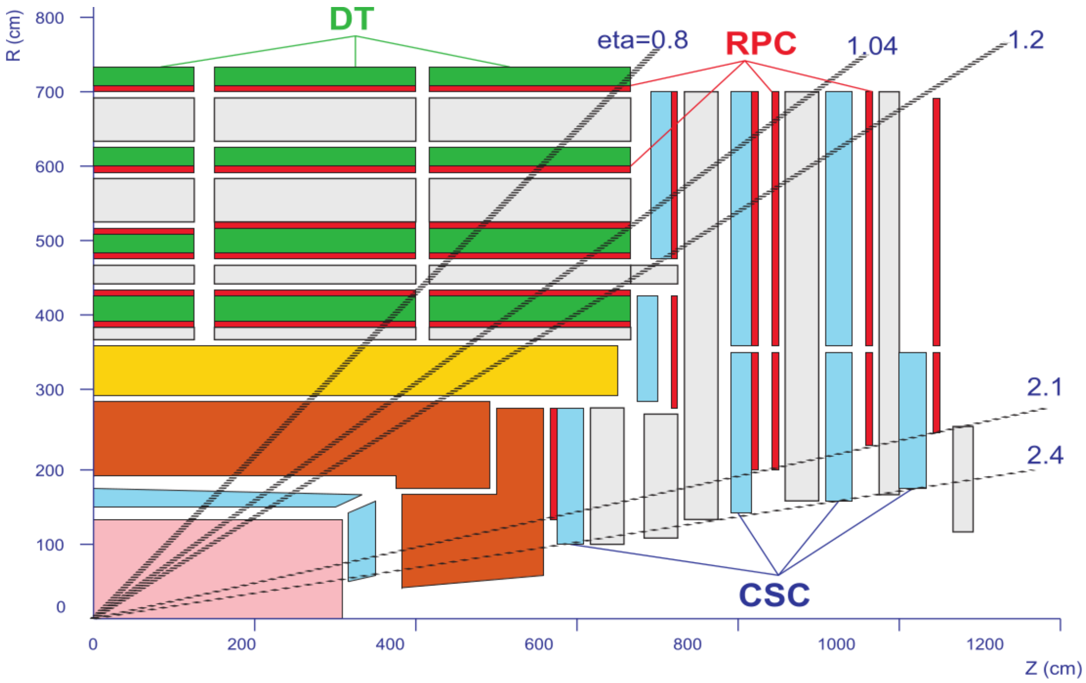

Figure 4.5: Layout of the CMS muon chambers with the location of the different types of gaseous detectors. Shown are drift tubes (DT), resistive place chambers (RPC) and cathode strip chambers (CSC). Reproduced from [45].

uses programmable electronics to analyze coarsely segmented energy deposits in the calorimeters as well as signals in the muon chambers to provide the global calorimeter and global muon trigger information for a given event. Thresholds on these result in a reduced data rate of at most 100 kHz. Detector information is then aggregated by the data acquisition (DAQ) system, which provides the specialized HLT software with a complete data read-out. The combined trigger system provides a reduction of data by a factor of $\approx 10^6$ [40].

The recorded data is stored and processed in the CMS offline computing system, which further provides the data to the Worldwide LHC Computing Grid (WLCG) used for the individual physics analyses.

4.1.6 Luminosity

For a given process with cross section σ, the instantaneous luminosity is given by the ratio of the rate of produced events per unit of time dN/dt and the cross section of the process,

$$\mathcal{L}(t) = \frac{1}{\sigma}\frac{dN}{dt}. \tag{4.1.2}$$

For a collider with two colliding beam bunches with number of particles n_1 and n_2, the luminosity is given by

$$\mathcal{L}(t) = \frac{n_1 n_2 f n_b}{4\pi\sigma_x\sigma_y}, \tag{4.1.3}$$

with the collision frequency f, number of bunches n_b, and transverse and longitudinal widths of the overlapping beams σ_x and σ_y. The amount of data collected during a time period of data-taking t is measured in terms of integrated luminosity,

$$\mathscr{L}_{\text{int}} = \int \mathcal{L}(t)dt. \tag{4.1.4}$$

In the case of the CMS experiment, an absolute scale of the luminosity is measured using van der Meer scans [47]. The area of the overlapping beams $4\pi\sigma_x\sigma_y$ is determined by varying the transverse separation of the two beams over time, and by measuring the rate of a physical observable, e.g. the number of charged particles passing through the tracker volume. Using known parameters n_1, n_2, and n_b, the instantaneous luminosity is determined using Eq. 4.1.3.

4.2 Event reconstruction

In this section, the track reconstruction and the particle flow (PF) algorithms are introduced, which are used to perform the event reconstruction within the CMS experiment. Particular emphasis is placed on the track reconstruction algorithm. The PF algorithm aims to identify all final state particles of each collision event, including jets and leptons as well as missing transverse momentum, and also distinguishes the final state particles from pile-up interactions.

4.2.1 Track reconstruction

This section provides an overview of the tracking algorithm and introduces track properties relevant to the analysis. The following description is based on [48].

The track reconstruction algorithm identifies track trajectories from a collection of measured hits in the tracking detector, as described in Sec. 4.1.1. Tracks are produced by charged particles, which are subsequently identified by a trail of hits, which lie along helical trajectories inside the tracker volume in the presence of a magnetic field. Before the track reconstruction algorithm can be run, the charge clusters collected from traversing charged particles in single tracker layers are merged into tracker layer hits. Tracks are reconstructed using a combinatorial track finder based on Kalman Filtering in three stages. First, a small number of tracker layer hits $n_{\text{hit}} \geq 2$ are selected from consecutive layers which are compatible with a track trajectory for the initial seed generation. The next step takes all tracker layer hits into account to construct a trajectory. Finally, a track fit is performed to obtain further properties such as the track origin, transverse momentum, and direction.

A certain number of tracks is not reconstructed, even though a charged particle traversed the tracker. Furthermore, a spurious track can be reconstructed without the presence of a charged particle. To reduce the misreconstruction rate given by

$$\epsilon_{\text{misreconstructed}} = \frac{n_{\text{reconstructed track not associated with any charged particle}}}{n_{\text{reconstructed}}}, \tag{4.2.1}$$

the combinatorial track finder is re-run for successive iterations. Tracks from iterations with a value of χ^2/ndof close to one and with the track origin compatible with a reconstructed primary vertex are selected. In total, ten iterations of the combinatorial track finder are run, with later iterations aiming to recover tracks which would be discarded by too stringent requirements, such as on the number of missing hits. Missing hits can occur for a given track if the trajectory traverses a tracker layer without a measurement, giving rise to missing inner hits (hits missing between the interaction point and first tracker layer with a measured hit), missing middle hits (between the first and last tracker layers with measured hits) and missing outer hits (beyond the outermost layer with a registered hit). The identification of such tracks is of particular importance for reconstructing disappearing tracks in this thesis.

The primary vertex (PV) can be identified as the vertex with the largest sum of charged tracks, jets and missing energy p_T^2.

4.2.2 Particle flow algorithm

In the following, final-state objects of importance to this analysis which are identified by the PF algorithm are discussed. This includes the reconstruction of leptons, charged and neutral hadrons as well as the missing transverse momentum in an event. PF algorithms in general rely on a fine-grained tracking detector in conjunction with a strong magnetic field, as well as hermetic electromagnetic and hadronic calorimeters, as is the case for the CMS detector.

The PF algorithm aims to link individual detector measurements comprised of *PF elements* into *PF blocks*, which are included in the PF candidate collection of final state objects, if they satisfy all requirements. Once a final state object is identified, the corresponding PF blocks are removed and the PF algorithm processes the remaining blocks. Following [49], the criteria for the final state objects of interest are included in the following.

Muons

In the first step, muons are identified. A muon can be reconstructed either as a *standalone*, a *global* or a *tracker* muon. Standalone muons are reconstructed by forming track seeds from hits in the drift tubes or cathode strip chambers of the muon detector, and a track-fitting is performed using all hits from the DT, CSC and resistive place chambers along the track trajectory. A global muon combines a standalone muon with a compatible inner track, for which the muon hits are within a cone of $\Delta R < 0.3$. In comparison to standalone muons, the momentum resolution for $p_T < 200$ GeV is improved significantly. A tracker muon is reconstructed from tracks with $p_T > 0.5$ GeV and $p > 2.5$ GeV, which can be extrapolated to at least one hit in one muon segment. In the PF algorithm, global and tracker muons are considered. In order to reject hadrons, that would otherwise be mis-identified as muons, the sum $\sigma p_T^{\text{track}} + E_T^{\text{calo}}$ must not exceed 10% of the transverse muon momentum, which acts as a isolation requirement.

Electrons

Electrons are identified in the second step. For isolated electrons which are relevant to the analysis, the PF algorithm incorporates two approaches to perform the reconstruction, depending on the amount of Bremsstrahlung the electron radiates. A Bremsstrahlung process occurs once an electron passes close by a nucleus, which leads to the radiation of a photon. On the other hand, photons can convert into electron-positron pairs, and thus the electron and photon reconstruction are closely related in the PF algorithm. The *ECAL approach* aims to reconstruct an isolated electron by measuring the complete radiated Bremsstrahlung energy in the electromagnetic calorimeter within a small η and extended ϕ window, for which calorimeter deposits with $E > 4$ GeV are considered. The energy deposition in the hadronic calorimeter in a cone of $\Delta R < 0.15$ around the electromagnetic energy deposit is required not to exceed 10% of the energy measured in the electromagnetic calorimeter. Tracks are then iteratively linked with the energy deposit if the track momentum and the measured energy deposit is compatible with the electron hypothesis, namely

$$E_{\text{ECAL}}^2 \approx m_e^2 + p_{\text{track}}^2. \tag{4.2.2}$$

For non-radiating electrons with $p_T > 2$ GeV, a separate track reconstruction is performed in order to allow for a sudden and substantial energy loss along the track trajectory. Here, a Gaussian sum filter is used in place of the Kalman filter employed in Sec. 4.2.1. A resulting track with $\chi^2/\text{ndof} \approx 1$, which can be matched to a deposit in the electromagnetic calorimeter is then classified as an isolated electron, unless the energy deposit itself can be matched to ≥ 3 tracks. Contrarily, energy deposits in the electromagnetic calorimeter without a linked track are classified as photons.

Hadrons

Hadrons are identified in the next step using the remaining PF blocks containing calorimeter deposits not linked to any track. A distinction is made for calorimeter deposits within the tracker acceptance ($\eta < 2.5$) and beyond, as within the tracker acceptance, photons can be reconstructed from the electromagnetic calorimeter deposits, and neutral hadrons from the hadronic calorimeter deposits. Beyond the tracker acceptance, a different strategy has to be employed, therefore electromagnetic calorimeter deposits which are linked to hadronic calorimeter deposits are considered to belong to the same hadron shower, and non-linked electromagnetic calorimeter deposits are identified as photons.

Missing transverse momentum

The negative vectorial sum of the transverse momentum of all particles is defined as the missing transverse momentum vector,

$$\vec{p}_T^{\text{miss}} = - \sum_{i=1}^{N_{\text{PF particles}}} \vec{p}_{T,i}. \tag{4.2.3}$$

Due to momentum conservation, $\vec{p}_T^{\text{miss}}$ is required to be zero for an ideal detector, since the colliding particles ideally have no transverse momentum. However due to detector inefficiencies and due to neutrinos traversing the detector material without interactions, a non-zero missing transverse momentum can be measured for events. The presence of new, hypothetical particles such as dark matter in a collision event could contribute to $\vec{p}_T^{\text{miss}}$ as well.

Chapter 5

Search for disappearing tracks

In this chapter, the search for semi-stable, charged particles using disappearing tracks is presented. First, the strategy and methodology of the search are discussed with an introduction to the targeted signal models, and to the experimental data collected by the CMS experiment used for the analysis. Analysis objects relevant to the search are then defined, and a disappearing track tag based on pre-selected tracks is introduced. Details are then given about the event and trigger selection, for which events with at least one disappearing track are selected. Background sources that may mimic the signature of the signal in the search are identified, and the procedures for estimating them are described. Sources of systematic uncertainty are estimated for the background estimation methods and for the Monte Carlo simulations. The chapter concludes with the results using 137 fb^{-1} of Run 2 data collected by CMS at a centre-of-mass energy of $\sqrt{s} = 13$ TeV.

5.1 Introduction

This search targets highly compressed supersymmetric models featuring a small mass splitting between the two lightest supersymmetric particles,

$$m_\pi \lesssim \Delta m(\tilde{\chi}_1^\pm, \tilde{\chi}_1^0) \lesssim 200\ \text{MeV}. \tag{5.1.1}$$

As introduced in Sec. 3.3, this leads to long proper lifetimes on the order of $\mathcal{O}(\text{ns})$ due to the compressed phase space of the suppressed decay. In particular, wino-like charginos with a mass splitting of $\Delta m(\tilde{\chi}_1^\pm, \tilde{\chi}_1^0) \approx 160$ MeV decay dominantly into a wino-like neutralino and a pion with low momentum [50]. This is illustrated in Fig. 5.1-left, which shows a Feynman graph for the decay $\tilde{\chi}_1^\pm \rightarrow W\tilde{\chi}_1^0$, in which the SM pion is created in the final state though W decay.

In the case of a SM particle in the final state with a sufficiently small momentum so that it is not reconstructed in the particle reconstruction process, the chargino $\tilde{\chi}_1^\pm$ may create the signature of a disappearing track (DTk), which is characterized by missing outer hits in the tracking detector and a negligible energy deposition E_{dep} in the electromagnetic and hadronic calorimeters. This signature is particularly striking, as it is not expected to occur from any SM particle.

Figure 5.1-right shows a Monte Carlo generator event display for a simulated event containing pair-produced long-lived charginos from gluino decays. Overlaid is a diagram of the CMS pixel detector in its Phase 1 configuration with four inner pixel tracking layers. After traversing multiple tracker layers, the chargino eventually decays into a neutralino $\tilde{\chi}_1^0$ and a pion with low transverse momentum p_T, whose trajectory is indicated by the curled track. In or-

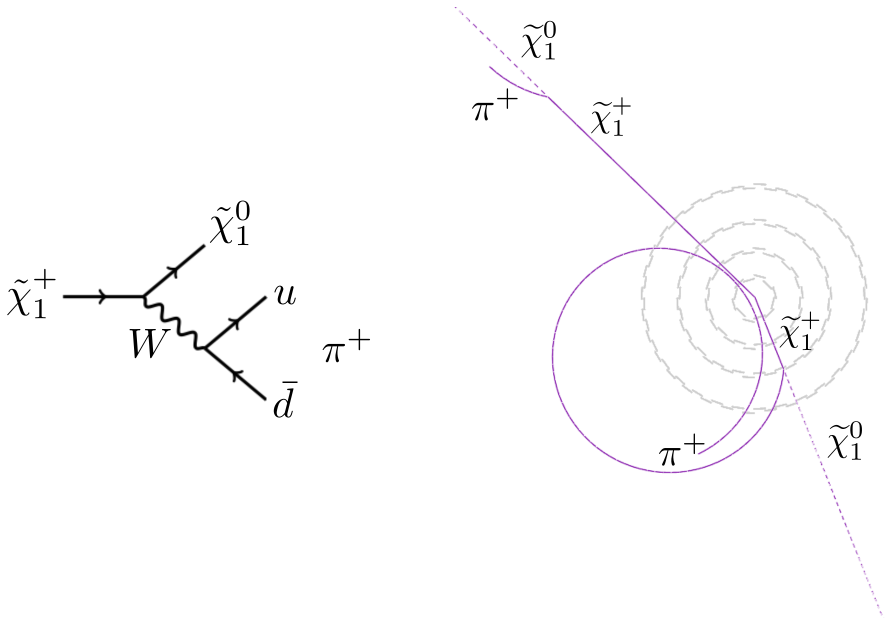

Figure 5.1: Left: Feynman diagram for the decay $\tilde{\chi}_1^{\pm} \to \tilde{\chi}_1^0 W(W \to \pi^+)$. Right: Monte Carlo generator event display for two pair-produced long-lived charginos $\tilde{\chi}_1^{\pm}$ decaying hadronically.

der to ascertain if such low-momentum tracks can be reconstructed, the transverse momentum distribution of the daughter pion and the parent chargino are shown in Fig. 5.2 for a mass splitting of $\Delta m(\tilde{\chi}_1^{\pm}, \tilde{\chi}_1^0) = 180$ MeV. Most pions exhibit a transverse momentum of around $p_T \approx 100$ MeV, which is significantly smaller than the transverse momentum of the parent chargino. For charged hadrons, such as pions, the reconstruction efficiency reaches below 40% at small p_T for $p_T < 200$ MeV, with the particles undergoing nuclear interactions within the tracker material [49]. Therefore, in most cases, the pion from the $\tilde{\chi}_1^{\pm}$ decay is not reconstructed as a track. The chargino decay then produces the signature of a disappearing track.

Due to their high transverse momentum and large mass, charginos $\tilde{\chi}_1^{\pm}$ are expected to be highly-ionizing. As described in Ch. 4.1.1, the energy loss dE/dx is described by the Bethe-Bloch equation with a dependence of the particle velocity and particle mass. The energy loss dE/dx is calibrated as described further below, and dE/dx is used to increase the sensitivity of the search.

Fig. 5.3 shows a diagram of the analysis channels and the analysis binning, which corresponds to different targeted chargino properties. In the analysis, two separate track categories based on the track length are considered. *Short tracks* are defined as tracks which only contain hits measured in the innermost pixel detector, while *long tracks* have hits in the pixel and strip detector with an additional requirement of at least two missing outer hits in the strip tracker. The different track length categories are sensitive to the chargino decay length $c\tau$. In the case of pair-produced charginos with a sufficient decay length $c\tau$, a possible additional scenario includes a disappearing track signature from one chargino with the second chargino mis-reconstructed as a muon. A binning in low and high values of the energy loss dE/dx provides sensitivity to the mass of the chargino, with a large energy loss dE/dx corresponding to a more massive chargino. The binning in number of jets, number of b-tagged jets and $\not{E}_T$ provides sensitivity to the chargino production mechanism.

In the following, specific signal models are discussed, with different chargino production mechanisms and different final states.

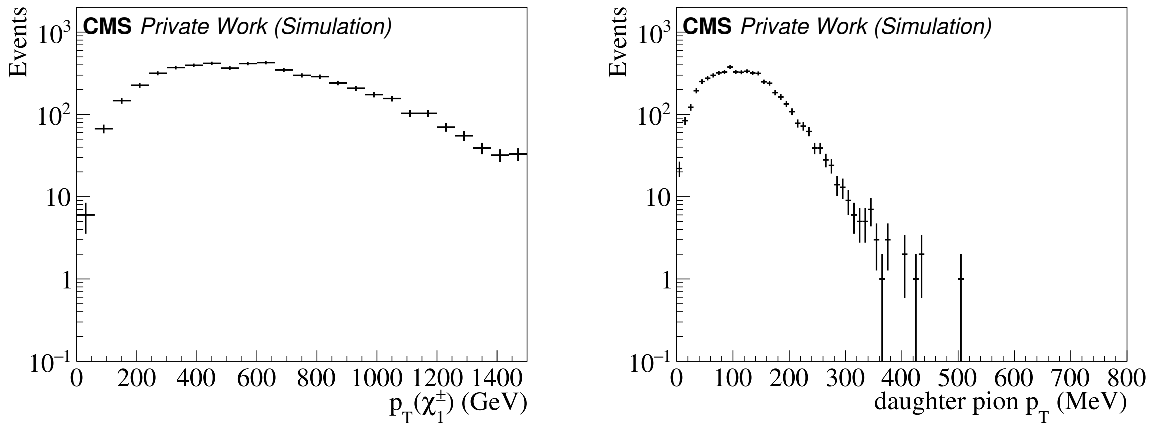

Figure 5.2: Monte Carlo generator transverse momentum p_T distributions of the chargino (left) and the daughter pion (right) for a decay $\tilde{\chi}_1^\pm \rightarrow \tilde{\chi}_1^0\pi^\pm$ with a mass splitting of $\Delta m(\tilde{\chi}_1^\pm, \tilde{\chi}_1^0) = 180$ MeV. The chargino is produced via gluino-associated production with $m_{\tilde{g}} = 1.8$ TeV, and the LSP mass is set to $m_{\tilde{\chi}_1^0} = 1.4$ TeV.

5.2 Signal models

Signal models are identified from simplified models in the context of the MSSM and the pMSSM, as introduced in Sec. 3.2. Simplified models describe hypothetical particles and their production and decay sequences [51], based on a very small number of free parameters, in this case, the mass and lifetime of long-lived charginos $\tilde{\chi}_1^\pm$, as well as the mass of an additional associated SUSY particle. Particle masses for particles which are not considered in a given simplified model are set to infinity. Gluino- and squark-associated $\tilde{\chi}_1^\pm$ production are considered, along with both hadronic and leptonic final states. Leptons can enter the final state through electroweak processes such as $Z \rightarrow l\bar{l}$ decays, or off-shell heavy quark decays such as $b \rightarrow tW(W \rightarrow l\bar{\nu})$. Furthermore, a separate simplified model is considered in order to interpret the results of this search in terms of a nearly-pure Higgsino DM candidate [52, 53]. Simulated MC samples are generated using Madgraph5 aMC@NLO for each simplified model [54]. These are afterwards used to construct the disappearing track tag, to optimize the signal region binning, to obtain scale factors and to interpret the results of the analysis. In the following, details of the simplified models are provided, with the models categorized as hadronic final states, leptonic-inclusive final states and nearly-pure Higgsino LSP configuration.

Simplified models are categorized in a `Tx-finalstate` naming scheme, where in the case of one vertex per branch $x = 1$ is used for gluino-associated production, and $x = 2$ is used for squark-associated production. In the case of ≥ 2 vertices per branch, $x = 5$ and $x = 6$ are used instead, respectively [51]. The products in the final state are then included as `finalstate`. Thus, the simplified model shown in Fig. 5.4-left is referred to as T1qqqq, and the Fig. 5.4-right is referred to as T2qq.

5.2.1 Hadronic final states

Figure 5.4 shows two simplified models with mostly hadronic final states with gluino-associated chargino production (T1qqqq, Fig. 5.4-left) and squark-associated chargino production (T2qq, Fig. 5.4-right). Both squarks and gluinos are being produced in pairs. In the case of gluino-associated chargino production, the branching fraction $\tilde{g} \rightarrow q\bar{q}\tilde{\chi}_1^0$ is assumed to be 33% in the simplified model, while the branching fraction for $\tilde{g} \rightarrow q\bar{q}\tilde{\chi}_1^\pm$ is assumed to be 66% due to the

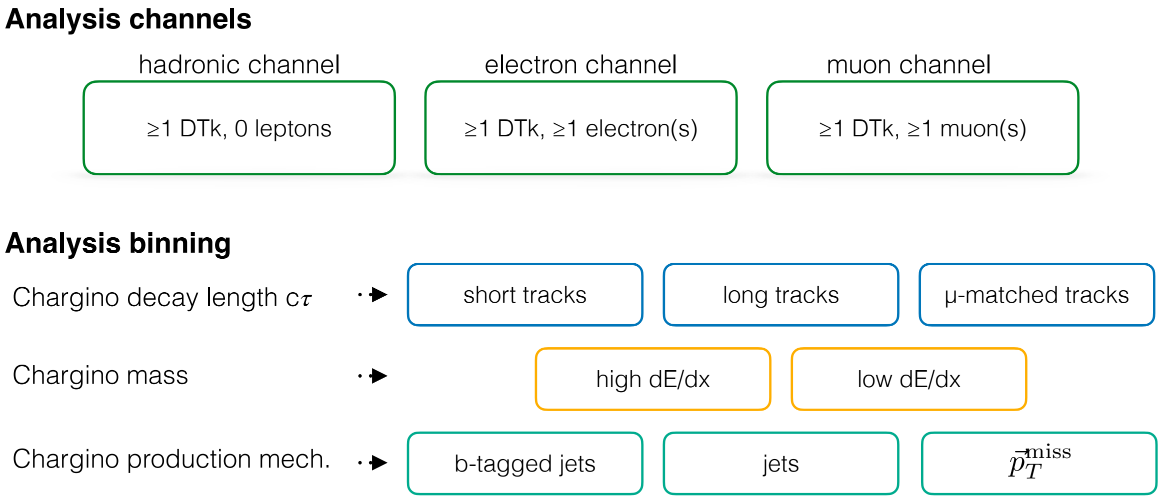

Figure 5.3: Diagram depicting the analysis channels and the analysis binning, which corresponds to different targeted chargino properties.

differently charged charginos in the latter decay. For squark-associated chargino production, the charge of the quark determines the chargino charge, therefore the branching fraction of both decays $\tilde{q} \to q\tilde{\chi}_1^\pm$ and $\tilde{q} \to q\tilde{\chi}_1^0$ are 50%.

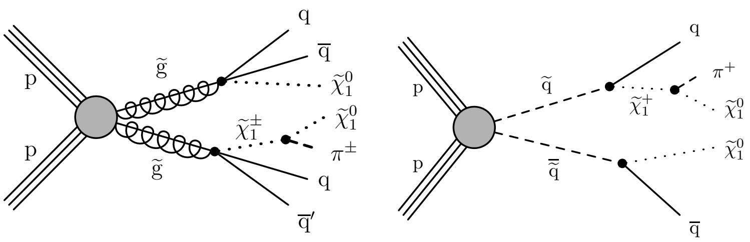

Figure 5.4: Diagrams of simplified models relevant for the hadronic final state, left: gluino-associated chargino $\tilde{\chi}_1^\pm$ production (T1qqqq), right: squark-associated chargino $\tilde{\chi}_1^\pm$ production (T2qq).

The proper decay length $c\tau$ is set to 10, 50, 100 and 200 cm, resulting in different decay lengths in the detector frame, depending on the boost of the chargino decay products. Simplified models with a hadronic final state are used in the training of boosted decision trees to select disappearing tracks, while for the interpretation of the results simplified models with a leptonic-inclusive final state are used, as described in the next section.

5.2.2 Single-electron and single-muon final states

Simplified models allowing for leptons in the final state are shown in Fig. 5.5, which include gluino-associated $\tilde{\chi}_1^\pm$ pair production (T5btbtLL) and pair production of top squarks (T6btLL) and bottom squarks (T6tbLL). Leptons can arise in the final state from leptonic top quark decays ($t \to bW(W \to l\nu)$).

A scan of the model space is performed for the top squark and bottom squark masses and the LSP mass $m_{\tilde{\chi}_1^0}$ in order to interpret the results. Details are given in Ch. 6.3. The proper decay length $c\tau$ is a free parameter between 10-200 cm.

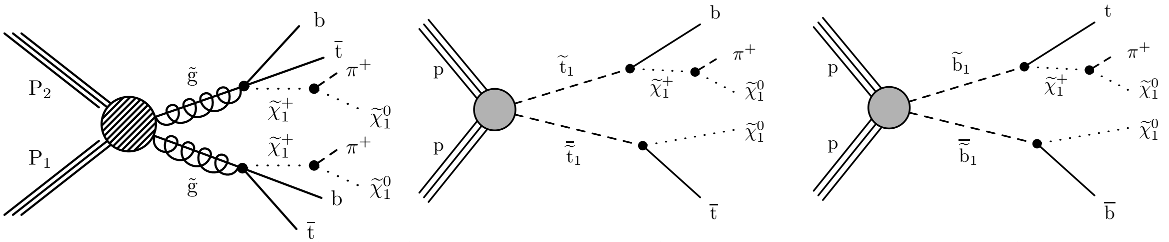

Figure 5.5: Diagrams of simplified models relevant for the leptonic and hadronic final states. Final state leptons can arise trough e.g. top decay. From left to right: T5btbtLL, T6btLL and T6tbLL.

Model name	Description	Decays
T6btLL	top squark-associated $\tilde{\chi}^\pm_1$ production	$\tilde{t} \to t\tilde{\chi}^0_1, \tilde{t} \to b\tilde{\chi}^\pm_1$
T6tbLL	bottom squark-associated $\tilde{\chi}^\pm_1$ production	$\tilde{b} \to b\tilde{\chi}^0_1, \tilde{b} \to t\tilde{\chi}^\pm_1$
T5btbtLL	gluino-associated $\tilde{\chi}^\pm_1$ production	$\tilde{g} \to b\bar{b}\tilde{\chi}^0_1, t\bar{t}\tilde{\chi}^0_1, t\bar{b}\tilde{\chi}^-_1, \bar{t}b\tilde{\chi}^+_1$
TChiWZ	models containing a nearly pure higgsino LSP	$\tilde{\chi}^0_2 \to Z\tilde{\chi}^0_1, \tilde{\chi}^\pm_1 \to \tilde{\chi}^0_1\pi^\pm$
TChiWW		$\tilde{\chi}^\pm_1 \to \tilde{\chi}^0_1\pi^\pm, \tilde{\chi}^\mp_1 \to \tilde{\chi}^0_1\pi^\mp$
TChiZ		$\tilde{\chi}^\pm_1 \to \tilde{\chi}^0_1\pi^*, \tilde{\chi}^0_1$

Table 5.1: Overview of the simplified models considered in this analysis.

5.2.3 Nearly-pure Higgsino LSP

As introduced in Sec. 3.3, the nearly-pure Higgsino LSP is a prime dark matter candidate that it is not excluded by recent observational data [27]. In order to interpret the results in terms of a nearly-pure Higgsino LSP, an additional simplified model is considered, for which further constraints are placed on the relationship between the mass eigenstates $\tilde{\chi}^0_2$, $\tilde{\chi}^\pm_1$ and $\tilde{\chi}^0_1$. The mass difference $\Delta m^0 = \Delta m(\tilde{\chi}^0_2, \tilde{\chi}^\pm_1)$ is taken to be twice the value of that between the charged and lightest states $\Delta m^\pm = \Delta m(\tilde{\chi}^\pm_1 \tilde{\chi}^0_1)$, consistent with the limit at large tanβ. Both the mass difference $\Delta m^\pm$ and the mass of the chargino are free parameters in this model. Figure 5.6 shows Feynman graphs for the simplified model with single-$\tilde{\chi}^\pm_1$ and $\tilde{\chi}^\pm_1$ pair production, including TChiL and TChiLL.

In the case of nearly-pure Higgsino dark matter, radiative corrections invoke an irreducible mass splitting $\Delta m^\pm$ on the order of $\mathcal{O}(100)$ MeV [27].

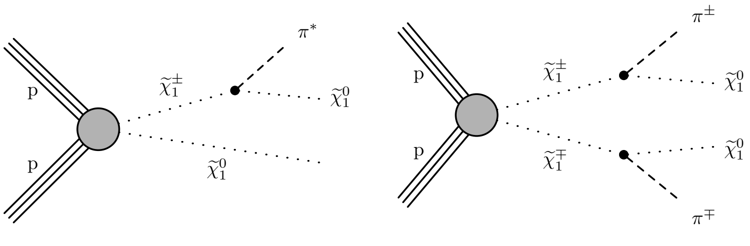

Figure 5.6: Feynman diagrams for a simplified model featuring a nearly-pure Higgsino LSP with single-$\tilde{\chi}^\pm_1$ production (left, TChiL) and $\tilde{\chi}^\pm_1$ pair production (right, TChiLL).

Similarly to lepton-inclusive final state simplified models, a grid mass scan is performed based on $\Delta m^\pm$ and $m_{\tilde{\chi}^\pm_1}$, with details given in Ch. 6.3 for the interpretation of the results in terms of this simplified model.

Tab. 5.1 provides a summary of the simplified models considered in this analysis.

5.3 Datasets

This section provides details on the data used in the analysis and on the simulation of MC samples for both SM background and simplified signal models.

5.3.1 Collected data

This analysis uses data recorded by CMS during Run 2 from 2016 to 2018 with a centre-of-mass energy of $\sqrt{s} = 13$ TeV. The amount of data collected during data-taking is measured in terms of integrated luminosity, as defined in Ch. 4.

Various high-level triggers (HLT) are used in this analysis for both signal selection and the selection of control regions, that are later used for background estimates. Specifically, the E_T^{miss}, single-electron, and single-muon datasets are used for both purposes. The JetHT datastream is used to estimate part of the SM background (Sec. 5.11).

Table 5.2 shows the recorded luminosity for the analyzed run periods, with total integrated luminosities for all years of Run 2 given in Tab. 5.3. Data are only processed for the analysis for luminosity blocks that correspond to calibrated detector conditions and have been approved for physics, and nominal data-taking and detector conditions can be ensured.

2016 Dataset	**–**	B	C	D	E	F	G	H	Total
MET	–	5.82	2.60	4.29	4.07	3.14	7.65	8.74	36.30
JetHT	–	5.79	2.60	4.28	4.06	3.14	7.65	8.74	36.26
SingleElectron	–	5.82	2.60	4.29	4.07	3.14	7.65	8.74	36.30
SingleMuon	–	5.82	2.60	4.29	4.07	3.14	7.65	8.74	36.30
2017 Dataset	–	B	C	D	E	F	G	H	Total
MET	–	4.07	9.60	2.72	9.89	15.09		–	41.37
JetHT	–	5.32	8.74	4.09	10.09	13.27		–	41.51
SingleElectron	–	4.63	10.13	4.06	9.62	13.01		–	41.44
SingleMuon	–	6.05	7.58	4.02	8.89	14.99		–	41.52
2018 Dataset	A	B	C	D	–	–	–	–	Total
MET	13.15	5.67	7.43	32.84	–	–	–	–	59.09
JetHT	14.77	6.83	6.55	31.22	–	–	–	–	59.37
EGamma	14.33	6.63	6.65	31.96	–	–	–	–	59.58
SingleMuon	14.35	7.46	6.70	30.52	–	–	–	–	59.03

Table 5.2: Data recorded by CMS during Run 2 data-taking, with integrated luminosity values given in fb^{-1} for all individual run periods.

Run 2	Total (fb^{-1})
MET	136.76
JetHT	137.15
SingleElectron, EGamma	137.32
SingleMuon	136.85

Table 5.3: Integrated luminosity for Run 2.

During Run 2 data-taking, a number of detector-related issues have been identified, which require a time-dependent veto on certain detector regions for the run number ranges in which the particular issue caused the detector to deviate from nominal data-taking conditions.

5.3.2 Radiation damage to the innermost tracker layer

During data-taking in 2016, the innermost layer in the pixel detector barrel suffered radiation damage, requiring the installation of a new pixel detector for data-taking in 2017 and 2018, as discussed in Ch. 4.1.1. Figure 5.7 shows the hit efficiency before and after the installation of the upgraded pixel detector. The inefficiency of the innermost pixel layer is in particular relevant for the reconstruction of very short disappearing tracks.

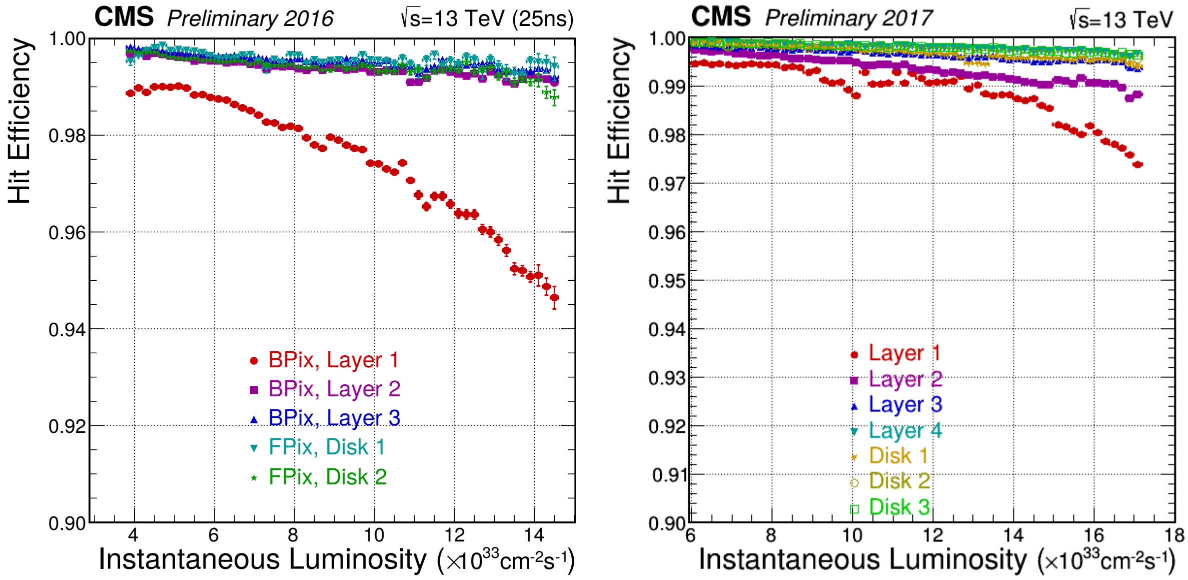

Figure 5.7: Hit efficiency for the pixel barrel layers and forward discs, shown for the instantaneous luminosity during data-taking in 2016 (left) and 2017 (right). A decrease in hit efficiency is visible for 2016 due to radiation damage effects, which is mitigated by the updated pixel detector in use since 2017. Taken from [55].

5.3.3 Level-1 pre-firing inefficiency

The level-1 pre-firing inefficiency was found for data recorded in 2016 and 2017 in the forward hadron calorimeter region (for large pseudorapidities of $\eta > 2.5$). It was caused by particles interacting in the photomultiplier anodes, rather than in the calorimeter itself [56]. The run period most strongly affected by the inefficiency is found to be `2017F`. The inefficiency is studied for signal Monte Carlo samples, as it can potentially decrease the signal event yield.

5.3.4 Electromagnetic calorimeter endcap noise

In 2017, the electromagnetic calorimeter exhibited increased noise in the endcap region between $2.65 < |\eta| < 3.14$ due to a loss in transparency. This affected the ParticleFlow missing transverse energy calculation. This in turn showed a rising disagreement between data and MC for increasing luminosity. The issue is corrected by re-calculating the missing transverse energy with vetoing jets and associated PF candidates in this η region for $p_T < 75$ GeV, as well as all unclustered PF candidates. In the data samples listed above, $E_{T,\mathrm{PF}}^{\mathrm{miss}}$ has been re-calculated to account for this issue.

5.3.5 Hadronic calorimeter Front End Driver (FED) inactivity

Two sectors of the hadronic calorimeter[1] were no longer operable after power interruptions on the 30th June 2018 until the end of data-taking in 2018. Starting with run number 319077 in 2018, electrons and disappearing track candidates from a 40 degree section ($-3.2 < \eta < -1.2$ and $-1.77 < \phi < -0.67$) are discarded in this analysis in order to not include the affected region.

5.4 Simulated Monte-Carlo samples

Monte Carlo generators are used to model high-energy collision processes. Depending on the generator, the *hard process* as well as the final state parton shower and hadronization is generated. Here, *hard process* refers to a hard scattering process between partons, while a parton shower generator aims to additionally simulate the underlying event and further radiation. The standard output format of such generators is the Les Houches Event (LHE) file format, as defined by [57]. The output is then further used in the detector response simulation.

Madgraph5 aMC@NLO [54] is a versatile framework which is capable of simulating both SM and BSM processes. For a given initial and final state, it determines the cross section and generates the hard interactions. QCD corrections to SM processes can be determined with next-to-leading order (NLO) accuracy. POWHEG BOX [58] is a general framework for NLO MC particle shower calculations. It provides integrated simulation of SM and BSM processes, and furthermore it can also be used with other MC generators for showering. Pythia8 [59] models high-energy collision processes at leading order and features integrated hard processes and models for initial and final state parton showers, parton-parton interactions and particle decays.

The CMS detector response simulation may be simulated with either a full or a parameterized simulation. The full CMS detector simulation is performed using the GEANT4 toolkit [60], which is included in the CMS software (CMSSW) framework. It simulates the passage of particles through matter, which may be arranged in a complex geometry as it is the case of the CMS detector. The physics simulation includes electromagnetic, hadronic and optical processes with a library of predefined particles, materials and geometrical elements. The program itself uses Monte Carlo techniques to model the passage and decay with subsequent showering of particles, where different kinds of matter yield respective stochastic parameters for the simulation [60].

FastSim, on the other hand, offers an advantage in computing time by a factor of ≈ 20 [61, 62]. This is achieved by using a simplified version of the material geometry and calculating a parameterized response for a given simulated particle.

5.4.1 Standard Model Monte-Carlo background

Leptonic W decays, top-antitop quark decays, QCD as well as leptonic Drell-Yan processes are simulated using Madgraph5 aMC@NLO and Pythia8. POWHEG BOX is used to simulate single-top production and the leptonic WW diboson background. Tables 5.4-5.5 show the background MC datasets with the respective dataset paths, along with the cross section and resulting luminosity, for Phase 0 and Phase 1, respectively.

---

[1] Specifically, the affected sectors are `HEM15` and `HEM16`.

2016 dataset name	σ (pb)	$\int Ldt$ (fb^{-1})
WJetsToLNu_HT-100To200_TuneCUETP8M1_13TeV-madgraphMLM-pythia8	1627.45	6.11
WJetsToLNu_HT-200To400_TuneCUETP8M1_13TeV-madgraphMLM-pythia8	435.24	89.57
WJetsToLNu_HT-400To600_TuneCUETP8M1_13TeV-madgraphMLM-pythia8	59.18	131.12
WJetsToLNu_HT-600To800_TuneCUETP8M1_13TeV-madgraphMLM-pythia8	14.58	1281.72
WJetsToLNu_HT-800To1200_TuneCUETP8M1_13TeV-madgraphMLM-pythia8	6.660	1175.76
WJetsToLNu_HT-1200To2500_TuneCUETP8M1_13TeV-madgraphMLM-pythia8	1.608	4273.91
WJetsToLNu_HT-2500ToInf_TuneCUETP8M1_13TeV-madgraphMLM-pythia8	0.039	67792.88
TTJets_TuneCUETP8M1_13TeV-madgraphMLM-pythia8	831.76	12.26
TTJets_SingleLeptFromT_TuneCUETP8M1_13TeV-madgraphMLM-pythia8	182.72	337.24
TTJets_SingleLeptFromTbar_TuneCUETP8M1_13TeV-madgraphMLM-pythia8	182.72	330.25
TTJets_DiLept_TuneCUETP8M1_13TeV-madgraphMLM-pythia8	88.34	349.06
TTJets_HT-600to800_TuneCUETP8M1_13TeV-madgraphMLM-pythia8	2.685	5343.28
TTJets_HT-800to1200_TuneCUETP8M1_13TeV-madgraphMLM-pythia8	1.096	9607.90
TTJets_HT-1200to2500_TuneCUETP8M1_13TeV-madgraphMLM-pythia8	0.194	15097.94
TTJets_HT-2500toInf_TuneCUETP8M1_13TeV-madgraphMLM-pythia8	0.002	646450.58
ST_s-channel_4f_leptonDecays_13TeV-amcatnlo-pythia8_TuneCUETP8M1	3.340	116.20
ST_t-channel_top_4f_inclusiveDecays_13TeV-powhegV2-madspin-pythia8_TC	136.02	493.35
ST_t-channel_antitop_4f_inclusiveDecays_13TeV-powhegV2-madspin-pythia8_TC	80.95	479.44
ST_tW_antitop_5f_NoFullyHadronicDecays_13TeV-powheg_TuneCUETP8M1	19.47	167.27
ST_tW_top_5f_NoFullyHadronicDecays_13TeV-powheg_TuneCUETP8M1	19.47	167.29
QCD_HT200to300_TuneCUETP8M1_13TeV-madgraphMLM-pythia8	1717000.00	0.03
QCD_HT300to500_TuneCUETP8M1_13TeV-madgraphMLM-pythia8	351300.00	0.15
QCD_HT500to700_TuneCUETP8M1_13TeV-madgraphMLM-pythia8	31630.00	1.98
QCD_HT700to1000_TuneCUETP8M1_13TeV-madgraphMLM-pythia8	6802.00	2.30
QCD_HT1000to1500_TuneCUETP8M1_13TeV-madgraphMLM-pythia8	1206.00	12.61
QCD_HT1500to2000_TuneCUETP8M1_13TeV-madgraphMLM-pythia8	120.40	98.33
QCD_HT2000toInf_TuneCUETP8M1_13TeV-madgraphMLM-pythia8	25.24	238.49
ZJetsToNuNu_HT-100To200_13TeV-madgraph	344.83	70.39
ZJetsToNuNu_HT-200To400_13TeV-madgraph	95.53	259.19
ZJetsToNuNu_HT-400To600_13TeV-madgraph	13.20	747.31
ZJetsToNuNu_HT-600To800_13TeV-madgraph	3.148	1831.99
ZJetsToNuNu_HT-800To1200_13TeV-madgraph	1.451	1495.71
ZJetsToNuNu_HT-1200To2500_13TeV-madgraph	0.355	1447.84
ZJetsToNuNu_HT-2500ToInf_13TeV-madgraph	0.009	47414.35
DYJetsToLL_M-50_HT-100to200_TuneCUETP8M1_13TeV-madgraphMLM-pythia8	181.30	60.77
DYJetsToLL_M-50_HT-200to400_TuneCUETP8M1_13TeV-madgraphMLM-pythia8	50.42	190.59
DYJetsToLL_M-50_HT-400to600_TuneCUETP8M1_13TeV-madgraphMLM-pythia8	6.984	1392.58
DYJetsToLL_M-50_HT-600to800_TuneCUETP8M1_13TeV-madgraphMLM-pythia8	1.681	4932.14
DYJetsToLL_M-50_HT-800to1200_TuneCUETP8M1_13TeV-madgraphMLM-pythia8	0.775	3447.37
DYJetsToLL_M-50_HT-1200to2500_TuneCUETP8M1_13TeV-madgraphMLM-pythia8	0.186	3200.91
DYJetsToLL_M-50_HT-2500toInf_TuneCUETP8M1_13TeV-madgraphMLM-pythia8	0.004	91105.26
WWTo1L1Nu2Q_13TeV_amcatnloFXFX_madspin_pythia8	50.00	40.69
WWTo2L2Nu_13TeV-powheg	12.18	164.15
WZTo1L1Nu2Q_13TeV_amcatnloFXFX_madspin_pythia8	10.71	764.54
WZTo1L3Nu_13TeV_amcatnloFXFX_madspin_pythia8	3.058	170.33
WWZ_4F_TuneCP5_13TeV-amcatnlo-pythia8	0.165	1172.24
WZZ_TuneCP5_13TeV-amcatnlo-pythia8	0.056	3468.14
ZZZ_TuneCP5_13TeV-amcatnlo-pythia8	0.014	13043.84

Table 5.4: Simulated SM samples used in the analysis for Phase 0 (2016 MC). The cross sections are calculated to NNLO.

5.4.2 Signal Monte-Carlo samples

The simplified models discussed in Sec. 5.2 are simulated using Madgraph5 aMC@NLO, with parton showering simulated with Pythia8. For simplified models with a hadronic final state as introduced in Sec. 5.2.1, a full detector simulation has been performed for Phase 0, and a parameterized fast detector simulation using FastSim has been performed for Phase 1. For simplified models with an lepton-inclusive final state as well as for the simplified model fea-

2017 dataset name	σ (pb)	$\int L dt$ (fb^{-1})
WJetsToLNu_HT-100To200_TuneCP5_13TeV-madgraphMLM-pythia8	1627.45	21.96
WJetsToLNu_HT-200To400_TuneCP5_13TeV-madgraphMLM-pythia8	435.24	48.56
WJetsToLNu_HT-400To600_TuneCP5_13TeV-madgraphMLM-pythia8	59.18	239.73
WJetsToLNu_HT-600To800_TuneCP5_13TeV-madgraphMLM-pythia8	14.58	1471.62
WJetsToLNu_HT-800To1200_TuneCP5_13TeV-madgraphMLM-pythia8	6.660	3020.20
WJetsToLNu_HT-1200To2500_TuneCP5_13TeV-madgraphMLM-pythia8	1.608	12269.07
WJetsToLNu_HT-2500ToInf_TuneCP5_13TeV-madgraphMLM-pythia8	0.039	508831.27
TTJets_TuneCP5_13TeV-madgraphMLM-pythia8	831.76	9.63
TTJets_SingleLeptFromT_TuneCP5_13TeV-madgraphMLM-pythia8	182.72	337.26
TTJets_SingleLeptFromTbar_TuneCP5_13TeV-madgraphMLM-pythia8	182.72	309.66
TTJets_DiLept_TuneCP5_13TeV-madgraphMLM-pythia8	88.34	320.56
TTJets_SingleLeptFromT_genMET-150_TuneCP5_13TeV-madgraphMLM-pythia8	9.684	1476.65
TTJets_SingleLeptFromTbar_genMET-150_TuneCP5_13TeV-madgraphMLM-pythia8	9.658	848.46
TTJets_DiLept_genMET-150_TuneCP5_13TeV-madgraphMLM-pythia8	5.919	1463.03
TTJets_HT-600to800_TuneCP5_13TeV-madgraphMLM-pythia8	2.685	29849.58
TTJets_HT-800to1200_TuneCP5_13TeV-madgraphMLM-pythia8	1.096	35778.74
TTJets_HT-1200to2500_TuneCP5_13TeV-madgraphMLM-pythia8	0.194	65027.68
TTJets_HT-2500toInf_TuneCP5_13TeV-madgraphMLM-pythia8	0.002	1899830.47
ST_s-channel_4f_leptonDecays_TuneCP5_PSweights_13TeV-amcatnlo-pythia8	3.340	1154.17
ST_t-channel_top_4f_inclusiveDecays_TuneCP5_13TeV-powhegV2-madspin-pythia8	136.02	43.13
ST_t-channel_antitop_4f_inclusiveDecays_TuneCP5_13TeV-powhegV2-madspin-pythia8	80.95	48.67
ST_tW_antitop_5f_NoFullyHadronicDecays_TuneCP5_PSweights_13TeV-powheg-pythia8	19.47	272.59
ST_tW_top_5f_NoFullyHadronicDecays_TuneCP5_PSweights_13TeV-powheg-pythia8	19.47	237.87
QCD_HT200to300_TuneCP5_13TeV-madgraph-pythia8	1717000.00	0.03
QCD_HT300to500_TuneCP5_13TeV-madgraph-pythia8	351300.00	0.06
QCD_HT500to700_TuneCP5_13TeV-madgraph-pythia8	31630.00	1.77
QCD_HT700to1000_TuneCP5_13TeV-madgraph-pythia8	6802.00	2.92
QCD_HT1000to1500_TuneCP5_13TeV-madgraph-pythia8	1206.00	13.81
QCD_HT1500to2000_TuneCP5_13TeV-madgraph-pythia8	120.40	94.55
QCD_HT2000toInf_TuneCP5_13TeV-madgraph-pythia8	25.24	226.31
ZJetsToNuNu_HT-100To200_13TeV-madgraph	344.83	65.74
ZJetsToNuNu_HT-200To400_13TeV-madgraph	95.53	225.69
ZJetsToNuNu_HT-400To600_13TeV-madgraph	13.20	686.16
ZJetsToNuNu_HT-600To800_13TeV-madgraph	3.148	1789.28
ZJetsToNuNu_HT-800To1200_13TeV-madgraph	1.451	1396.10
ZJetsToNuNu_HT-1200To2500_13TeV-madgraph	0.355	929.88
ZJetsToNuNu_HT-2500ToInf_13TeV-madgraph	0.009	722.32
DYJetsToLL_M-50_HT-100to200_TuneCP5_13TeV-madgraphMLM-pythia8	181.30	78.00
DYJetsToLL_M-50_HT-200to400_TuneCP5_13TeV-madgraphMLM-pythia8	50.42	226.83
DYJetsToLL_M-50_HT-400to600_TuneCP5_13TeV-madgraphMLM-pythia8	6.984	1512.70
DYJetsToLL_M-50_HT-600to800_TuneCP5_13TeV-madgraphMLM-pythia8	1.681	4791.67
DYJetsToLL_M-50_HT-800to1200_TuneCP5_13TeV-madgraphMLM-pythia8	0.775	3920.47
DYJetsToLL_M-50_HT-1200to2500_TuneCP5_13TeV-madgraphMLM-pythia8	0.186	3267.32
DYJetsToLL_M-50_HT-2500toInf_TuneCP5_13TeV-madgraphMLM-pythia8	0.004	84618.62
WWTo1L1Nu2Q_13TeV_amcatnloFXFX_madspin_pythia8	50.00	39.76
WZTo1L1Nu2Q_13TeV_amcatnloFXFX_madspin_pythia8	10.71	629.88
WZTo1L3Nu_13TeV_amcatnloFXFX_madspin_pythia8_v2	3.058	483.67
ZZTo2L2Q_13TeV_amcatnloFXFX_madspin_pythia	83.220	3521.70
WWZ_4F_TuneCP5_13TeV-amcatnlo-pythia8	0.165	1172.24
WZZ_TuneCP5_13TeV-amcatnlo-pythia8	0.056	3468.14
ZZZ_TuneCP5_13TeV-amcatnlo-pythia8	0.014	13043.84

Table 5.5: Simulated SM samples used in the analysis for Phase 1 (2017 MC). The cross sections are calculated to NNLO.

turing a nearly-pure Higgsino LSP, a parameterized fast detector simulation using FastSim is performed for both phases.

5.5 Physics objects

In the following section, all necessary physics objects are defined which are used in the analysis. A pre-selection is defined for tracks, which is further used to develop a track tag in order to select disappearing tracks.

5.5.1 Electrons

Electrons are required to have $p_T > 40$ GeV and $|\eta| < 2.4$, ensuring an electron selection with a trigger efficiency of greater than 80%, visible in Fig. 5.31 of Sec. 5.10.2. Electrons are selected with a tight working point for the cut-based identification requirements, which include cuts on the second moment of the log-weighted distribution of crystal energies[2] $\sigma_{i\eta i\eta}$, the ratio of hadronic over electromagnetic measured energy H/E and the combined PF isolation. The tight working point ensures $\geq 70\%$ efficiency in selecting genuine electrons [63].

5.5.2 Muons

For muons, the same selection criteria as for electrons regarding p_T and $|\eta|$ are used. Muons are required to have $p_T > 40$ GeV and $|\eta| < 2.4$, ensuring a muon selection with a trigger efficiency of more than 80%. Muons are selected with a medium muon identification (ID), which corresponds to a tracker or global muon selected by the PF algorithm (referred to as a *loose* muon), with the added requirement of a measurement in more than 80% of all tracker layers which intersect its trajectory [64].

5.5.3 Jets

Jets are formed by clustering PF candidates by using the anti-k_t FastJet jet clustering algorithm using a cone size of $\Delta R = 0.4$ [65, 66]. Jets are selected with $p_T > 30$ GeV and $|\eta| < 2.4$. Nearby electrons and muons, as defined above, are vetoed within a cone around the jet using $\Delta R(\text{jet, lepton}) < 0.4$.

Heavy-flavour jets, in particular b-tagged jets, are identified using the DeepCSV algorithm, which uses a deep neural network with information about the vertices, tracks and jets given as input [67].

5.5.4 Pre-selected tracks

Tracks are obtained from the standard track collection produced by the event reconstruction sequence, and a set of selection criteria is applied in order to obtain well-reconstructed, isolated tracks. High quality, high purity tracks are selected following [48], which describes a set of quality criteria concerning the pixel triplet used as a seed to construct the track, as well as criteria to increase the purity of the track selection with respect to *spurious* tracks. *Spurious* tracks enter the standard track collection as a result of random combination of hits, leading to the spurious track background. Furthermore, tracks are required to have zero missing inner hits, which ensures a continuous hit pattern for the track. Tracks are then selected in the fiducial volume of the tracking detector with the following kinematic cuts:

---

[2] The second moment of the log-weighted distribution of crystal energies $\sigma_{i\eta i\eta}$ is determined around the crystal with the highest energy deposition, with the exact expression given in [63].

- $p_T > 25$ (40) GeV for short (long) tracks; and
- $|\eta| < 2.0$,

with short and long tracks referring to the two main track categories as defined in Sec. 5.1. To select only isolated tracks, candidate tracks are discarded if other tracks are present in a cone around the track within $\Delta R(\text{track, other tracks}) < 0.3$ with a relative isolation of greater than 0.2. Furthermore, tracks with either a PF candidate, electron or muon within $\Delta R < 0.1$ are vetoed.

In order to select tracks originating close to the primary vertex and to reduce the number of spurious tracks, a small value of the impact parameter is imposed, which is the distance of the closest approach between the track trajectory and the primary vertex. In the transverse plane, a distance of $d_{xy} < 0.1$ cm is required, as well as $d_z < 0.1$ cm in the longitudinal plane.

Extreme outliers are vetoed by requiring $\Delta p_T / p_T^2 < 10\ \text{GeV}^{-1}$.

5.5.5 Hadronic activity (H_T)

Hadronic activity, abbreviated H_T, is defined as the sum of the transverse momenta p_T of all jets as defined above.

5.5.6 Hard missing transverse momentum ($\not{H}_T$)

The chargino $\tilde{\chi}_1^\pm$ producing a disappearing track is not expected to be included in the collection of PF candidates due to the low-momentum SM particle of its decay, which is not reconstructed in most of the cases. Hard $\not{H}_T$ is used as a proxy for the missing transverse momentum, and is defined as the negative vectorial sum of PF jets in the event satisfying $p_T > 30$ GeV and $|\eta| < 5.0$, with jets with a pre-selected track in a cone around $\Delta R(\text{jet, tracks}) < 0.4$ not being included in the calculation. This ensures that the chargino $\tilde{\chi}_1^\pm$ producing a disappearing track does not contribute to the negative vectorial sum. For clarity, $\not{H}_T$ is used when referencing to hard $\not{H}_T$ in the following.

5.6 Disappearing track signal characteristics

As introduced in Sec. 5.1, tracks are categorized in short and long tracks, with an additional requirement of at least two missing outer hits in the strip tracker for long tracks. This requirement ensures that only disappearing tracks are selected and discards $\tilde{\chi}_1^\pm$ with a laboratory frame decay length greater than the radius of the tracking detector, as this analysis is only sensitive for decays within the tracker volume. Another characteristic quantity, besides missing outer hits, is the deposited energy in the calorimeters, E_{dep}, which is defined by the sum of the energy measurements in the electromagnetic and hadron calorimeter clusters within $\Delta R < 0.5$ around the track,

$$E_{\text{dep}} = \sum_{i \in \text{ECAL, HCAL}}^{\Delta R < 0.5} E_i, \tag{5.6.1}$$

with E_i taken from the AOD (Analysis Object Data) collections containing reconstructed hit clusters in the electromagnetic calorimeter (`reducedEcalRecHitsEB`, `reducedEcalRecHitsEE`, `reducedEcalRecHitsES`) and in the hadronic calorimeter (`reducedHcalRecHits`).

Heavy charginos as considered in this search are expected to be highly-ionizing. In the following, the measured energy loss dE/dx is used to further optimize the sensitivity of the search. As described in Sec. 4.1.1, the Bethe-Bloch equation describes the energy loss of a charged, heavy particle in matter, as measured in each tracker layer. In order to provide a comparable observable for both short and long tracks only, the energy loss in the pixel detector is considered. The pixel tracking layers have a thickness of $100 - 150$ μm [68]. In this case of an energy loss in a thin material, the Bethe-Bloch equation has to be convoluted with a Landau distribution to account for δ-electrons escaping the layer [69].

In order to provide a single observable for each track, a "harmonic-2" estimator is used instead of a simpler approach of using the mean value of the individual dE/dx measurements in each pixel layer. This has the advantage of suppressing the effects of outlier measurements [70, 71]. The "harmonic-2" estimator I_h is given by

$$I_h = \left(\frac{1}{N} \sum_{i=1}^{N} (\Delta E / \Delta x)_i^{-2} \right)^{-1/2}, \tag{5.6.2}$$

with N total measurements of the energy loss ΔE per path length Δx in the i-th tracking layer. I_h is determined separately from either hits in the pixel detector, and from hits in the strips detector. To preserve consistency between the track categories, only I_h derived using pixel hits is used in the following. Outlier measurements of dE/dx can enter the determination of I_h due to radiation damage effects, which are especially relevant for the inner tracking layers [68]. As a consequence, the suppression of such outliers leads to a downward bias of I_h, which is corrected by a time-dependent calibration of the pixel tracking detector response, which will be discussed in Sec. 5.8. In the following, I_h will be referred as dE/dx when discussing a per-track measurement of dE/dx.

In order to investigate characteristic signal properties, reconstructed tracks from the standard track collection are matched to generated charginos $\tilde{\chi}_1^\pm$ by requiring $\Delta R(\text{track}, \tilde{\chi}_1^\pm) < 0.01$. The transverse displacement of the secondary vertex corresponds to the transverse decay length of the chargino, as is defined by

$$L_{xy}^{\text{lab}} = \sqrt{\left((\tilde{\chi}_1^\pm)_x - (\tilde{\chi}_1^0)_x\right)^2 + \left((\tilde{\chi}_1^\pm)_y - (\tilde{\chi}_1^0)_y\right)^2}, \tag{5.6.3}$$

with the x and y coordinates of the chargino $\tilde{\chi}_1^\pm$ and one of the daughter particles, e.g. the neutralino $\tilde{\chi}_1^0$. Figure 5.8 shows characteristic features of the $\tilde{\chi}_1^\pm$-matched tracks, including the generator transverse track momentum p_T^{gen} and the transverse generator decay length in the laboratory frame L_{xy}^{lab}. Short tracks are shown on the left, and long tracks on the right side. The signal tracks are weighted with the production cross section σ divided by the number of generated signal events. Three example gluino mass and LSP mass configurations for the T5btbtLL signal model are included. Depending on the regime, the transverse momentum exhibits its maximum value between 250 and 1000 GeV for the selected mass configurations. The transverse generator decay length of the chargino in the laboratory frame follows an exponential decay, which is best visible for long tracks. Fig. 5.9 shows characteristic features of the signal for reconstructed detector quantities, including the deposited energy in the calorimeters, the number of missing outer hits in the strip tracker, and the energy loss dE/dx. The deposited energy E_{dep} is expected to be small due to the subsequent decay of the chargino $\tilde{\chi}_1^\pm$ into a neutralino $\tilde{\chi}_1^0$ and a non-reconstructed SM particle. The number of missing outer hits exhibits the maximum value at 9 missing hits for short tracks, since most of the strip layers are expected to be without measurement. For long tracks, the number of missing outer hits is expected to be lower due to the increased track length. Fig. 5.9-bottom shows the energy loss dE/dx of the chargino, with more massive charginos exhibiting a larger energy loss due to the chargino being highly-ionizing.

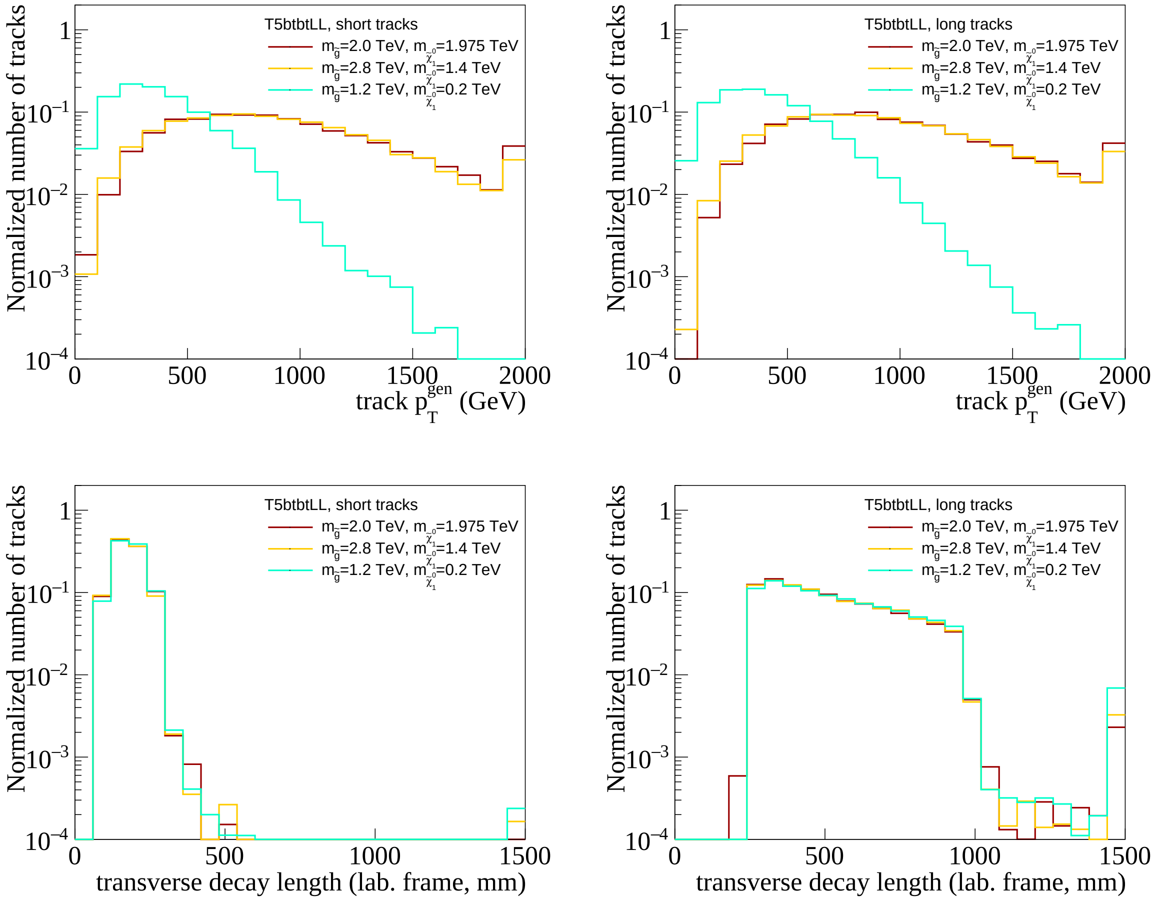

Figure 5.8: MC generator transverse momentum p_T (top) and MC generator transverse decay length (bottom) for different mass configurations ($m_{\tilde{g}}$, $m_{\tilde{\chi}_1^0}$) of T5btbtLL shown for short tracks (left) and long tracks (right). The last bin indicates the overflow bin, see text for further explanations.

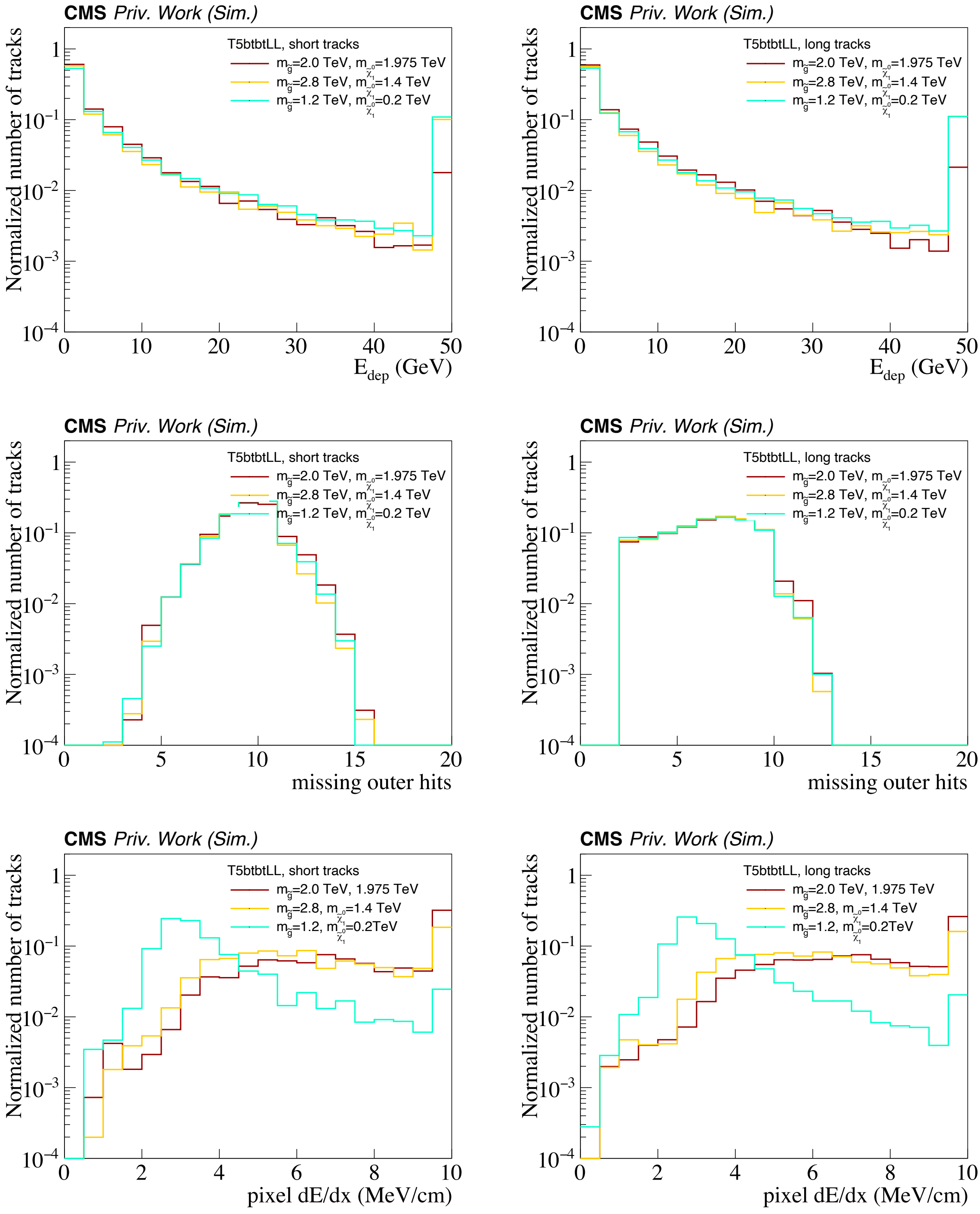

Figure 5.9: Deposited energy E_{dep} (top), number of missing outer hits (middle), and dE/dx (bottom) for different mass configurations ($m_{\tilde{g}}$, $m_{\tilde{\chi}^0_1}$) of T5btbtLL shown for short tracks (left) and long tracks (right). The last bin indicates the overflow bin, see text for further explanations.

While kinematic properties as the transverse momentum p_T depend on the $\tilde{\chi}^{\pm}_1$ production mechanism and the mass regime for a given simplified model, characteristic features of the signature of a disappearing track including E_{dep} and the number of missing outer hits remain largely independent of the chargino production itself.

5.7 Identification of disappearing tracks

Building on the characteristic properties of the disappearing track signal laid out in Sec. 5.6 and the track pre-selection introduced in Sec. 5.5, in this section a disappearing track tag is constructed and its efficiency to select signal and to reject background tracks is evaluated. A multivariate classification is used in order to identify disappearing tracks. The method chosen is the boosted decision tree (BDT), described in the following.

5.7.1 Multivariate track classification

A BDT is a multivariate analysis method based on the concept of a decision tree. Decision trees can be used for classification of samples among two or more categories, or as a method for regression. Here, binary decision trees are used, whose classifier indicates the degree to which the input is either signal- or background-like. A decision tree is defined by a number of nodes n, each creating two new nodes based on a decision expression. The number of nodes per layer n_d then is

$$n_d = 2^d, \tag{5.7.1}$$

with d defined as the number of layers, or more precisely, the maximum number of traversed consecutive nodes. Figure 5.10 shows an illustration of a binary decision tree with 2 layers, for which three variables x_i, x_j and x_k are considered, one per layer. In the case of a binary decision tree, an expression containing a single variable is evaluated for each node to identify whether the variable exceeds or is smaller than a given threshold, which corresponds to signal- or background-like regimes of the variable distribution.

The training is performed in N iterations, according to the number of trees N. Both parameters d and N can be adjusted in order to achieve an optimal separation of signal and background.

The training itself is performed by splitting the input signal and background in a training and testing sample. The classifiers of multiple trees can then be combined into a single, weighted classifier. To obtain this classifier, each tree output $h(\vec{x})$ as a function of its input $\vec{x}$ is associated with a weight w, which characterizes how well the tree distinguishes signal from background [72]. Then, the weighted sum,

$$\hat{y}(x) = \sum_i w_i h_i(\vec{x}), \tag{5.7.2}$$

is the combined output of the N decision trees. Combining a selection of weaker individual classifiers into a single, better performing classifier is referred to as *boosting*. This analysis utilizes the BDT implementation provided by the multivariate analysis toolkit, TMVA [72]. In this toolkit, adaptive boosting (`AdaBoost`), which is designed for binary decision trees, is used as the boosting algorithm [73].

5.7.2 Training of the BDTs

BDTs are trained separately for short and long tracks, as well as for the Phase 0 and Phase 1 detector configurations, since the modified design of the pixel detector impacts the reconstruction of short tracks considerably. Pre-selected tracks as described in Sec. 5.5.4 are obtained from MC simulation, and are used for the training of the BDTs in order to separate signal tracks from background tracks. This approach has the advantage of using MC generator information for

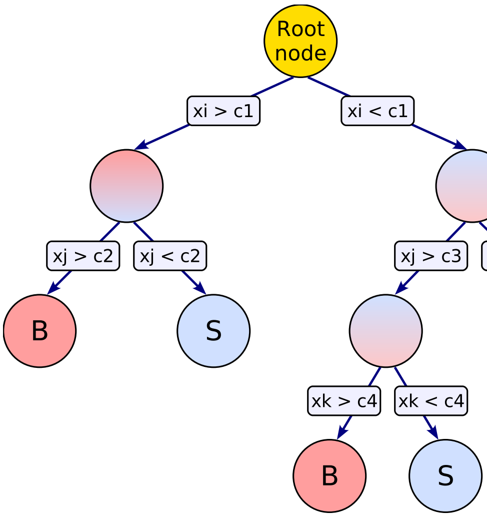

Figure 5.10: Example of a simplified binary decision tree with two layers. For each node, exactly one variable is evaluated with a specified threshold value. In this example, three variables x_i, x_j and x_k are considered in the decision tree. The output of the decision tree is a classifier to determine if the input is signal- or background-like. Figure taken from [72].

the true nature of a track-forming particle with respect to signal and background tracks, thus allowing supervised learning. The accuracy of MC simulation in the training of the BDTs will be evaluated in MC with respect to data in Sec. 5.7.3 by comparing real and simulated distributions of tracks in control regions, and by measuring the signal tagging efficiency in data in Sec. 5.12.

For signal, pre-selected tracks are obtained from FullSim samples for the simplified models T5btbtLL and T6btLL with a proper decay length $c\tau = 200$ cm used for Phase 0, while for Phase 1 FastSim detector simulation samples for T5btbtLL with $c\tau = (10, 50, 200)$ cm are used due to signal sample availability. Pre-selected tracks for both phases are matched to a MC generator chargino $\tilde{\chi}_1^\pm$ with $\Delta R(\text{track}, \tilde{\chi}_1^\pm) < 0.01$, ensuring that no SM background tracks enter the training. For SM background, pre-selected tracks are used from FullSim samples with leptonic W decays, leptonic Drell-Yan processes, $t\bar{t}$ processes as well as diboson decays, as listed in Tab. 5.4 and 5.5.

To check for overtraining, the pre-selected tracks are randomly split into a training and testing sample with equal proportions. The BDTs are trained with 200 iterations and 4 layers. Boosting is performed using `AdaBoost` with $\beta = 0.5$, and a `GiniIndex` node splitting separation criterion is used in order to construct the variable threshold cut requirements for the nodes [72].

The input variables to the BDT are selected based on the track property characteristics of $\tilde{\chi}_1^\pm$-matched tracks. As discussed in Sec. 5.6, emphasis is placed on variables that are independent of the chargino production mechanism. For short tracks the variables are, ordered by importance for Phase 0 detector conditions,

1. d_{xy}(track, primary vertex);
2. d_z(track, primary vertex);
3. relative track isolation;
4. χ^2/number of degrees of freedom;
5. $\Delta p_T / p_T^2$; and
6. number of valid hits in the pixel detector.

Here, d_{xy} and d_z denote the transverse and longitudinal distance of the track to the primary vertex at the point of closest approach, Δp_T indicates the transverse momentum resolution and

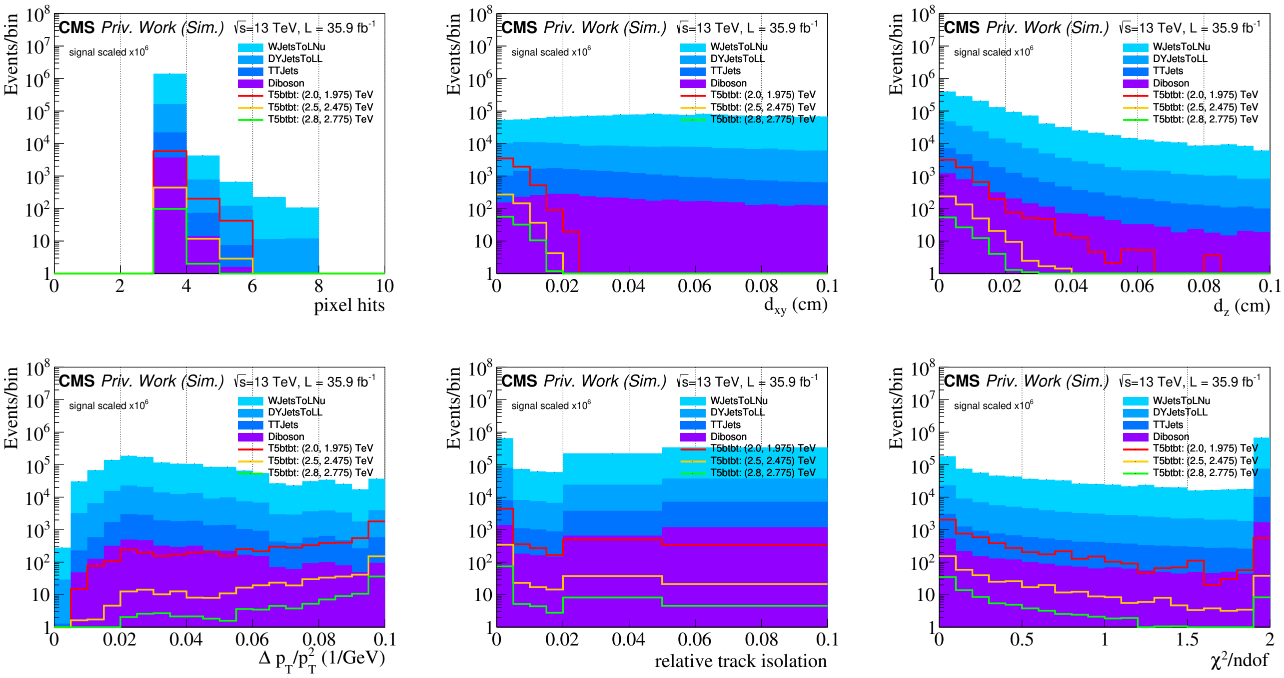

Figure 5.11: BDT input distributions for short tracks (Phase 0), with T5btbtLL signal mass points given as $(m_{\tilde{g}}, m_{\tilde{\chi}_1^0})$. The last bin includes the overflow.

χ^2 refers to the goodness-of-fit parameter of the track fitting algorithm. Figure 5.11 shows the corresponding distributions for signal and background MC simulation, with three example signal mass points from the compressed regime denoted by $(m_{\tilde{g}}, m_{\chi_1^0})$. The number of signal tracks is scaled by a factor of 10^6 for ease of comparison. For larger pseudorapidities $|\eta| > 1.4$ of the track, short tracks can exhibit more than 3 (4) hits in tracker layers with measurements, as can be seen in the corresponding distribution and in Fig. 4.4. The most significant difference between signal and background shape can be seen for d_{xy}, for which the MC background shows a flat shape compared to a steeply falling signal distribution, indicating a dominating background due to spurious tracks. The second-leading BDT input variable, d_z, is useful in particular for rejecting pile-up background. The third-leading BDT input observable indicates a higher relative track isolation for signal tracks.

The deposited energy E_{dep}, which has been identified as a characteristic variable for disappearing tracks, is not used as input to the BDT, but is used separately to define control regions for the determination of the prompt background. The number of missing hits in the strip detector is not utilized for short tracks, as the track selection is only dependent on the pixel detector.

Taking post-upgrade Phase 1 detector conditions into account, the variables ordered by importance are

1. d_{xy}(track, primary vertex);
2. relative track isolation;
3. d_z(track, primary vertex);
4. number of valid hits in the pixel detector;
5. χ^2/number of degrees of freedom; and
6. $\Delta p_T / p_T^2$,

and are shown in Fig. 5.12. Due to the added pixel layer in Phase 1, short signal tracks with three and four hits can be reconstructed in approximately equal proportion, which raises the

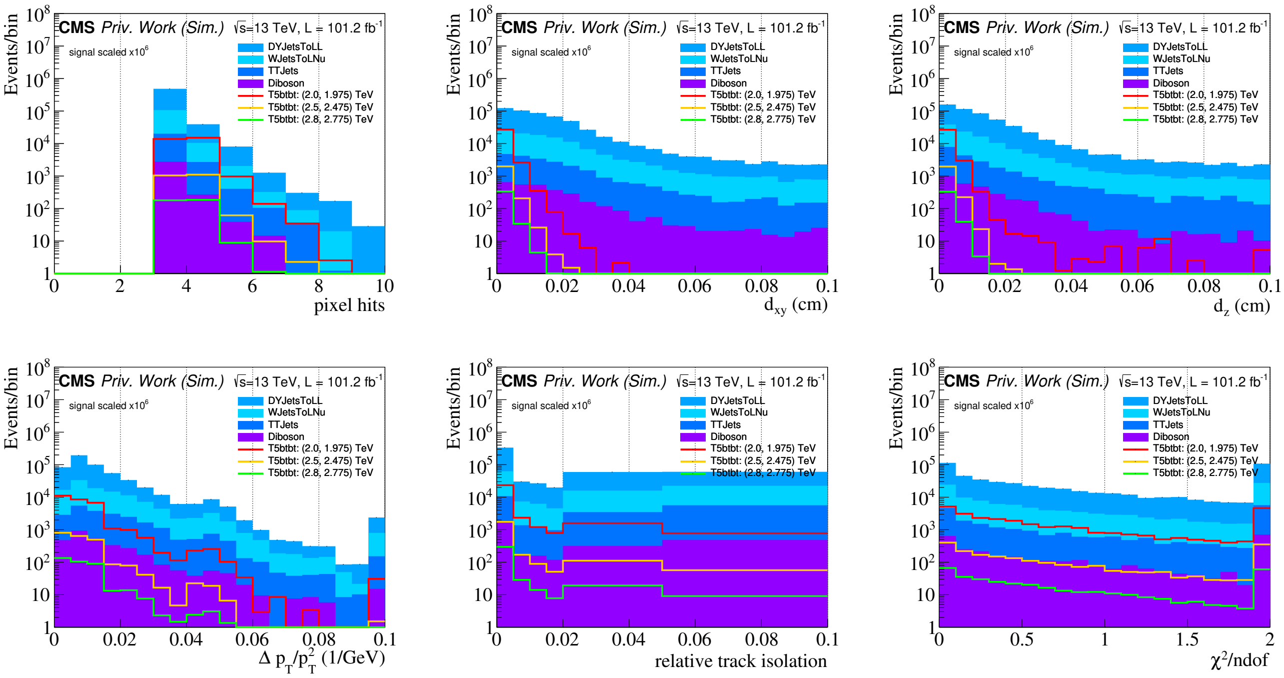

Figure 5.12: BDT input distributions for short tracks (Phase 1), with T5btbtLL signal mass points given as $(m_{\tilde{g}}, m_{\tilde{\chi}_1^0})$. The last bin includes the overflow.

importance of the number of valid hits in the pixel detector. Inspecting the shape of d_{xy} for Phase 1 further reveals a more steeply falling SM background when compared to Phase 0, indicating a lower contribution of spurious tracks due to the improved pixel detector.

For long tracks the input variables are, again ordered by importance for Phase 0 detector conditions,

1. d_{xy}(track, primary vertex);
2. number of valid hits in the strip detectors;
3. d_z(track, primary vertex);
4. $\Delta p_T / p_T^2$;
5. number of valid hits in the pixel detector;
6. relative track isolation;
7. χ^2/number of degrees of freedom; and
8. missing outer hits.

Their distributions are shown in Fig. 5.13. Again, d_{xy} is the leading input variable, followed by the number of valid hits in the strip detectors. Here, the background exhibits a strong peak in the number of tracker hits centered at the value 5, which is not apparent for signal. This is a result of a complex convolution of tracker geometry and cut-offs in the pattern reconstruction. Also background due to Bremsstrahlung may contribute to this effect, with a photon radiating off a decelerating electron, leading to missing outer hits and measurement in less than the total number of tracker layers.

For Phase 1, a significant improvement in the measurement of the transverse momentum resolution Δp_T is seen for long tracks, due to a more precise measurement in the pixel detector and re-calibrated strip detector conditions and alignment. This influences the BDT input variables ordered by importance, which in this case are given by

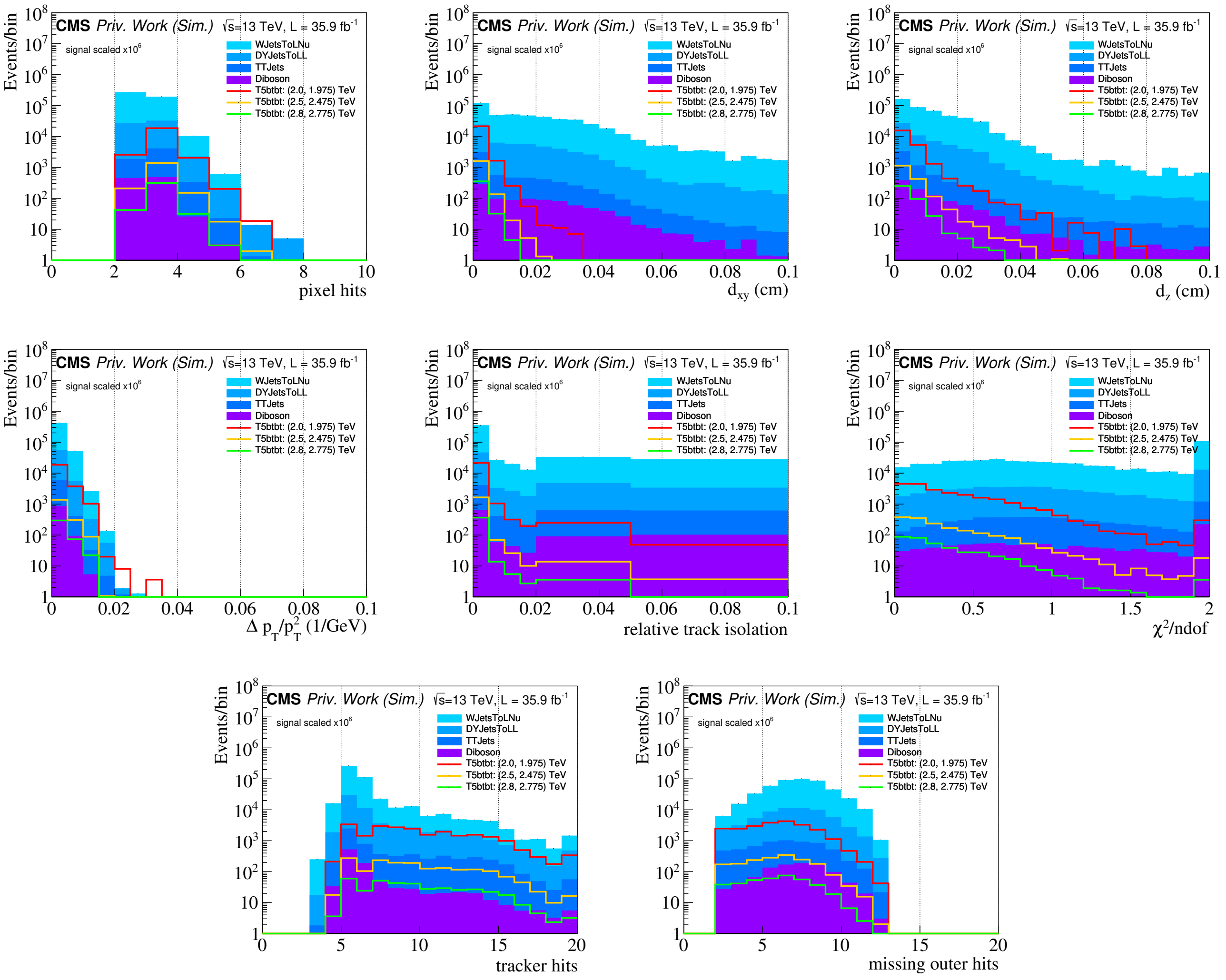

Figure 5.13: BDT input distributions for long tracks, Phase 0, with T5btbtLL signal mass points given as $(m_{\tilde{g}}, m_{\tilde{\chi}_1^0})$. The last bin includes the overflow.

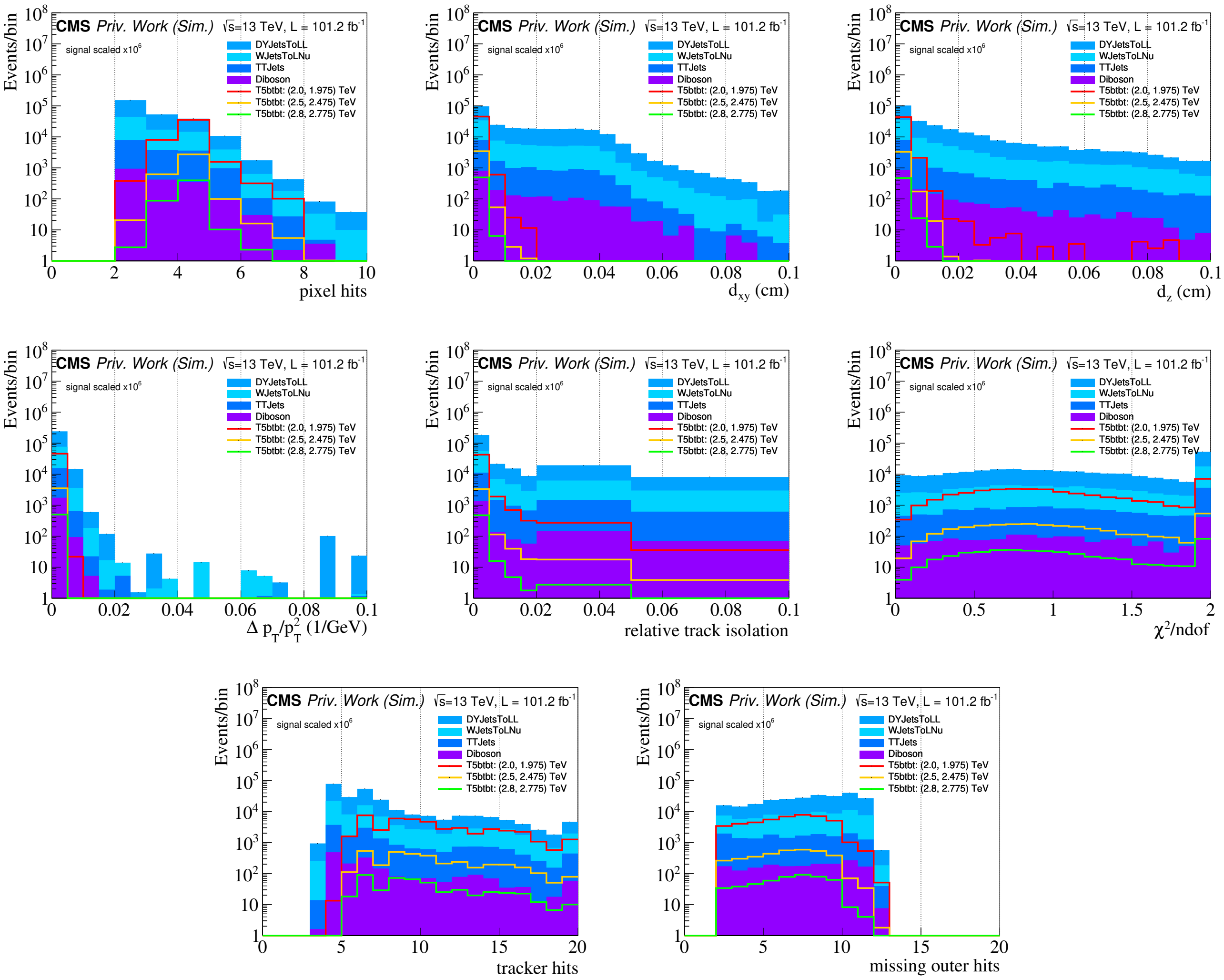

Figure 5.14: BDT input distributions for long tracks, Phase 1, with T5btbtLL signal mass points given as $(m_{\tilde{g}}, m_{\tilde{\chi}_1^0})$. The last bin includes the overflow.

1. $\Delta p_T/p_T^2$;
2. number of valid hits in the strip detectors;
3. number of valid hits in the pixel detector;
4. d_z(track, primary vertex);
5. missing outer hits;
6. χ^2/number of degrees of freedom;
7. d_{xy}(track, primary vertex); and
8. relative track isolation.

Differences in detector conditions, pattern recognition, and the length of the track directly influence the BDT input distributions as visible in Figs. 5.11-5.14, requiring an optimized BDT training for each of the four conditions. The BDT classifier obtained after the training is shown in Fig. 5.15 for the datasets used for training and testing. The BDT classifier distribution for both is expected to be similar; larger differences between the two could indicate overtraining due to too-small training samples or due to complex architecture. No overtraining is observed for the BDT classifiers, as shown in the figure[3].

---

[3] In order to quantify the likeness of the two distributions, a Kolmogorov-Smirnov test is performed as im-

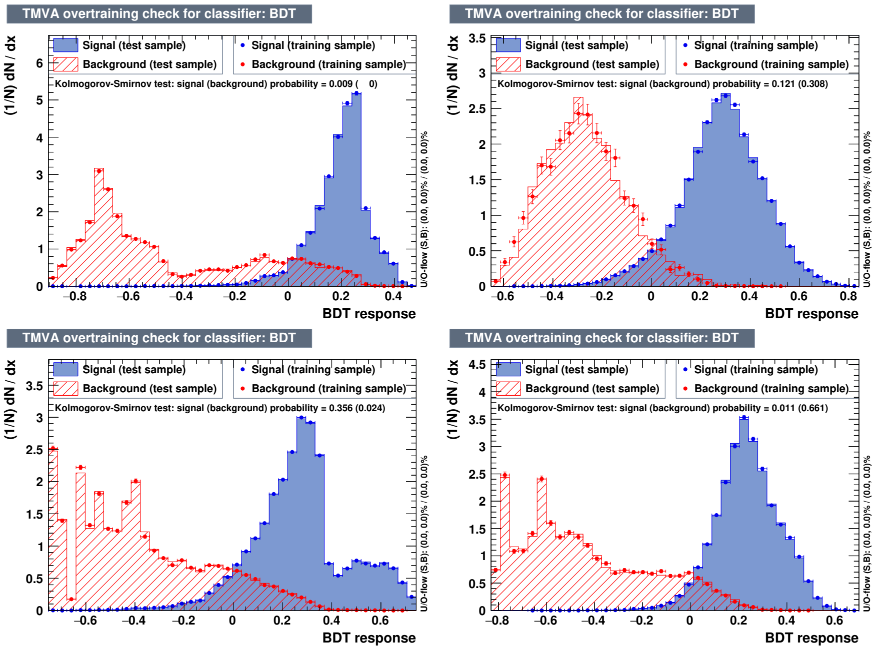

Figure 5.15: BDT classifier for Phase 0 (top) and Phase 1 (bottom), shown for short (left) and long tracks (right). The BDT classifier distribution is shown for the sample used for training and testing, separately.

5.7.3 Validation of BDT input observables

As this search does not rely on MC simulation for the final estimation of background sources, any mismodeling of track properties in the MC simulation used to train the BDTs could lead to a less-than-optimal classifier. However, a less-than-optimal modeling of the input observables for the BDT training can affect the signal and background rejection efficiency when applied to data. In this section, the agreement between data and MC is investigated for the BDT input observables.

A validation region is selected to be orthogonal to the signal region. Events are selected that contain at least one electron and a further pre-selected track, for which the invariant mass of the track-electron pair is calculated with the assumption of a massless track $m_{\text{track}} = 0$ GeV from the two four-vectors $\mathbf{P}_e$ and $\mathbf{P}_{\text{track}}$ given by

$$m_{\text{inv}} = (\mathbf{P}_e + \mathbf{P}_{\text{track}})^2 = m_e^2 + m_{\text{track}}^2 + 2(E_e E_{\text{track}} - |\vec{p_e}| \cdot |\vec{p_{\text{track}}}| \cdot cos\theta). \tag{5.7.3}$$

The invariant mass is required to be in the interval $m_{\text{inv}}(\text{track}, \text{electron}) = (85, 95)$ GeV. In this interval around the Z^0 mass, electron+track samples are expected to be dominated by $Z^0 \to e^+e^-$ decays and from spurious tracks from other processes with electrons. Figure 5.16-top shows the invariant mass $m_{\text{inv}}(\text{track}, \text{electron})$ and d_{xy} distributions for short tracks and Phase 0 detector conditions. They show an underprediction of the SM background in the MC simulation. In order to understand differences between the simulated and data distributions, an average correction factor $\omega = (\text{data}/\text{MC})$ is determined and applied to correct for differences in the relative contribution from spurious and prompt tracks between the simulation and data, as short tracks in particular have a more significant contribution from spurious tracks in

---

plemented in TMVA. For an unbinned distribution, the expected outcome of the test is 0.5, indicating similarity between the training and testing datasets. In TMVA, the test is repeated with a fixed number of iterations of 1000, and the result shown in Fig. 5.15 is the normalized number of Kolmogorov-Smirnov tests with a result of greater than 0.5.

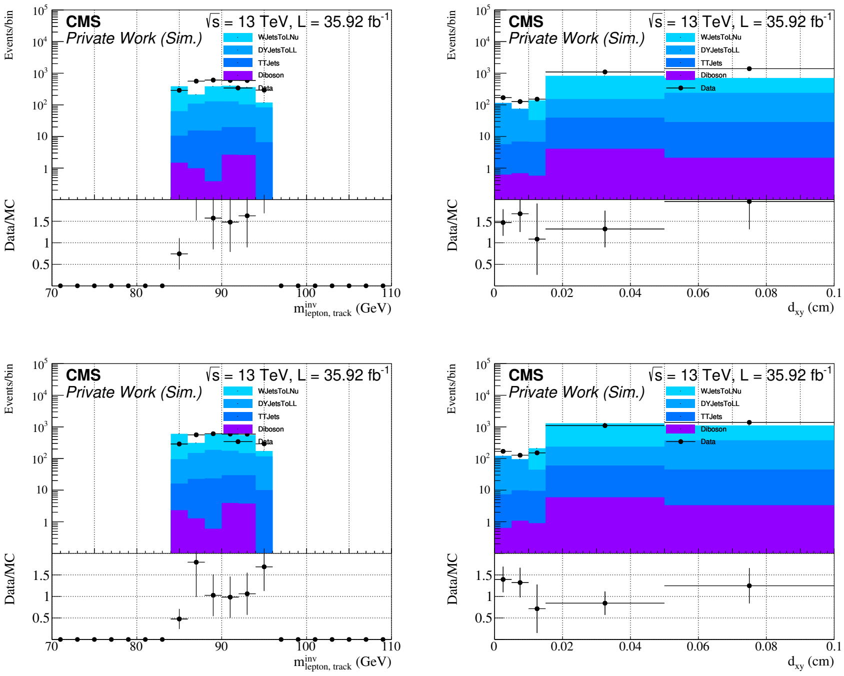

Figure 5.16: Control region around the Z^0 mass for short tracks, Phase 1, before (top row) and after (bottom row) weighting the spurious track component in each SM background sample by ω to match the spurious track contingent in data.

data when compared to MC. The correction factor ω is measured in a high-d_{xy} window saturated with spurious tracks. Figure 5.17 shows the number of the true simulated spurious tracks compared to the total number of simulated background tracks, with the ratio between the two quantities defined as the purity with respect to spurious tracks. For $d_{xy} > 0.01$ cm and $d_{xy} > 0.015$ cm for Phase 0 and Phase 1, respectively, spurious tracks are selected with high purity, and ω is determined in this region.

Table 5.6 shows the obtained values for ω, determined separately for short and long tracks, as well as for Phase 0 and Phase 1. Spurious tracks in MC simulation are weighted by ω in order to apply a correction for spurious tracks. Figure 5.16-bottom shows the distributions for m_{inv} and d_{xy} after applying the correction factor ω, yielding an improved description of data by SM MC, as evidenced by the ratio data/MC compatible with one within statistical uncertainties.

	Phase 0	Phase 1
short tracks	1.57 ± 0.38	6.22 ± 1.37
long tracks	3.18 ± 2.54	11.50 ± 5.37

Table 5.6: Measurement of $\omega = (\text{data}/\text{MC})$, which is used to account for the spurious track component in data. Spurious tracks in MC simulation are weighted by ω to correct for this effect. The uncertainty on ω is determined as the sum of the fractional uncertainties of the number of tracks in data and MC.

Figure 5.18 shows the three most important BDT input variables for Phase 0. Data are compared to MC simulation, in particular in histogram bins for which a significant contribution of signal is expected (see Sec. 5.7.2). For d_{xy} and d_z, the largest signal contribution is for smallest values, for which a good description of data by MC simulation is visible for long tracks. For short tracks, the ratio data/MC fluctuates around one, however shows significant deviations in bins of large signal contribution. To a certain degree, differences in data/MC are expected for the BDT input variables, as the selected tracks in the Drell-Yan validation region are mostly tracks

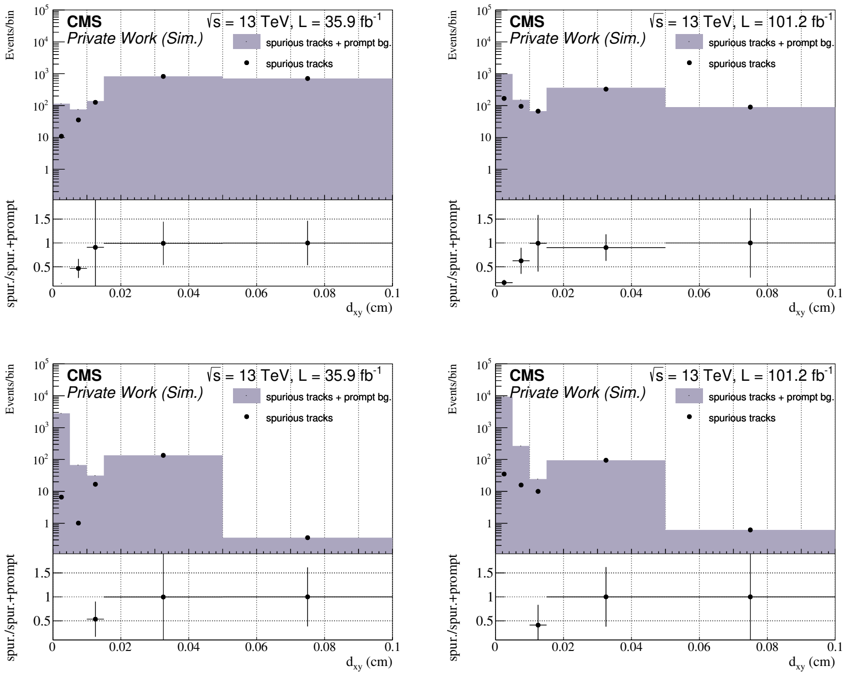

Figure 5.17: Purity of the spurious track selection in background MC as used in the BDT training for the d_{xy} distribution. Top row: short tracks, bottom row: long tracks with Phase 0 (Phase 1) shown on the left (right) side. Above $d_{xy} > 0.01$ (0.015) cm mostly spurious tracks are selected in MC for short (long) tracks.

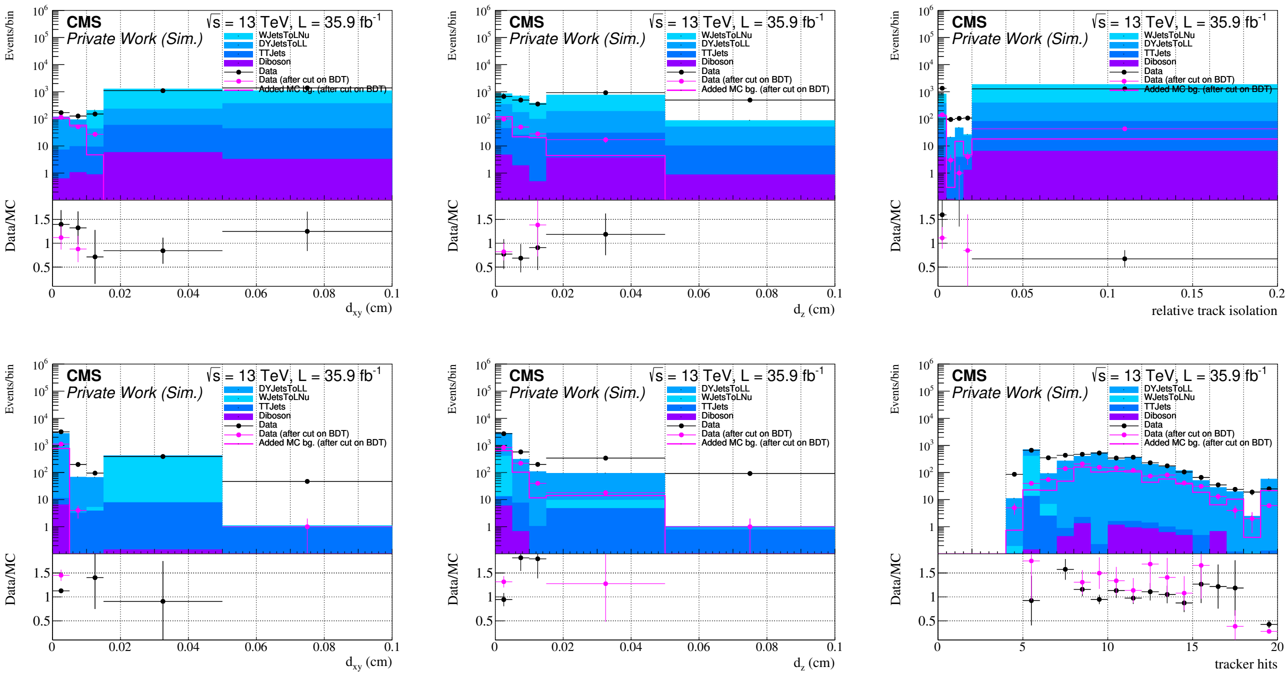

Figure 5.18: Importance-leading BDT input variables for short (top) and long tracks (bottom) in a Drell-Yan validation region, shown for Phase 0. The last bin includes the overflow. Also shown is a comparison of data and total background after a cut on the BDT classifier.

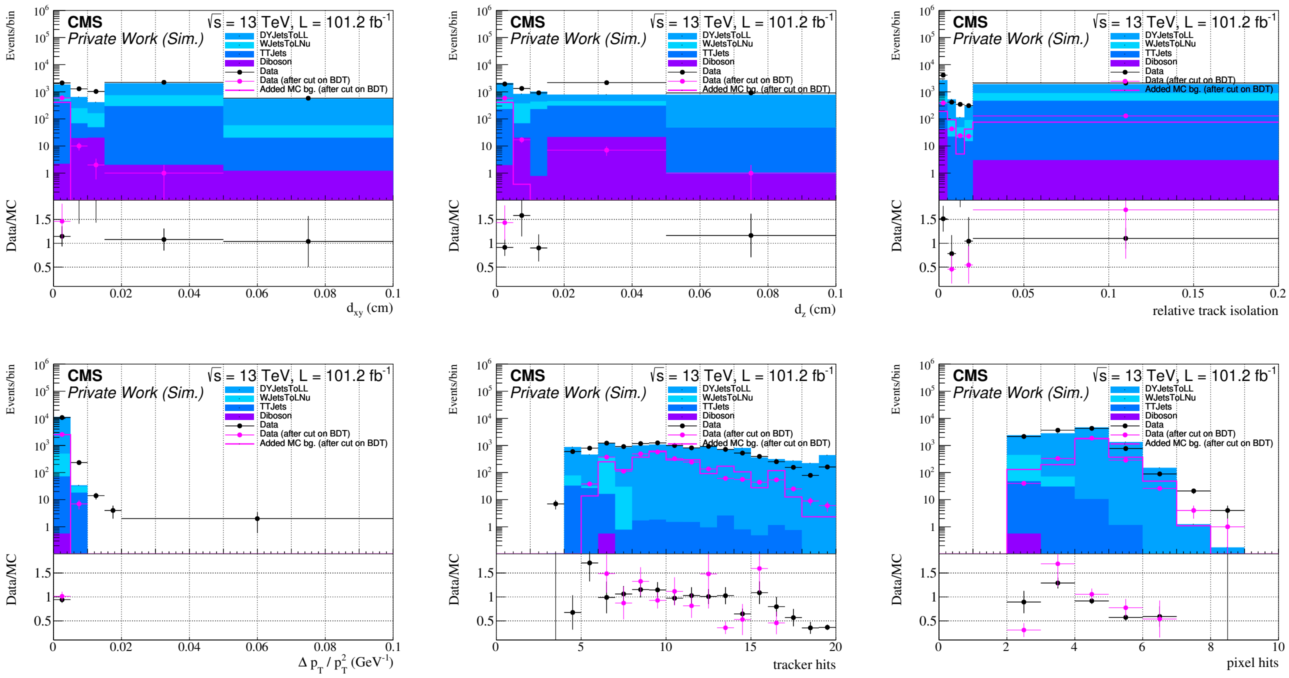

Figure 5.19: Importance-leading BDT input variables for short (top) and long tracks (bottom) in a Drell-Yan validation region, shown for Phase 1. The last bin includes the overflow. Also shown is a comparison of data and total background after a cut on the BDT classifier.

from non-reconstructed electrons, which are selected along with a well-reconstructed electron within the imposed Z window cut. Tracks due to the decay of long-lived charginos have little in common with such selected tracks, and differences between data/MC are not expected to result in other issues with the analysis, e.g., the background determination. In this analysis, MC simulation is only used to train BDTs, and to obtain scale factors for the disappearing track signal systematic. Therefore, any deviation of data/MC from one in Fig. 5.18 would only lead to a slightly non-optimal classifier algorithm.

Figure 5.19 shows the three most important BDT input variables for short and long tracks, depicted for Phase 1. The distributions show an improved agreement between data and MC simulation for short tracks, for which the differences are largely compatible within statistical uncertainties.

5.7.4 Working point determination

For each track passing the pre-selection, the BDT is evaluated using the same input observables as used for the training. Choosing a lower cut threshold $\text{BDT}_{\text{threshold}}$ on the BDT classifier shown in Fig. 5.15 allows to separate signal from background with a corresponding signal efficiency ϵ_{sg} and background efficiency ϵ_{bg}, given by

$$\epsilon = \frac{n_{\text{tracks}}(\text{BDT} \geq \text{BDT}_{\text{threshold}})}{n_{\text{tracks}}}, \tag{5.7.4}$$

with n_{tracks} referring to either pre-selected signal tracks, or pre-selected background tracks. The background rejection efficiency is defined as $1 - \epsilon_{bg}$. The receiver-operator characteristics (ROC) curve is defined as a function $f(\epsilon_{\text{sg}}(\text{BDT}), \epsilon_{\text{bg}}(\text{BDT}))$, with a scan of the BDT classifier

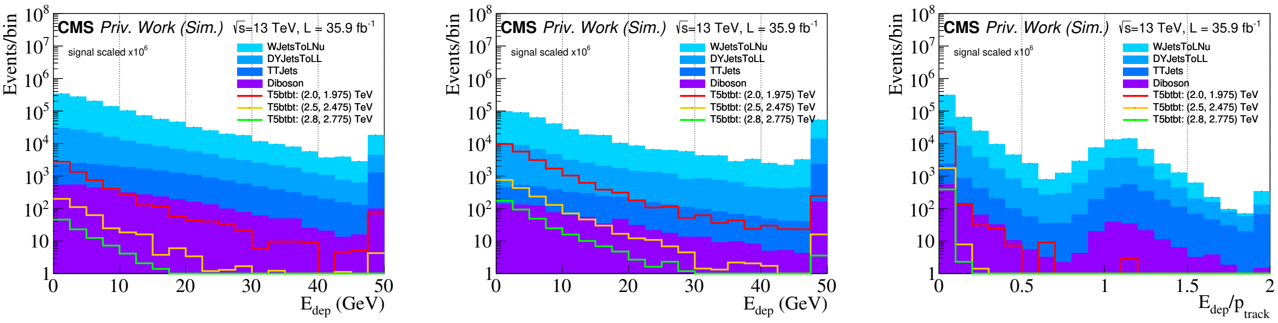

Figure 5.20: E_{dep} for short tracks (left) and long tracks (middle), E_{dep}/p distribution for long tracks (right). Signal events are scaled by a factor 10^6 for better shape comparison, and are shown for three mass point configurations, given by $(m_{\tilde{g}}, m_{\chi_1^0})$, respectively. The last bin includes the overflow.

between -1 and 1. The ROC curve after the BDT training is shown as a solid yellow curve in Fig. 5.21, both for short and long tracks as well as for Phase 0 and Phase 1. All efficiencies are calculated using the same denominator of pre-selected tracks, albeit with a lower transverse momentum of $p_T > 15$ GeV instead of 25 GeV for short tracks in order to facilitate further comparison within the signal efficiency and background rejection efficiency plane. Maximizing the area under the curve would move it to its theoretical limit of 100% signal efficiency and background rejection efficiency. A specific choice of a cut threshold $\text{BDT}_{\text{threshold}}$ corresponds to a point on the ROC curve, which is referred to as a working point.

In order to further optimize the background rejection, a cut on the deposited energy in the calorimeters E_{dep} is imposed, as motivated in Sec. 5.6. Figure 5.20-left shows E_{dep} for short tracks, for which a cut of $E_{\text{dep}} < 15$ GeV is introduced to isolate signal tracks. For long tracks, a dependence on the transverse momentum can be observed when comparing Fig. 5.20-center showing E_{dep} to the ratio E_{dep}/p shown in Fig. 5.20-right. The signal exhibits a steeper falling slope with a maximum at small values of E_{dep}/p when comparing to the E_{dep} distribution. Furthermore, a peak structure in the background centered around $E_{\text{dep}}/p \approx 1.2$ caused by prompt background from Bremsstrahlung processes can be reduced by imposing a cut of $E_{\text{dep}}/p < 20\%$.

The ROC curve indicated in red color in Fig. 5.21 includes the cut on E_{dep} and E_{dep}/p, respectively. A working point is chosen on the shoulder of the ROC curve and is indicated as a point on the ROC curve in red color.

A track is classified as *disappearing* if it passes the pre-selection and satisfies

- $E_{\text{dep}} < 15$ GeV for short tracks, $E_{\text{dep}}/p < 0.20$ for long tracks;
- $|\eta| < 2.0$;
- $\text{BDT} > 0.1$ (0.15) for short tracks (Phase 0, Phase 1);
- $\text{BDT} > 0.12$ (0.08) for long tracks (Phase 0, Phase 1),

each corresponding to the working point from Fig. 5.21.

The exact requirement on the BDT classifier and the deposited energy E_{dep} and E_{dep} is determined by requiring high purity in the signal regions and low contamination in the background estimation control regions discussed in Sec. 5.11.

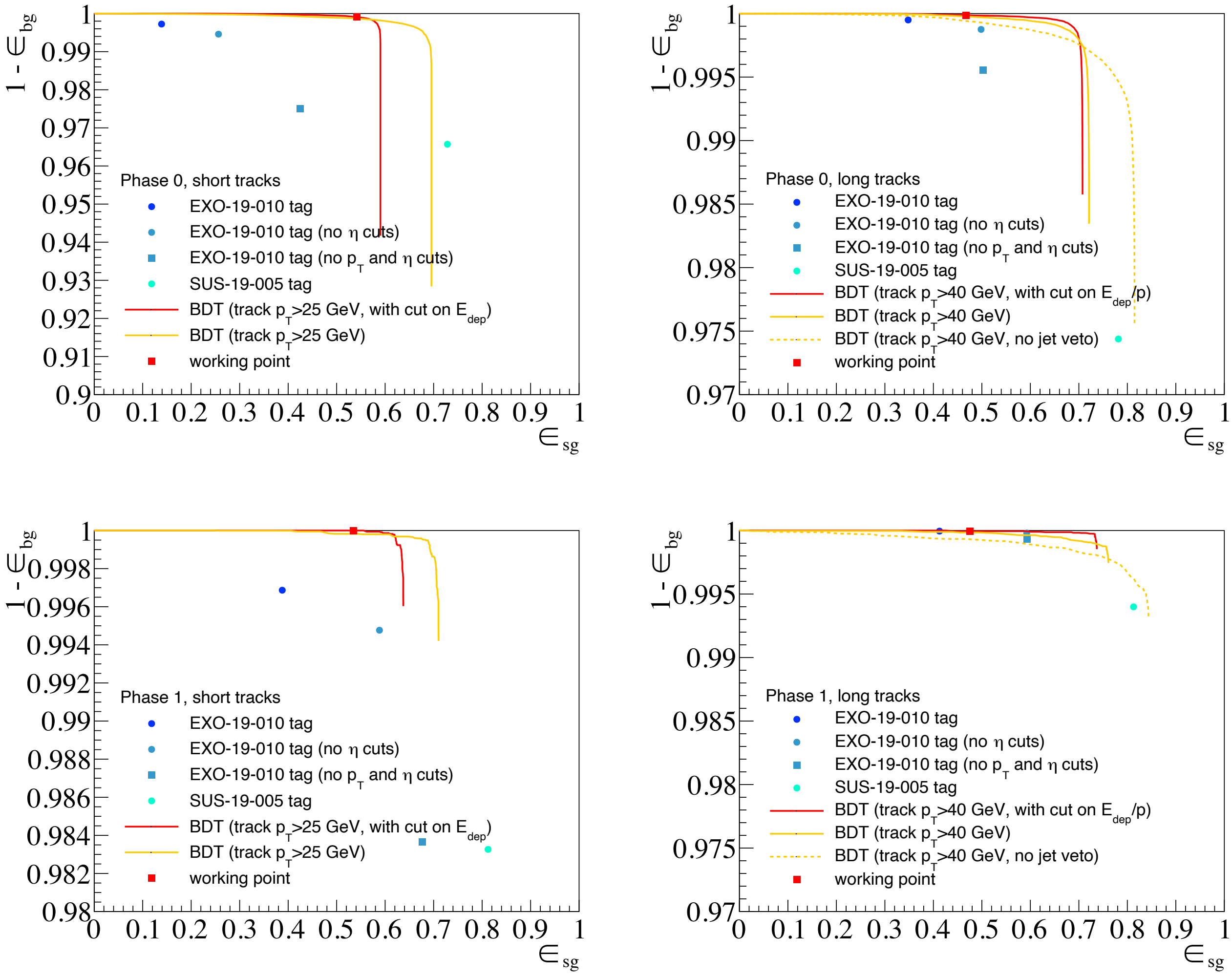

Figure 5.21: Signal efficiency vs. background rejection for the disappearing track tag. For comparison, efficiencies of other published CMS analyses are shown. Top row: Phase 0, bottom row: Phase 1. Left: short tracks, right: long tracks. The ROC curve before (yellow) and after (red) applying the cut on E_{dep} and E_{dep}/p, respectively, is shown, along with the chosen working point. All efficiencies are calculated using the same denominator of pre-selected tracks, with a lower transverse momentum of $p_T > 15$ GeV instead of 25 GeV for short tracks in order to facilitate the comparisons.

5.7.5 Calorimeter masking

In addition to the cut of $E_{\text{dep}}/p < 20\%$ motivated in Fig. 5.20-right for long tracks, the prompt background can be further reduced by masking sections of the detector in which E_{dep} is not measured reliably. Inefficient detector sections, cloudy or disabled electromagnetic crystals or noisy data-acquisition channels can contribute to a mismeasurement of E_{dep}. Electrons which fail the lepton reconstruction criteria and have a lower measured E_{dep} and E_{dep}/p value, respectively, can be falsely classified as a disappearing track.

Detector sections of interest can be analyzed in the $\eta - \phi$ plane. A loose version of the disappearing track classification outlined above is evaluated in Run 2 data, using a lower BDT threshold of $\text{BDT}_{\text{threshold}} > -0.2$, shown in Fig. 5.22-top for each year of data-taking. The $\eta - \phi$ plane thus shows the occupancy of the detector volume, with problematic regions of E_{dep} visible as non-occupied bins. Visible as well is the transition region of $|\eta| \gtrless 1.479$ separating the barrel from the endcap region, as introduced in Sec. 4.1.1, for which a higher occupancy can be seen in the barrel region.

The bin size in Fig. 5.22 is chosen to match the granularity of the electromagnetic calorimeter[4] [74]. Figure 5.22 shows the occupancy map for 2016, 2017, 2018 and the entirety of Run 2 in the first two rows, which is used to create a detector mask to detect detector hotspots. This is done by identifying bins which exceed the average bin occupancy by three standard deviations on the corresponding Poisson probability with a mean parameter equal to the average occupancy, and is shown in the bottom row of Fig. 5.22. A rejection of 50% of prompt background can be achieved by masking only a small detector volume depicted as non-colored bins.

5.7.6 Previous analyses

The background rejection and signal efficiency are compared with two other CMS searches, SUS-19-005 [75] and EXO-19-010 [76]. SUS-19-005 is based on selecting events using the *stransverse mass* M_{T2}, which iteratively quantifies the mass of pair-produced particles, whose decays both yield final states with the same type of undetected particle. Jets are clustered into pseudojets, and a minimization is performed by pairing hypothetical invisible particle momenta with each of the pseudojets with transverse mass M_T. The stransverse mass is given by

$$M_{\text{T2}} = \min_{\vec{p}_{\text{T}}^{\text{miss}\,(1)} + \vec{p}_{\text{T}}^{\text{miss}\,(2)} = \vec{p}_{\text{T}}^{\text{miss}}} \left[\max\left(M_{\text{T}}^{(1)}, M_{\text{T}}^{(2)} \right) \right], \tag{5.7.5}$$

with the invisible unknown momenta $\vec{p}_T^{\,\text{miss}(i)}$ of the undetected particle [77]. EXO-19-010 extends the Run 1 disappearing track analysis [78] to include short tracks. Fig. 5.21 also includes a comparison of the signal efficiency and background rejection efficiency with the two other CMS searches, showing a high background rejection efficiency for the search presented here, with the caveat that no dedicated event selection is replicated for this comparison. For long tracks, the dashed line additionally shows the ROC curve without a cut on E_{dep}/p and without the veto on nearby jets, indicating an improved background rejection efficiency at the cost of a reduced signal efficiency of $\approx 10\%$.

---

[4] This choice results in a bin size of $\Delta\eta \cdot \Delta\phi = 3 \cdot 10^{-4}$.

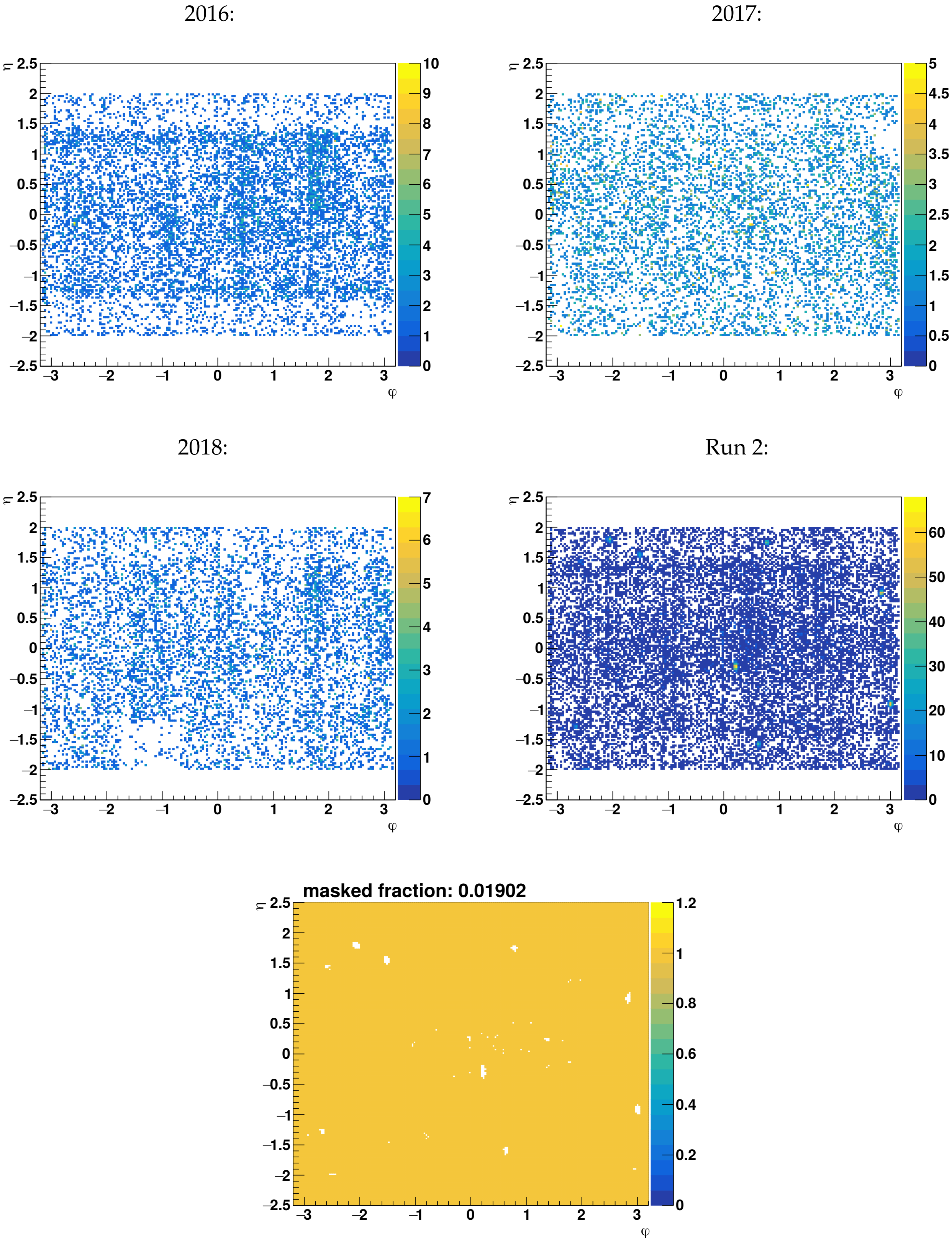

2016:

2017:

2018:

Run 2:

Figure 5.22: Detector hotspot occupancy in the $\eta - \phi$ plane for 2016, 2017, 2018 and the entirety of Run 2 (top and middle row, from left to right). Regions are flagged as masked if they exceed the average occupancy by three standard deviations on the corresponding Poisson probability with a mean parameter equal to the average occupancy.

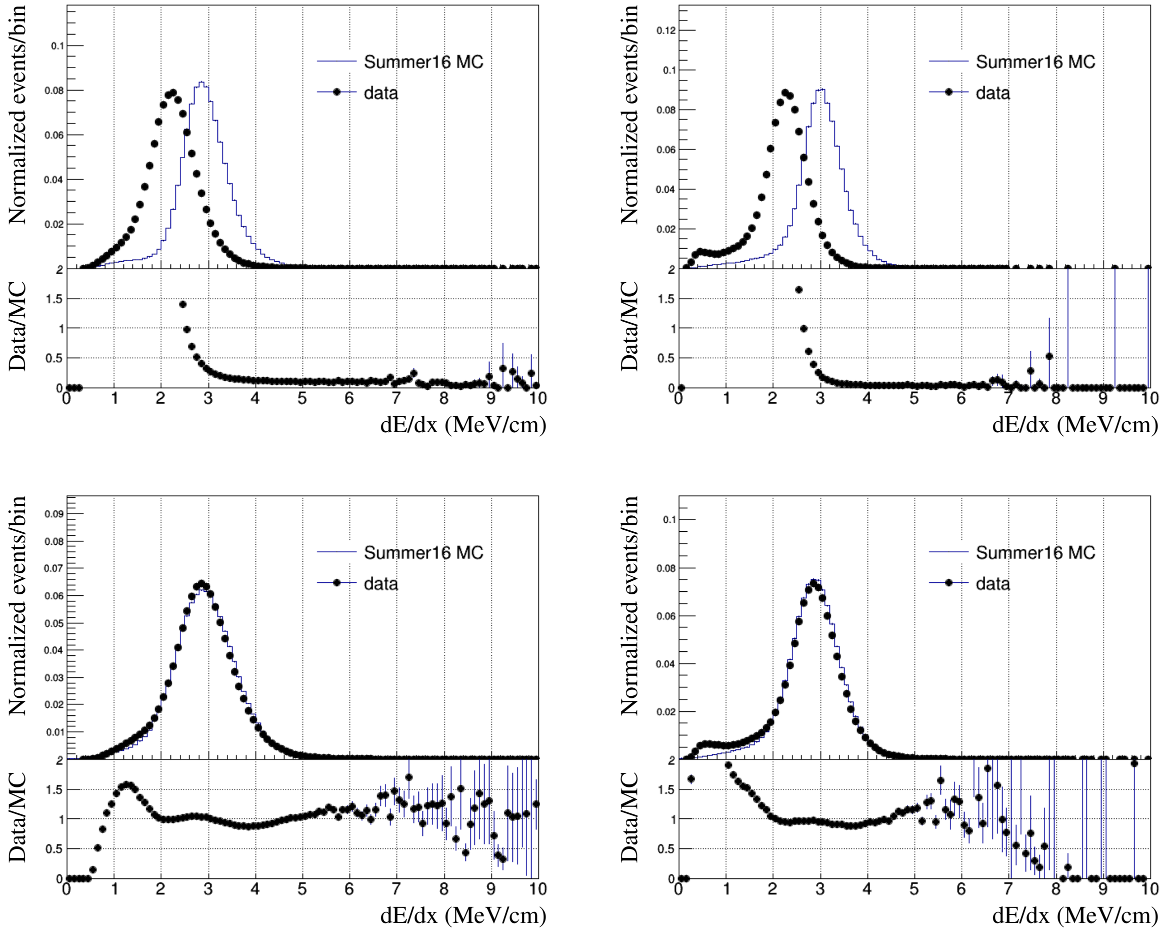

Figure 5.23: Muon track dE/dx measurement for Phase 0 data and SM MC simulation before calibration (top) and after calibration (bottom). Shown are the barrel region (left) and endcap region (right).

5.8 Calibration of the energy loss dE/dx

A time-dependent calibration has been performed and described in [79]. Events are selected with a pair of muons, each satisfying the muon selection criteria as defined in Sec. 5.5. In order not to reveal a possible signal in data, the invariant mass is selected around the Z pole mass of 86 GeV $< m_{\text{inv}} <$ 106 GeV. A track is then matched to each muon within a cone of $\Delta R < 0.01$, and its dE/dx value is obtained. Calibration factors are determined with respect to the Phase 0 MC SM simulation, for which the calibration factor is set to a value of one by construction.

To calibrate the dE/dx measurement for MC SM simulation, resolution effects are taken into account by Gaussian smearing of the shape of dE/dx to match the shape of the distribution in data. For both Phase 0 and Phase 1, a Gaussian fit of the dE/dx distribution is performed for MC and data. The Gaussian function for smearing is constructed with a mean value of $\mu_{\text{smear}} = 1$ and $\sigma_{\text{smear}} = \sqrt{\sigma^2_{data} - \sigma^2_{MC}}$. Figure 5.23 shows the dE/dx distribution before and after performing the calibration for Phase 0, separated in the barrel and endcap regions.

Figure 5.24 shows the calibrated value of dE/dx for short and long pre-selected tracks. The SM background exhibits a mean measured value of $dE/dx \approx 3.0$ MeV/cm, as expected from the convolution of the Bethe-Bloch equation with a Landau distribution [80]. The $\tilde{\chi}_1^{\pm}$-matched tracks in signal exhibit significantly higher dE/dx values when compared to SM background

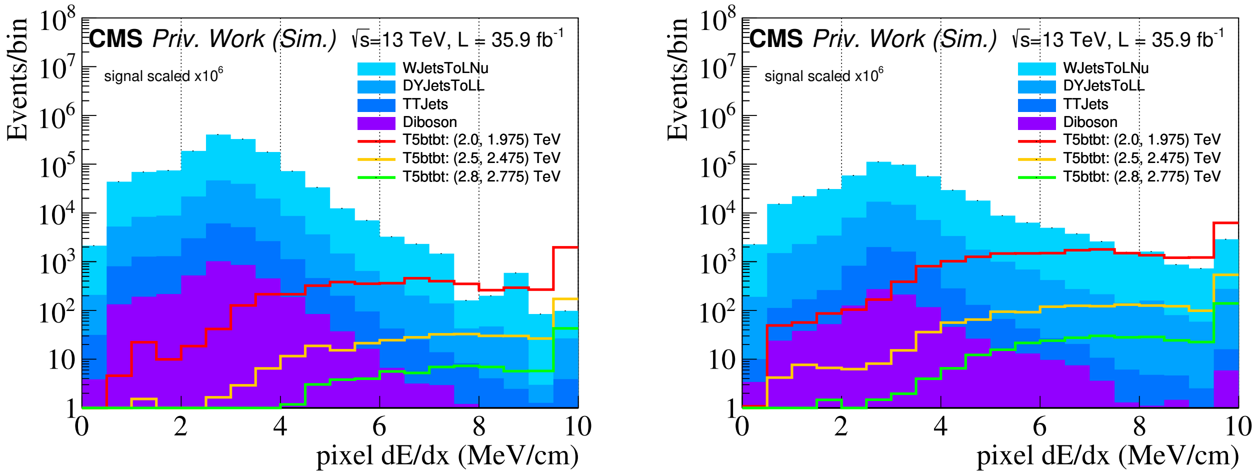

Figure 5.24: Measured energy loss dE/dx for pre-selected short tracks (left) and long tracks (right). Three example signal mass points are included, with masses given by $(m_{\tilde{g}}, m_{\chi_1^0})$. The last bin includes the overflow.

due to the highly-ionizing massive charginos.

The calibrated value of dE/dx can further be used to derive the mass of the highly-ionizing particle using

$$\frac{dE}{dx} = K\frac{m^2}{p^2} + C, \tag{5.8.1}$$

which is valid for singly charged particles [81]. The constants K and C have been determined in [82] using a sample of low-momentum protons, and are found to be $K = 2.684 \pm 0.001$ MeV cm^{-1} and $C = 3.375 \pm 0.001$ MeV cm^{-1}.

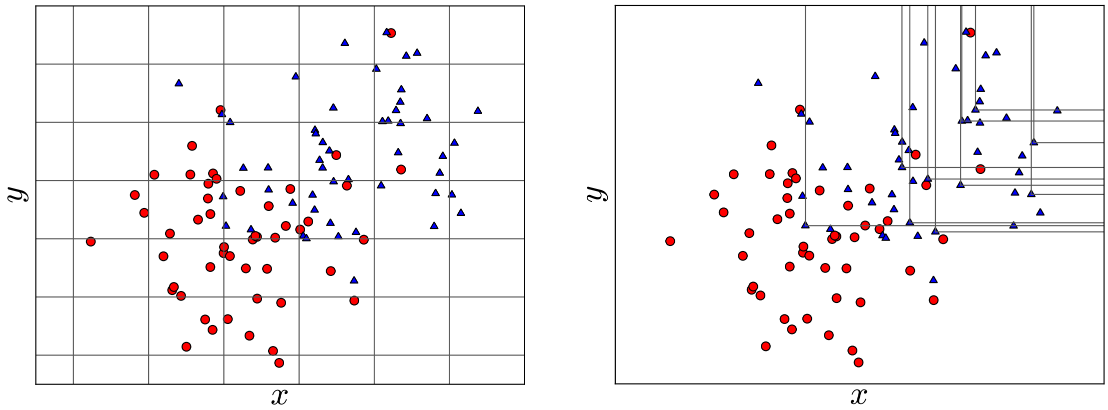

Figure 5.25: Random grid search (RGS) principle. Left: Equidistant scan for a two-dimensional optimization problem, showing a large fraction of the grid bins including areas with zero or low significance. Right: Scan over signal points to determine the best significance for the cuts on the two variables to discriminate between signal and background. Figure taken from [83].

5.9 Event selection

In order to comprehensively probe the diverse range of signals described in Sec. 5.2, the analysis is separated into a hadronic channel, an electron channel and a muon channel. Each channel is required to have at least one disappearing track and at least one jet, which for the hadronic channel is necessary in order to provide a trigger requirement. Firstly, the channels are differentiated by $\not{E}_T$, hadronic activity H_T and numbers of electrons and muons, as defined in Sec. 5.5. For each channel, a further binning is performed to be sensitive to the various signal production modes, e.g., squark, gluino, and electroweakino production. To increase sensitivity to chargino $\tilde{\chi}_1^{\pm}$ pair production, the channels are binned in the number of jets n_{jets} and number of b-tagged jets $n_{\text{b-jets}}$. To further bin in properties of a disappearing track, the energy loss through ionization dE/dx, and the track length as well as track multiplicity is included.

In the following, the optimization of the cut boundaries is discussed, followed by a detailed overview of the cuts used for each channel.

5.9.1 Cut optimization

A random grid search (RGS) is employed to identify the boundaries of the variables $\not{E}_T$, n_{jets} and $n_{\text{b-jets}}$. Given one or more discriminating variables which separate signal and background, the subsequent selection of optimal cuts poses a non-trivial problem, as the computational complexity rises with the number of dimensions, thus quickly prohibiting an equidistant multidimensional grid pattern. A RGS approach solves this problem by selecting cut values from signal tracks and applying the cut values to SM MC background tracks, and counting the number of signal tracks n_s and background tracks n_b. A measure of the significance, such as $\frac{n_s}{\sqrt{n_s+n_b}}$, is then used to determine the cut values with the highest significance [83]. Figure 5.25 shows the principle of the RGS search, Fig. 5.25-left shows a two-dimensional equidistant grid to determine the region with the highest significance. In Fig. 5.25-right, only actual signal tracks are evaluated for the choice of optimal bin boundaries.

5.9.2 Hadronic channel

For the hadronic channel, the baseline selection prior to the binning in properties of the disappearing tracks is given by $\not{E}_T > 150$ GeV and $H_T > \not{E}_T$, at least one jet $n_{\text{jets}} \geq 1$ and no reconstructed leptons $n_e = n_\mu = 0$. Figure 5.26 shows the quantities for pre-selected tracks. All quantities are shown as $n-1$ distributions, meaning that all cuts have been applied, except the cut on the quantity displayed on the x-axis.

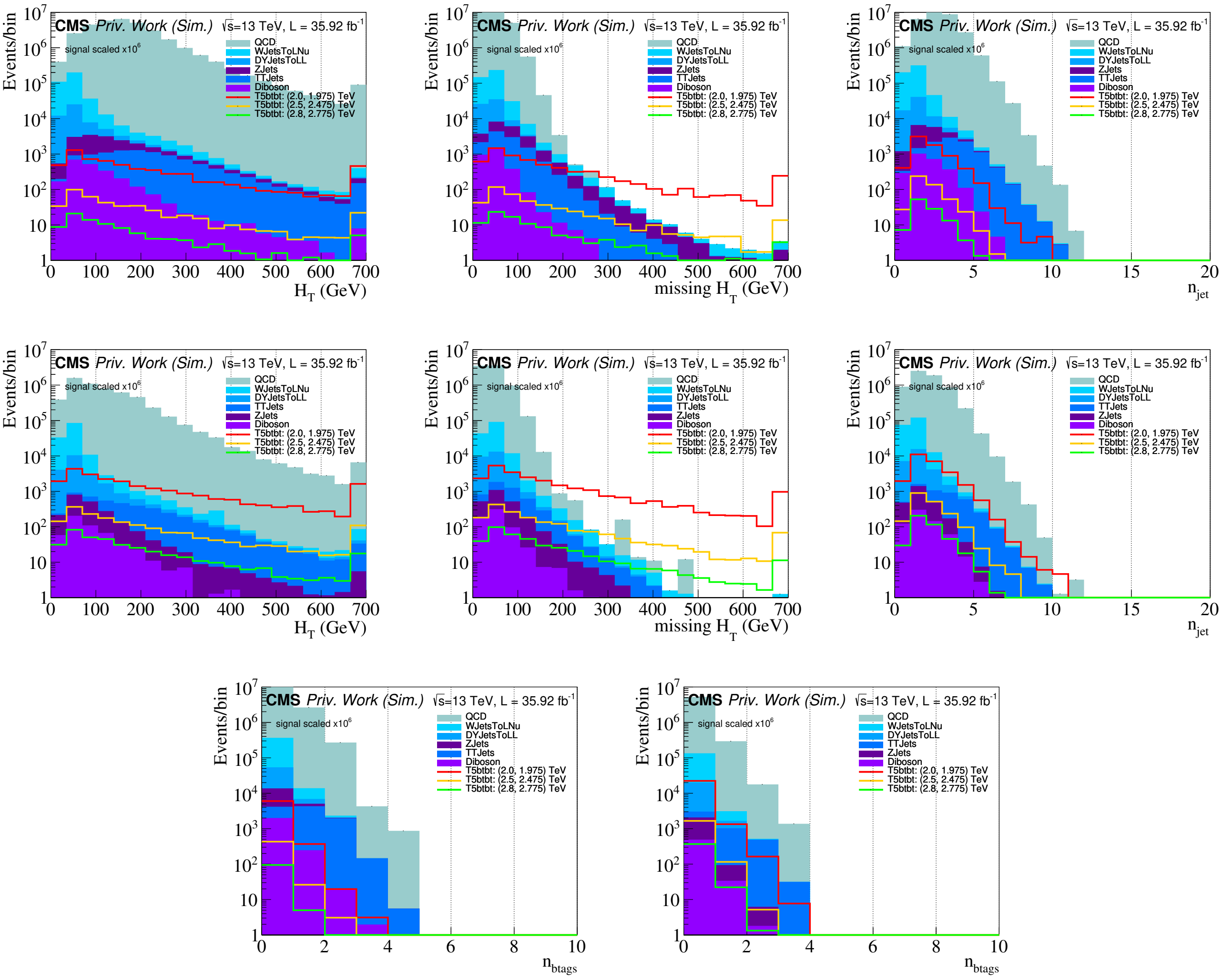

Figure 5.26: $n-1$ distributions for the hadronic channel, shown for short (top row) and long tracks (middle row); from left to right: hadronic activity H_T, $\not{E}_T$, n_{jets}. The bottom row shows $n_{\text{b-jets}}$ for short (left) and long tracks (right).

The signal regions are chosen to incorporate regions of increasing trigger efficiency ($\not{E}_T = (150, 300)$ GeV), and the plateau region of the trigger efficiency ($\not{E}_T > 300$ GeV; see Sec. 5.10). A binning in terms of jets and b-tagged jets is chosen to provide sensitivity to the chargino production mechanism. Signal regions are introduced for both short and long tracks, and a final binning in terms of the energy loss dE/dx is performed for low and high energy loss ($dE/dx \geq 4.0$ MeV/cm, $dE/dx < 4.0$ MeV/cm). Table 5.7 shows the 24 signal regions (SR) for the hadronic channel.

$\not\!\!E_T$	$n_{\text{b-tags}}$	n_{jets}	n_{short}	n_{long}	dE/dx (MeV/cm)	SR
hadronic channel (n_μ=0, n_e=0)						
150-300 GeV	0	[1,3)	0	1	< 4.0	1
					≥ 4.0	2
			1	0	< 4.0	3
					≥ 4.0	4
		$\geq$3	0	1	< 4.0	5
					≥ 4.0	6
			1	0	< 4.0	7
					≥ 4.0	8
	$\geq$1	[1,3)	0	1	< 4.0	9
					≥ 4.0	10
			1	0	< 4.0	11
					≥ 4.0	12
		$\geq$3	0	1	< 4.0	13
					≥ 4.0	14
			1	0	< 4.0	15
					≥ 4.0	16
>300 GeV	any	[1,3)	0	1	< 4.0	17
					≥ 4.0	18
			1	0	< 4.0	19
					≥ 4.0	20
		$\geq$3	0	1	< 4.0	21
					≥ 4.0	22
			1	0	< 4.0	23
					≥ 4.0	24

Table 5.7: Definition of the signal regions for the analysis with one disappearing track and zero leptons.

5.9.3 Muon channel

For the muon channel, the baseline selection is given by $\not{E}_T > 30$ GeV and at least one jet $n_{\text{jets}} \geq 1$, at least one muon $n_\mu \geq 1$ and zero electrons $n_e = 0$. In order to be able to construct control regions for validating the selection, further cuts on the transverse mass of the muon m_T and the invariant mass of the muon-disappearing-track system are imposed to select signal-like events. The transverse mass m_T of a lepton is defined as

$$m_T = \sqrt{2 p_T^{\text{lep}} \not{E}_T (1 - \cos \Delta\phi(\vec{\text{lep}}, \vec{\not{E}_T}))}. \tag{5.9.1}$$

Figure 5.27 shows $n-1$ distributions for the muon channel. To select signal-like tracks, $m_T > 110$ GeV is imposed, while the invariant mass is required to be larger than the peak position of the Z resonance $m_{\text{DTk},\mu} > 120$ GeV. The invariant mass is determined assuming massless tracks $m_{\text{DTk}} = 0$ GeV.

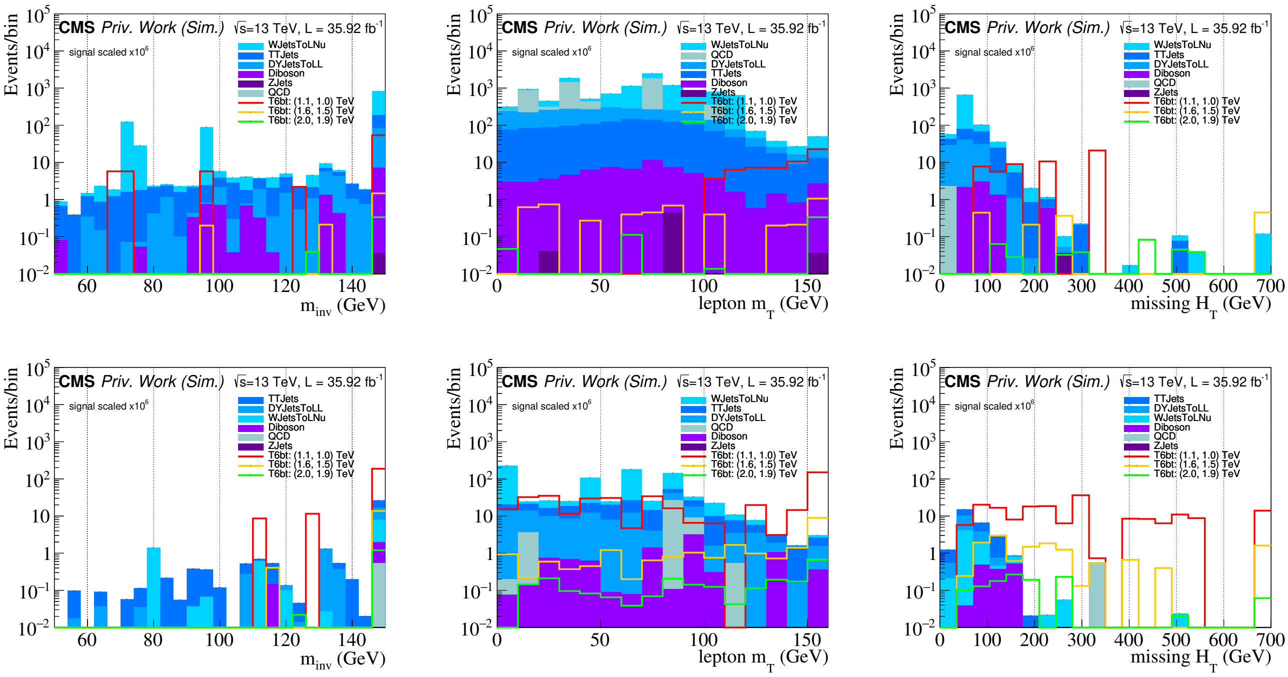

Figure 5.27: $n-1$ distributions for the muon channel, shown for short (top row) and long tracks (bottom row); from left to right: invariant mass of the leading muon and disappearing track, transverse mass of the leading muon, and $\not{E}_T$.

Table 5.8 shows the 12 signal regions for the muon channel.

5.9.4 Electron channel

For the electron channel, the baseline selection is given by $\not{E}_T > 30$ GeV and at least one jet ($n_{\text{jets}} \geq 1$) and one electron ($n_e = 1$). Figure 5.28-top shows the variable distributions for the electron channel, Fig. 5.28-bottom shows the selection of signal-like tracks with $m_T > 110$ GeV and an invariant mass larger than the peak of the Z resonance, $m_{\text{DTk},e} > 120$ GeV. Table 5.9 shows the 12 signal regions for the electron channel.

$\not{E}_T$	$n_{\text{b-tags}}$	n_{jets}	n_{short}	n_{long}	dE/dx (MeV/cm)	SR
muon channel ($n_\mu \geq 1$, n_e=0)						
30-100 GeV	0	≥1	0	1	< 4.0	25
					≥ 4.0	26
			1	0	< 4.0	27
					≥ 4.0	28
	≥1		0	1	< 4.0	29
					≥ 4.0	30
			1	0	< 4.0	31
					≥ 4.0	32
>100 GeV	any		0	1	< 4.0	33
					≥ 4.0	34
			1	0	< 4.0	35
					≥ 4.0	36

Table 5.8: Definition of the signal regions for the analysis with one disappearing track and ≥ 1 muon(s).

$\not{E}_T$	$n_{\text{b-tags}}$	n_{jets}	n_{short}	n_{long}	dE/dx (MeV/cm)	SR
electron channel ($n_e \geq 1$)						
30-100 GeV	0	≥1	0	1	< 4.0	37
					≥ 4.0	38
			1	0	< 4.0	39
					≥ 4.0	40
	≥1		0	1	< 4.0	41
					≥ 4.0	42
			1	0	< 4.0	43
					≥ 4.0	44
>100 GeV	any		0	1	< 4.0	45
					≥ 4.0	46
			1	0	< 4.0	47
					≥ 4.0	48

Table 5.9: Definition of the signal regions for the analysis with one disappearing track and ≥ 1 electron(s).

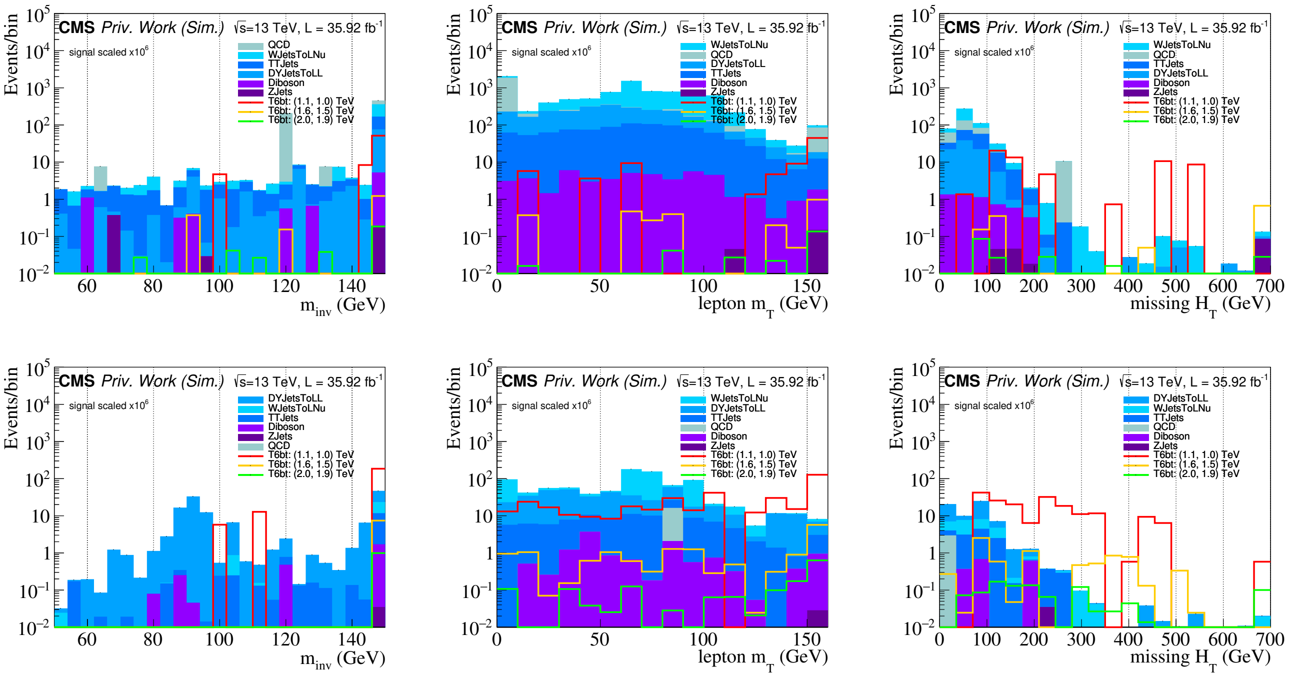

Figure 5.28: $n-1$ distributions for the electron channel, shown for short (top row) and long tracks (bottom row); from left to right: invariant mass of the leading electron and disappearing track, transverse mass of the leading electron, and $\not{E}_T$.

n_{DTk}	$\not{E}_T$	$n_{\text{b-tags}}$	n_{jets}	n_{short}	n_{long}	dE/dx (MeV/cm)	SR
$n_{\text{DTk}} \geq 2$	any						49

Table 5.10: Definition of a signal region containing two or more disappearing tracks.

5.9.5 Events containing ≥ 2 disappearing tracks

Pair-produced charginos $\tilde{\chi}_1^{\pm}$ can produce two disappearing tracks in a given event. The detection of two or more tracks which are disappearing is expected to be rare, thus a single bin is added with $n_{\text{DTk}} \geq 2$ which is inclusive in $\not{E}_T$, n_{jets} and $n_{\text{b-jets}}$ as well as the disappearing track properties, as shown in Tab. 5.10.

5.10 Trigger

Events in data are selected if they satisfy the L1 and HLT requirements for the corresponding analysis channel. The HLT selection is either based on missing transverse energy $\not{E}_T$ (or `MET`) and missing hadronic transverse momentum $\not{H}_T$ for the hadronic channel, or, in the case of the leptonic channels, on a well-reconstructed electron or muon. The efficiency of the trigger selection is measured for each channel and applied to simulated data via event weights.

5.10.1 Hadronic channel

For the hadronic channel, a combination of $\not{E}_T$ and $\not{H}_T$ trigger paths is used, selecting events with a trigger turn-on of $\not{E}_T, \not{H}_T > (90, 100, 110, 120, 130, 140)$ GeV. Different trigger paths are used to compensate for any loss in efficiency due to pre-scaled lower thresholds in periods of higher luminosity. This is necessary in order to reduce the otherwise too high event rate. Events

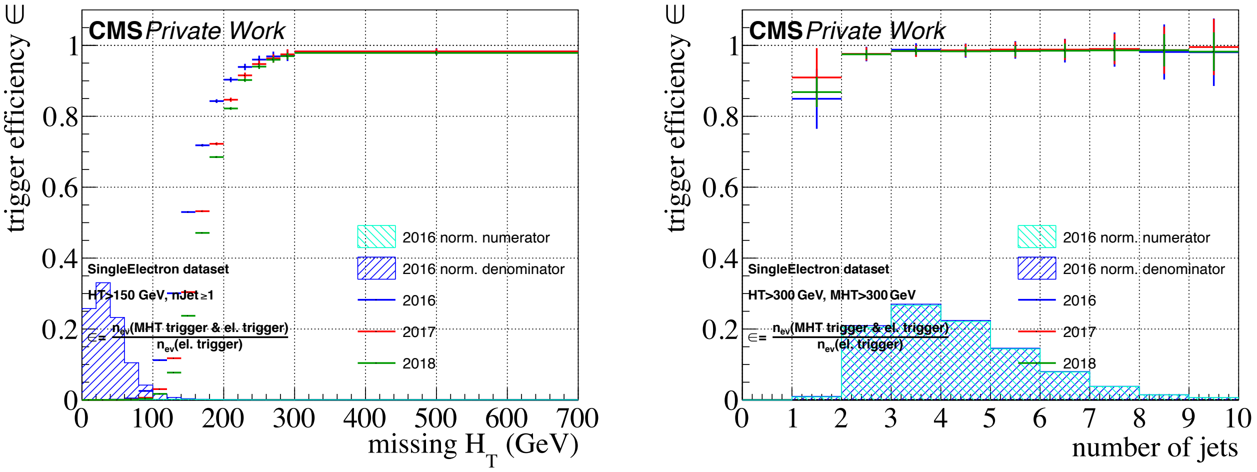

Figure 5.29: The efficiency of the set of $\not{E}_T - MHT$ cross triggers measured in a single-electron control region, shown for $\not{E}_T$ (left) and number of jets (right). The jet multiplicity is shown for $\not{E}_T > 300$ GeV to account for the trigger turn-on.

are selected in data if at least one trigger fires. The trigger efficiency is defined as the ratio of events passing the trigger requirements to the total number of events in a reference sample,

$$\epsilon = \frac{n_{\text{ev}}(\text{passing trigger requirements in reference sample})}{n_{\text{ev}}(\text{reference sample})}. \tag{5.10.1}$$

The trigger efficiency is measured in a reference sample which is orthogonal to the trigger which is being studied. In this case, a single-electron dataset is chosen. Single-electron events are selected by requiring at least one single-electron trigger, with an online threshold on the transverse momentum of the electron $p_T^e > (27, 32, 35)$ GeV and an offline electron reconstructed and identified with a tight working point. As for the combination of $\not{E}_T$ and $\not{H}_T$ trigger paths, different trigger turn-on values of p_T are considered to compensate efficiency losses due to pre-scaled lower trigger thresholds.

Figure 5.29 shows the trigger efficiency as a function of the offline $\not{E}_T$ and number of jets, with baseline selection cuts $H_T > 150$ GeV and $n_{\text{jet}} \geq 1$ applied. The trigger is found to be greater than 95% efficient for $\not{E}_T > 250$ GeV, and nearly 100% efficient for $\not{E}_T > 300$ GeV. An inefficiency up to 15% is seen in the lowest jet multiplicity categories in Fig. 5.29-right, and is accounted for as the event weight applied to simulated events. To account for the increasing trigger efficiency for one and two jets, Fig. 5.30 shows the trigger efficiency for low and high jet multiplicity depending on $\not{E}_T$, as it is applied in the further analysis.

5.10.2 Leptonic channel

The leptonic analysis, in which events with a disappearing track and a lepton are selected, uses single-lepton triggers. For the electron channel, events are selected with online thresholds on the transverse momentum of the electron $p_T^e > (27, 32, 35)$ GeV with a tight working point. For the muon channel, events with a valid muon trigger are selected with a trigger threshold of $p_T^\mu > (24, 27, 50)$ GeV, with the two lowest trigger thresholds selecting isolated muons. A baseline cut following the lepton selection is made by requiring either an electron or muon, and $H_T > 30$ GeV, $\not{E}_T > 30$ GeV and $n_{\text{jet}} \geq 1$. The single-electron trigger efficiency is measured by using the single-muon trigger selection as a reference sample for the single-electron trigger

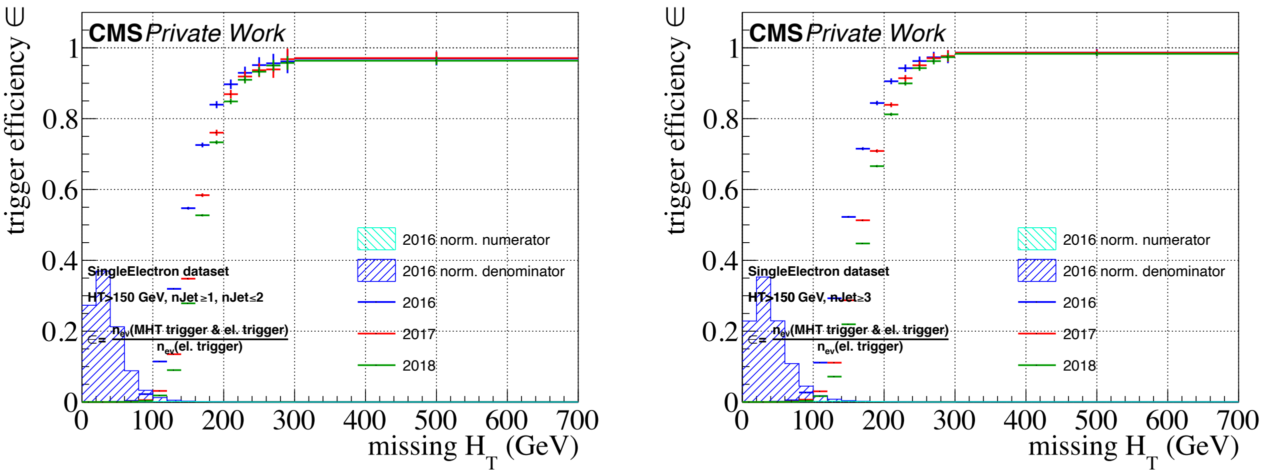

Figure 5.30: The efficiency of the set of $\not{E}_T - \not{H}_T$ cross triggers measured in a single-electron control region. Left: trigger efficiency for $n_{\text{jet}} \geq 1, \leq 2$. Right: trigger efficiency for $n_{\text{jet}} \geq 3$.

efficiency, and vice versa.

Figure 5.31 shows the single-electron trigger efficiency (left side), and the single-muon trigger efficiency (right side). The single-electron trigger efficiency reaches more than 80% efficiency for $p_T > 50$ GeV, while the single-muon trigger efficiency reaches more than 90% efficiency for $p_T > 50$ GeV.

2016 (electron channel): 2016 (muon channel):

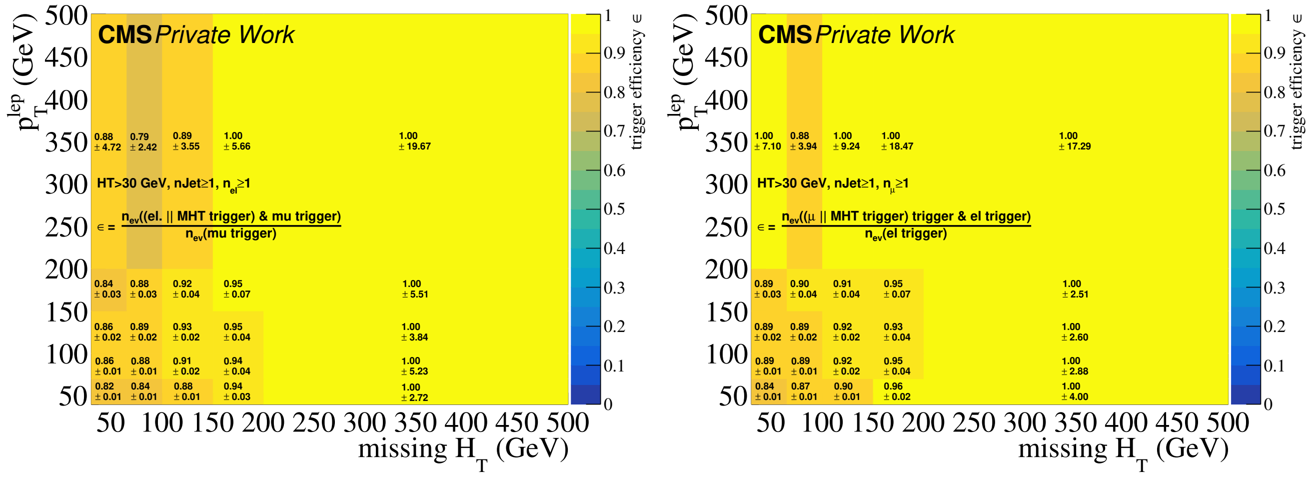

2017 (electron channel): 2017 (muon channel):

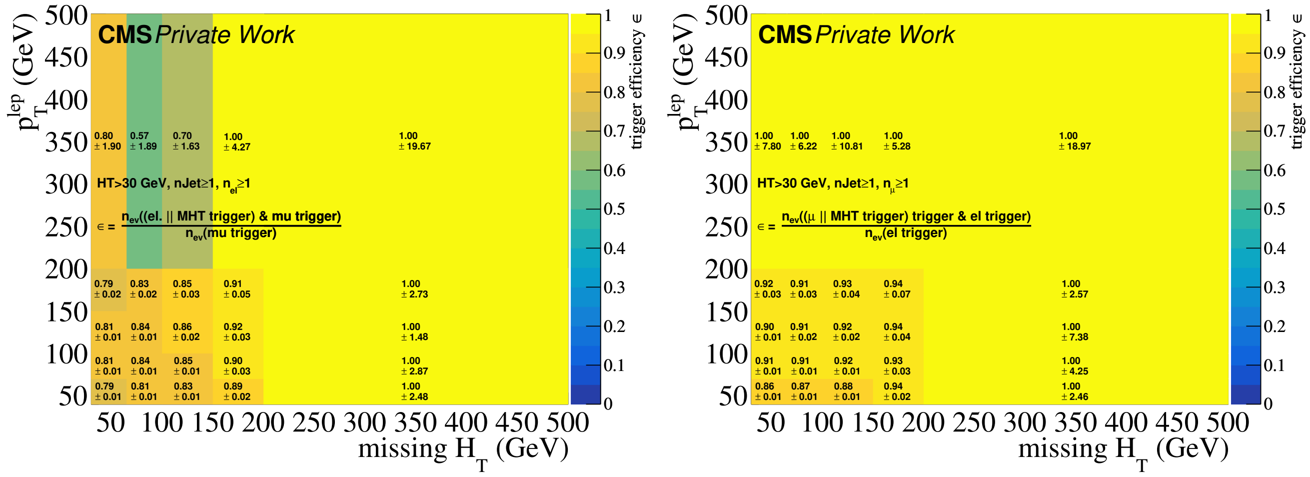

2018 (electron channel): 2018 (muon channel):

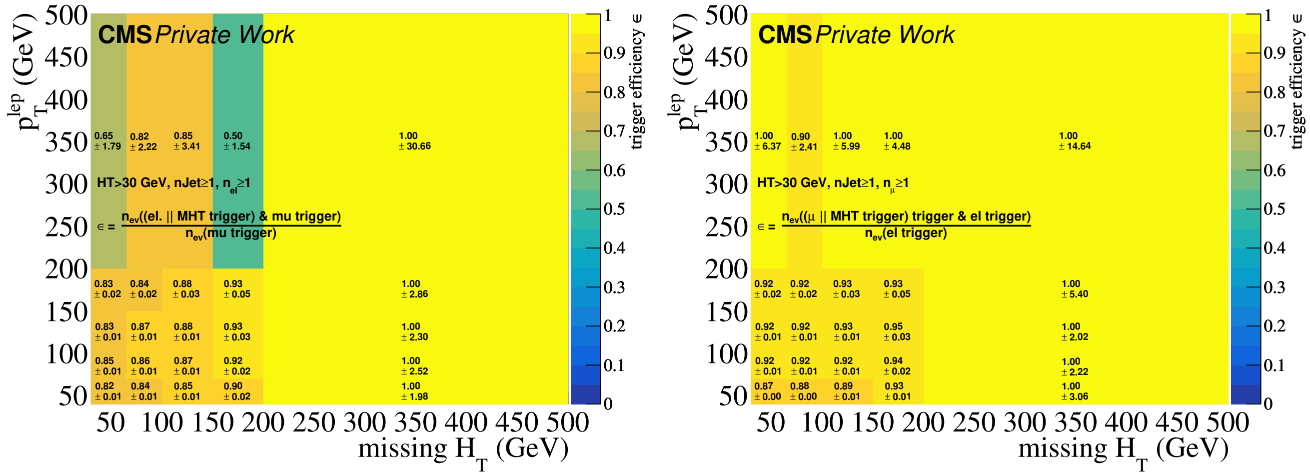

Figure 5.31: Single lepton trigger efficiency for the electron channel (left) and muon channel (right) dependent on lepton p_T of the triggered lepton in the numerator and $\not{E}_T$, as applied in the analysis. Shown are values for 2016, 2017 and 2018 from top to bottom.

5.11 Background estimation

This section discusses sources of background which enter the search regions and can mimic the signature of a disappearing track. It describes data-driven background estimation methods for each source of background. Tests of the methods are also presented, including closure tests based on SM background MC simulation samples, as well as validation tests performed in separate data control regions that are orthogonal to the signal regions.

5.11.1 Types of background sources

In addition to charged long-lived particles such as a chargino $\tilde{\chi}_1^{\pm}$, the signature of a disappearing track can also occur either due to SM particles, which are not fully reconstructed because of detector inefficiencies, or due to track trajectories constructed by incidentally combining hits from different particles at the track reconstruction stage. Two main backgrounds enter the search and can mimic disappearing tracks. The first source is *prompt* background from real particles including electrons, pions and muons, which are not reconstructed. As a consequence, they are not entering the collection of PF candidates. This can occur if e.g. an electron undergoes a catastrophic Bremsstrahlung emission, in which a decelerating electron traverses the magnetic field on a curved path and radiates a photon that carries most of the energy of the original electron. Another possibility are detector inefficiencies in the electromagnetic and hadronic calorimeter, which can lead to an under-measured energy of electrons and pions and causing them to be not reconstructed. For muons, a flawed reconstructed hit pattern in the muon chambers can lead to a muon not being reconstructed. If the track is not matched to any reconstructed lepton in the PF candidate collection, it can be tagged by the disappearing track tag provided the track trajectory contains no missing inner hits, but contains at least two missing outer hits.

The second source of background is due to combinatoric effects of the tracking algorithm, in which hits from various unrelated particles align by chance in a pattern resembling a track. This is expected to occur by chance, either due to particles from a different interaction point or due to detector noise. This source of background is referred to as the *spurious track* background.

In order to assess the background composition for short and long tracks, both signal samples containing long-lived charginos and SM background are compared in MC simulation. Pre-selected tracks are matched to generator particles within a cone of $\Delta R < 0.04$. A pre-selected track can be classified as a spurious track if it can not be matched to a generator electron, muon, prompt tau or hadronic tau decay. Otherwise, the track is classified to originate due to prompt background sources.

Figure 5.32 shows the background composition in the hadronic channel for Phase 0, Phase 1 and for combined Run 2 scaled to the respective luminosity, with long tracks depicted in the first bin and short tracks in the second bin. The same set of background MC simulation samples as used in the training of the BDTs is shown in the figure, including W+jets production, DYJets, $\mathrm{t\bar{t}}+$ jets, and diboson background MC simulation samples. The dominating background for short tracks is found to be due to spurious background (89.6% for Run 2 MC simulation), followed by prompt background. For long tracks, prompt background is the dominating background (64.1% for Run 2 MC simulation). Comparing Phase 0 to Phase 1 shows a reduction in spurious tracks from 46.8% to 23.3% for long tracks due to the upgraded pixel detector in Phase 1.

For the combined Run 2 MC simulation, Fig. 5.33 shows the background composition in the hadronic channel for $\not{E}_T$, number of tracker hits and the transverse impact parameter d_{xy}. The d_{xy} distributions further confirm that the spurious track background is the dominant source of

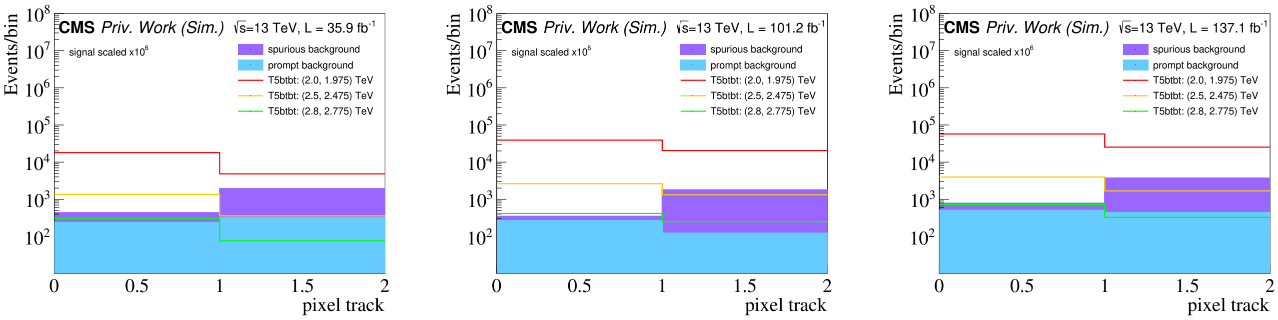

Figure 5.32: Background composition for Phase 0 (left), Phase 1 (center) and Run 2 (right), derived from MC truth information for the hadronic channel. The first bin indicates long tracks, while the second bin indicates short tracks. Three example mass points from the T5btbtLL signal are included as reference, given as $(m_{\tilde{g}}, m_{\tilde{\chi}_1^0})$.

background for $d_{xy} > 0.02$ cm.

A realistic description of background sources for long-lived particle decays is not expected in background MC simulation, therefore data-driven methods are introduced in the following sections. As the generator information about the background nature is available in background MC samples, it can however provide a closure test for the methodology.

In the following, methods are presented to estimated the prompt and spurious background. For the prompt background, a separate approach is used for the background due to electrons and pions (showering background) and the background due to muons, which are minimally-ionizing particles (MIP background).

5.11.2 Methodology for the prompt background from showering particles

In the following, the prompt background is estimated assuming that it is due to non-reconstructed showering particles.

A well established data-driven method, the *ABCD* method, relies on two uncorrelated variables, which are both used to split the data into two regions. Figure 5.34 shows a sketch of this method for the prompt background from showering particles. For uncorrelated variables, the ratio of the event counts in the split regions of the first variable is equal to the ratio of the event counts in the split regions of the second variable,

$$\frac{n_A}{n_B} = \frac{n_C}{n_D}. \tag{5.11.1}$$

Solving Equation 5.11.1 for $n_D = n_C \cdot n_B / n_A$ then yields the predicted count n_D of background events in the signal region as a function of the event count in the control region n_C and the transfer factor n_B / n_A.

For the prompt background estimation from showering particles, the uncorrelated variables are the invariant mass of a system of a disappearing track and an electron, and the deposited energy E_{dep}. The deposited energy E_{dep} is split into a signal region with $E_{\text{dep}} < 15$ GeV for short tracks and $E_{\text{dep}}/p < 0.2$ for long tracks; and a sideband region defined by $E_{\text{dep}} = (30, 300)$ GeV for short tracks and $E_{\text{dep}}/p = (0.3, 1.2)$ for long tracks. Fig. 5.35 depicts the background composition of the deposited energy E_{dep} in the hadronic channel. As is visible in Fig. 5.35, the signal contribution is largest for small values of E_{dep} and E_{dep}/p, respectively. The boundaries of the sideband region are chosen in order to achieve close proximity but orthogonality to the signal

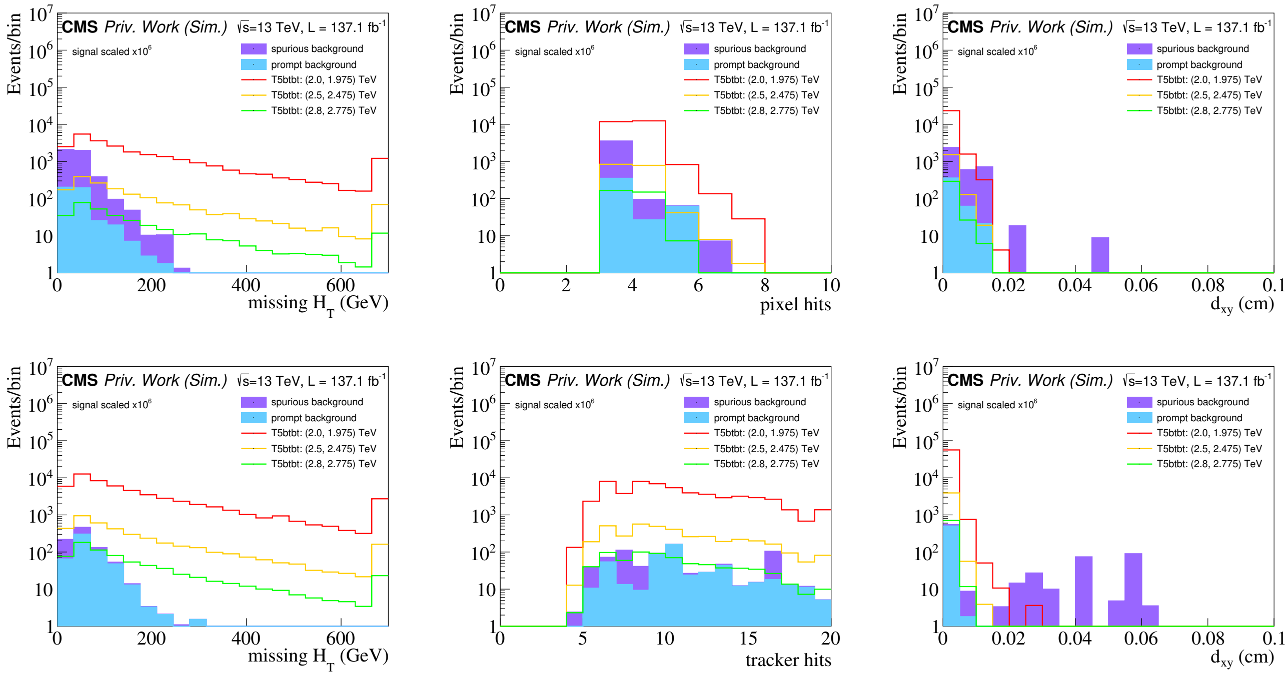

Figure 5.33: Background composition in the hadronic channel shown for short (top) and long tracks (bottom) as $n-1$ distributions. From left to right: $\not{E}_T$, number of tracker hits and the transverse impact parameter d_{xy}.

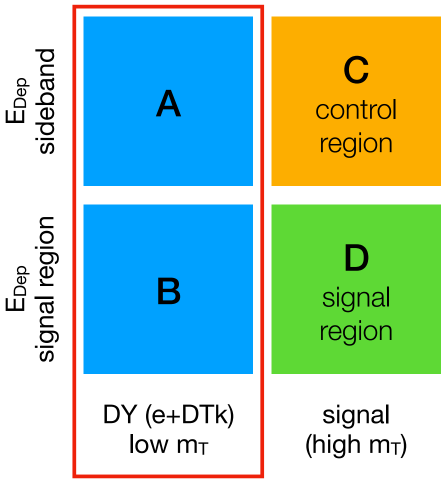

Figure 5.34: Regions used in the data-driven background estimation method for the prompt background from showering particles, with the DY electron + DTk region being using to measure the transfer factor indicated in red. The invariant mass of the electron + DTk system $m_{l,\text{track}}$ (and in the case of the leptonic channels, both the transverse mass m_T and $m_{l,\text{track}}$) and the deposited energy E_{dep} are used as uncorrelated observables.

region, while simultaneously minimizing contamination from spurious tracks. The choice of cuts defining this sideband region is also constrained by the need for sufficient statistics in the sideband, such that n_B/n_A is small. The use of E_{dep} and E_{dep}/p for this sideband is the reason for omitting E_{dep} in the BDT training.

For the second uncorrelated variable, two regions are considered, the signal region selection and an orthogonal Drell-Yan (DY) region. In the DY region, a pair of a disappearing track and

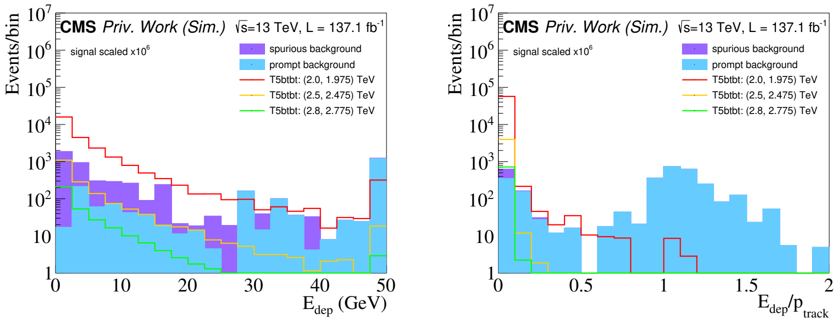

Figure 5.35: Background composition for the deposited energy E_{dep} in the hadronic channel, shown for short (left) and long tracks (right). E_{dep} is used to construct a sideband region in addition to the signal region for low values of E_{dep} and E_{dep}/p, respectively.

category	Phase 0	Phase 1	Run 2
short tracks	0.922 ± 0.14	0.547 ± 0.058	0.645 ± 0.056
long tracks	0.475 ± 0.031	0.622 ± 0.043	0.537 ± 0.026

Table 5.11: Transfer factor κ_e for the estimation of the prompt background from showering particles in data. The values are measured in the DY electron + DTk region defined by the selection of an electron-DTk pair with an invariant mass consistent with the Z boson mass.

an electron is selected from events with one electron and zero muons. In order to maintain orthogonality with respect to the signal region, a window cut on the invariant mass $m_{l,\text{track}} = (70, 105)$ GeV is required for short tracks ($m_{l,\text{track}} = (75, 100)$ GeV for long tracks), as well as a cut on the transverse lepton mass of $m_T < 100$ GeV. Fig. 5.36-left shows the background composition for the invariant mass distribution in the DY electron + DTk region. The majority of the background origins from prompt background for both short and long tracks. In order to increase the statistics in the sideband region, the jet veto is lowered to $\Delta R(\text{DTk}, \text{jets}) > 0.1$. This is not reducing the purity of the DY electron + DTk region, as shown in 5.36-center.

Figure 5.36-right shows the background composition for the azimuthal angle ϕ between the $\not{E}_T$ and the disappearing track, which shows that the majority of prompt background tracks have small values of $\Delta\phi(\not{E}_T, \text{track})$. A contamination of spurious tracks in the DY electron + DTk region can thus be reduced by requiring small values of $\Delta\phi(\not{E}_T, \text{track}) < \pi/4$ for short tracks and $\Delta\phi(\not{E}_T, \text{track}) < \pi/2$ for long tracks.

Measurement of the transfer factor κ_e

The transfer factor $\kappa_e = \frac{n_B}{n_A}$ measured in the DY electron + DTk region is given by the ratio of the number of tracks in the signal-like region of E_{dep} (E_{dep}/p) for short (long) tracks divided by the number of tracks in the sideband region, and is shown in Tab. 5.11 for short and long tracks. While Tab. 5.11 includes separate measurements of the transfer factor for Phase 0 and Phase 1, a consolidated transfer factor for Run 2 data is used in the final analysis.

The purity of prompt background in the DY electron + DTk region for short tracks is estimated as low as $\approx 50\%$. A correction factor of 0.5 is therefore applied to the prompt background from showering particles transfer factor for short tracks, along with a 100% systematic uncertainty on the prompt background from showering particles for short tracks.

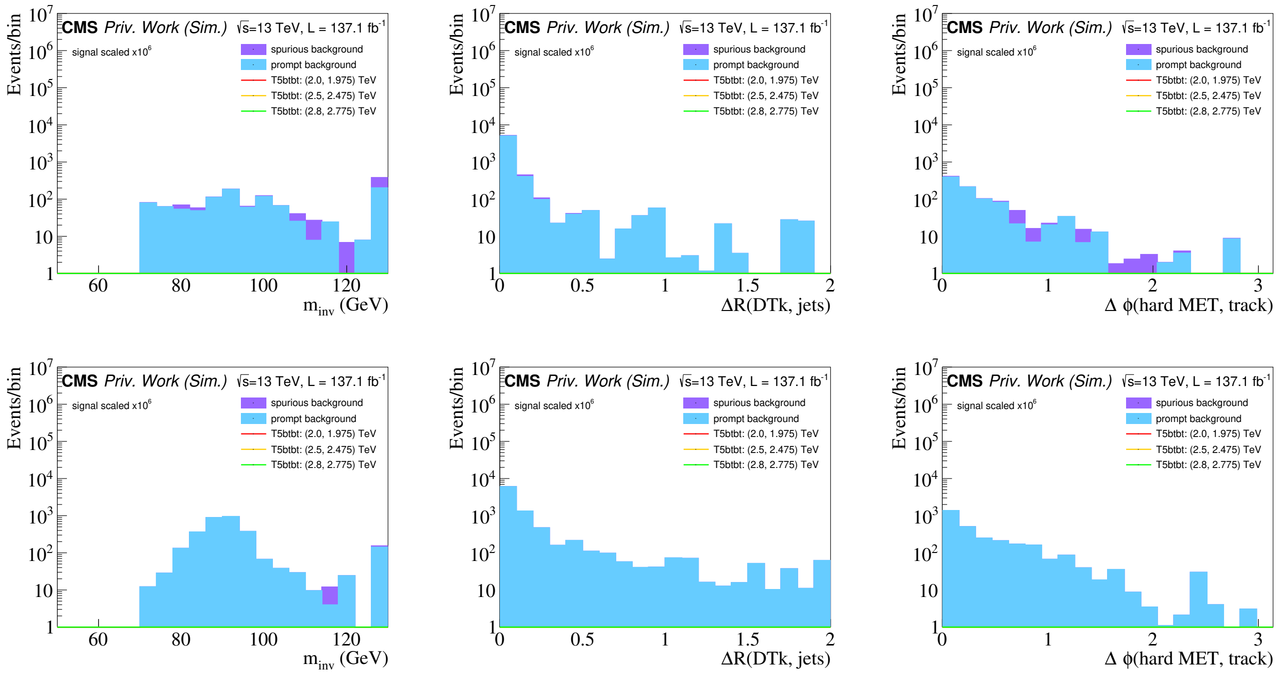

Figure 5.36: Background composition in the DY electron + DTk region. Shown are $n-1$ distributions for the invariant mass $m_{e,\text{track}}$, $\Delta R(\text{DTk, jets})$, and the azimuthal angle $\Delta\phi(\not\!\!E_T, \text{track})$ for short (top) and long tracks (bottom). A window cut in the invariant mass of the electron and disappearing track is used to construct the DY electron + DTk region, while the cut on $\Delta R(\text{DTk, jets})$ is relaxed to enhance statistics in the sideband region. A cut on $\Delta\phi(\not\!\!E_T, \text{track})$ is introduced to reduce contamination from spurious tracks (see text).

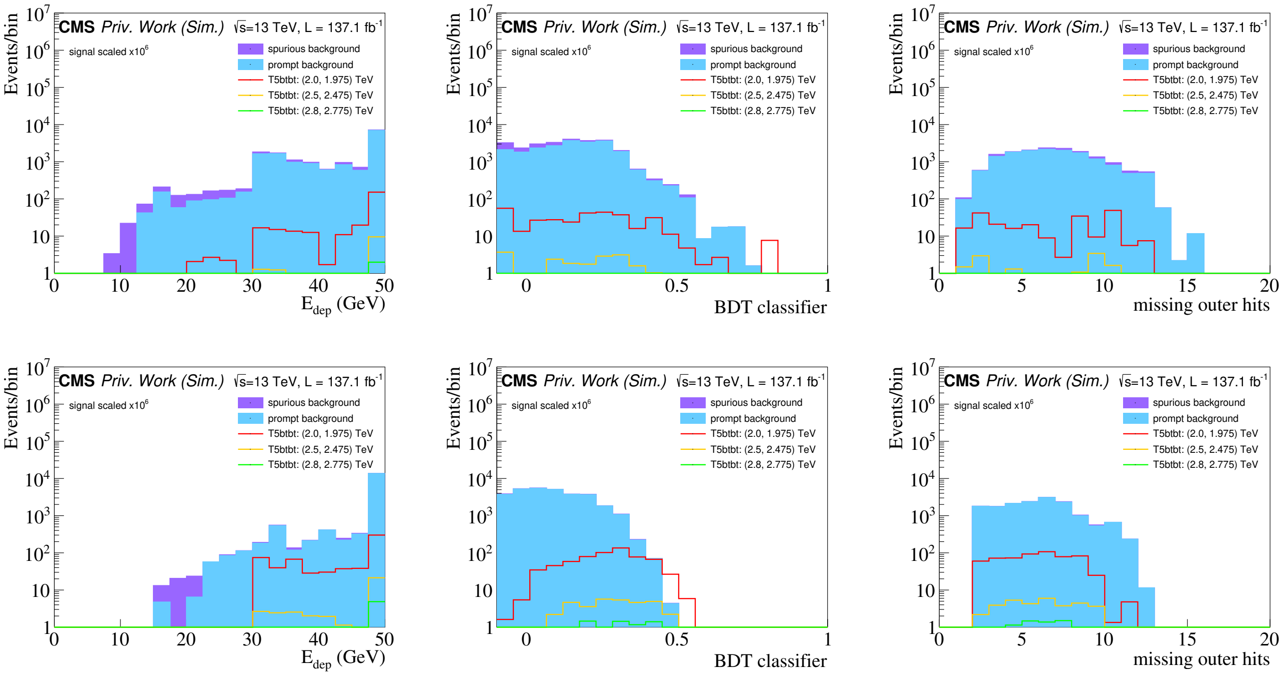

Figure 5.37: Background composition in MC for the prompt background from showering particles control region in the hadronic channel, showing the deposited energy E_{dep}, the BDT classifier and the number of missing outer hits. Top row: short tracks, bottom row: long tracks.

Prompt background from showering particles control region

Before determining the predicted number of tracks in the signal region D by multiplying the transfer factor κ_e with the number of tracks in the control region C, the purity of the control region is investigated. The control region is constructed by applying the complete signal region selection, but inverting E_{dep} to the E_{dep} sideband region. Additionally, the lower bound on the BDT classifier is slightly adjusted in order to increase statistics in the control region to BDT > 0.1 from BDT > 0.12 for long tracks (Phase 0); and to BDT > 0.05 from BDT > 0.15 for short tracks (Phase 1).

Figure 5.37 shows the background composition for the prompt background from showering particles control region based on MC simulation, showing a high purity of 98.8% for long tracks (91.8% for short tracks) in terms of prompt background tracks relative to spurious tracks. While the background estimation method is purely data-driven, MC simulation can give an assessment of the optimization of the control region boundaries and increase the purity.

5.11.3 Methodology for the prompt background from muons

A small contribution to the prompt background from non-reconstructed muons is present for long tracks. It is estimated with a similar method as that used for the prompt background from showering particles, but using an inverted cut on the muon veto, as well as an inverted cut on the veto on nearby PF candidates around the track. The transfer factor $\kappa_\mu = \frac{B}{A}$ is obtained in a DY muon + DTk region, requiring a pair of one muon and a disappearing track, and its numerical values are given in Tab. 5.12.

category	Phase 0	Phase 1	Run 2
long tracks	0.00102 ± 0.00017	0.00047 ± 0.00012	0.00075 ± 0.00011

Table 5.12: Transfer factor κ_μ for the estimation of the prompt particle background from muons in data. The values are measured in the DY muon + DTk region, defined by the selection of a muon-DTk pair with an invariant mass consistent with the Z boson mass.

5.11.4 Methodology for the spurious track background

The spurious track background is estimated using a data-driven ABCD method, but using a sideband of the track BDT classifier. In this case, the transfer factor $\theta = \frac{n_B}{n_A}$ is measured in a region with low $\not{E}_T$ found to be highly pure in spurious tracks from QCD processes. The ratio is determined with respect to the BDT classifier, in which a sideband region is defined adjacent to the signal region, as shown in Fig. 5.38. The signal region in the BDT classifier distribution, as stated in Sec. 5.7, is defined as BDT > 0.1 (0.15) for short tracks for Phase 0 (Phase 1); and BDT > 0.12 (0.08) for long tracks for Phase 0 (Phase 1).

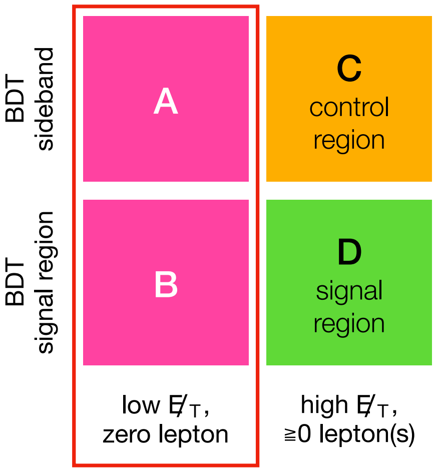

Figure 5.38: Regions used in the data-driven background estimation method for the spurious background, with a low-$\not{E}_T$ QCD region with zero leptons being using to measure the transfer factor indicated in red.

The spurious track background increases for decreasing values of the BDT classifier, as can be seen in Fig. 5.39, and a sideband region is constructed using

- BDT $= (-0.1, -0.05)$ (Phase 0) and BDT $= (-0.1, -0.0)$ (Phase 1) for short tracks; and
- BDT $= (-0.1, 0)$ for long tracks.

This choice ensures low signal contamination from prompt background in the BDT classifier sideband, while remaining relatively close to the signal region, which is important to mostly retain the same characteristics as in the signal region. The transfer factor is measured in the low-$\not{E}_T$ QCD region, defined by $\not{E}_T = (30, 60)$ GeV with at least one jet $n_{\text{jets}} \geq 1$, zero leptons and zero b-tagged jets, and is indicated in red in Fig. 5.38. The low-$\not{E}_T$ QCD region is further purified by requiring $\min(\Delta\phi(\not{E}_T, \text{jets})) > 0.4$, as well as requiring the transverse mass of the track-$\not{E}_T$ pair to be of $m_T^{\text{track},\not{E}_T} > 20$ GeV. Figure 5.40 shows the background composition for the $\not{E}_T$, number of jets, and the BDT classifier in the low-$\not{E}_T$ QCD region. The low-$\not{E}_T$ QCD region is expected to be very pure in terms of spurious track background, with a purity of

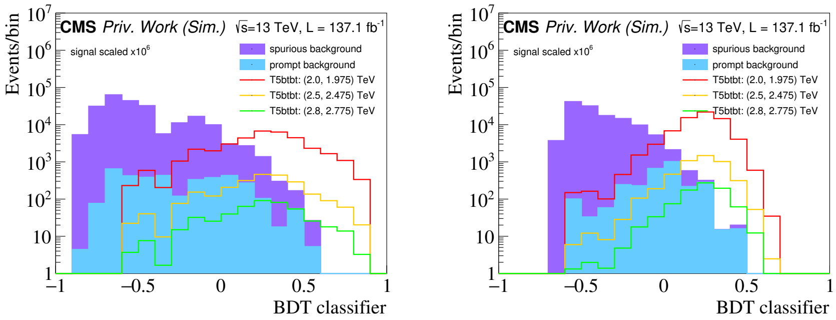

Figure 5.39: Background composition in MC simulation for the BDT classifier in the hadronic channel, shown for short (left) and long tracks (right). The BDT classifier is used to construct a sideband region in addition to the signal region for large values of the BDT classifier.

category	Phase 0	Phase 1	Run 2
short tracks	0.698 ± 0.074	0.217 ± 0.02	0.337 ± 0.023
long tracks	0.088 ± 0.015	0.051 ± 0.021	0.08 ± 0.012

Table 5.13: Spurious track background transfer factor θ measured in the low-$\not{E}_T$ QCD region in data for short (top row) and long tracks (bottom row).

99.6% for long prompt background tracks, and a purity of 99.9% for short prompt background tracks found in MC simulation.

Measurement of the transfer factor θ

The transfer factor θ is determined as the ratio of counts in the signal region in the BDT classifier distribution to that in the sideband region. Again, a constant transfer factor θ is determined, and is shown in Table 5.13 for short and long tracks, as well as for Phase 0 and Phase 1.

Spurious track background control region

As for the prompt background estimation, the predicted number of tracks in the signal region D is obtained by weighting the number of tracks in control region C by the transfer factor θ. Before performing the estimation, the purity of the control region is investigated. The control region is constructed by applying the complete signal region selection, but using the sideband of the BDT classifier distribution.

Figure 5.41 shows the background composition for the spurious track background control region based on MC simulation, showing a high purity of 99.9% for short tracks (99.8% for long tracks) in terms of spurious background tracks relative to prompt background tracks. While the background estimation method is purely data-driven, MC simulation can give a qualitative description of the relative purity of background sources, and is useful in the assessment of the optimization of the control region boundaries to maintain a high purity. The relative purity in data can differ significantly from MC simulation, however.

5.11.5 Events with ≥ 2 disappearing tracks

The search is furthermore sensitive to events with $\geq$ 2 disappearing tracks, which are accounted for in signal region bin 49 (see Tab. 5.9). In the case of ≥ 2 tagged disappearing tracks

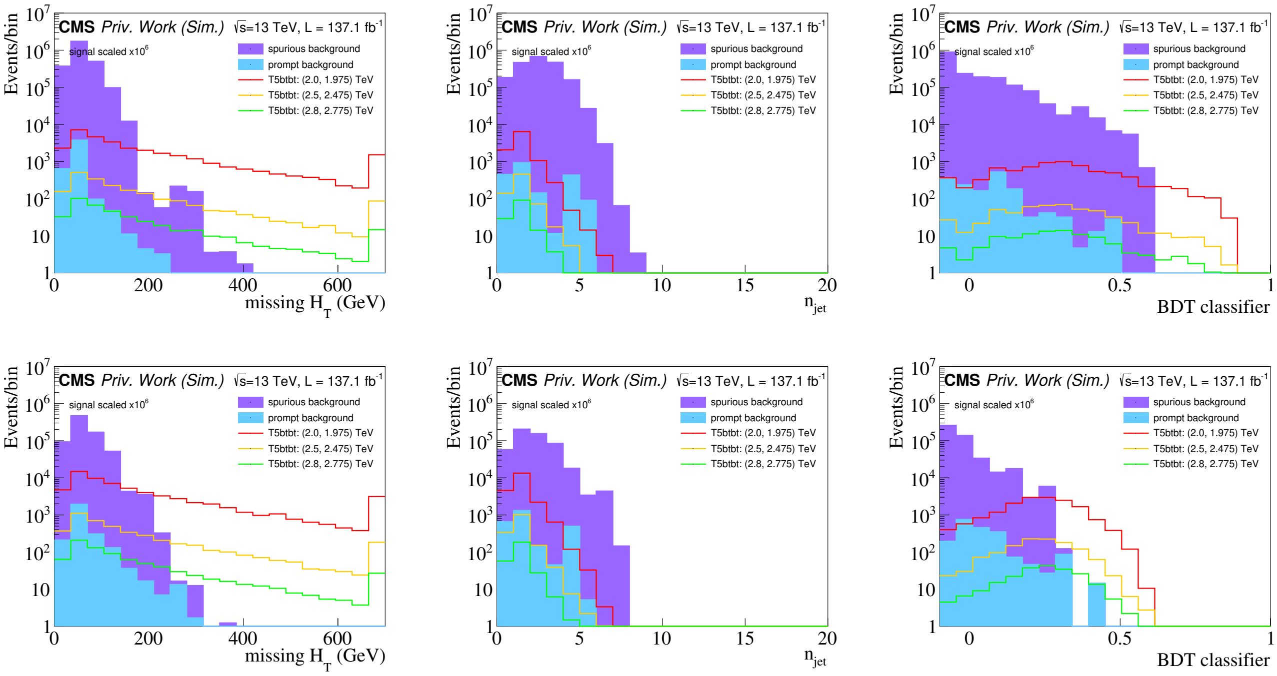

Figure 5.40: Background composition in MC simulation in the low-$\not{H}_T$ QCD region used to measure the transfer factor θ, shown as $n-1$ distributions for $\not{H}_T$, number of jets, and the BDT classifier. The low-$\not{H}_T$ QCD region is defined by $\not{H}_T = (30, 60)$ GeV, ≥ 1 number of jets, zero b-tagged jets and zero leptons. A very small contribution on the order of less than 0.5% of prompt background tracks is visible in MC for $\not{H}_T = (30, 60)$ GeV. Top row: short tracks, bottom row: long tracks.

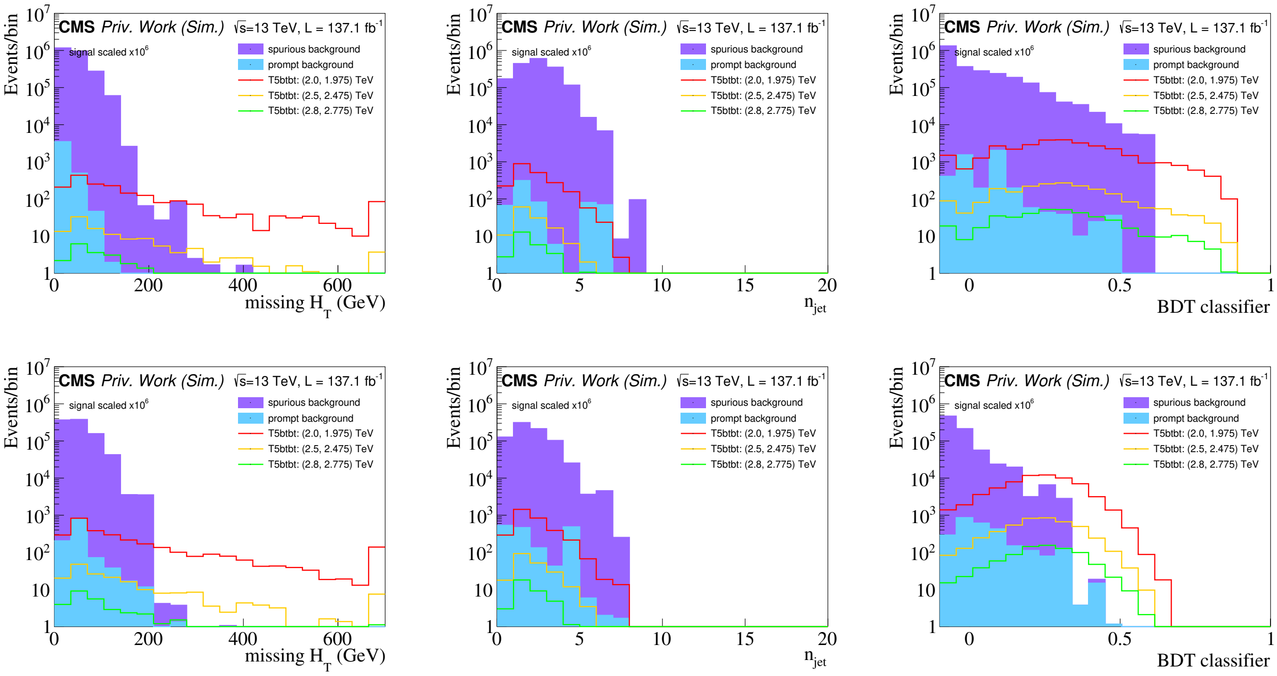

Figure 5.41: Background composition in MC simulation for the spurious track background control region in the hadronic channel, showing $\not{H}_T$, number of jets, and the BDT classifier. Top row: short tracks, bottom row: long tracks.

	Phase 0		Phase 1	
category	short tracks	long tracks	short tracks	long tracks
BDT for SR samples	>0.1	>0.12	>0.15	>0.08
E_{dep} for SR samples	<15 GeV	$<0.2p$	<15 GeV	$<0.2p$
E_{dep} for showering bg. CR	$[30, 300]$ GeV	$[0.3, 1.2]p$	$[30, 300]$ GeV	$[0.3, 1.2]p$
BDT for showering bg. CR	>0.1	>0.05	>0.05	>0.08
BDT for spurious tr. bg. CR	$[-0.1, -0.05]$	$[-0.1, 0.0]$	$[-0.1, 0.05]$	$[-0.1, 0.0]$

Table 5.14: Selection criteria on the BDT classifier and on the deposited energy in the calorimeter E_{dep} associated with a disappearing track candidate for the search (SR) and control (CR) regions.

per event, the leading disappearing track with the highest p_T is selected, which determines the prediction of background in this bin. The background prediction is then carried out as described above.

As a summary, Tab. 5.14 provides an overview of the cuts on the BDT classifier and E_{dep} used to construct the signal and control regions for the prompt background from showering particles as well as for the background from spurious tracks.

5.11.6 Closure of the methodology

With the methodology of the background estimation described in Secs. 5.11.2-5.11.4, a closure test using MC simulation is performed as a logical test of the methods. The background estimation methods for the prompt background and the spurious track background are applied in MC simulation to obtain the number of predicted tracks in a "closure test region", which is then compared to the number of observed tracks. Closure is achieved if observed and predicted counts agree within the statistical uncertainties. As closure test regions, the DY electron + DTk region, the low-$\not{E}_T$ QCD region, the baseline selection region and finally the signal region are considered.

Closure in the DY electron + DTk and low-$\not{E}_T$ QCD regions

Closure is first examined in the DY electron + DTk region, and is shown in Fig. 5.42 for Phase 0 MC simulation, and in Fig. 5.43 for Phase 1 MC simulation. The number of observed events for $\not{E}_T$, the invariant mass $m_{l,\text{track}}$, and the track momenta are determined from MC simulation using the complete disappearing track tag. The predicted counts are shown for the prompt and the spurious track background for short and long tracks, with the prompt background from muons shown as well for long tracks. The comparison shows the observed count to be compatible within the statistical uncertainties. However, given the limited statistics available from MC simulation in the DY electron + DTk region, no further systematic uncertainties are inferred using this closure test.

Conversely, Fig. 5.44 and Fig. 5.45 show the closure in the low-$\not{E}_T$ QCD region for both Phase 0 and Phase 1, respectively. Here, the predicted number of events describes the observed counts in MC simulation within the statistical uncertainties.

Closure in the baseline selection

The results of the closure test for the sum of the three analysis channels as introduced in Sec. 5.9 are shown in Figs. 5.46 and 5.47 for Phase 0 and Phase 1 separately. For Phase 0, the distribution

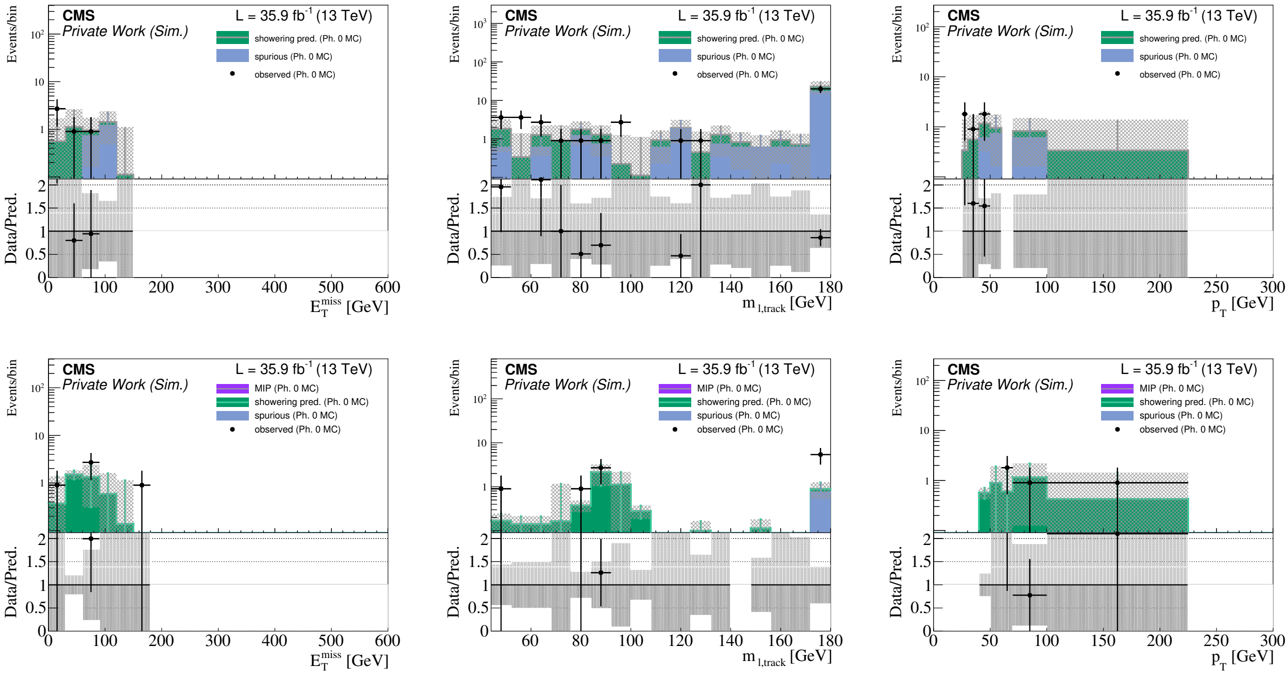

Figure 5.42: Closure in the DY electron + DTk region after applying the background estimation methodology in MC simulation, based on Phase 0 conditions. Top row: short tracks, bottom row: long tracks. The included uncertainties are statistical.

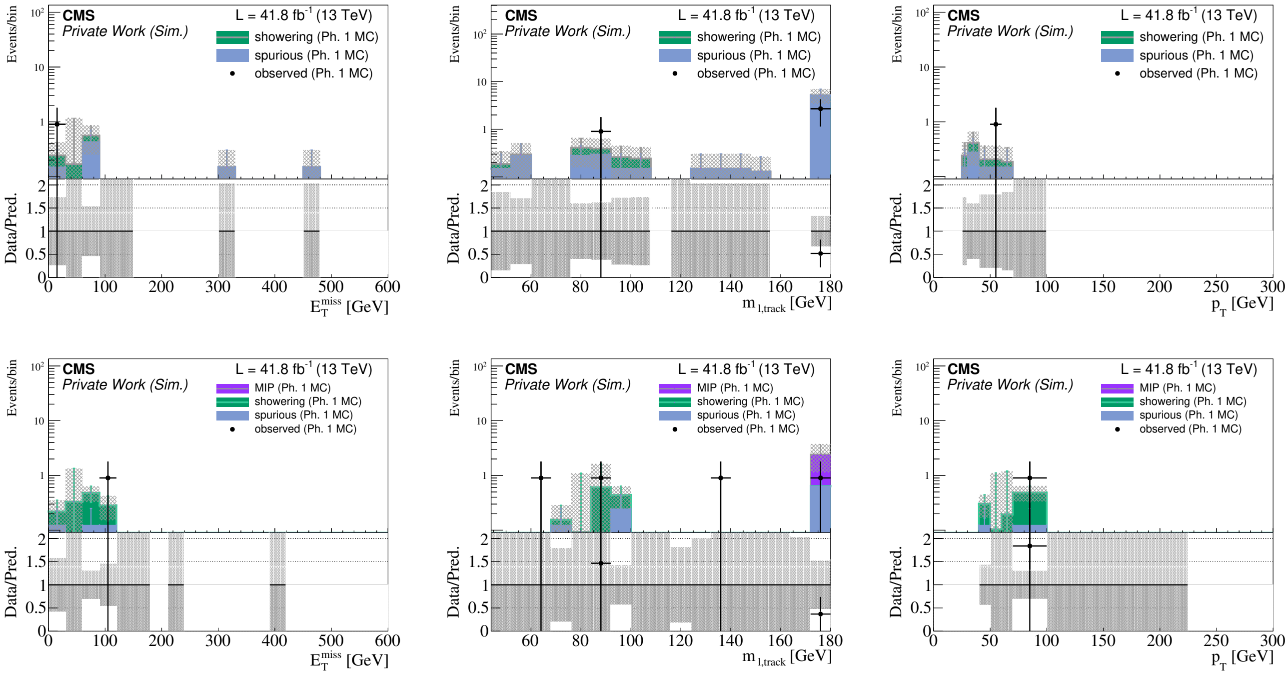

Figure 5.43: Closure in the DY electron + DTk region after applying the background estimation methodology in MC simulation, based on Phase 1 conditions. Top row: short tracks, bottom row: long tracks. The included uncertainties are statistical.

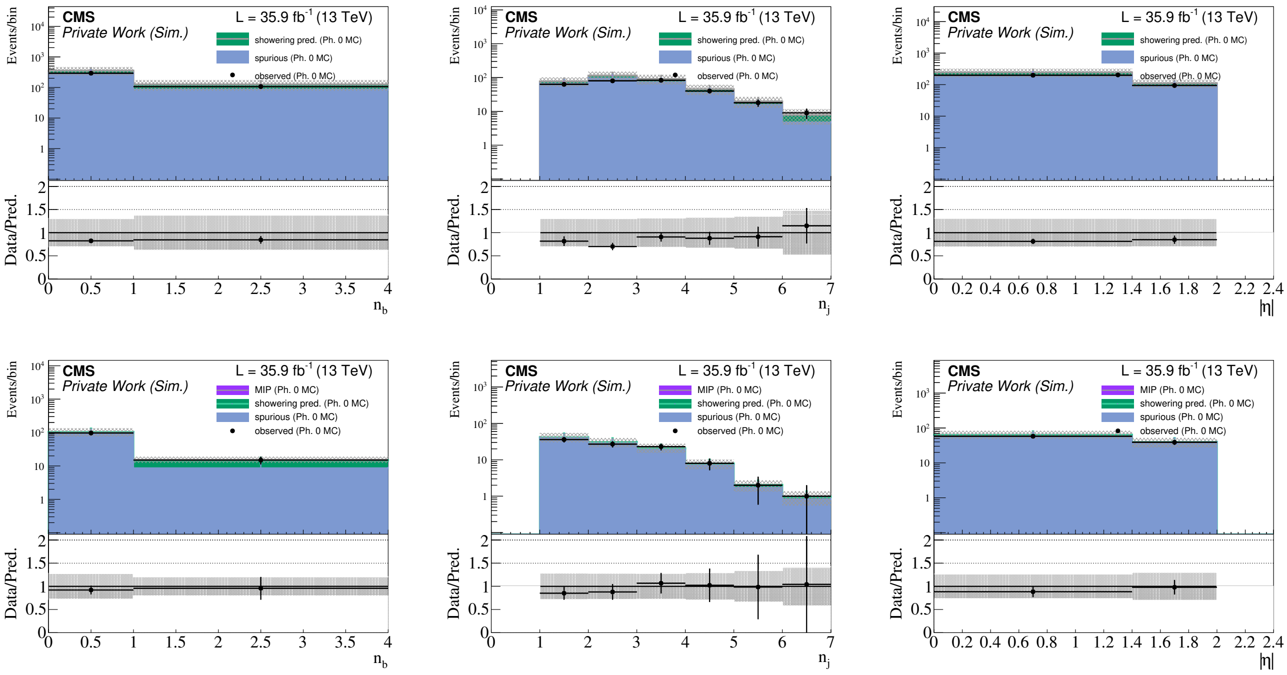

Figure 5.44: Closure in the low-$\not{E}_T$ QCD region after applying the background estimation methodology in MC simulation, based on Phase 0 conditions. Top row: short tracks, bottom row: long tracks. The included uncertainties are statistical.

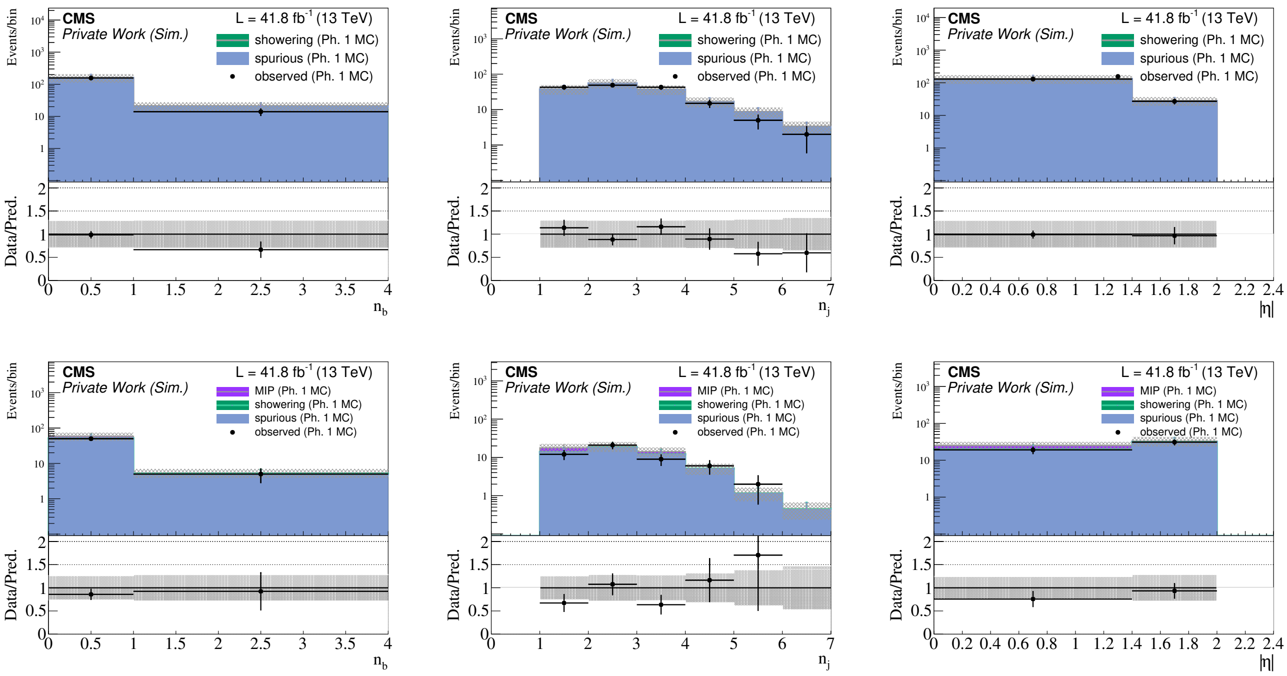

Figure 5.45: Closure in the low-$\not{E}_T$ QCD region after applying the background estimation methodology in MC simulation, based on Phase 1 conditions. Top row: short tracks, bottom row: long tracks. The included uncertainties are statistical.

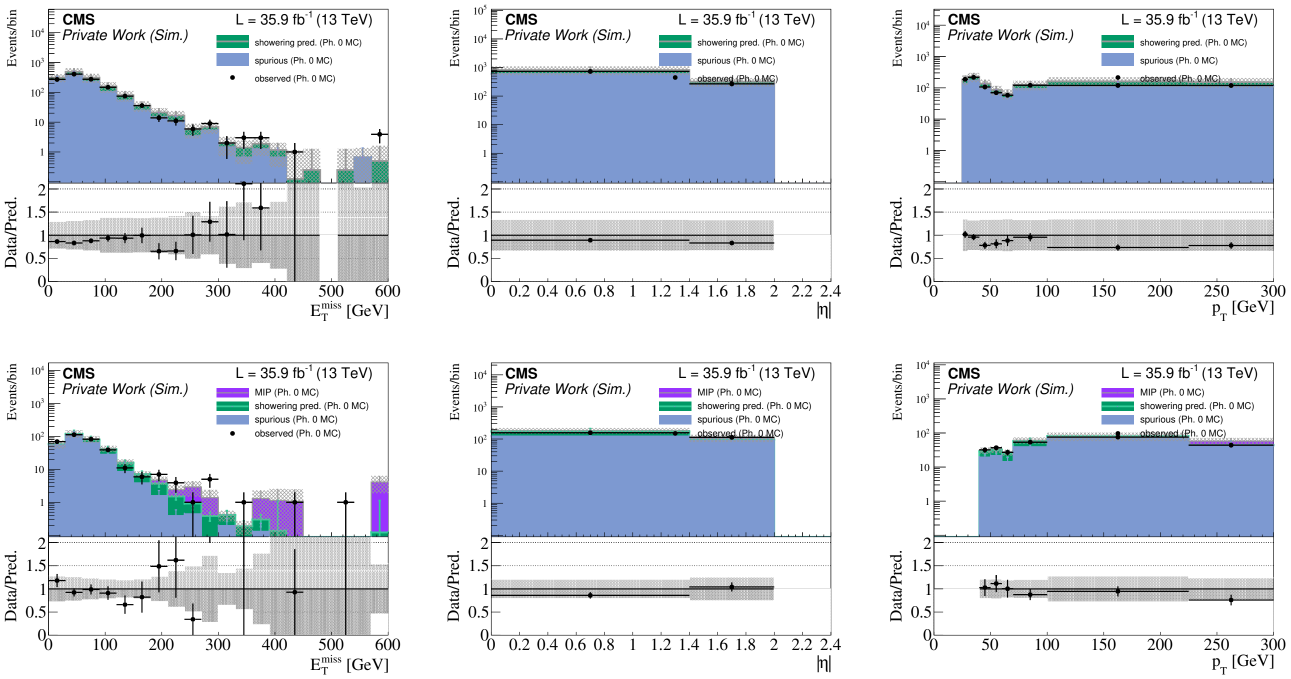

Figure 5.46: Closure in the analysis baseline region, which includes all three analysis channels, after applying the background estimation methodology in MC simulation, based on Phase 0 data-taking conditions. Top row: short tracks, bottom row: long tracks. The included uncertainties are statistical.

of the number of predicted events is compatible with the statistical uncertainties for the $\not{E}_T$, track $|\eta|$ and track p_T distributions. For long tracks in Phase 1, an overprediction is visible, especially for tracks with low p_T below 100 GeV. This overprediction is covered by the statistical uncertainties.

Closure in the signal regions

As a final closure test, Figure 5.48 shows closure of the methodology separated by Phase 0 and Phase 1 for all signal regions as introduced in Sec. 5.9. For each detector phase, a pull distribution is additionally shown to gauge the compatibility of all three predictions with respect to the observed count in the MC simulation signal region. The pull distribution is defined by

$$\text{pull} = \frac{n_{\text{observed}} - n_{\text{predicted}}}{\sigma}, \tag{5.11.2}$$

with the number n of observed and predicted events in each signal bin, as well as the statistical uncertainty in the quantity $n_{\text{observed}} - n_{\text{predicted}}$. Both pull distributions for Phase 0 and Phase 1 show an overall consistency between the predicted and observed number of events in MC simulation. This is further evidenced by a compatibility of the pull distributions with a Gaussian distribution, as quantified by $\chi^2/\text{ndof} = 8.33/11$ for Phase 0, and $\chi^2/\text{ndof} = 10.22/7$ for Phase 1.

The closure of the method seen in MC simulation provides a first validation of the background estimation methods. The methodology is further tested using real data in the following section.

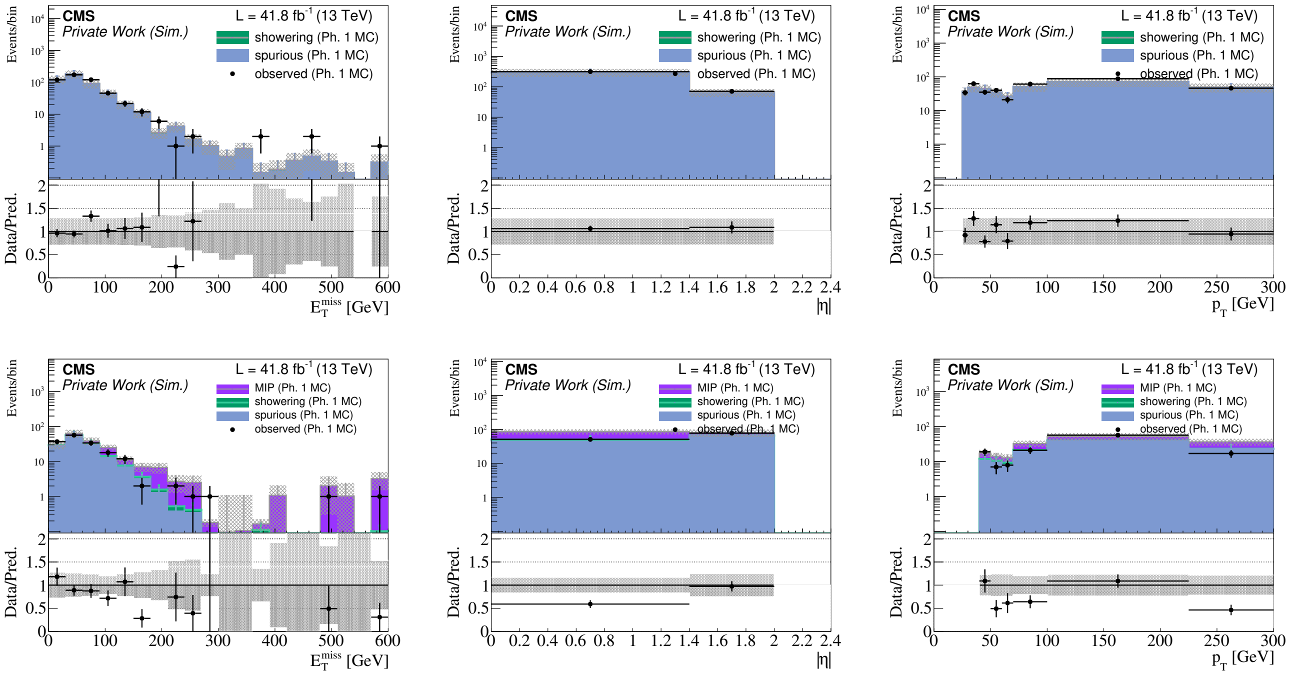

Figure 5.47: Closure in the analysis baseline region, which includes all three analysis channels, after applying the background estimation methodology in MC simulation, based on Phase 1 data-taking conditions. Top row: short tracks, bottom row: long tracks. The included uncertainties are statistical.

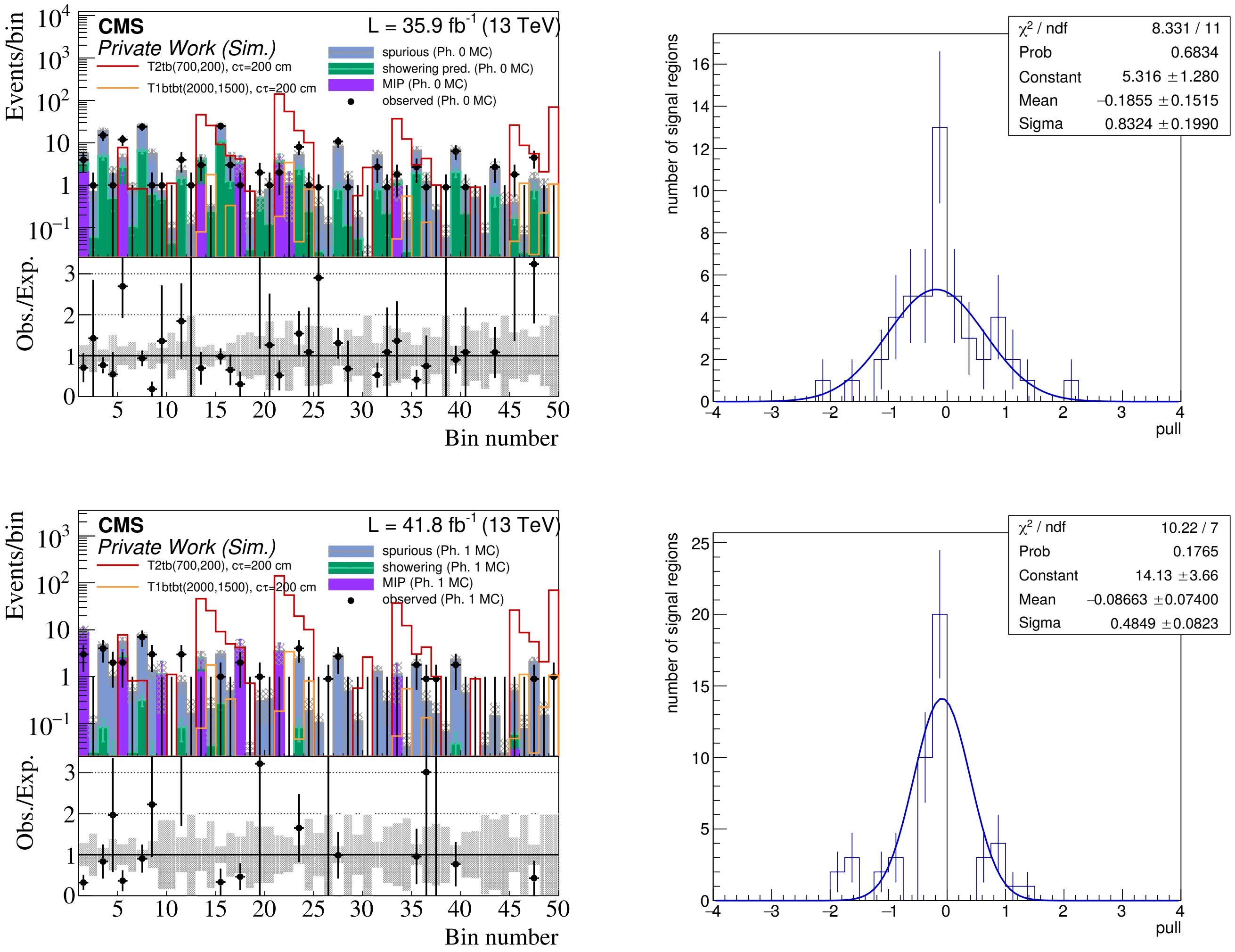

Figure 5.48: Left: closure test in MC simulation for all analysis signal bins, after applying the background estimation methodology in MC simulation for events passing the individual signal bin selection. Phase 0 is shown in the top row, while Phase 1 is shown in the bottom row. The included uncertainties are statistical; signal model masses are given in GeV. Right: pull distributions showing overall agreement between the number of observed counts in MC simulation and the number of predicted events.

5.11.7 Validation of the background methods in data

In the following, the methodology is validated in dedicated real-data control regions orthogonal to the signal regions. First, the observed data are compared with the predicted background in the regions used to measure the individual transfer factors for each background source. Here, in contrast to Fig. 5.34 and Fig. 5.34, the regions C and D chosen are identical to the measurement regions A and B. By construction, the normalization is correct, but comparisons as a function of other analysis variables allow an independent test of unforeseen dependencies in the transfer factor. The methodology is also validated in events with one disappearing track and a single lepton with an additional inverted cut on the lepton transverse mass m_T, and again with an inverted cut on the invariant mass m_{inv} of the lepton and disappearing track. The largest contribution of each background determines the lepton type considered for the validation step. For the prompt background, events with a disappearing track and an electron are considered for the validation step, while for the spurious track background events with a disappearing track in the low-$\not{E}_T$ regime are selected. In each case, the inverted cut on either m_T or m_{inv} ensures orthogonality to the signal region selection. The comparison of predicted to observed counts is shown separately for Phase 0 and Phase 1 detector conditions.

Validation in the DY electron + DTk region

The methods are tested in the DY electron + DTk region for events with a long disappearing track and an electron. Figures 5.49 and 5.50 show the comparison between observed and predicted counts in this region for Phase 0 and Phase 1, respectively. The invariant mass of the DTk+electron system, number of b-tagged jets and number of jets, $\not{E}_T$, $m(dE/dx)$ as defined in Sec. 5.8 and track p_T are shown. Since the normalization of the prediction matches the observed data by construction, this validation step could reveal shape distortions or dependencies in the background prediction. The distributions do not show a significant distortion. The predicted and observed distributions are compatible within the statistical uncertainties.

Validation in the low-$\not{E}_T$ QCD region

As spurious tracks are the dominant background source for short tracks, events with a short disappearing track in the low-$\not{E}_T$ QCD region are selected, and shown in Figs. 5.51 and 5.52 for Phase 0 and Phase 1, respectively. The distribution of the number of vertices provides information about the activity in the event, which is of relevance for the spurious tracks background. The predicted and observed distributions are compatible within the statistical uncertainties, and no statistically significant shape distortions are visible.

Validation in the single-lepton final state with small m_T

Validation is further carried out in a region which combines the electron channel signal region bins 37-48 as defined in Tab. 5.9.4, while selecting exactly one electron $n_e = 1$ and inverting the cut on the transverse electron mass $m_T < 100$ GeV. Figures 5.53 and 5.54 show the comparison between the observed counts in data and the number of predicted counts for Phase 0 and Phase 1.

The same approach is carried out for the muon channel, relevant to the signal region bins 25-36, by selecting events with exactly one muon $n_\mu = 1$ and also inverting the cut on the transverse muon mass, $m_T < 100$ GeV. The comparison is shown in Figs. 5.55 and 5.56 for Phase 0 and Phase 1, respectively. The number of observed and predicted events in data is

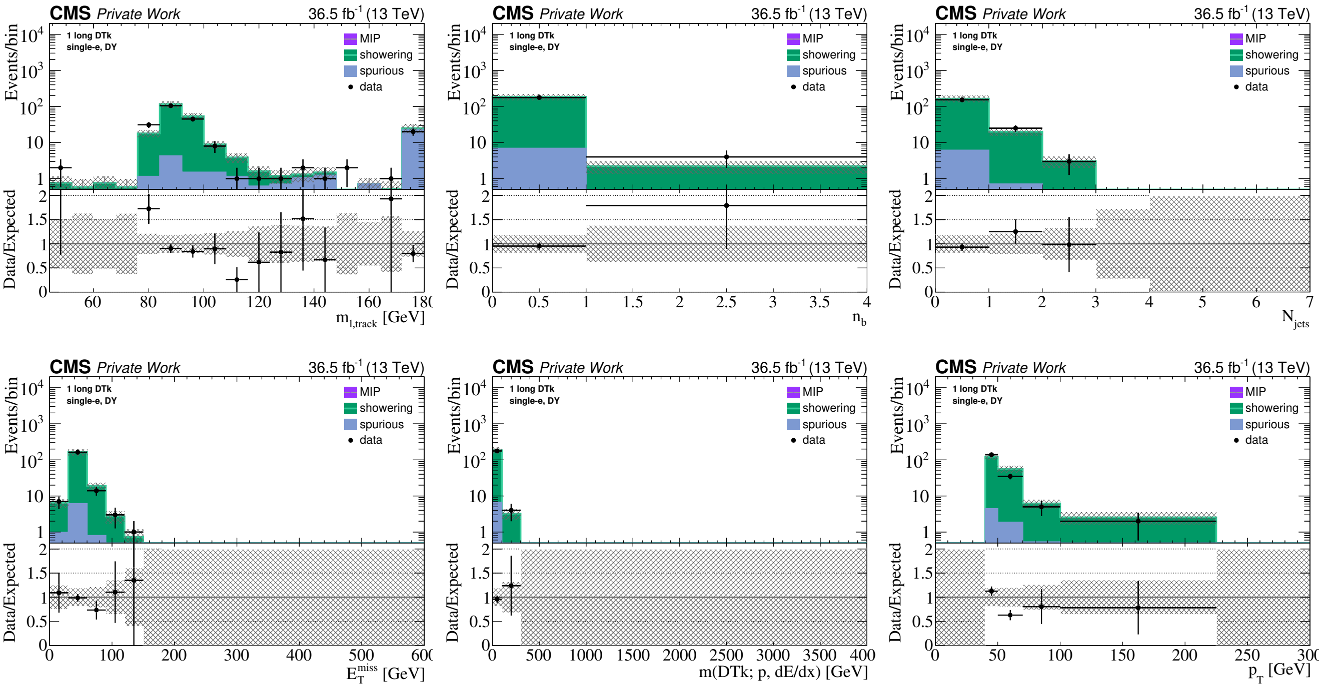

Figure 5.49: Validation of the methodology in the DY electron + DTk region for events with a long disappearing track and an electron. The observed data is compared to the expected count derived from the estimated background predictions, and is shown for the Phase 0 data.

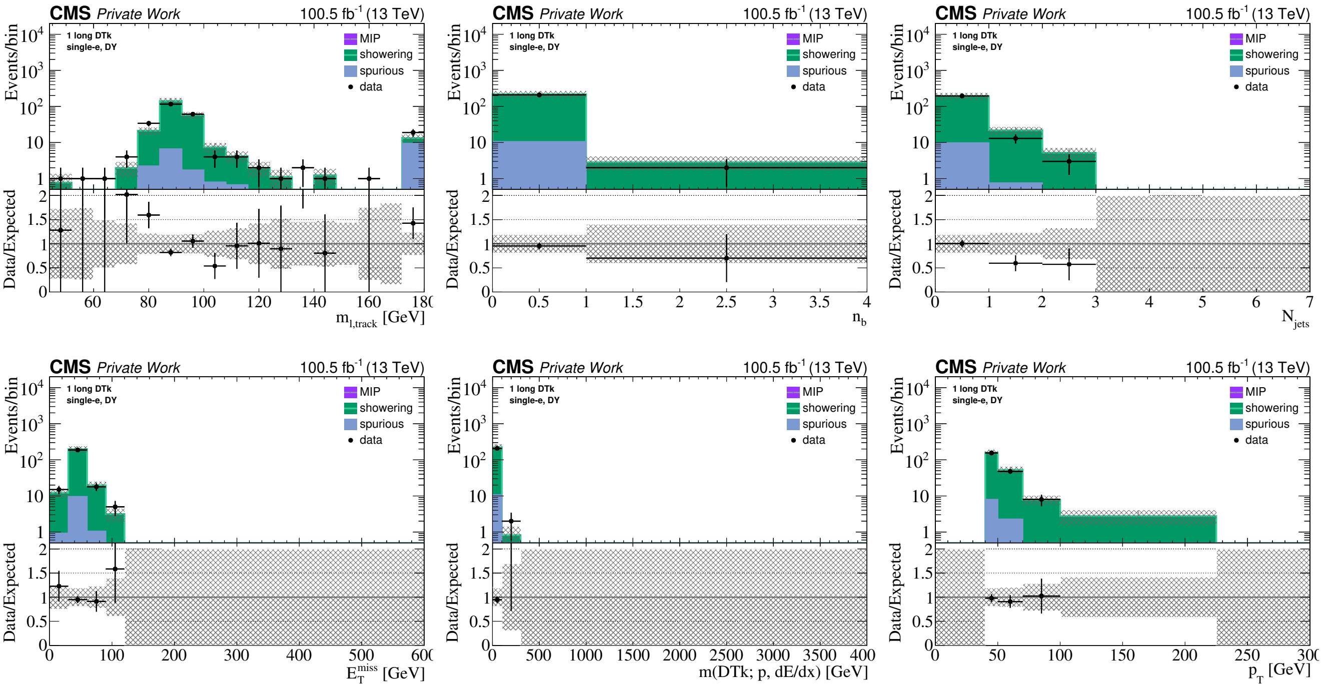

Figure 5.50: Validation of the methodology in the DY electron + DTk region for events with a long disappearing track and an electron. The observed data is compared to the expected count derived from the estimated background predictions, and is shown for the Phase 1 data.

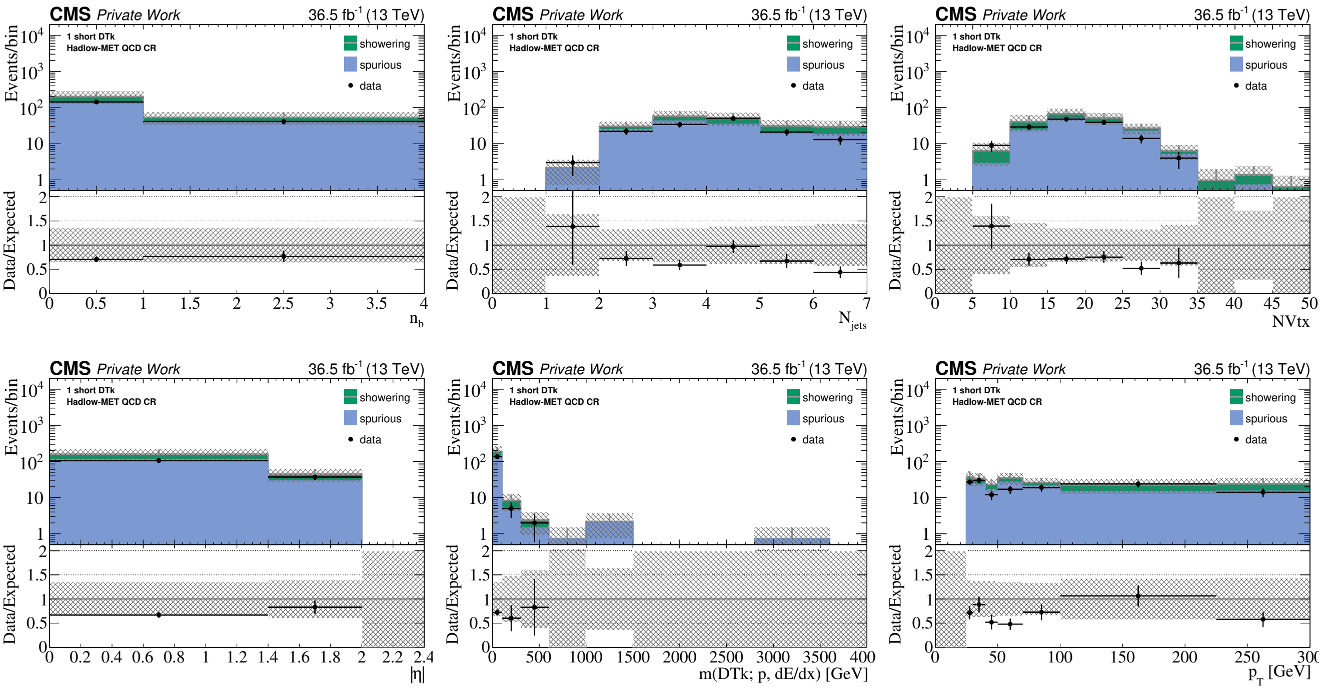

Figure 5.51: Validation in data of the methodology in the low-$\not{E}_T$ QCD region for short tracks. The observed data is compared to the expected count derived from the estimated background predictions, and is shown for the Phase 0 data.

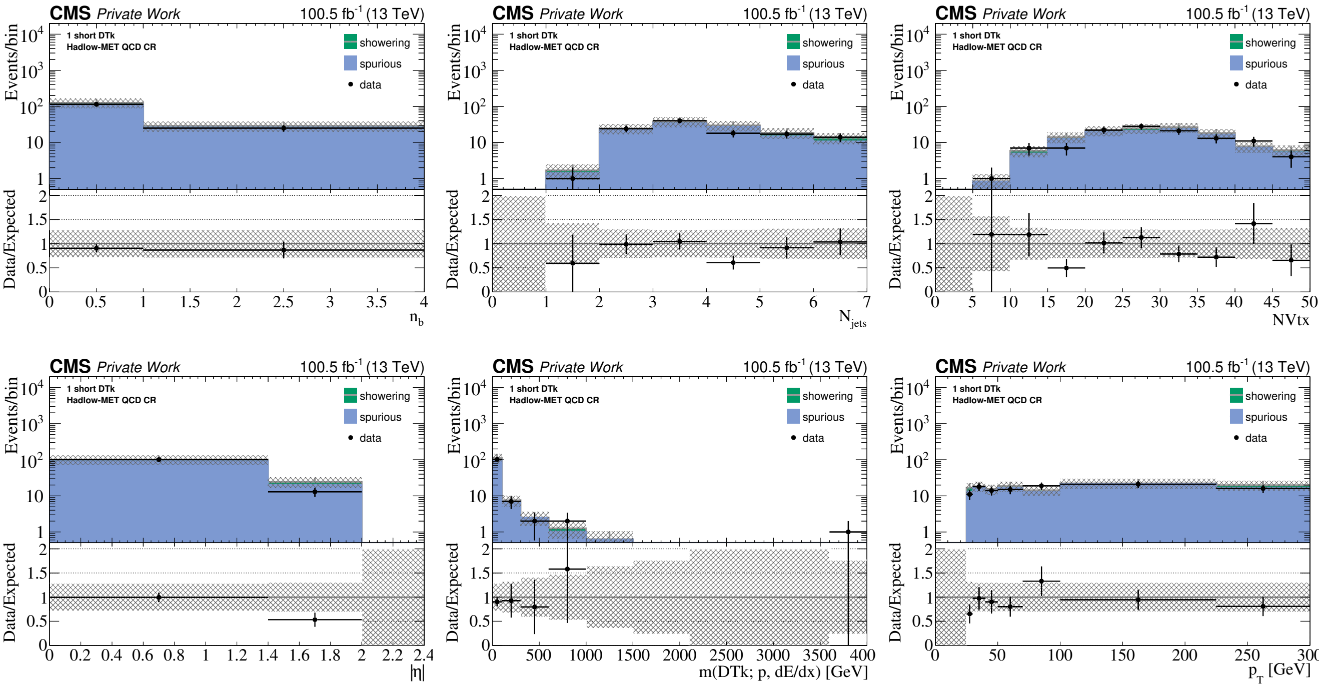

Figure 5.52: Validation in data of the methodology in the low-$\not{E}_T$ QCD region for short tracks. The observed data is compared to the expected count derived from the estimated background predictions, and is shown for the Phase 1 data.

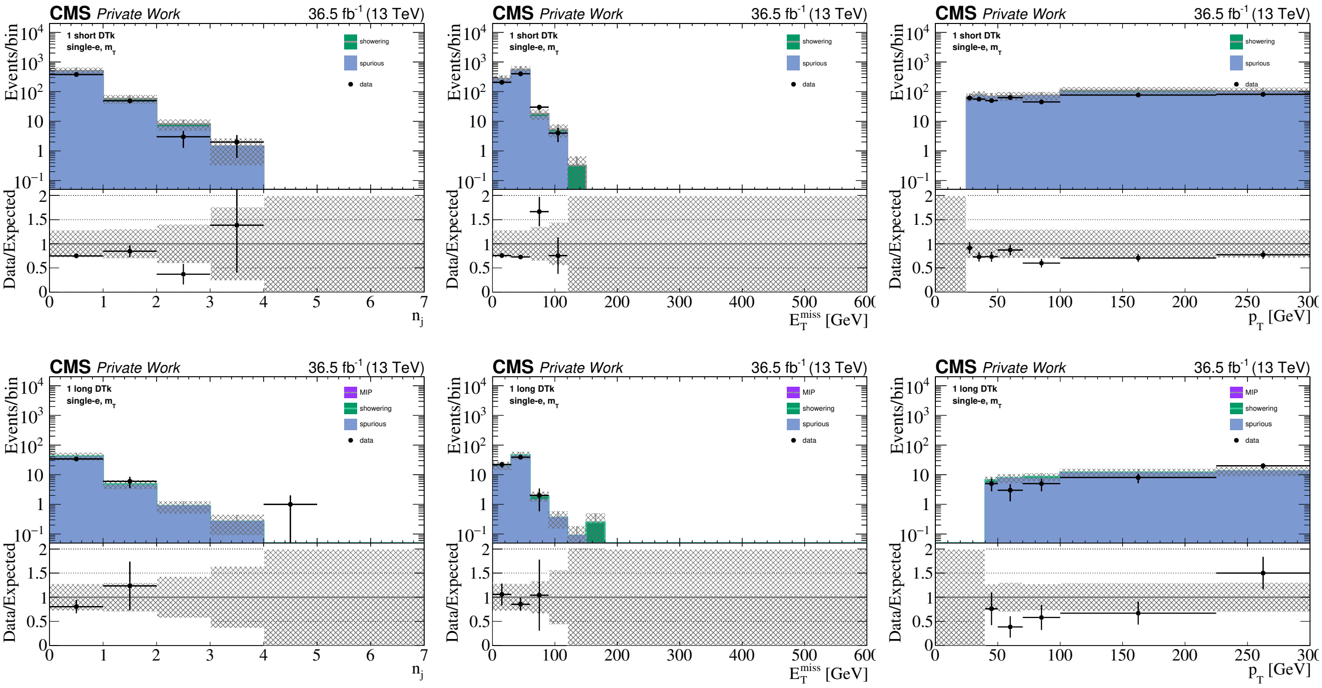

Figure 5.53: Validation in data of the methodology in the single-electron signal region with an inverted cut on m_T. The observed data is compared to the expected count derived from the estimated background predictions, and is shown for the Phase 0 data. Top: short tracks, bottom: long tracks.

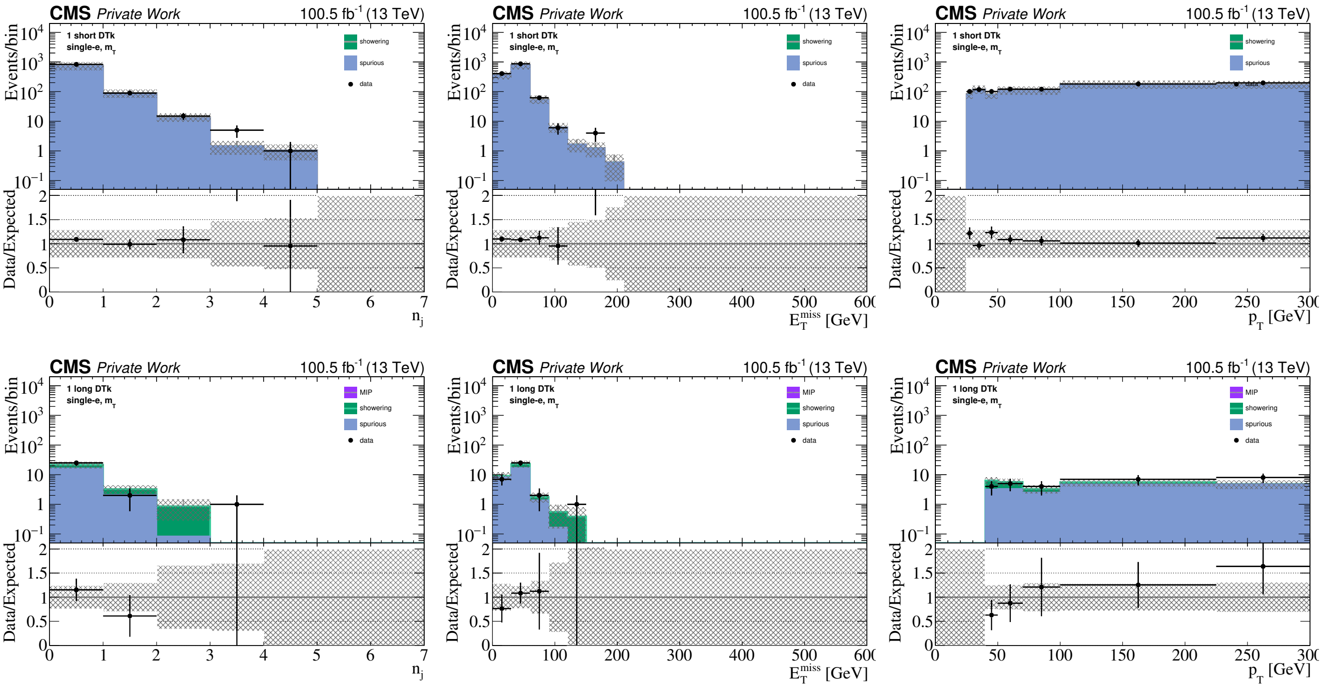

Figure 5.54: Validation in data of the methodology in the single-electron signal region with an inverted cut on m_T. The observed data is compared to the expected count derived from the estimated background predictions, and is shown for the Phase 1 data. Top: short tracks, bottom: long tracks.

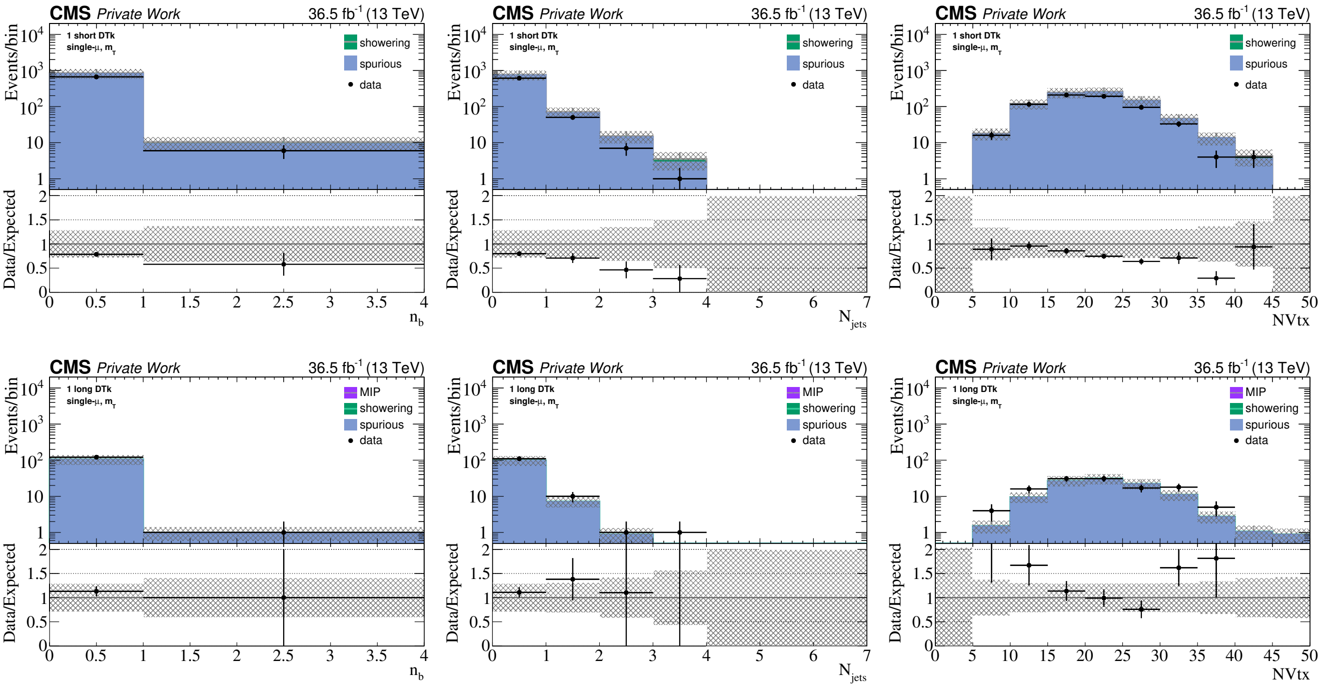

Figure 5.55: Validation in data of the methodology in the single-muon signal region with an inverted cut on m_T. The observed data is compared to the expected count derived from the estimated background predictions, and is shown for the Phase 0 data. Top: short tracks, bottom: long tracks.

consistent within the statistical uncertainties. An opposing trend is visible in the number of vertices per event for long tracks, which shows a slight underprediction for $n_{\text{vtx}} < 20$. For short tracks, an overprediction is visible in the number of jets for Phase 0. A likely explanation are statistical fluctuations, as the overprediction does not occur in Phase 1.

Validation in the single-electron final state on the Z peak

Lastly, the compatibility of the predicted counts with the observed count in data is investigated in the region with an inverted cut on the invariant mass of the electron + DTk system $m_{l,\text{track}}$, where a window cut around the Z mass pole is selected with $m_{l,\text{track}} = [70, 110]$ GeV. Figures 5.57 and 5.58 show agreement between data and the prediction within the statistical uncertainties for both Phase 0 and Phase 1.

5.11.8 Conclusion

In this section, the different types of background sources have been identified, and data-driven methods have been developed to reliably predict from data each source of background, including prompt background from showering particles and muons, and background from spurious tracks. The latter has been identified as the dominant source of background for short tracks, while prompt background due to mis-reconstructed charged particles is the dominant source for long tracks. MC simulation has been used to both analyze the proportion of each background per track category, and to perform a closure test using MC truth information. The data-driven background estimation has been validated in final states with inverted cuts on the transverse lepton mass and the invariant mass of the DTk-lepton system. The observed counts in data are compatible with the background predictions from all background sources within

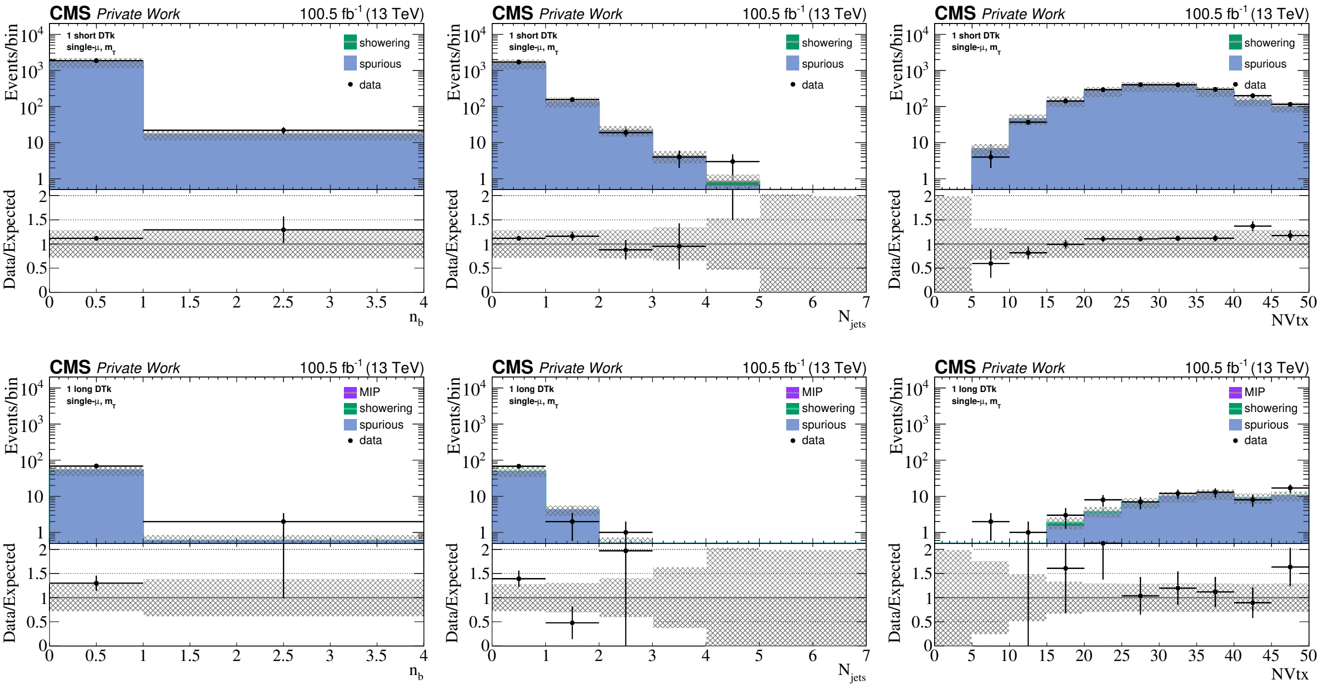

Figure 5.56: Validation in data of the methodology in the single-muon signal region with an inverted cut on m_T. The observed data is compared to the expected count derived from the estimated background predictions, and is shown for the Phase 1 data. Top: short tracks, bottom: long tracks.

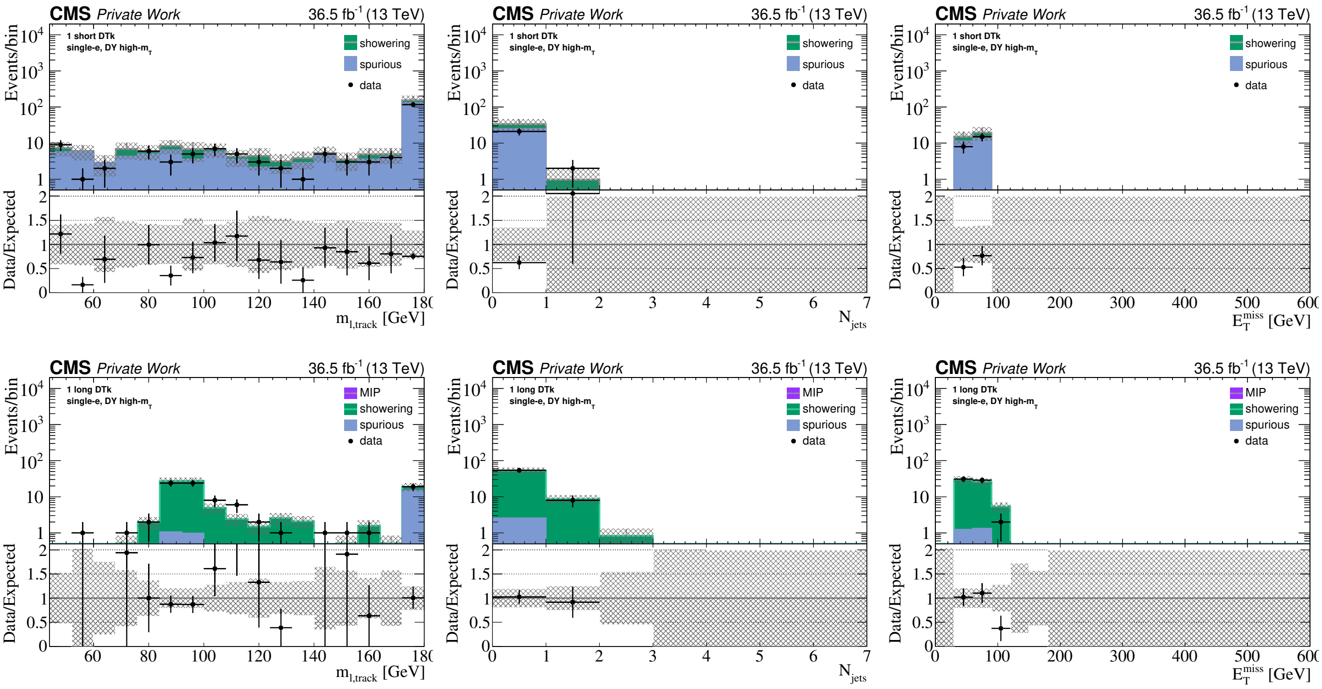

Figure 5.57: Validation in data of the methodology in the single-electron signal region with an inverted cut on $m_{l,\text{track}}$. The observed data is compared to the expected count derived from the estimated background predictions, and shown for Phase 0 data-taking conditions. Top: short tracks, bottom: long tracks.

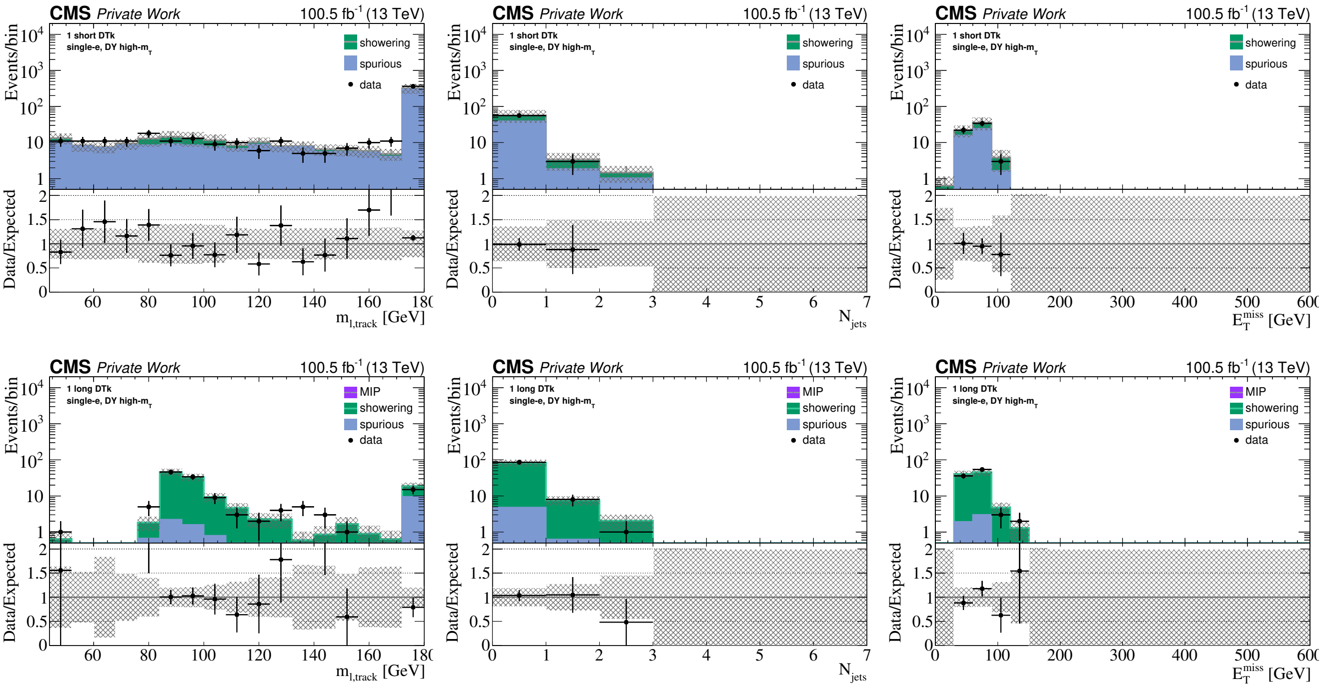

Figure 5.58: Validation in data of the methodology in the single-electron signal region with an inverted cut on $m_{l,\text{track}}$. The observed data is compared to the expected count derived from the estimated background predictions, and shown for Phase 1 data-taking conditions. Top: short tracks, bottom: long tracks.

the statistical uncertainties, and the methodology is considered to be thoroughly validated.

5.12 Sources of systematic uncertainty

In this section, various sources of systematic uncertainty are discussed, including intrinsic uncertainties related to the methodology of the background estimation methods, as well as with the simulation when it comes to the efficiency of the expected signal. All identified sources of systematic uncertainty are considered as nuisance parameters in the final fit of the results presented in Sec. 6.2.

5.12.1 Sources of background systematic uncertainty

Systematic uncertainty in the background estimation methods is studied and quantified in data. The effectiveness of the ABCD method relies on both the statistics and purity of the measurement region and control region, as well as the orthogonality of the chosen variables. In addition, the control region is required to have low signal contamination in order to provide a reliable estimate of its respective background. In the following, systematic uncertainty inherent in the background prediction is discussed.

Statistics of the control regions

The statistics of each control region per background source are taken into account for each signal bin in the final fit, as well as the statistics of the transfer factor measurement regions for the prompt and spurious track backgrounds.

Contamination of the transfer factor measurement region

The contamination from other background sources in the transfer factor measurement region has been studied in MC simulation for each background in Sec. 5.11, as well as in real data control regions. In data, a 100% uncorrelated uncertainty is assigned for short tracks in the estimation of the prompt background from electrons due to a contamination of the transfer measurement region from spurious tracks, as described in Sec. 5.11.2.

Shape distortions

An additional source of systematic uncertainty are shape distortions due to differences between the observed and predicted counts in the transfer factor measurement regions. In order to study potential bias effects, the track p_T spectrum is studied using a finer binning.

Figure 5.59 shows the track p_T spectrum in the prompt background transfer factor measurement region, for Phase 0 and Phase 1 data-taking periods as well as the combined Run 2. Using the combined Run 2 version, a systematic uncertainty of 20% for long tracks independent of p_T is assigned to cover the shape distortions in the track p_T spectrum.

The spurious track background transfer measurement region is depicted in Fig. 5.60, again showing the track p_T spectrum, for which discrepancies statistically compatible with a deviation of 30%, which is the assessed systematic uncertainty assigned for long tracks, are visible.

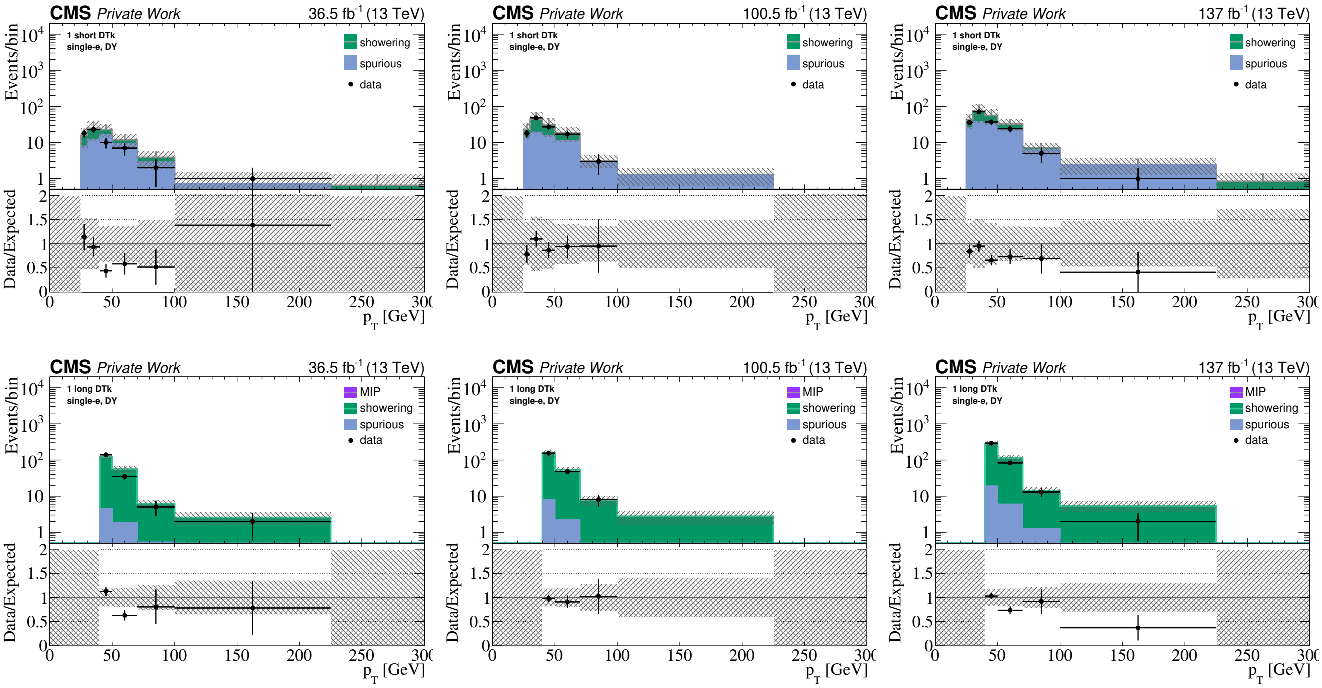

Figure 5.59: Track p_T spectrum shown for the DY electron + DTk region for events with a disappearing track and an electron. From left to right: Phase 0, Phase 1 and combined Run 2. The observed count is compared to the expected count derived from the added background estimation predictions, and is shown for short (top) and long tracks (bottom).

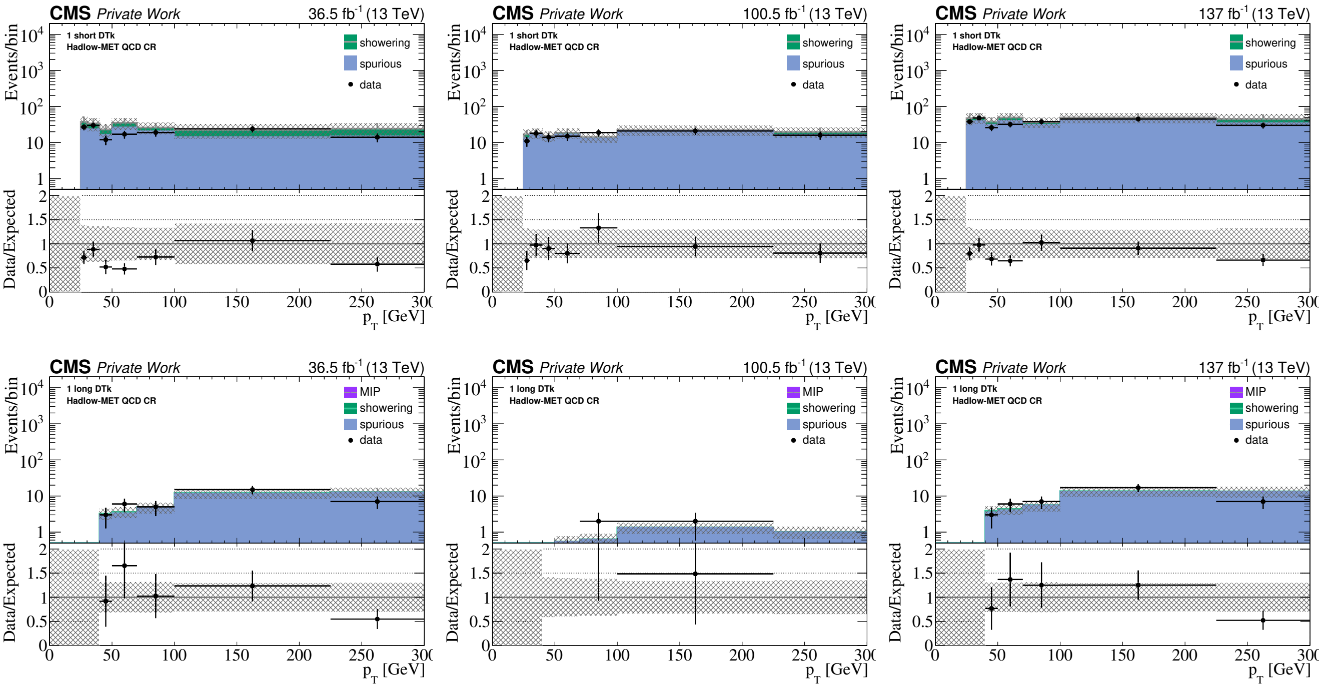

Figure 5.60: Track p_T spectrum shown for the low-$\not{E}_T$ QCD region with small values of $\not{E}_T$ and zero leptons. From left to right: Phase 0, Phase 1 and combined Run 2. The observed count is compared to the expected count derived from the added background estimation predictions, and is shown for short (top) and long tracks (bottom).

5.12.2 Sources of signal systematic uncertainty

Systematic uncertainties for the simulated MC signal are discussed in the following. Several sources of systematic uncertainty are taken into account following standard CMS recommendations regarding MC simulation, such as uncertainty in the integrated luminosity, jet energy measurements, renormalization and factorization scales, initial-state radiation and pile-up reweighting. For this analysis, three additional sources of uncertainty are of relevance, which impact the estimate of the efficiency of tagging disappearing tracks in real data, the calibration of dE/dx, and the selection of tracks in FastSim.

To estimate differences between data and simulation in the efficiency of selecting disappearing tracks, a novel technique has been developed in [84] and deployed as presented below. The results of this technique are used to correct the efficiency of selecting disappearing tracks in simulation to better match the data.

Integrated luminosity

The absolute scale of the integrated luminosity is measured using van der Meer scans as discussed in Sec. 4.1.6. Following standard CMS recommendations, an uncertainty of 1.6% is applied to this measurement, which incorporates time-dependent uncertainties on the integrated luminosity ranging from 1.2% (2016), 2.3% (2017) to 2.5% for 2018 [85].

Jet energy scale and resolution

A systematic uncertainty arises from the calibration of the jet energy scale and resolution due to a time-dependent detector response and pile-up [86]. Corrections to the jet energy scale are varied using p_T and η-dependent uncertainties, and the variations are propagated to higher level variables such as jet multiplicity, H_T, and $\not{E}_T$.

B-tagged jet efficiency and mis-tagging

The efficiency to reconstruct b-tagged jets and the mis-tagging rate using the DeepCSV algorithm as described in Sec. 5.5 enters as a systematic uncertainty, and flavor-dependent uncertainties for data / FullSim and FullSim / FastSim b-jet tagging and light jet mis-tagging scale factors are applied in bins of p_T and η [67].

Renormalization and factorization scale

The renormalization and factorization scales are varied to account for theoretical uncertainty in the parton density functions (PDFs) used in the generation of MC simulation. In proton-proton collisions, PDFs model the probability to find hadron constituents (partons), namely quarks and gluons, depending on the fraction x of the proton momentum carried by the parton and the factorization scale Q^2 [87]. The renormalization scale signifies the lower limit on the virtualities of loop particles included in the definition of the renormalized coupling, while the factorization scale gives an upper limit on virtualities of partons included in the definition of the PDF [88]. To determine a systematic uncertainty, both the renormalization and factorization scale are each independently varied by a factor of 2.0 and 0.5 [89–92].

Initial-state radiation

To improve on the MadGraph modeling of the multiplicity of additional jets from initial state radiation (ISR), Madgraph $t\bar{t}$ Monte Carlo events are reweighted based on the number of ISR jets (N_J^{ISR}) to make the jet multiplicity agree with data. The same re-weighting procedure is applied to SUSY Monte Carlo events. The re-weighting factors vary between 0.92 and 0.51 for N_J^{ISR} between 1 and 6. One half of the deviation from unity is taken as the systematic uncertainty on these re-weighting factors.

Pile-up re-weighting

In order to model additional pile-up collisions entering an event, the number of proton-proton interactions is determined using the instantaneous luminosity based on a cross section of 69.2 mb for Run 2 with an uncertainty of 4.6% [93]. The uncertainty is taken into account as a systematic uncertainty.

Level-1 trigger pre-firing

The 2016 and 2017 data-taking periods are affected by a well-known issue whereby the Level-1 trigger erroneously pre-fired on adjacent bunch crossings, prohibiting a triggering of some fraction of potential signal events. The impact of this pre-firing on the signal acceptance is evaluated using the preliminary Level-1 pre-firing efficiency map based on Run2017F, which is taken as a worst-case scenario.

FastSim correction

The efficiency of tagging charginos as disappearing tracks for displacements below 30 cm in fast simulation is found to be 25% larger than with fully simulated signal, due to differences in the tracking performance in FastSim and FullSim. A constant scale factor of 0.75 is thus applied.

Calibration of the energy loss dE/dx

The measurement of the separate dE/dx values in each pixel layer used to construct the harmonic-2 estimator I_h as introduced in Sec. 5.8 exhibits a characteristic long tail in the dE/dx distribution. This, in turn, induces a significant uncertainty on the mean of the distribution [94].

The uncertainty on the calibration of dE/dx is taken as the difference of the dE/dx calibration factors derived using muons, as described in Sec. 5.8, and using protons. A time-dependent inter-calibration of the pixel detector response has been performed in [79] using dE/dx measured from tracks associated with a muon, with the corresponding dE/dx value extracted from a Gaussian fit around the peak of the dE/dx distribution. A similar set of calibration factors is derived from a sample of highly ionizing particles, namely, low-p_T protons originating from decays of Λ^0 baryons in [79]. Their decay vertices are slightly displaced with respect to the PV. The difference in derived calibration factors forms the basis of a systematic uncertainty, totalling a maximum of 5% on the signal count for some models.

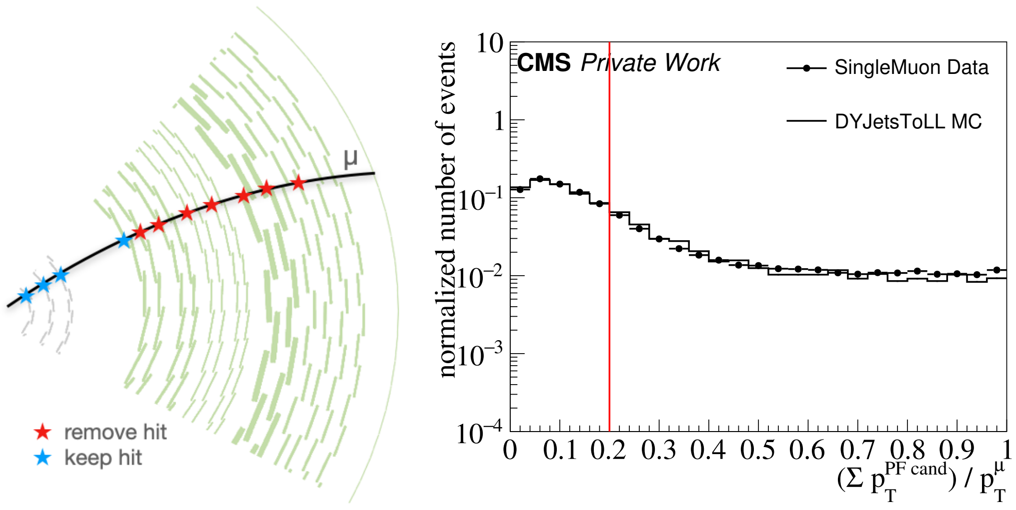

Figure 5.61: Left: Depiction of the artificial track shortening method. Hit clusters connected to a μ-matched track are removed from the end of the track until only a certain number of layers with measurements remain. In this example, the track is shortened to 4 layers with measurements. Right: relative isolation calculated in the vicinity of PF candidates excluding the muon itself, shown for selected muons with $p_T > 40$ GeV and $|\eta| < 2.0$ (data shown for a subset of Run2016F, with a subset of DY Phase 0 MC).

Disappearing track signal efficiency

A further source of systematic uncertainty comes from the track reconstruction efficiency and the efficiency of tagging a disappearing track, which in principle can be different in data and MC simulation. As the BDT training described in Sec. 5.7.1 is based on MC simulation, scale factors for the track reconstruction and tagging efficiency as well as combined scale factors are determined in the following.

In order to determine the reconstruction and tagging efficiency in data, tracks matched to well-reconstructed muons are artificially shortened, and are taken as a proxy for semi-stable charginos. This method was developed in [84] and has been applied to all run periods of Run 2 in order to study time-dependent effects. The efficiency of selecting these muons using the disappearing track selection is estimated in simulation and data. Figure 5.61-Left illustrates the principle showing the reduction of track hits down to e. g. four remaining tracking layers.

First, well-reconstructed, isolated muons are selected from a data sample, as well as in a DY MC sample. Tracker hits associated with the muon are iteratively removed from the event record, starting from the outermost hit and working in, until only three tracker hits remain. This artificial shortening of muon tracks gives rise to a proxy sample of semi-stable charged particles. After each removal iteration, the complete event reconstruction step is re-run, and it is checked whether the tracking algorithm and disappearing track classifier identify a track matched within $\Delta R < 0.01$. This procedure is carried out in samples corresponding to a representative set of data-taking periods for both simulation and data. Comparisons between data and MC are used to derive a correction factor applied to the values of the d_{xy} and d_z of tracks in simulation, and subsequently the selection efficiency is determined and compared between MC and data. The data-to-MC ratio of the efficiencies is later applied as a scale factor to the efficiency in signal MC.

Events with one isolated muon are selected by calculating the sum of transverse momenta of all PF candidates in a cone of $\Delta R < 0.3$ around the muon, while excluding the muon itself,

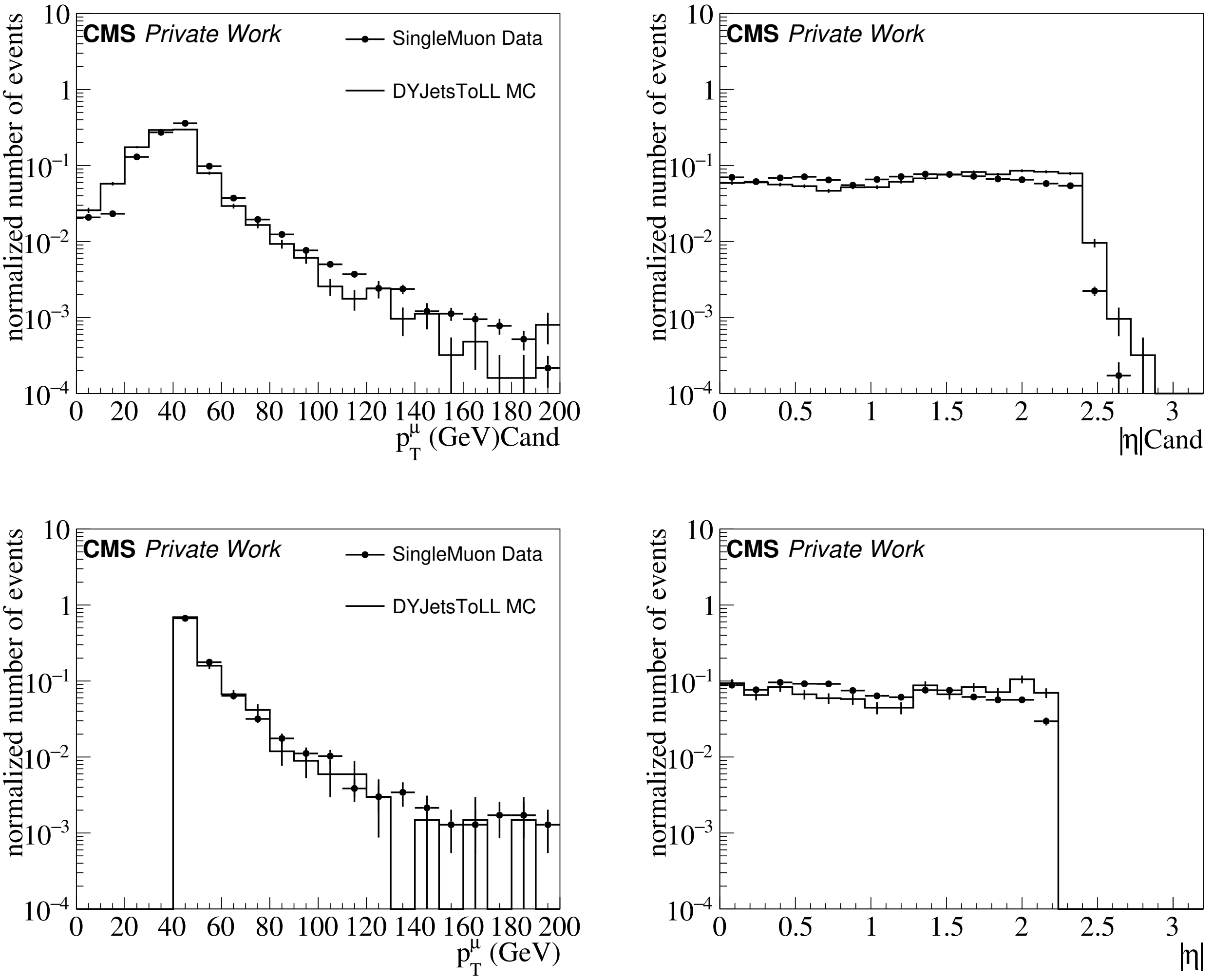

Figure 5.62: Top: Normalized muon transverse momentum and $|\eta|$ distribution for selected muons passing $p_T^\mu > 45$ GeV, $|\eta| < 2.2$ and $\sum p_{T,i}/p_T^\mu < 0.2$. Bottom: Muons matched to well-reconstructed tracks within $\Delta R < 0.01$. Data are shown for a subset of Run2016F, with a subset of Phase 0 MC being used for background.

and applying a cut of $\sum p_{T,i}/p_T^\mu < 0.2$. Fig. 5.61-Right shows the cut on the PF candidate isolation for a representative subset of data. For each muon with $p_T^{\text{track}} > 40$ GeV and $|\eta^{\text{track}}| < 2.0$, the reconstructed track connected to the muon identified by the PF muon identification is selected. In order to select only well-reconstructed tracks close to the primary vertex, ≥ 10 layers with measurement, $d_{xy} < 0.2$ cm and $d_z < 0.1$ cm are further required. Figure 5.62 shows the muon transverse momentum and $|\eta|$ distributions before (top row) and after the track-matching (bottom row).

Tracker hit clusters of the corresponding track are then removed in each iteration, starting from the outermost hit cluster towards the innermost 3 hit clusters of the track. In each iteration, the complete track reconstruction is re-run, and the non-shortened μ-matched track is matched to the shortened track within a cone of $\Delta R < 0.01$. For the shortened track, either $p_T^{\text{track}} > 25$ GeV for short tracks or $p_T^{\text{track}} > 40$ GeV for long tracks is required, and the full disappearing track tag is evaluated on the shortened track.

To gain deeper insight, the track selection efficiency is decomposed into two efficiencies measured in data and MC, the reconstruction efficiency and the tagging efficiency. The reconstruc-

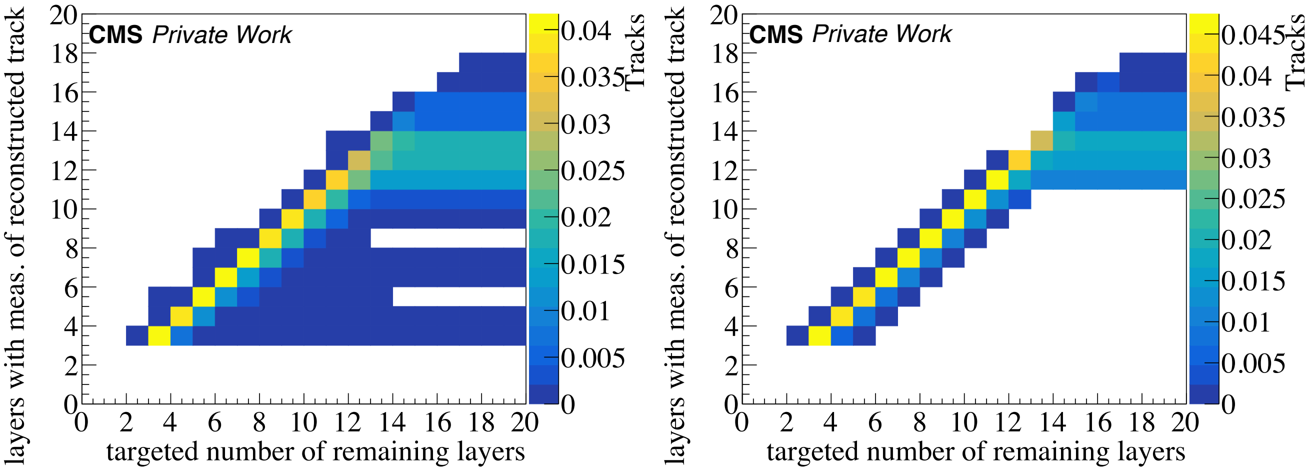

Figure 5.63: Track matching verification showing the number of remaining layers with measurement given to the track shortening tool vs. the number of layers with measurement of the shortened track for a representative subset of Phase 0 data (Run2016F, left) and Phase 0 MC simulation (right). Ideally, entries should be on the diagonal of the 2D plane.

tion efficiency is defined as the ratio of the number of shortened tracks to the original number of μ-matched tracks, and is therefore a measure how well the shortened track can tag charged particles. The tagging efficiency is the ratio of the number of shortened tracks which are tagged as disappearing tracks to the total number of reconstructed shortened tracks. The artificial shortening procedure is flexible enough to determine the dependence of the efficiency on the track length.

Figure 5.63 shows the verification of the matching criterion, with a successful match yielding the same targeted number of layers given to the track shortening tool and the number of layers of the re-reconstructed track. Entries not on the diagonal indicate a track mismatch, which is not a significant effect for $\leq$ 10 layers with measurement, which is the main track selection criterion.

Track mismatches visible in Fig. 5.63 can also occur when the transverse momentum of the track before and after the shortening procedure is very different. Figure 5.64 shows the μ-matched track p_T versus the shortened track p_T for data and MC. They are similar, albeit the distinction of reconstructed momenta of shortened tracks will depend strongly on the number of remaining layers with hits. Fig. 5.65 shows the ratio of the shortened track p_T divided by the μ-matched track p_T for data and MC and targeted number of layers with measurement, ranging from 3 layers to 6 layers. As expected, $p_T^{\text{shortened track}} / p_T^{\mu\text{-matched track}}$ becomes smaller for longer track lengths. Data and MC simulation agree up to the tails of the distributions.

Shortened track reconstruction and tagging efficiency Figure 5.66 shows the reconstruction and tagging efficiency depending on the number of remaining layers with measurement. The reconstruction efficiency is defined as the ratio of the number of shortened tracks to the number of μ-matched tracks, and is therefore a measure how well the shortened track can be retrieved. The tagging efficiency is the ratio of the number of shortened tracks which are tagged as disappearing tracks to the total number of shortened tracks. By artificially shortening the tracks, the disappearing track tag efficiency can thus be determined depending on the track length. Phase 1 is shown in Sec. A of the appendix in Fig. A.1.

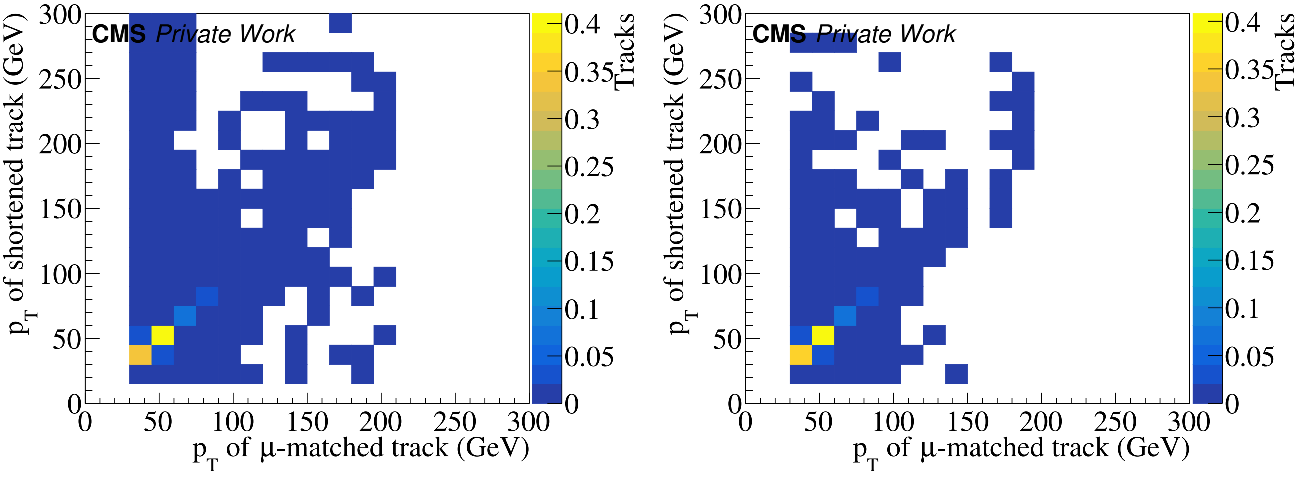

Figure 5.64: Muon-matched track p_T vs. shortened track p_T for data and background MC. Shown is a representative subset of data (2016F, left) and Phase 0 background MC (right). The plot shows an overlay of all remaining numbers of layers of the shortening procedure for each initial track, thus combining short and long tracks.

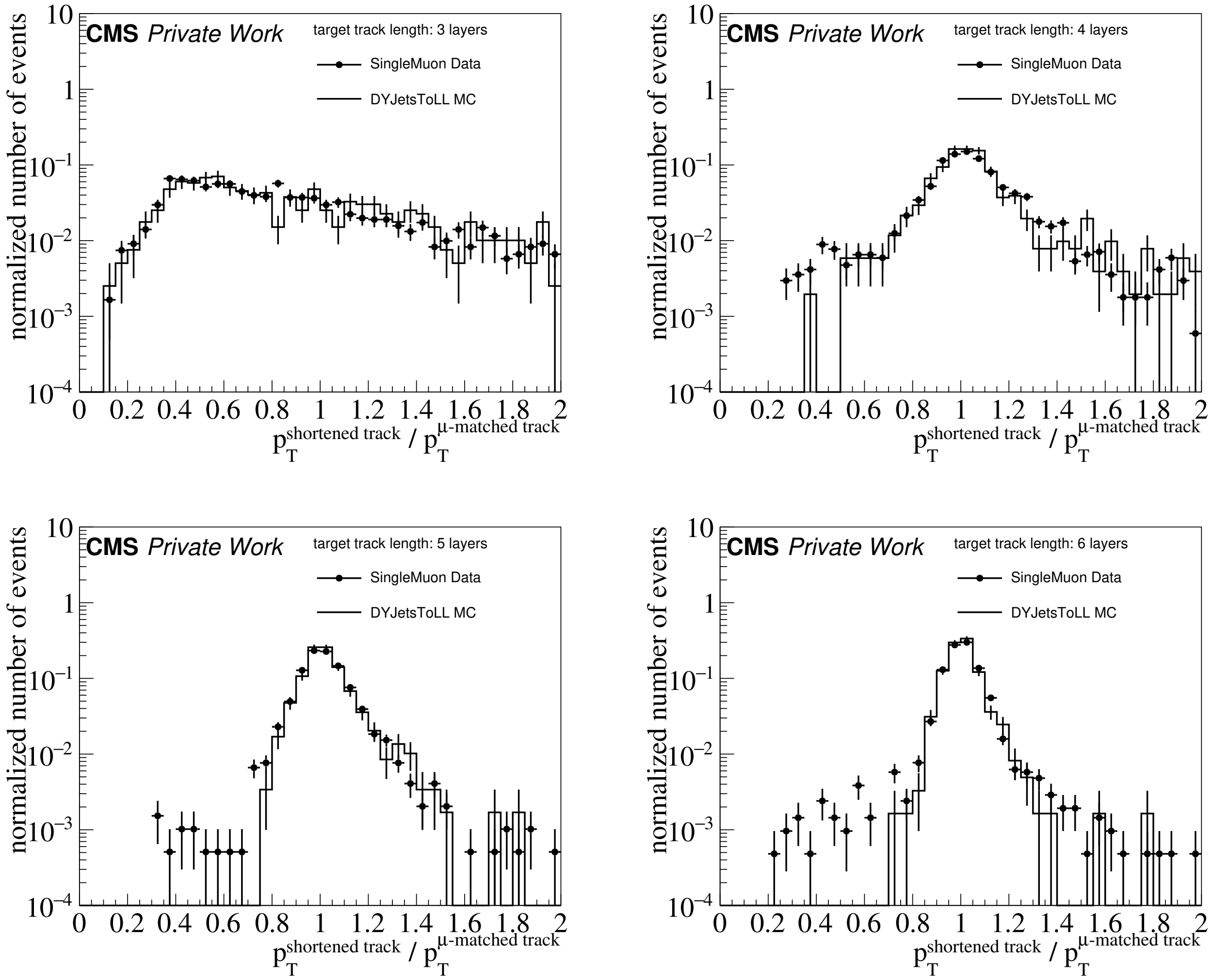

Figure 5.65: Ratio of muon-matched track p_T by shortened track p_T for Phase 0 data and background MC. Shown is a representative subset of data (2016F) and Phase 0 background MC for 3-6 targeted number of layers with measurement.

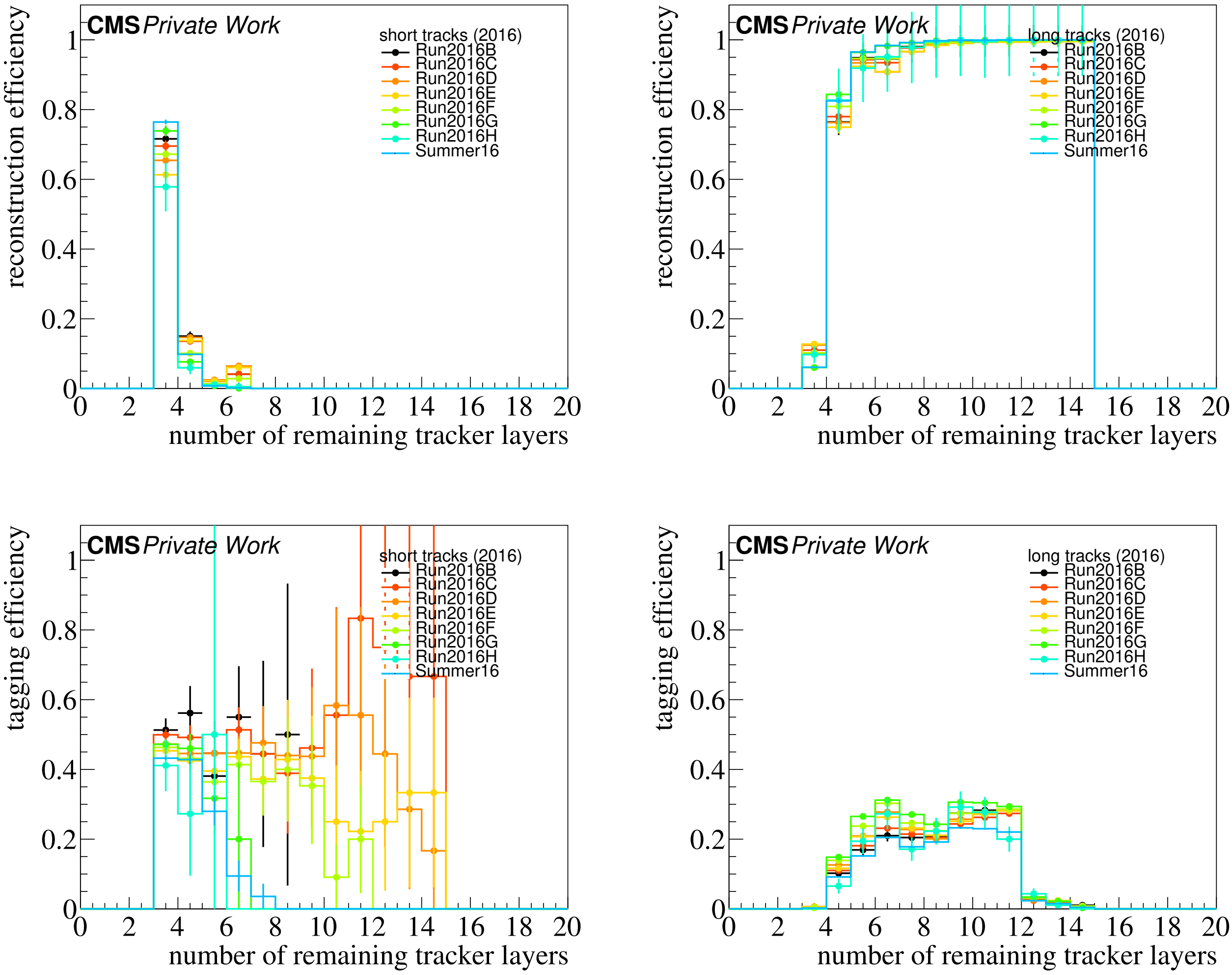

Figure 5.66: Shortened track reconstruction efficiency (top) and disappearing track tagging efficiency (bottom) depending on remaining layers with measurement, shown for Phase 0. Left: short tracks, right: long tracks.

For a sufficient number of layers (≥ 10) with measurement, shortened tracks can be matched to their original μ-matched tracks with more than 95% efficiency. For the disappearing track tag evaluation, the BDTs for short and long tracks differ in their efficiency, with e.g. more than 75% (40%) of short (long) tracks tagged as disappearing tracks for Run2017B. Data and MC background simulation agree well.

Figure 5.67 shows the reconstruction and disappearing track tagging efficiency for all run periods and background MC, exemplary for 3, 4 and 7 remaining layers. In order to examine time-dependent changes in efficiency, the luminosity-weighted average values for each year are calculated by adding the numerators and denominators separately, scaled with the luminosity and divided by the total integral of the dataset for e.g. data. This procedure is then repeated for background MC. For short tracks, a higher disappearing track tagging efficiency is visible, while for long tracks the overall reconstruction efficiency for shortened tracks is higher. Long tracks furthermore exhibit stable efficiencies over the three years, as visible for tracks with 7 layers of measurement. Short tracks show a decrease in shortened track reconstruction efficiency for each year, however in this case efficiencies for tracks with 3 layers with measurement in 2016 have to be compared to tracks with 4 layers with measurement in 2017 and 2018 due to the change in detector configuration.

Scale factor determination Scale factors for each track category and year are determined which include both the reconstruction and disappearing track tagging efficiencies,

$$\begin{aligned}\text{scale factor} &= (\epsilon_{\text{reco}} \cdot \epsilon_{\text{tag}})_{\text{data}} / (\epsilon_{\text{reco}} \cdot \epsilon_{\text{tag}})_{\text{MC}} \\ &= (\frac{n_{\text{rereco}}}{n_{\text{reco}}} \cdot \frac{n_{\text{tagged}}}{n_{\text{rereco}}})_{\text{data}} / (\frac{n_{\text{rereco}}}{n_{\text{reco}}} \cdot \frac{n_{\text{tagged}}}{n_{\text{rereco}}})_{\text{MC}} \\ &= (\frac{n_{\text{tagged}}}{n_{\text{reco}}})_{\text{data}} / (\frac{n_{\text{tagged}}}{n_{\text{reco}}})_{\text{MC}},\end{aligned} \tag{5.12.1}$$

with the number of μ-matched tracks n_{reco}, the number of shortened tracks n_{rereco}, and the number of shortened tracks tagged as a disappearing track n_{tagged}.

For each run period, the scale factor is first determined dependent on the number of layers with measurement separately for short and long tracks. A constant fit is then performed to get the central value of the scale factor, with the uncertainty measured for a fixed number of layers with measurement in order not to include correlations between the bins. For short tracks, the uncertainty is measured from 3 layers with measurement, and for long tracks from 5 layers with measurement. The fits are provided in Sec. A of the appendix in Fig. A.2.

The results from all fits are shown in Fig. 5.68 for the total scale factor, as well as the factorized reconstruction and tagging scale factors. The figure also shows the luminosity-weighted average for the three years in order to indicate time-dependent trends. The scale factor for short (long) tracks is compatible with 0.9 (1.1) within the statistical uncertainties.

The overall signal scale factors from Fig. 5.68 are summarized as numerical values in Table 5.15. The uncertainty on the scale factors is used as a signal systematic, ranging from 6-7% for short tracks and 9-11% for long tracks.

Mismodeling of d_{xy} and d_z For short tracks in Phase 1, the method described above resulted in significantly smaller tagging scale factors, shown in Fig. 5.69 in the top-left corner. It was found that the short track BDT selects shortened tracks from muons in MC more readily than in data, due to an overly-optimistic vertex resolution in Phase 1 MC compared with data. This is

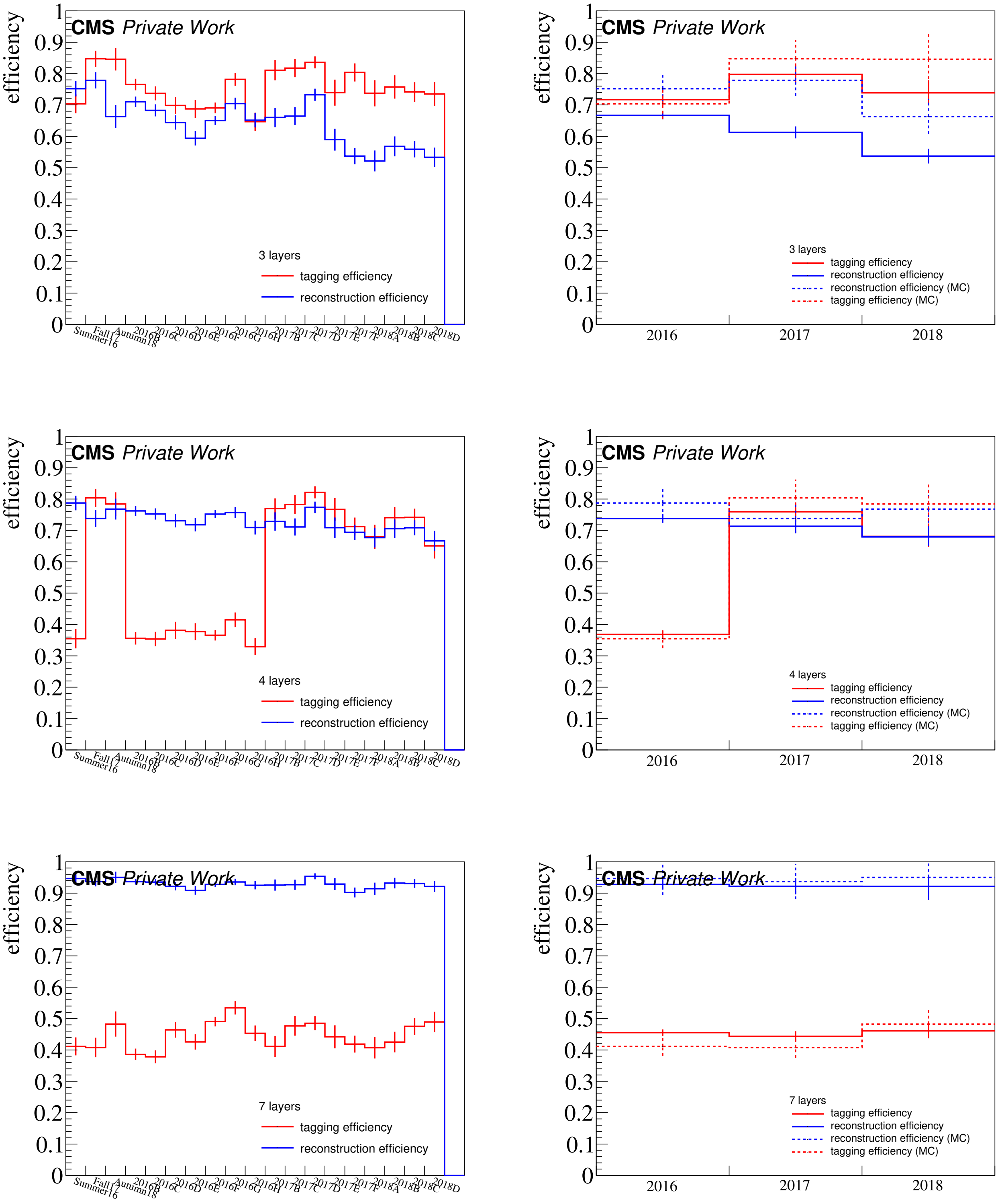

Figure 5.67: Left side: Reconstruction and disappearing track tagging efficiency for all run periods and background MC, shown for 3 layers (top), 4 layers (middle) and 7 layers (bottom) with measurement. Right side: Luminosity-weighted average for the three years.

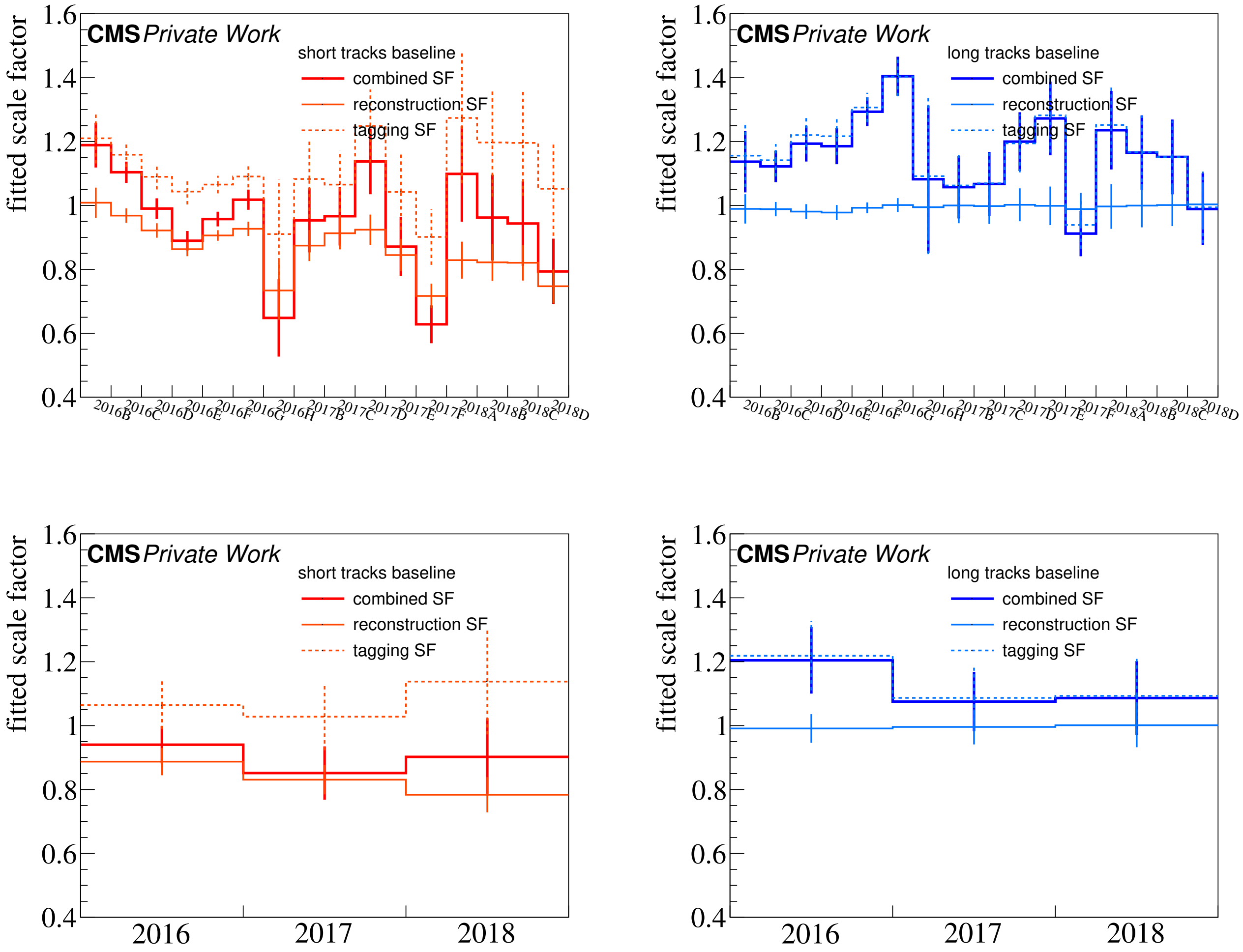

Figure 5.68: Top: Total, reconstruction and tagging scale factors for short (left) and long tracks (right). Bottom: Luminosity-weighted average for all years.

Year	Track category	Scale factor
2016	short	0.94 ± 0.05
2016	long	1.20 ± 0.10
2017	short	0.85 ± 0.08
2017	long	1.07 ± 0.09
2018	short	0.90 ± 0.12
2018	long	1.08 ± 0.11

Table 5.15: Numerical values for the signal scale factors shown in Fig. 5.68 as applied in the analysis for each track category and year.

especially the case for Run 2017F, and can be corrected by adjusting the values of the impact parameters d_{xy} and d_z based on a cumulative transform derived between the comparison of data and MC. The top-right corner of Fig. 5.69 shows the correction map for d_{xy}, which is applied to MC. The effect is shown in the bottom row of Fig. 5.69, which shows the d_{xy} distribution before and after applying the correction. The correction for d_z is carried out analogously and is shown in Fig. A.3 in the appendix.

The signal scale factor shows a significant improvement after the corrections have been applied, as has been shown in Fig. 5.68.

5.12.3 Conclusion

This section summarized various sources of systematic uncertainties, as well as how they are quantified and taken into account for the data-driven background prediction and the simulated MC signal. Table 5.16 summarizes all systematic uncertainty sources which are assigned for each signal bin. The most relevant sources of systematic uncertainty for the background estimation are due to statistics and contamination of the control regions, with the largest systematic uncertainty of up to 104% stemming from transfer factor measurement region contamination for short tracks in the prompt background estimation, followed by the uncertainty on the long track prediction for the spurious track background of up to 52%.

For systematic uncertainties in the signal MC simulation, a set of standard uncertainties following CMS recommendations have been assigned, as well as systematic uncertainties in the dE/dx measurement, FastSim correction, and in the disappearing track scale factor determination. The systematic uncertainty on the dE/dx measurement and the FastSim correction are very minor backgrounds in bins where they are relevant. For the last source, a novel technique has been applied in order to derive the efficiency of reconstructing shortened muon tracks in both data and MC, allowing for the determination of scale factors applicable to charginos. For simulated signal, the largest source of systematic uncertainty is the jet energy scale and resolution of up to 24%.

Source	Relative uncertainty (%)
DTk selection efficiency	10–17
Integrated luminosity	1.6
Jet energy scale and resolution	0–24
b-jet tagging	0–4
Renormalization and factorization scales	0–2
Initial-state radiation	0–3
Pileup modeling	0–2
Trigger efficiency	0–4
dE/dx calibration	3–8
Showering background (long tracks)	20–28
Showering background (short tracks)	24–104
Spurious tracks background (long tracks)	5–52
Spurious tracks background (short tracks)	6–28
MIP background (long tracks)	25–38

Table 5.16: Systematic uncertainties considered for the simulated signal (top) and for the data-driven background prediction (bottom), with ranges given for the total prefit uncertainty used for all signal bins. The value 0 is used when the relative uncertainty is determined to be less than 0.5%.

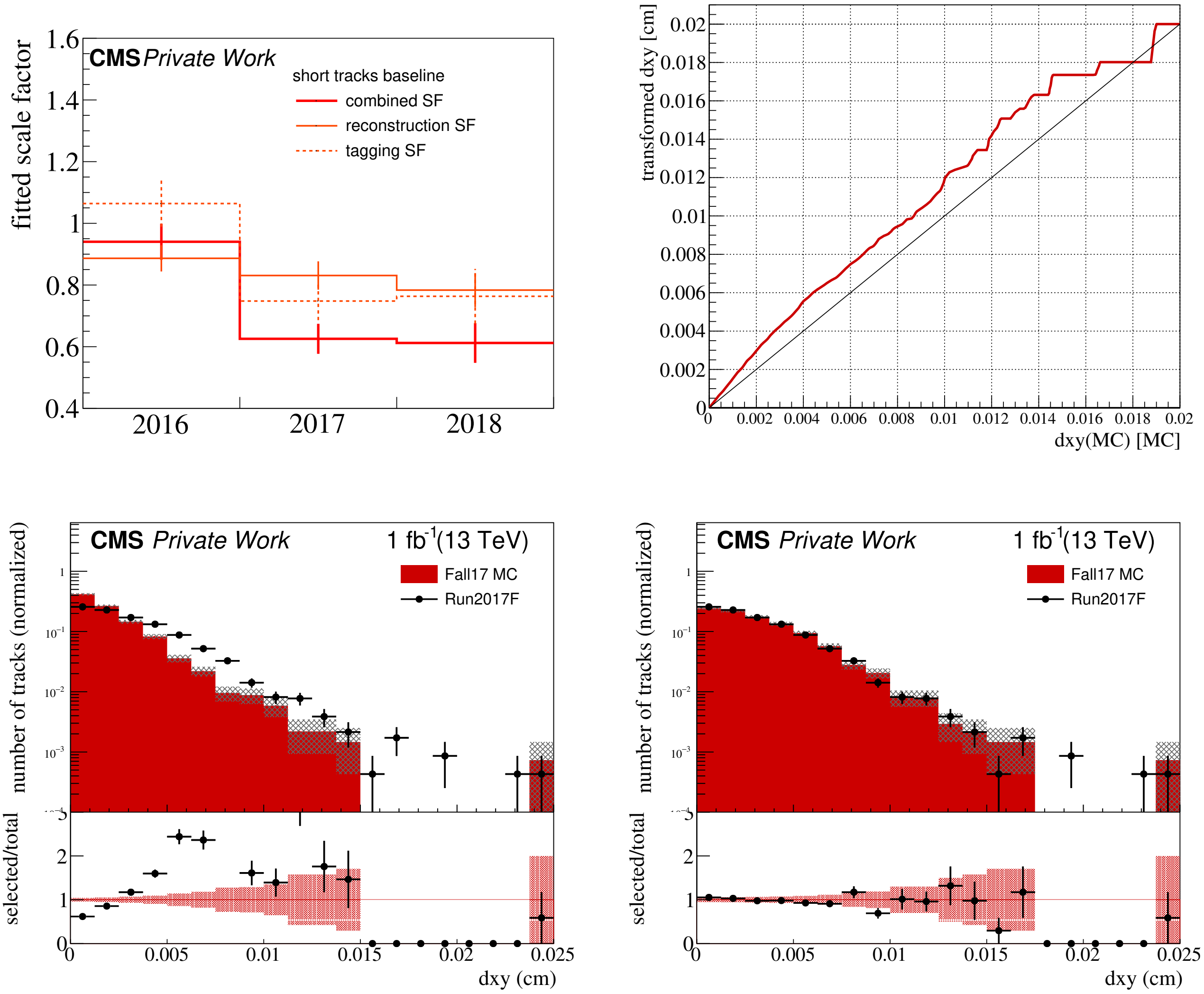

Figure 5.69: Top row: Luminosity-weighted signal scale factors for short tracks before applying the corrections to d_{xy} and d_z in Phase 1 MC (left); correction map for MC d_{xy} based on the cumulative transform for Phase 1 (right). Bottom row: Distributions of d_{xy} for short tracks derived from the track shortening method for the data-taking period 2017F (black dots) and for Phase 1 MC, before (left) and after (right) the application of the corrections to d_{xy}.

Chapter 6

Results

6.1 Observed data

For the signal regions defined in Sec. 5.9.2, data are shown in Fig. 6.1. The figure includes the observed data in Run 2 and the background predictions and their total uncertainties, including the prediction for the prompt background from showering particles, for the prompt background from muons, and for the spurious track background.

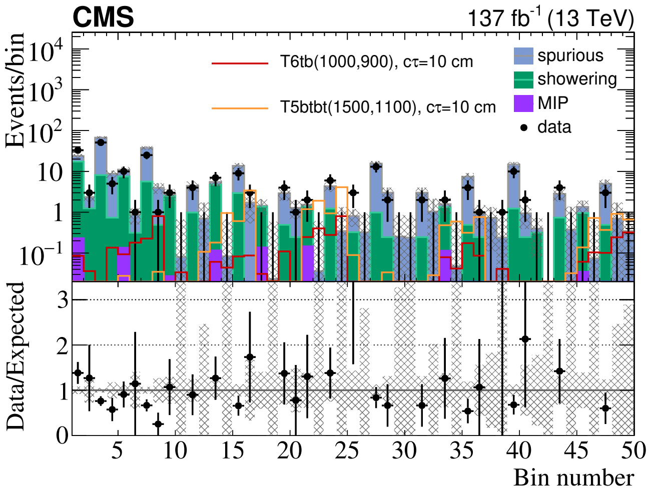

Figure 6.1: Results for Run 2, showing the number of observed and predicted background counts as well as two simplified signal models (T6tbLL and T5btbtLL). The vertical black uncertainty bars indicate the Poisson (top) or scaled Poisson (bottom) uncertainty in the observed count, whereas the shaded bands indicate the statistical and systematic uncertainty in the background prediction added in quadrature.

Two simplified signal models, discussed in Sec. 5.2, with a proper decay length of $c\tau = 10$ cm are included to gauge the signal population across the signal bins, T5btbtLL and T6tbLL. For observed data, the Poisson uncertainty is shown as uncertainty bars, while for the background prediction the gray bands show the Poisson uncertainty in the control regions, as well as the 100% systematic uncertainty on the prompt short tracks from showering particles due to the transfer measurement region contamination, as discussed in Sec. 5.12.1.

The number of observed data counts are within the combined statistical and systematic uncertainties of the number of predicted background counts, and no statistically significant deviation can be seen. The largest deviation of 2.2σ is visible in the first signal region bin, which includes events with a long disappearing track with dE/dx<4 MeV/cm in the low $\not{E}_T$ regime of 150-300 GeV, 1-2 jets with zero b-tagged jets. The second-largest deviation is visible in signal region bin 25, which corresponds to events containing a single long disappearing track with dE/dx<4 MeV/cm in the muon channel with low $\not{E}_T = (30, 100)$ GeV, $\geq$ 1 jets and zero b-tagged jets. No observed data is measured in the corresponding signal bin of the electron channel, signal bin 37. Furthermore, no events are observed in the last signal region bin 49, which includes events with two disappearing tracks. Observed and predicted background counts are provided in Sec. A of the appendix for the signal and control regions, as well as the event count in the control regions for each background.

Figure 6.2 shows the number of jets, b-tagged jets, $\not{E}_T$, invariant mass of the lepton-DTk system $m_{l,\text{track}}$, $m(dE/dx)$ as defined in Sec. 5.8 and the track p_T for the combined signal regions, depicted separately for short and long tracks. The included uncertainties are statistical uncertainties (Poisson statistics of the control region statistics) and uncorrelated systematic uncertainties added in quadrature, while correlated uncertainties are omitted.

For both short and long tracks, the $\not{E}_T$ distribution shows a structure which reflects the triggers turn-on starting at a $\not{E}_T$ value around 120 GeV. The number of observed counts is within the statistical and systematic uncertainties of the background prediction for long tracks, showing no deviation. A systematic over-prediction is visible of $\approx 25\%$ for short tracks, and is covered within the statistical and systematic uncertainties of the background prediction. This over-prediction is likely due to the contamination of the transfer region for short tracks in the prompt background estimation with spurious tracks, which is accounted for in the discussion of the post-fit results in the following section. The overall agreement of the observed counts in data with the number of predicted events indicates no evidence for BSM physics, and upper limits on the signal production cross section are derived using the post-fit results.

6.2 Interpretation

The results of the search presented in Sec. 6.1 are interpreted in terms of the simplified models discussed in Sec. 5.2. In order to obtain both expected and observed limits, the standard CL_s technique is used, which is described in the following. A statistical fit is performed in which the systematic uncertainties discussed in Sec. 5.12 are included as log-normal density functions or gamma functions, depending on whether the uncertainty is inherently statistical or not, encoding the size of the uncertainty as the width of these functions. By performing the fit and letting the nuisance parameters float, the post-fit distributions are obtained.

6.2.1 The CL_s technique

The frequentist CL_s technique is used as a statistical method to perform exclusion tests by determining the confidence of two hypotheses, the *null* hypothesis, which is the background (b) hypothesis, and the signal + background ($s + b$) hypothesis. In the case of the null hypothesis, data is assumed to be fully described by SM background. BSM physics enters as signal in the $s + b$ hypothesis. Any background process which mimics the signal, in this case prompt background from showering particles, prompt background from muons (included as “MIP”), and the spurious track background, is included. For both hypotheses, the standard tail probabilities CL_b and CL_{s+b} are determined, with CL_b corresponding to the p-value [95].

For a general test statistic q with an observed value q_{obs}, the p-value for the null hypothesis is

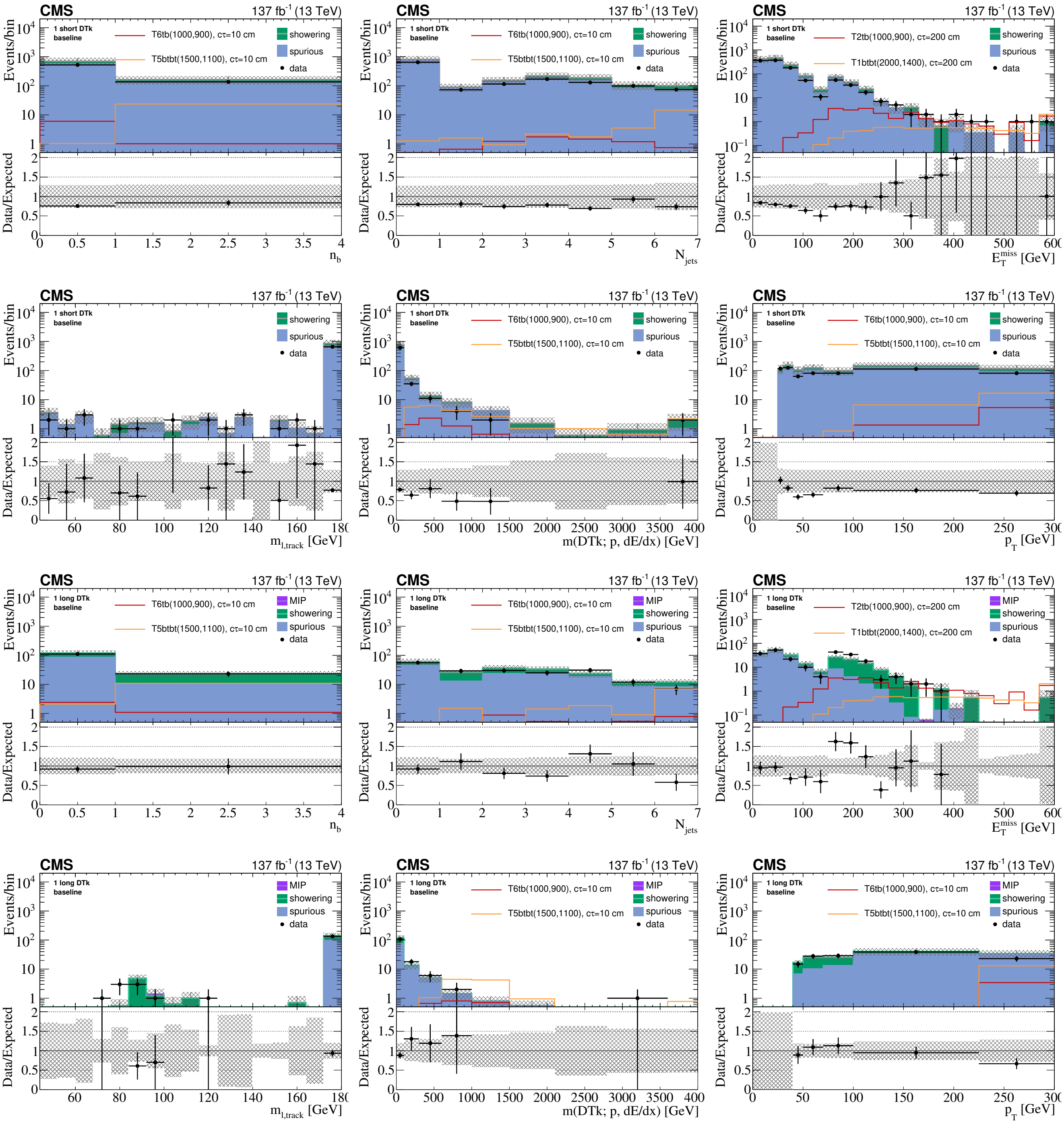

Figure 6.2: Results for Run 2, showing the number of observed and predicted counts in the signal region for short (top) and long tracks (bottom). The three analysis channels have been combined in this figure.

determined via

$$p_b = P\left(q \leq q_{\text{obs}} \mid b\right) = \int_{-\infty}^{q_{\text{obs}}} f(q \mid b)dq, \tag{6.2.1}$$

while for the $s+b$ hypothesis, the p-value becomes

$$p_{s+b} = P\left(q \geq q_{\text{obs}} \mid s+b\right) = \int_{q_{\text{obs}}}^{\infty} f(q \mid s+b)dq. \tag{6.2.2}$$

Using p_{s+b}, a signal model can be excluded at a confidence level (C.L.) of $1-\alpha = 95\%$ ($\alpha = 0.05$) for

$$p_{s+b} < \alpha, \tag{6.2.3}$$

which is also referred to as CL_{s+b} [96]. However, using this requirement would exclude models with little sensitivity. In this case, a low sensitivity corresponds to closely matching values for p_{s+b} and p_b, and the CL_s method is used instead, which prevents the exclusion of a signal hypothesis by requiring

$$\text{CL}_s \equiv \frac{p_{s+b}}{1-p_b} < \alpha. \tag{6.2.4}$$

A maximum likelihood fit is performed with the observed, predicted and signal counts in each signal region given as input. The systematic uncertainties are treated as nuisance parameters in the fit. A penalty term constrains each nuisance parameter and is associated with its uncertainty [97].

6.2.2 Post-fit distribution of the signal regions

Figure 6.3 shows the pre-fit and post-fit distributions of the signal region bins. By allowing freely-floating nuisance parameters in the fit, the impact of the systematic uncertainty can be reduced [97]. In the case of the large systematic uncertainty of 100% for short tracks in the prompt background estimation, the treatment of the nuisance parameters in the fit allows to reduce this uncertainty to near-zero.

The post-fit distribution of the signal region bins is used to derive expected upper limits on the cross section of the different simplified signal models.

6.2.3 Derivation of limits

The upper 95% C.L. limits on the cross sections are shown in Figs. 6.4 and 6.5 for the T6tbLL, T6btLL and T5btbtLL simplified models. For each interpretation, two choices of $c\tau$ are shown, $c\tau = 10$ cm and $c\tau = 200$ cm. For the higgsino simplified model, as described in Sec. 5.2, the upper limit on the signal cross sections is shown in Fig. 6.6, for which the chargino lifetime is determined as a function of Δm^{+} [52].

The expected and observed limits are included as contours, for which the upper 95% C.L. limit on the cross section is equal to the theoretical prediction of the cross section of the hard process. By convention, the uncertainty on the observed limit only includes the uncertainty of the cross section calculation of the hard process, while the uncertainty on the expected limit includes the sources of systematic uncertainty discussed in Sec. 5.12.

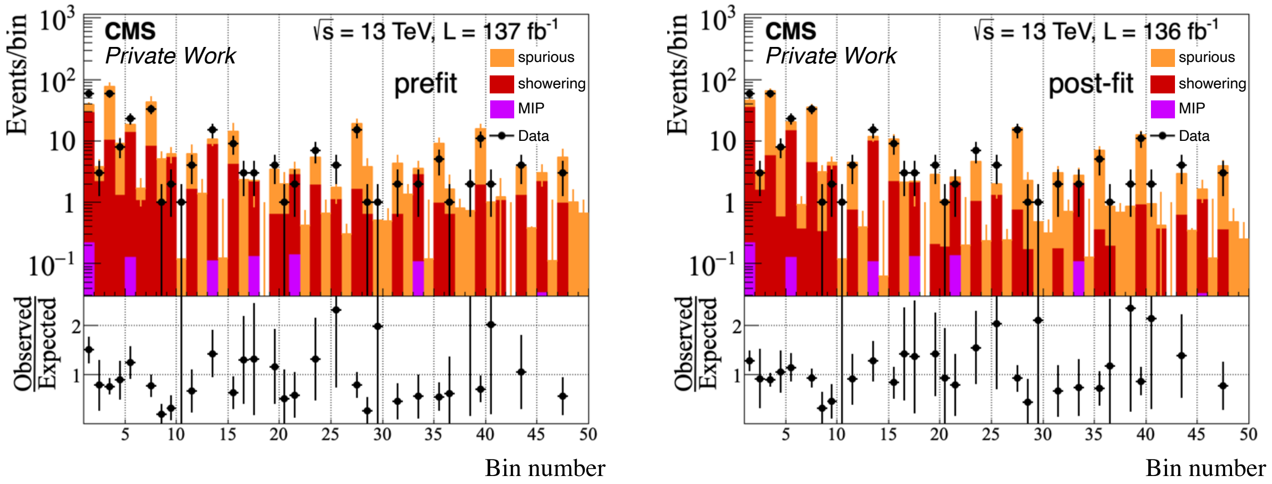

Figure 6.3: Pre-fit (left) and post-fit (right) results for the combined statistics of the Run 2 analysis. The pre-fit results shown for the signal region bins are the same as in Fig. 6.1. Poisson uncertainty is shown for the observed counts.

For simplified models as introduced in Sec. 5.2.1 and Sec. 5.2.2, different regimes can be identified, depending on the relationship between the mass of the initial heavy particle ($m_{\tilde{g}}$, $m_{\tilde{q}}$) and the mass of the LSP $m_{\tilde{\chi}_1^0}$. The *compressed* regime is defined by either a nearly mass-degenerate gluino $\tilde{g}$ or squark $\tilde{q}$ and the LSP $\tilde{\chi}_1^0$. The *bulk* regime refers to $m_{\tilde{g}}, m_{\tilde{q}} \gtrsim 1$ TeV and $m_{\tilde{g}}, m_{\tilde{q}} > m_{\tilde{\chi}_1^0}$, and the *boosted* regime refers to a light LSP $m_{\tilde{\chi}_1^0} \lessapprox 200$ GeV with $m_{\tilde{g}}, m_{\tilde{q}} \gg m_{\tilde{\chi}_1^0}$, for gluino-associated and squark-associated $\tilde{\chi}_1^{\pm}$ production, respectively.

For the T6tbLL simplified model, the upper 95% C.L. limits on the production cross section of $m_{\tilde{b}}$ and $m_{\tilde{\chi}_1^0}$ are shown in Fig. 6.4-top for a smaller $c\tau$ of 10 cm, and a longer $c\tau$ of 200 cm. The observed limit reaches up to $m_{\tilde{b}} \approx 1.575$ TeV and up to $m_{\tilde{\chi}_1^0} \approx 1.15$ TeV for $c\tau = 200$ cm.

For the T6btLL simplified model, Fig. 6.4-bottom shows the upper 95% C.L. limits on $m_{\tilde{t}}$ and $m_{\tilde{\chi}_1^0}$, for which the observed limit reaches up to $m_{\tilde{t}} \approx 1.6$ TeV and up to $m_{\tilde{\chi}_1^0} \approx 1.2$ TeV, again for $c\tau = 200$ cm.

Upper 95% C.L. limits on the gluino-associated chargino production are shown in Fig. 6.5, which correspond to the T5btbtLL simplified model. For $c\tau = 200$ cm, the observed limit reaches up to $m_{\tilde{g}} \approx 2.25$ TeV and up to a LSP mass of $m_{\tilde{\chi}_1^0} \approx 1.7$ TeV.

For the simplified model featuring a nearly-pure Higgsino DM candidate, upper 95% C.L. limits on the production cross section are shown in Fig. 6.6. Here, a green line is included to represent the set of model points corresponding to the pure higgsino model where only radiative corrections to the mass splitting are assumed [53]. The mass splitting between the two lightest SUSY states is thus given by radiative corrections only, and in this case, chargino and LSP masses can be excluded up to 180 GeV. This exclusion limit corresponds to the intersection of the observed limit and the set of model points indicated by the green line.

6.3 Comparison of exotic long-lived particle detection sensitivity

With upper 95% C.L. limits on the cross section determined for different simplified models, this section focuses on the comparison of the newly-derived exclusion limits with respect to other CMS and ATLAS searches. Special attention has to be given in order to select the same

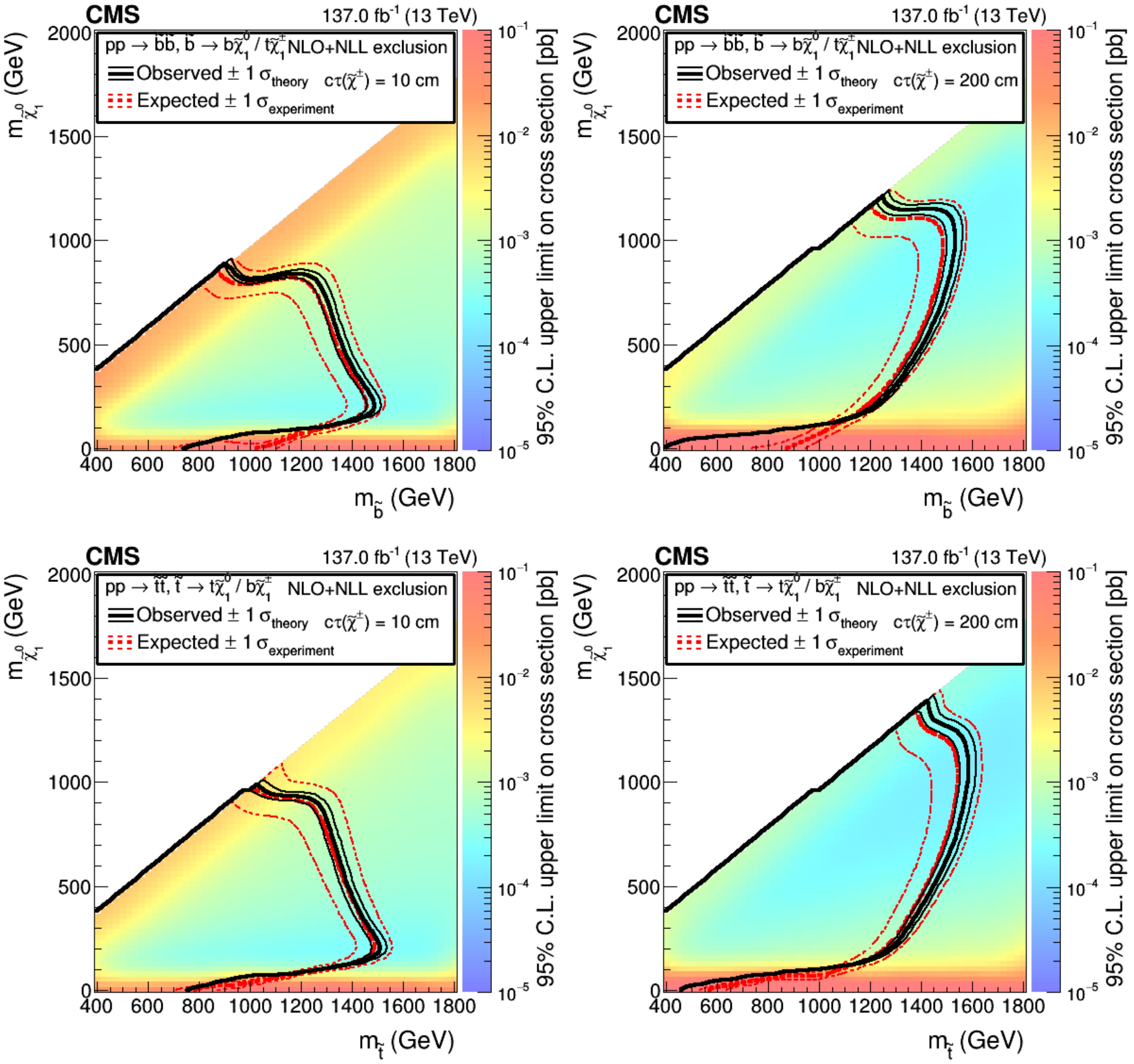

Figure 6.4: Upper 95% C.L. limits on the signal cross sections using the asymptotic CL$_s$ method versus bottom (top) squark and neutralino masses for the T6tbLL (top) and T6btLL (bottom) model for a $c\tau_{\tilde{\chi}_1^\pm}$ of 10 cm (left) and 200 cm (right), based on the combined (hadronic+leptonic) analysis. Here, the probability for the decay of either a top squark or bottom squark into a final state including a $\tilde{\chi}_1^\pm$ is assumed to be 50%. Also shown are the contours corresponding to the observed and expected lower limits, including their uncertainties.

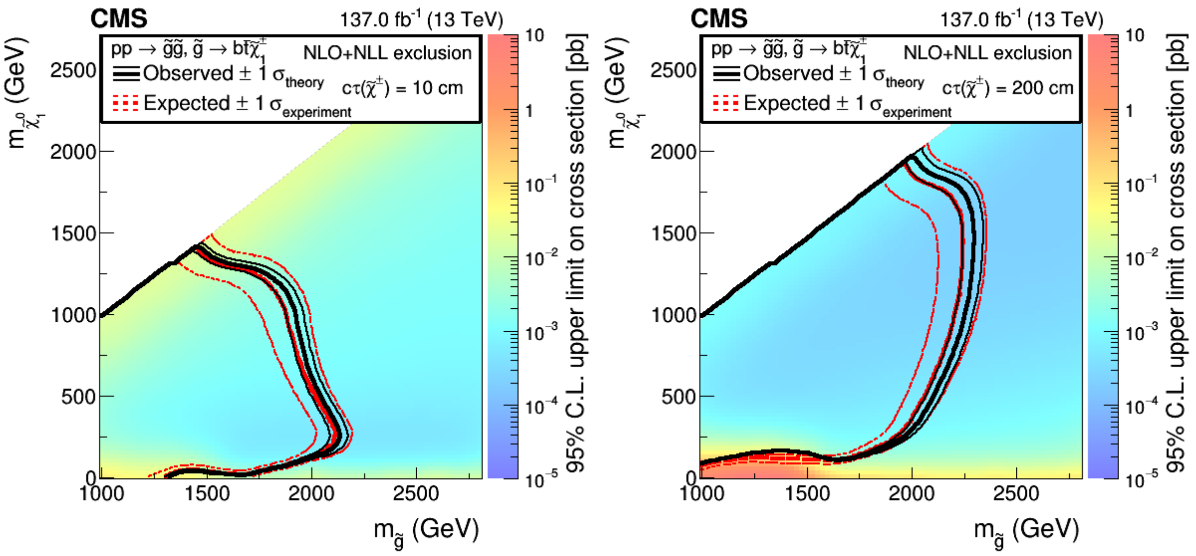

Figure 6.5: Upper 95% C.L. limits on the signal cross sections using the asymptotic CL$_s$ method versus gluino and neutralino masses for the T5btbtLL model with $c\tau$ of 10 cm (left) and 200 cm (right), based on the combined (hadronic+leptonic) analysis. Here, the probability for the decay of a gluino into a final state including either $\tilde{\chi}_1^+$ or $\tilde{\chi}_1^-$ is assumed to be 25% each. Also shown are the contours corresponding to the observed and expected lower limits, including their uncertainties.

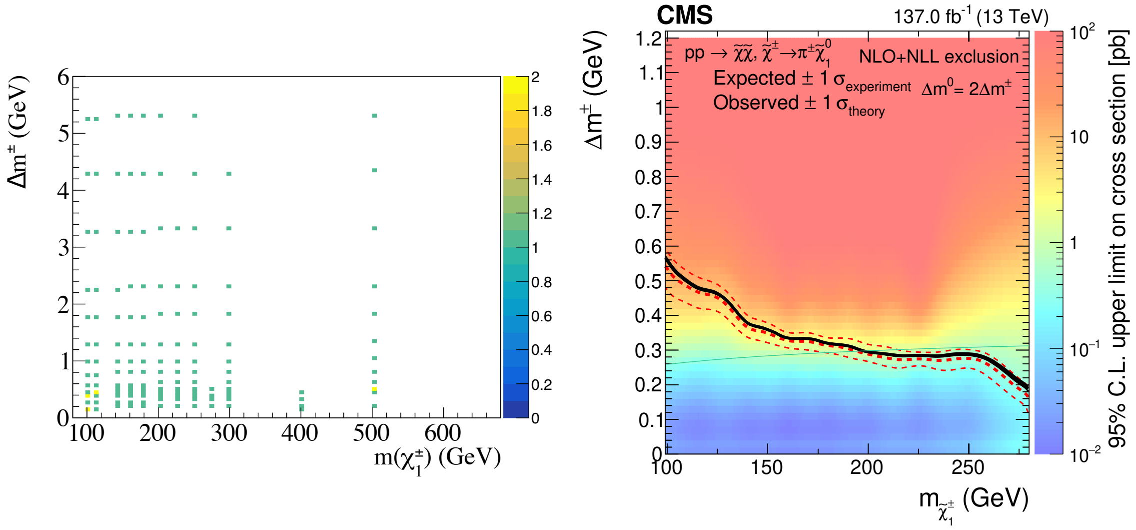

Figure 6.6: Upper 95% C.L. limits on the signal cross sections using asymptotic CLs versus the mass splitting between the lightest electroweakinos and the chargino mass. The probability for decays into a final state including a $\tilde{\chi}_1^{\pm}$ is assumed to be 50%. The red solid line indicates the boundary where the upper limit is equal to the cross section of fully degenerate higgsino production [98, 99]. The green line represents the set of model points corresponding to the pure higgsino model where only radiative corrections to the mass splitting are assumed [53]. The chargino lifetime is determined as a function of $\Delta m^{\pm}$, as described in [52].

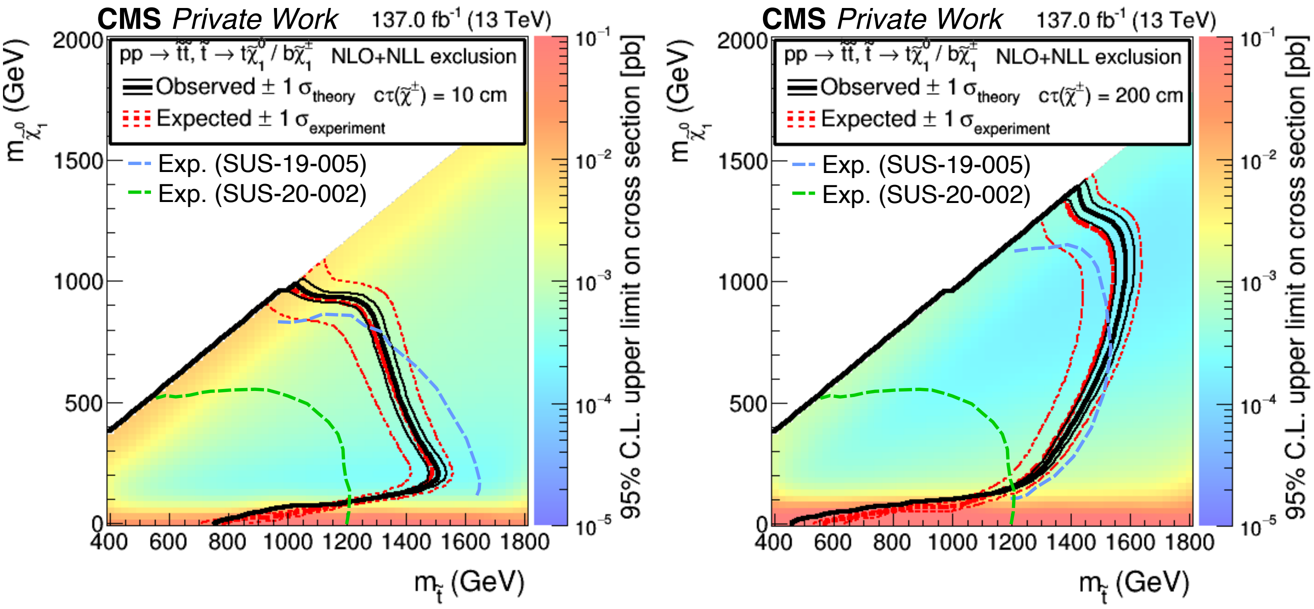

Figure 6.7: Comparison of expected and observed excluded limits using the T6btLL simplified model interpretation for a $c\tau_{\tilde{\chi}_1^\pm}$ of 10 cm (left) and 200 cm (right) to other CMS searches. SUS-19-005 includes a disappearing track interpretation targeting long-lived charginos $\tilde{\chi}_1^\pm$, while SUS-20-002 includes the most recent exclusion limits on prompt $\tilde{t}$-squark production.

production mechanism, final state as well as specific decay length $c\tau$ when comparing long-lived chargino searches.

Figure 6.7 shows a comparison to other CMS searches for top squark production. This includes the previously discussed SUS-19-005 search, which also targets long-lived charginos in the final state with a disappearing track signature [75]. A second comparison is made to a prompt top squark production search, which is referred to as SUS-20-002 [100]. A significantly extended reach in excluded phase space is visible in the compressed region for dedicated long-lived searches in comparison to the search probing prompt top squark decays (SUS-20-002). The exclusion limits derived in this analysis reach higher LSP masses by an increase of ≈ 200 GeV ($c\tau = 10$ cm) and ≈ 300 GeV ($c\tau = 200$ cm), compared to SUS-19-005, reaching $m_{\tilde{\chi}_1^0} \approx 1.0$ TeV ($c\tau = 10$ cm) and $m_{\tilde{\chi}_1^0} \approx 1.4$ TeV ($c\tau = 200$ cm).

Figure 6.8 shows 95% C.L. limits on the cross section in the $m_{\tilde{b}}$ vs. $m_{\tilde{\chi}_1^0}$ plane for CMS and ATLAS searches. An additional CMS result is included as SUS-19-006, which originates from a search for SUSY in final states with jets and missing transverse momentum [89]. Here, the CMS results SUS-19-005 and SUS-19-006 drive the exclusion limits in the boosted region, while this analysis extends the compressed region as well as the bulk [75, 89], as defined in Sec. 6.2.3.

A comparison to prompt ATLAS searches is also shown, which includes two results from $\tilde{b}$ pair production searches. The results are compared in the $m_{\tilde{b}}$-$m_{\tilde{\chi}_1^0}$ phase space, with the ATLAS results featuring $\tilde{b} \to b\tilde{\chi}_1^0$ production (included as ATLAS 1711.03301 [101, 102]), as well as chargino production with subsequent top quark decay $\tilde{b} \to t\tilde{\chi}_1^\pm$ (included as ATLAS 1909.08457 [103]). The large $\Delta m(\tilde{\chi}_1^\pm, \tilde{\chi}_1^0)$ of 100 GeV in the second ATLAS result corresponds to a relatively short lifetime comparable to prompt decays. No direct long-lived comparisons can be made with ATLAS due to different production mechanisms and choice of $c\tau$, a comparison to prompt searches yields lower 95% C.L. limits on the cross section derived by ATLAS. The newly-derived exclusion limits in this analysis allow for extended mass exclusion limits com-

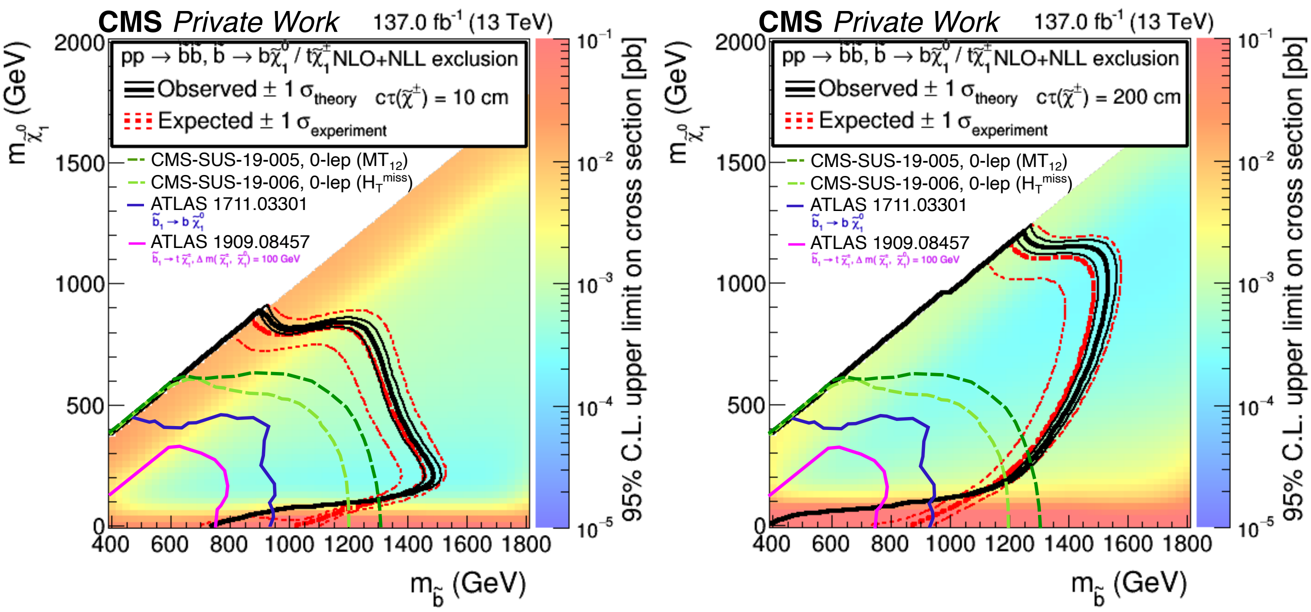

Figure 6.8: Comparison of expected and observed excluded limits using the T6tbLL simplified model interpretation for a $c\tau_{\tilde{\chi}_1^{\pm}}$ of 10 cm (left) and 200 cm (right) to CMS searches, as well as to prompt ATLAS searches.

pared to prompt ATLAS results, with an increase of ≈ 500 GeV for the excluded $\tilde{b}$-squark mass, given a constant $m_{\tilde{\chi}_1^0}$ of ≈ 200 GeV for $c\tau = 10$ cm. For $c\tau = 200$ cm, a comparable increase of ≈ 400 GeV is visible for $m_{\tilde{b}}$, corresponding to $m_{\tilde{\chi}_1^0} \approx 450$ GeV. As seen in the comparison with other CMS searches, this analysis is particularly successful in probing the previously non-excluded compressed phase space, which is also visible when comparing to prompt ATLAS searches.

Chapter 7

Conclusion

This thesis presented a new signature-driven approach for a search for exotic long-lived heavy particles and dark matter, using the full available data recorded by CMS during Run 2. The search is part of a larger effort to uncover a hidden sector of physics with potential exotic long-lived particles. The results were interpreted in the context of both the MSSM and pMSSM, which provide a suitable candidate for dark matter. A case for the likely existence of dark matter has been made, which has been motivated by astrophysical evidence, and a suitable WIMP dark matter candidate has been introduced. This dark matter candidate has been considered in the final state of the decay of the long-lived particle in this search, which arises in supersymmetric models due to a small mass splitting between the two lightest new particles. The resulting signature of a disappearing track used to identify long-lived charginos which decay into dark matter and a SM particle, which is not reconstructed, proved to be very useful to explore previously non-excluded regions in phase space. The precise silicon tracking detector of the CMS experiment proved to be well-suited for this signature, in particular after its upgrade between data-taking in 2016 and 2017.

In addition to events with one or more disappearing tracks, events with one or more additional lepton(s) were considered. In the case of the muon channel, this also allowed to probe for a second very long-lived chargino, which decays outside the tracker volume. This novel approach, which was previously not explored by the CMS experiment, as well as the usage of multivariate analysis techniques and an inclusive binning of the signal regions incorporating dE/dx, allowed this analysis to advance mass exclusion limits, particularly in the compressed phase space.

A disappearing track can be misidentified due to prompt real particles and spurious tracks, which constitute the background sources for this signature. In both cases, a fully data-driven estimation method has been developed, with background from prompt real particles being the dominant source of background for long tracks, and background due to spurious tracks being the dominant source of background for short tracks. This allowed this analysis to rely only to a minimal extent on MC simulation, which has been utilized in training the multivariate classifier for the disappearing track tag, and to derive scale factors. For the derivation of signal scale factors, a novel technique has been deployed to measure the efficiency of the disappearing track signal in data.

No new physics has been found, and upper 95% C.L. limits have been presented using 137 fb^{-1} of proton-proton collision data at $\sqrt{s} = 13$ TeV, with sbottom squark and dark matter masses being excluded up to $m_{\tilde{b}} \approx 1.575$ TeV and $m_{\tilde{\chi}_1^0} = 1.15$ TeV, as well as stop squark and dark matter masses up to $m_{\tilde{t}} \approx 1.6$ TeV and $m_{\tilde{\chi}_1^0} = 1.2$ TeV. For gluino-associated chargino production, gluino masses up to $m_{\tilde{g}} = 2.25$ TeV and dark matter masses up to $m_{\tilde{\chi}_1^0} = 1.7$ TeV are excluded.

In the wake of data-taking for Run 3, the search is expected to both benefit from an increased centre-of-mass energy, as well as an increase in luminosity in future endeavors, especially in the envisioned high-luminosity phase of the LHC. Dedicated track triggers using multivariate analysis techniques could also be fine-tuned to provide increased sensitivity to long-lived particle searches in Run 3.

In conclusion, this search successfully demonstrated an inclusive approach to discover new exotic long-lived particles and dark matter using multivariate analysis techniques and a fully data-driven background estimation.

Chapter 8

Acknowledgments

I would like to express my appreciation and gratitude to my PhD supervisor Prof. Dr. Peter Schleper for the opportunity to work on an interesting research project, and for the guidance and mentorship throughout my PhD journey. His insight and ideas were invaluable and essential to the analysis. I would also like to thank Dr. Isabell Melzer-Pellmann for her insight, and agreeing to act as secondary referee for this thesis.

My wholehearted appreciation also goes to Sam Bein for his insight and encouragement. I would also like to extend a heartfelt thank you to my friends and colleagues Sezen Sekmen, Sang-il Pak and Akshansh Singh together with Sam Bein. Working with you has been a great and exciting experience, and I will also fondly remember our exchanges of recipes.

I would like to thank Georg Steinbrück and Gregor Kasieczka for their insight regarding the CMS pixel detector and machine learning during the LLP discussions, and I would also like to thank all my friends and colleagues from the SUSY group of the University of Hamburg, Alexandra Tews, Yuval Nissan, Malte Mrowietz and Moritz Wolf, together with Sam Bein, for the fruitful discussions and a great working atmosphere.

Furthermore I would like to thank Benedikt Vormwald, Jory Sonneveld, Klaas Padeken, Alexander Fröhlich and Fengwangdong Zhang for a great time at CERN during my pixel detector service work. Working together with you and investigating challenges during Run 2 data-taking was exciting and fun.

I would like to thank Oliver, Tobias, Torben, Johannes, Patrick, Marcel, Philip, Karim, Yikun, Karla, Louis, Sven and all my colleagues from the UHH particle physics groups for a great time during my PhD project.

Finally I would like to thank my family and all my friends for their continuous support.

Appendix A

Appendix

Disappearing track signal efficiency

This section contains additional plots referred to in Sec. 5.12.2. Figure A.1 shows the reconstruction and tagging efficiency depending on the number of remaining layers with measurement for Phase 1, which corresponds to Fig. 5.66 showing Phase 0.

For each run period, the scale factor is first determined dependent on the number of layers with measurement separately for short and long tracks. A constant fit is then performed to get the central value of the scale factor, with the uncertainty measured for a fixed number of layers with measurement in order not to include correlations between the bins. The fits are shown in Fig. A.2 for short and long tracks.

Fig. A.3 shows the correction for d_z.

Results

Detailed event counts are provided for all signal regions, which include the number of observed and predicted events, as well as the number of events in each control region of the background sources. Additionally, the number of event counts for two simplified signal models, T6tbLL and T5btbtLL, are provided. Table A.1 provides the event counts for Phase 0 detector configuration, with Tab. A.2 including the event count for Phase 1. The combined statistics for Run 2 are included in Tab. A.3.

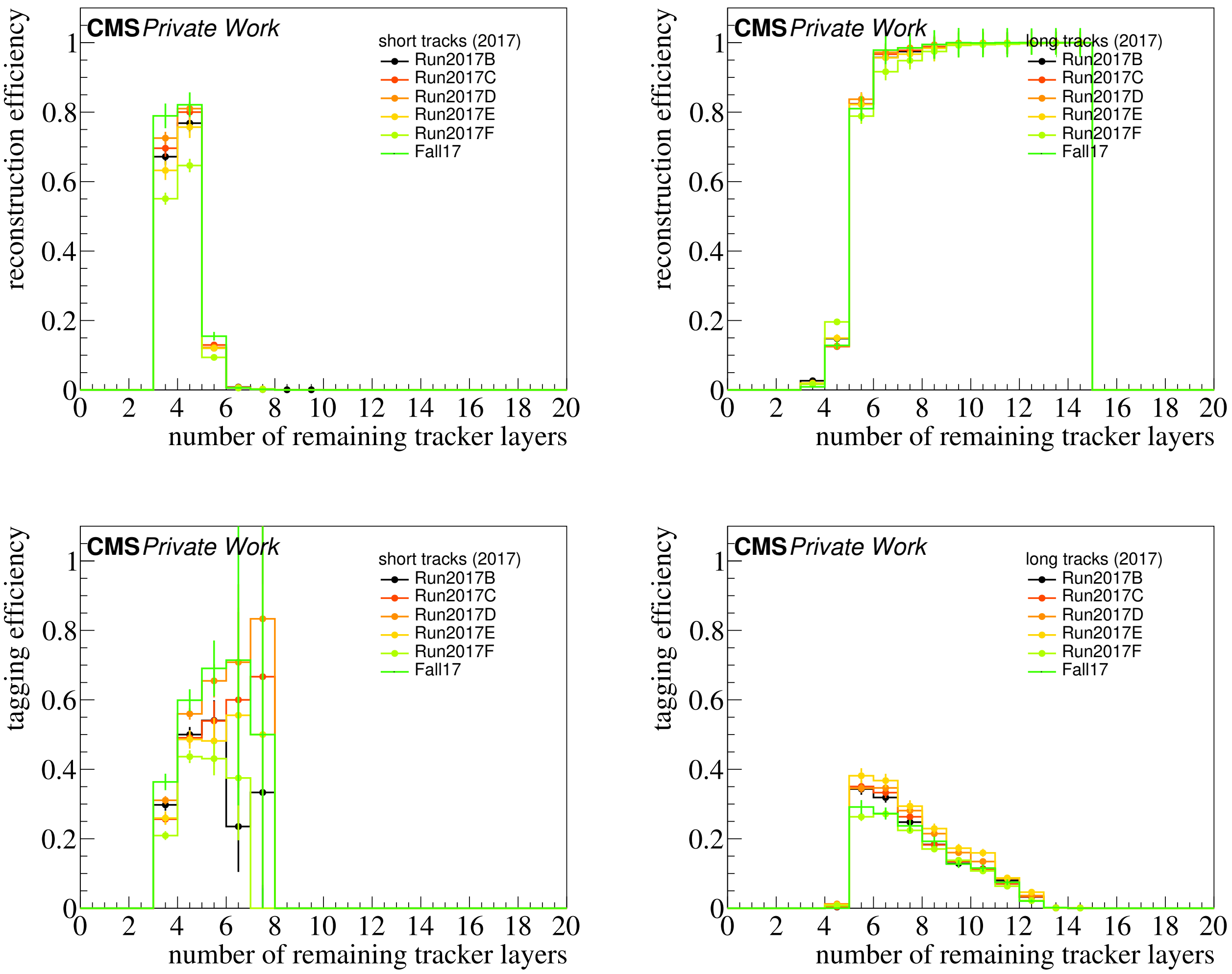

Figure A.1: Shortened track reconstruction efficiency (top) and disappearing track tagging efficiency (bottom) depending on remaining layers with measurement. Results are shown for Phase 1, for which 2017 is selected as a representative time period. Left: short tracks, right: long tracks.

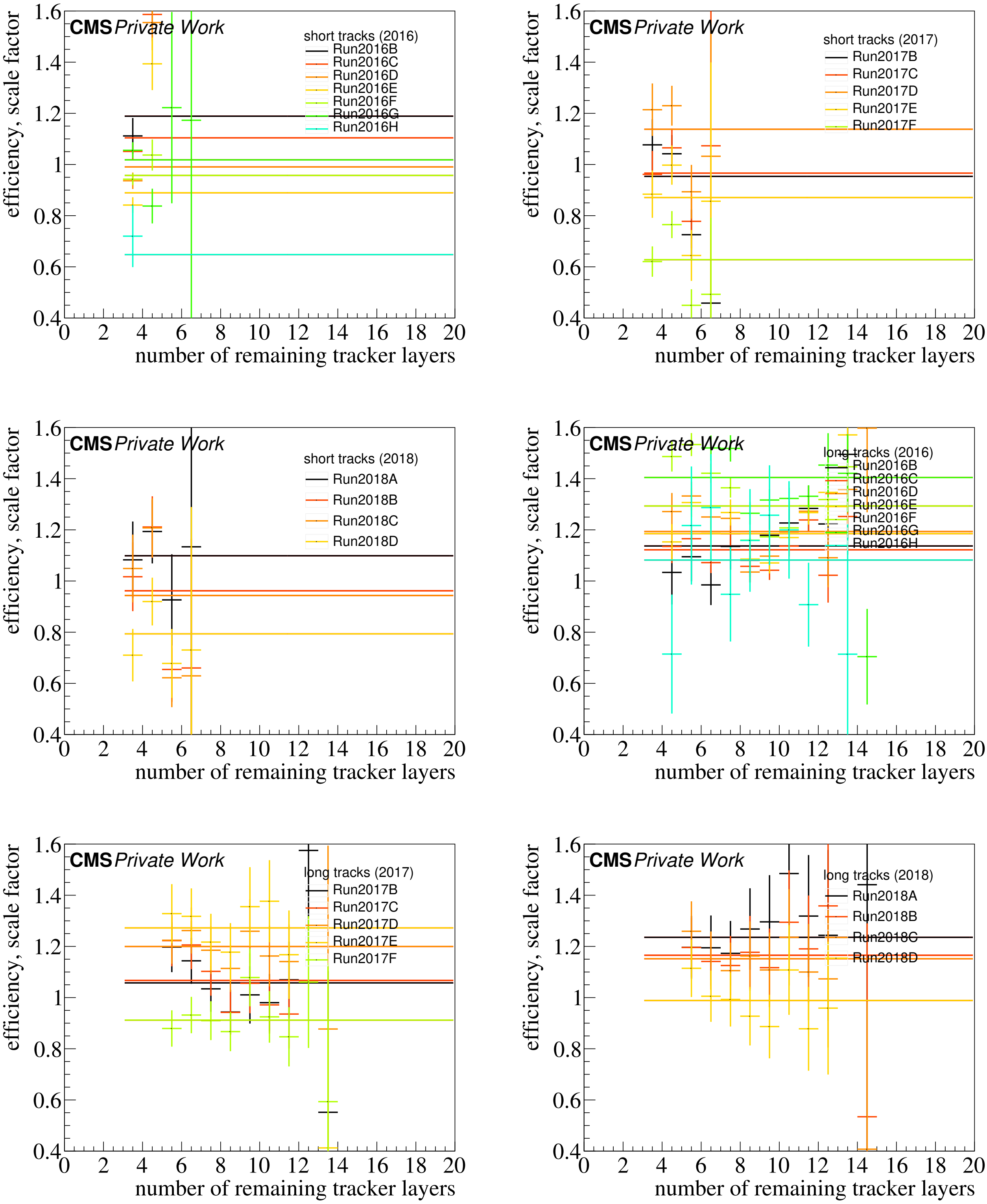

Figure A.2: Per-year scale factor fitting for short tracks (top row, left plot in middle row) and long tracks (right plot in middle row, bottom row).

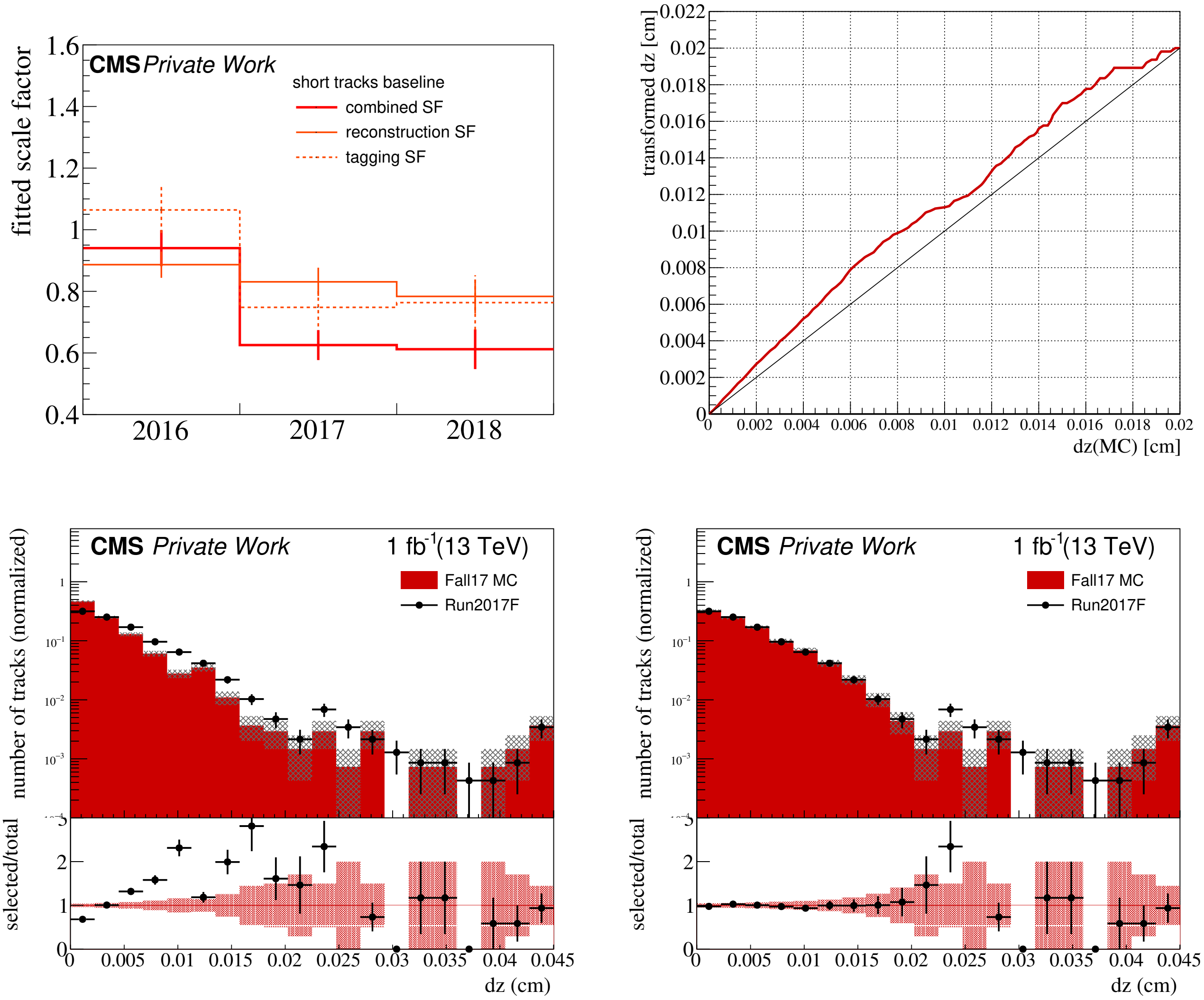

Figure A.3: Top row: Luminosity-weighted signal scale factors for short tracks before applying the corrections to d_{xy} and d_z in Phase 1 MC (left); correction map for MC d_z based on the cumulative transform for Phase 1 (right). Bottom row: Distributions of d_z for short tracks derived from the track shortening method for the data-taking period 2017F (black dots) and for Phase 1 MC, before (left) and after (right) the application of the corrections to d_z.

bin	CR	spurious	CR	showering	CR	MIP	tot. bkg.	T6tbLL	T5btbtLL	obs.
1	49	3.92 ± 0.56	36	11.07 ± 1.84	188	0.14 ± 0.01	15.13 ± 1.93	0.17 ± 0.10	0.00 ± 0.00	14
2	9	0.72 ± 0.24	3	0.92 ± 0.53	12	0.01 ± 0.00	1.65 ± 0.58	0.73 ± 0.26	0.00 ± 0.00	2
3	26	9.01 ± 1.77	20	4.92 ± 1.10	0	0.00 ± 0.00	13.92 ± 2.08	0.02 ± 0.02	0.00 ± 0.00	16
4	3	1.04 ± 0.60	0	0.00 ± 0.00	0	0.00 ± 0.00	1.04 ± 0.60	0.18 ± 0.11	0.00 ± 0.00	1
5	19	1.52 ± 0.35	18	5.53 ± 1.30	107	0.08 ± 0.01	7.13 ± 1.35	0.60 ± 0.19	0.00 ± 0.00	8
6	2	0.16 ± 0.11	1	0.31 ± 0.31	8	0.01 ± 0.00	0.47 ± 0.33	4.39 ± 0.61	0.01 ± 0.00	0
7	18	6.23 ± 1.47	14	3.44 ± 0.92	0	0.00 ± 0.00	9.68 ± 1.73	0.12 ± 0.08	0.00 ± 0.00	6
8	2	0.69 ± 0.49	1	0.25 ± 0.25	0	0.00 ± 0.00	0.94 ± 0.55	0.84 ± 0.23	0.00 ± 0.00	0
9	3	0.24 ± 0.14	7	2.15 ± 0.81	23	0.02 ± 0.00	2.41 ± 0.83	0.00 ± 0.00	0.00 ± 0.00	2
10	0	0.04 ± 0.04	0	0.00 ± 0.00	0	0.00 ± 0.00	0.04 ± 0.04	0.11 ± 0.11	0.00 ± 0.00	0
11	1	0.35 ± 0.35	1	0.25 ± 0.25	0	0.00 ± 0.00	0.59 ± 0.42	0.00 ± 0.00	0.00 ± 0.00	1
12	0	0.06 ± 0.06	0	0.00 ± 0.00	0	0.00 ± 0.00	0.06 ± 0.06	0.00 ± 0.00	0.00 ± 0.00	0
13	4	0.32 ± 0.16	12	3.69 ± 1.07	105	0.08 ± 0.01	4.09 ± 1.08	0.12 ± 0.11	0.03 ± 0.01	5
14	1	0.08 ± 0.08	0	0.00 ± 0.00	4	0.00 ± 0.00	0.08 ± 0.08	0.64 ± 0.21	0.85 ± 0.05	0
15	3	1.04 ± 0.60	6	1.47 ± 0.60	0	0.00 ± 0.00	2.51 ± 0.85	0.08 ± 0.06	0.01 ± 0.00	4
16	0	0.19 ± 0.19	0	0.00 ± 0.00	0	0.00 ± 0.00	0.19 ± 0.19	0.08 ± 0.07	0.18 ± 0.02	0
17	1	0.08 ± 0.08	2	0.61 ± 0.43	101	0.07 ± 0.01	0.77 ± 0.44	0.06 ± 0.06	0.00 ± 0.00	0
18	0	0.01 ± 0.01	0	0.00 ± 0.00	7	0.01 ± 0.00	0.02 ± 0.01	0.34 ± 0.18	0.00 ± 0.00	0
19	1	0.35 ± 0.35	1	0.25 ± 0.25	0	0.00 ± 0.00	0.59 ± 0.42	0.00 ± 0.00	0.00 ± 0.00	2
20	0	0.06 ± 0.06	1	0.25 ± 0.25	0	0.00 ± 0.00	0.31 ± 0.25	0.00 ± 0.00	0.00 ± 0.00	0
21	1	0.08 ± 0.08	3	0.92 ± 0.53	103	0.08 ± 0.01	1.08 ± 0.54	0.49 ± 0.19	0.15 ± 0.02	1
22	0	0.01 ± 0.01	0	0.00 ± 0.00	7	0.01 ± 0.00	0.02 ± 0.01	3.44 ± 0.53	2.68 ± 0.08	0
23	2	0.69 ± 0.49	1	0.25 ± 0.25	0	0.00 ± 0.00	0.94 ± 0.55	0.14 ± 0.11	0.05 ± 0.01	1
24	0	0.12 ± 0.12	0	0.00 ± 0.00	0	0.00 ± 0.00	0.12 ± 0.12	0.79 ± 0.24	0.64 ± 0.04	0
25	3	0.24 ± 0.14	0	0.00 ± 0.00	13	0.01 ± 0.00	0.25 ± 0.14	0.06 ± 0.06	0.00 ± 0.00	0
26	2	0.16 ± 0.11	0	0.00 ± 0.00	1	0.00 ± 0.00	0.16 ± 0.11	0.00 ± 0.00	0.00 ± 0.00	0
27	6	2.08 ± 0.85	3	0.74 ± 0.43	0	0.00 ± 0.00	2.82 ± 0.95	0.00 ± 0.00	0.00 ± 0.00	4
28	1	0.35 ± 0.35	1	0.25 ± 0.25	0	0.00 ± 0.00	0.59 ± 0.42	0.00 ± 0.00	0.00 ± 0.00	1
29	1	0.08 ± 0.08	0	0.00 ± 0.00	9	0.01 ± 0.00	0.09 ± 0.08	0.00 ± 0.00	0.00 ± 0.00	0
30	1	0.08 ± 0.08	0	0.00 ± 0.00	0	0.00 ± 0.00	0.08 ± 0.08	0.00 ± 0.00	0.01 ± 0.00	0
31	0	0.00 ± 0.00	0	0.00 ± 0.00	0	0.00 ± 0.00	0.00 ± 0.00	0.00 ± 0.00	0.00 ± 0.00	2
32	0	0.18 ± 0.18	0	0.00 ± 0.00	0	0.00 ± 0.00	0.18 ± 0.18	0.00 ± 0.00	0.00 ± 0.00	0
33	1	0.08 ± 0.08	3	0.92 ± 0.53	72	0.05 ± 0.01	1.06 ± 0.54	0.06 ± 0.06	0.02 ± 0.01	2
34	0	0.01 ± 0.01	0	0.00 ± 0.00	3	0.00 ± 0.00	0.02 ± 0.01	0.35 ± 0.21	0.43 ± 0.03	0
35	1	0.35 ± 0.35	1	0.25 ± 0.25	0	0.00 ± 0.00	0.59 ± 0.42	0.00 ± 0.00	0.00 ± 0.00	2
36	0	0.06 ± 0.06	0	0.00 ± 0.00	0	0.00 ± 0.00	0.06 ± 0.06	0.11 ± 0.10	0.11 ± 0.02	0
37	5	0.40 ± 0.18	0	0.00 ± 0.00	5	0.00 ± 0.00	0.40 ± 0.18	0.00 ± 0.00	0.00 ± 0.00	0
38	1	0.08 ± 0.08	0	0.00 ± 0.00	0	0.00 ± 0.00	0.08 ± 0.08	0.07 ± 0.07	0.00 ± 0.00	1
39	8	2.77 ± 0.98	2	0.49 ± 0.35	0	0.00 ± 0.00	3.26 ± 1.04	0.00 ± 0.00	0.00 ± 0.00	5
40	0	0.50 ± 0.50	0	0.00 ± 0.00	0	0.00 ± 0.00	0.50 ± 0.50	0.00 ± 0.00	0.00 ± 0.00	0
41	1	0.08 ± 0.08	1	0.31 ± 0.31	5	0.00 ± 0.00	0.39 ± 0.32	0.00 ± 0.00	0.00 ± 0.00	0
42	0	0.01 ± 0.01	0	0.00 ± 0.00	0	0.00 ± 0.00	0.01 ± 0.01	0.00 ± 0.00	0.01 ± 0.00	0
43	3	1.04 ± 0.60	1	0.25 ± 0.25	0	0.00 ± 0.00	1.28 ± 0.65	0.00 ± 0.00	0.00 ± 0.00	0
44	0	0.19 ± 0.19	0	0.00 ± 0.00	0	0.00 ± 0.00	0.19 ± 0.19	0.00 ± 0.00	0.00 ± 0.00	0
45	1	0.08 ± 0.08	2	0.61 ± 0.43	23	0.02 ± 0.00	0.71 ± 0.44	0.24 ± 0.14	0.06 ± 0.01	0
46	0	0.01 ± 0.01	0	0.00 ± 0.00	2	0.00 ± 0.00	0.02 ± 0.01	0.70 ± 0.28	0.77 ± 0.04	0
47	0	0.00 ± 0.00	0	0.00 ± 0.00	0	0.00 ± 0.00	0.00 ± 0.00	0.00 ± 0.00	0.01 ± 0.01	1
48	0	0.18 ± 0.18	0	0.00 ± 0.00	0	0.00 ± 0.00	0.18 ± 0.18	0.21 ± 0.13	0.16 ± 0.02	0
49	1	0.35 ± 0.35	0	0.00 ± 0.00	1	0.00 ± 0.00	0.35 ± 0.35	3.74 ± 0.54	0.76 ± 0.04	0

Table A.1: Predicted prefit background counts and uncertainties in the 49 analysis signal regions for the Phase 0 data-taking period. Statistical and bin-wise uncorrelated systematic uncertainties are added in quadrature, while correlated uncertainties are omitted. Two signal mass points are included, T6tbLL ($m_{\tilde{b}} = 1$ TeV, $m_{\tilde{\chi}_1^0} = 0.9$ TeV, $c\tau = 200$ cm) and T5btbtLL ($m_{\tilde{g}} = 2$ TeV, $m_{\tilde{\chi}_1^0} = 1.4$ TeV, $c\tau = 200$ cm).

bin	CR	spurious	CR	showering	CR	MIP	tot. bkg.	T6tbLL	T5btbtLL	obs.
1	31	2.48 ± 0.45	20	6.15 ± 1.37	125	0.09 ± 0.01	8.72 ± 1.45	0.45 ± 0.27	0.00 ± 0.00	19
2	5	0.40 ± 0.18	1	0.31 ± 0.31	5	0.00 ± 0.00	0.71 ± 0.36	1.96 ± 0.71	0.00 ± 0.00	1
3	144	49.88 ± 4.16	13	3.19 ± 0.89	0	0.00 ± 0.00	53.07 ± 4.25	0.06 ± 0.06	0.00 ± 0.00	35
4	20	6.93 ± 1.55	3	0.74 ± 0.43	0	0.00 ± 0.00	7.66 ± 1.61	0.49 ± 0.30	0.00 ± 0.00	4
5	25	2.00 ± 0.40	6	1.84 ± 0.75	76	0.06 ± 0.01	3.90 ± 0.85	1.62 ± 0.52	0.00 ± 0.00	2
6	5	0.40 ± 0.18	0	0.00 ± 0.00	1	0.00 ± 0.00	0.40 ± 0.18	11.82 ± 1.64	0.02 ± 0.01	1
7	74	25.63 ± 2.98	9	2.21 ± 0.74	0	0.00 ± 0.00	27.84 ± 3.07	0.31 ± 0.22	0.00 ± 0.00	19
8	8	2.77 ± 0.98	1	0.25 ± 0.25	0	0.00 ± 0.00	3.02 ± 1.01	2.26 ± 0.61	0.01 ± 0.01	1
9	1	0.08 ± 0.08	1	0.31 ± 0.31	14	0.01 ± 0.00	0.40 ± 0.32	0.00 ± 0.00	0.00 ± 0.00	1
10	1	0.08 ± 0.08	0	0.00 ± 0.00	0	0.00 ± 0.00	0.08 ± 0.08	0.30 ± 0.30	0.00 ± 0.00	0
11	9	3.12 ± 1.04	3	0.74 ± 0.43	0	0.00 ± 0.00	3.85 ± 1.12	0.00 ± 0.00	0.00 ± 0.00	3
12	2	0.69 ± 0.49	0	0.00 ± 0.00	0	0.00 ± 0.00	0.69 ± 0.49	0.00 ± 0.00	0.01 ± 0.01	0
13	6	0.48 ± 0.20	3	0.92 ± 0.53	52	0.04 ± 0.01	1.44 ± 0.57	0.32 ± 0.31	0.08 ± 0.02	2
14	0	0.09 ± 0.09	0	0.00 ± 0.00	1	0.00 ± 0.00	0.09 ± 0.09	1.72 ± 0.55	2.28 ± 0.12	0
15	28	9.70 ± 1.83	6	1.47 ± 0.60	0	0.00 ± 0.00	11.17 ± 1.93	0.21 ± 0.16	0.03 ± 0.01	5
16	5	1.73 ± 0.77	0	0.00 ± 0.00	0	0.00 ± 0.00	1.73 ± 0.77	0.21 ± 0.18	0.47 ± 0.05	3
17	0	0.00 ± 0.00	2	0.61 ± 0.43	85	0.06 ± 0.01	0.68 ± 0.43	0.17 ± 0.17	0.00 ± 0.00	0
18	0	0.18 ± 0.18	0	0.00 ± 0.00	5	0.00 ± 0.00	0.18 ± 0.18	0.91 ± 0.49	0.00 ± 0.00	0
19	6	2.08 ± 0.85	1	0.25 ± 0.25	0	0.00 ± 0.00	2.32 ± 0.88	0.00 ± 0.00	0.00 ± 0.00	2
20	3	1.04 ± 0.60	0	0.00 ± 0.00	0	0.00 ± 0.00	1.04 ± 0.60	0.00 ± 0.00	0.00 ± 0.00	1
21	1	0.08 ± 0.08	1	0.31 ± 0.31	95	0.07 ± 0.01	0.46 ± 0.32	1.30 ± 0.52	0.39 ± 0.05	1
22	0	0.01 ± 0.01	0	0.00 ± 0.00	3	0.00 ± 0.00	0.02 ± 0.01	9.26 ± 1.44	7.20 ± 0.22	0
23	7	2.42 ± 0.92	4	0.98 ± 0.49	0	0.00 ± 0.00	3.41 ± 1.04	0.38 ± 0.29	0.14 ± 0.03	5
24	1	0.35 ± 0.35	0	0.00 ± 0.00	0	0.00 ± 0.00	0.35 ± 0.35	2.12 ± 0.63	1.71 ± 0.10	0
25	3	0.24 ± 0.14	1	0.31 ± 0.31	10	0.01 ± 0.00	0.55 ± 0.34	0.17 ± 0.17	0.00 ± 0.00	3
26	2	0.16 ± 0.11	0	0.00 ± 0.00	0	0.00 ± 0.00	0.16 ± 0.11	0.00 ± 0.00	0.00 ± 0.00	0
27	36	12.47 ± 2.08	1	0.25 ± 0.25	0	0.00 ± 0.00	12.71 ± 2.09	0.00 ± 0.00	0.00 ± 0.00	9
28	7	2.42 ± 0.92	0	0.00 ± 0.00	0	0.00 ± 0.00	2.42 ± 0.92	0.00 ± 0.00	0.00 ± 0.00	1
29	2	0.16 ± 0.11	0	0.00 ± 0.00	10	0.01 ± 0.00	0.17 ± 0.11	0.00 ± 0.00	0.00 ± 0.00	0
30	2	0.16 ± 0.11	0	0.00 ± 0.00	0	0.00 ± 0.00	0.16 ± 0.11	0.00 ± 0.00	0.02 ± 0.01	0
31	8	2.77 ± 0.98	1	0.25 ± 0.25	0	0.00 ± 0.00	3.02 ± 1.01	0.00 ± 0.00	0.00 ± 0.00	0
32	3	1.04 ± 0.60	0	0.00 ± 0.00	0	0.00 ± 0.00	1.04 ± 0.60	0.00 ± 0.00	0.00 ± 0.00	0
33	2	0.16 ± 0.11	1	0.31 ± 0.31	83	0.06 ± 0.01	0.53 ± 0.33	0.16 ± 0.16	0.06 ± 0.02	0
34	0	0.03 ± 0.03	0	0.00 ± 0.00	3	0.00 ± 0.00	0.03 ± 0.03	0.95 ± 0.57	1.17 ± 0.09	0
35	19	6.58 ± 1.51	1	0.25 ± 0.25	0	0.00 ± 0.00	6.83 ± 1.53	0.00 ± 0.00	0.00 ± 0.00	2
36	2	0.69 ± 0.49	1	0.25 ± 0.25	0	0.00 ± 0.00	0.94 ± 0.55	0.28 ± 0.28	0.30 ± 0.04	1
37	4	0.32 ± 0.16	0	0.00 ± 0.00	2	0.00 ± 0.00	0.32 ± 0.16	0.00 ± 0.00	0.00 ± 0.00	0
38	2	0.16 ± 0.11	0	0.00 ± 0.00	1	0.00 ± 0.00	0.16 ± 0.11	0.18 ± 0.18	0.00 ± 0.00	0
39	31	10.74 ± 1.93	3	0.74 ± 0.43	0	0.00 ± 0.00	11.47 ± 1.97	0.00 ± 0.00	0.00 ± 0.00	5
40	2	0.69 ± 0.49	1	0.25 ± 0.25	0	0.00 ± 0.00	0.94 ± 0.55	0.00 ± 0.00	0.00 ± 0.00	2
41	0	0.00 ± 0.00	0	0.00 ± 0.00	7	0.01 ± 0.00	0.01 ± 0.00	0.00 ± 0.00	0.00 ± 0.00	0
42	0	0.18 ± 0.18	0	0.00 ± 0.00	0	0.00 ± 0.00	0.18 ± 0.18	0.00 ± 0.00	0.02 ± 0.01	0
43	3	1.04 ± 0.60	2	0.49 ± 0.35	0	0.00 ± 0.00	1.53 ± 0.69	0.00 ± 0.00	0.00 ± 0.00	4
44	0	0.19 ± 0.19	0	0.00 ± 0.00	0	0.00 ± 0.00	0.19 ± 0.19	0.00 ± 0.00	0.01 ± 0.01	0
45	4	0.32 ± 0.16	1	0.31 ± 0.31	24	0.02 ± 0.00	0.65 ± 0.35	0.65 ± 0.38	0.16 ± 0.03	0
46	0	0.06 ± 0.06	0	0.00 ± 0.00	1	0.00 ± 0.00	0.06 ± 0.06	1.88 ± 0.75	2.07 ± 0.12	0
47	13	4.50 ± 1.25	2	0.49 ± 0.35	0	0.00 ± 0.00	4.99 ± 1.30	0.00 ± 0.00	0.04 ± 0.01	2
48	2	0.69 ± 0.49	0	0.00 ± 0.00	0	0.00 ± 0.00	0.69 ± 0.49	0.56 ± 0.34	0.44 ± 0.05	0
49	0	0.00 ± 0.00	0	0.00 ± 0.00	0	0.00 ± 0.00	0.00 ± 0.00	10.06 ± 1.46	2.04 ± 0.12	0

Table A.2: Predicted prefit background counts and uncertainties in the 49 analysis signal regions for the Phase 1 data-taking period. Statistical and bin-wise uncorrelated systematic uncertainties are added in quadrature, while correlated uncertainties are omitted. Two signal mass points are included, T6tbLL ($m_{\tilde{b}} = 1$ TeV, $m_{\tilde{\chi}_1^0} = 0.9$ TeV, $c\tau = 200$ cm) and T5btbtLL ($m_{\tilde{g}} = 2$ TeV, $m_{\tilde{\chi}_1^0} = 1.4$ TeV, $c\tau = 200$ cm).

bin	CR	spurious	CR	showering	CR	MIP	tot. bkg.	T6tbLL	T5btbtLL	obs.
1	80	6.40 ± 0.72	56	17.22 ± 2.30	313	0.23 ± 0.01	23.85 ± 2.41	0.03 ± 0.03	0.00 ± 0.00	33
2	14	1.12 ± 0.30	4	1.23 ± 0.61	17	0.01 ± 0.00	2.36 ± 0.68	0.22 ± 0.08	0.00 ± 0.00	3
3	170	58.88 ± 4.52	33	8.11 ± 1.41	0	0.00 ± 0.00	66.99 ± 4.73	0.04 ± 0.03	0.00 ± 0.00	51
4	23	7.97 ± 1.66	3	0.74 ± 0.43	0	0.00 ± 0.00	8.70 ± 1.71	0.04 ± 0.03	0.00 ± 0.00	5
5	44	3.52 ± 0.53	24	7.38 ± 1.51	183	0.13 ± 0.01	11.03 ± 1.60	0.36 ± 0.10	0.00 ± 0.00	10
6	7	0.56 ± 0.21	1	0.31 ± 0.31	9	0.01 ± 0.00	0.87 ± 0.37	4.35 ± 1.61	0.01 ± 0.00	1
7	92	31.87 ± 3.32	23	5.65 ± 1.18	0	0.00 ± 0.00	37.52 ± 3.53	0.11 ± 0.06	0.00 ± 0.00	25
8	10	3.46 ± 1.10	2	0.49 ± 0.35	0	0.00 ± 0.00	3.96 ± 1.15	1.23 ± 0.83	0.00 ± 0.00	1
9	4	0.32 ± 0.16	8	2.46 ± 0.87	37	0.03 ± 0.00	2.81 ± 0.88	0.00 ± 0.00	0.00 ± 0.00	3
10	1	0.08 ± 0.08	0	0.00+0.57−0.00	0	0.00±0.00	0.08+0.57-0.08	0.03 ± 0.03	0.00 ± 0.00	0
11	10	3.46 ± 1.10	4	0.98 ± 0.49	0	0.00 ± 0.00	4.45 ± 1.20	0.00 ± 0.00	0.00 ± 0.00	4
12	2	0.69 ± 0.49	0	0.00+0.90−0.00	0	0.00 ± 0.00	0.69+1.03-0.69	0.00 ± 0.00	0.00 ± 0.00	0
13	10	0.80 ± 0.25	15	4.61 ± 1.19	157	0.12 ± 0.01	5.53 ± 1.22	1.34 ± 1.28	0.08 ± 0.02	7
14	1	0.08 ± 0.08	0	0.00+0.57−0.00	5	0.00 ± 0.00	0.08+0.57-0.08	0.46 ± 0.11	0.22 ± 0.03	0
15	31	10.74 ± 1.93	12	2.95 ± 0.85	0	0.00 ± 0.00	13.69 ± 2.11	0.02 ± 0.02	0.01 ± 0.00	9
16	5	1.73 ± 0.77	0	0.00+0.90−0.00	0	0.00 ± 0.00	1.73 ± 1.19	0.07 ± 0.03	0.06 ± 0.02	3
17	1	0.08 ± 0.08	4	1.23 ± 0.61	186	0.14 ± 0.01	1.45 ± 0.62	0.00 ± 0.00	0.00 ± 0.00	0
18	0	0.01 ± 0.01	0	0.00+0.57−0.00	12	0.01 ± 0.00	0.02+0.57-0.02	0.46 ± 0.15	0.00 ± 0.00	0
19	7	2.42 ± 0.92	2	0.49 ± 0.35	0	0.00 ± 0.00	2.92 ± 0.98	0.00 ± 0.00	0.00 ± 0.00	4
20	3	1.04 ± 0.60	1	0.25 ± 0.25	0	0.00 ± 0.00	1.28 ± 0.65	0.02 ± 0.02	0.00 ± 0.00	1
21	2	0.16 ± 0.11	4	1.23 ± 0.61	198	0.15 ± 0.01	1.54 ± 0.63	1.20 ± 0.94	1.09 ± 0.07	2
22	0	0.03 ± 0.03	0	0.00+0.57−0.00	10	0.01 ± 0.00	0.04+0.57-0.04	4.72 ± 1.38	3.34 ± 0.14	0
23	9	3.12 ± 1.04	5	1.23 ± 0.55	0	0.00 ± 0.00	4.35 ± 1.18	0.04 ± 0.03	0.19 ± 0.03	6
24	1	0.35 ± 0.35	0	0.00+0.90−0.00	0	0.00 ± 0.00	0.35+0.97-0.35	1.00 ± 0.50	0.52 ± 0.04	0
25	6	0.48 ± 0.20	1	0.31 ± 0.31	23	0.02 ± 0.00	0.80 ± 0.36	0.02 ± 0.02	0.00 ± 0.00	3
26	4	0.32 ± 0.16	0	0.00+0.57−0.00	1	0.00 ± 0.00	0.32+0.59-0.32	0.03 ± 0.03	0.00 ± 0.00	0
27	42	14.55 ± 2.24	4	0.98 ± 0.49	0	0.00 ± 0.00	15.53 ± 2.30	0.00 ± 0.00	0.00 ± 0.00	13
28	8	2.77 ± 0.98	1	0.25 ± 0.25	0	0.00 ± 0.00	3.02 ± 1.01	0.00 ± 0.00	0.00 ± 0.00	2
29	3	0.24 ± 0.14	0	0.00+0.57−0.00	19	0.01 ± 0.00	0.25+0.58-0.25	0.00 ± 0.00	0.00 ± 0.00	0
30	3	0.24 ± 0.14	0	0.00+0.57−0.00	0	0.00±0.00	0.24+0.58-0.24	0.00 ± 0.00	0.00 ± 0.00	0
31	8	2.77 ± 0.98	1	0.25 ± 0.25	0	0.00 ± 0.00	3.02 ± 1.01	0.00 ± 0.00	0.00 ± 0.00	2
32	3	1.04 ± 0.60	0	0.00+0.90−0.00	0	0.00 ± 0.00	1.04+1.09-1.04	0.00 ± 0.00	0.00 ± 0.00	0
33	3	0.24 ± 0.14	4	1.23 ± 0.61	155	0.11 ± 0.01	1.58 ± 0.63	0.06 ± 0.04	0.18 ± 0.03	2
34	0	0.04±0.04	0	0.00+0.57−0.00	6	0.00 ± 0.00	0.05+0.57-0.05	0.21 ± 0.08	0.56 ± 0.06	0
35	20	6.93 ± 1.55	2	0.49 ± 0.35	0	0.00 ± 0.00	7.42 ± 1.59	0.00 ± 0.00	0.02 ± 0.01	4
36	2	0.69 ± 0.49	1	0.25 ± 0.25	0	0.00 ± 0.00	0.94 ± 0.55	0.02 ± 0.02	0.08 ± 0.02	1
37	9	0.72 ± 0.24	0	0.00+0.57−0.00	7	0.01 ± 0.00	0.73 ± 0.61	0.03 ± 0.03	0.00 ± 0.00	0
38	3	0.24 ± 0.14	0	0.00+0.57−0.00	1	0.00 ± 0.00	0.24+0.58-0.24	0.04 ± 0.04	0.01 ± 0.01	1
39	39	13.51 ± 2.16	5	1.23 ± 0.55	0	0.00 ± 0.00	14.74 ± 2.23	0.00 ± 0.00	0.00 ± 0.00	10
40	2	0.69 ± 0.49	1	0.25 ± 0.25	0	0.00 ± 0.00	0.94 ± 0.55	0.00 ± 0.00	0.00 ± 0.00	2
41	1	0.08 ± 0.08	1	0.31 ± 0.31	12	0.01 ± 0.00	0.40 ± 0.32	0.00 ± 0.00	0.00 ± 0.00	0
42	0	0.01 ± 0.01	0	0.00+0.57−0.00	0	0.00±0.00	0.01+0.57-0.01	0.00 ± 0.00	0.00 ± 0.00	0
43	6	2.08 ± 0.85	3	0.74 ± 0.43	0	0.00 ± 0.00	2.82 ± 0.95	0.00 ± 0.00	0.00 ± 0.00	4
44	0	0.37 ± 0.37	0	0.00+0.90−0.00	0	0.00 ± 0.00	0.37+0.98-0.37	0.00 ± 0.00	0.00 ± 0.00	0
45	5	0.40 ± 0.18	3	0.92 ± 0.53	47	0.03 ± 0.01	1.36 ± 0.56	0.14 ± 0.07	0.37 ± 0.05	0
46	0	0.07 ± 0.07	0	0.00+0.57−0.00	3	0.00 ± 0.00	0.07+0.57-0.07	0.26 ± 0.09	1.05 ± 0.08	0
47	13	4.50 ± 1.25	2	0.49 ± 0.35	0	0.00 ± 0.00	4.99 ± 1.30	0.00 ± 0.00	0.05 ± 0.01	3
48	2	0.69 ± 0.49	0	0.00+0.90−0.00	0	0.00 ± 0.00	0.69+1.03-0.69	0.07 ± 0.04	0.17 ± 0.03	0
49	1	0.35 ± 0.35	0	0.00+0.57−0.00	1	0.00 ± 0.00	0.35+0.66-0.35	3.92 ± 1.07	0.74 ± 0.06	0

Table A.3: Predicted prefit background counts and uncertainties in the 49 analysis signal regions for the Run 2 data-taking period. Statistical and bin-wise uncorrelated systematic uncertainties are added in quadrature, while correlated uncertainties are omitted. Two signal mass points are included, T6tbLL ($m_{\tilde{b}} = 1$ TeV, $m_{\tilde{\chi}_1^0} = 0.9$ TeV, $c\tau = 200$ cm) and T5btbtLL ($m_{\tilde{g}} = 2$ TeV, $m_{\tilde{\chi}_1^0} = 1.4$ TeV, $c\tau = 200$ cm).

Bibliography

[1] S. Chatrchyan *et al.*, "Observation of a new boson at a mass of 125 GeV with the CMS experiment at the LHC," *Physics Letters B* **716** no. 1, (Sep, 2012) 30–61. `https://doi.org/10.1016%2Fj.physletb.2012.08.021`.

[2] **ATLAS** Collaboration, G. Aad *et al.*, "Observation of a new particle in the search for the Standard Model Higgs boson with the ATLAS detector at the LHC," *Phys. Lett. B* **716** (2012) 1–29, `arXiv:1207.7214 [hep-ex]`.

[3] S. F. Novaes, "Standard Model: An Introduction," in *10th Jorge Andre Swieca Summer School: Particle and Fields*, pp. 5–102. 1, 1999. `arXiv:hep-ph/0001283`.

[4] M. Herrero, "The Standard Model," *NATO Sci. Ser. C* **534** (1999) 1–59, `arXiv:hep-ph/9812242`.

[5] V. Kutzner, "Search for new physics in the mono-electron channel with the CMS experiment in pp collision data at $\sqrt{s} = 13$ TeV," Master's thesis, RWTH Aachen, Aachen, 2016. `https://publications.rwth-aachen.de/record/661716`.

[6] J. Ellis, "Higgs Physics," in *2013 European School of High-Energy Physics*, pp. 117–168. 2015. `arXiv:1312.5672 [hep-ph]`.

[7] M. Yamada, "Gauge hierarchy problem and scalegenesis," *PoS* **CORFU2019** (2020) 077, `arXiv:2004.00142 [hep-ph]`.

[8] J. A. Formaggio, A. L. C. de Gouvêa, and R. G. H. Robertson, "Direct Measurements of Neutrino Mass," *Phys. Rept.* **914** (2021) 1–54, `arXiv:2102.00594 [nucl-ex]`.

[9] A. D'Alise *et al.*, "Standard Model anomalies: lepton flavour non-universality, $g-2$ and W-mass," *JHEP* **08** (2022) 125, `arXiv:2204.03686 [hep-ph]`.

[10] K. Garrett and G. Duda, "Dark Matter: A Primer," *Adv. Astron.* **2011** (2011) 968283, `arXiv:1006.2483 [hep-ph]`.

[11] **Particle Data Group** Collaboration, P. A. Zyla *et al.*, "Review of Particle Physics," *PTEP* **2020** no. 8, (2020) 083C01.

[12] J. R. Brownstein and J. W. Moffat, "The Bullet Cluster 1E0657-558 evidence shows Modified Gravity in the absence of Dark Matter," *Mon. Not. Roy. Astron. Soc.* **382** (2007) 29–47, `arXiv:astro-ph/0702146`.

[13] **Planck** Collaboration, P. A. R. Ade *et al.*, "Planck 2015 results. XIII. Cosmological parameters," *Astron. Astrophys.* **594** (2016) A13, `arXiv:1502.01589 [astro-ph.CO]`.

[14] S. Tulin and H.-B. Yu, "Dark Matter Self-interactions and Small Scale Structure," *Phys. Rept.* **730** (2018) 1–57, `arXiv:1705.02358 [hep-ph]`.

[15] N. Jarosik *et al.*, "Seven-year Wilkinson Microwave Anisotropy Probe (WMAP) Observations: Sky Maps, Systematic Errors, and Basic Results," *APJS* **192** no. 2, (2, 2011) 14, `arXiv:1001.4744`.

[16] T. Marrodán Undagoitia and L. Rauch, "Dark matter direct-detection experiments," *J. Phys.* **G43** no. 1, (2016) 013001, `arXiv:1509.08767 [physics.ins-det]`.

[17] J. Lewin and P. Smith, "Review of mathematics, numerical factors, and corrections for dark matter experiments based on elastic nuclear recoil," *Astroparticle Physics* **6** no. 1, (1996) 87 – 112.
`http://www.sciencedirect.com/science/article/pii/S0927650596000473`.

[18] **XENON100** Collaboration, E. Aprile *et al.*, "Search for Event Rate Modulation in XENON100 Electronic Recoil Data," *Phys. Rev. Lett.* **115** no. 9, (2015) 091302, `arXiv:1507.07748 [astro-ph.CO]`.

[19] D. F. P. Pile, "Vacuum-ultraviolet source," *Nature Photonics* **12** (2018) 568.
`https://doi.org/10.1038/s41566-018-0270-9`.

[20] J. Aalbers *et al.*, "First Dark Matter Search Results from the LUX-ZEPLIN (LZ) Experiment," 2022. `https://arxiv.org/abs/2207.03764`.

[21] **PICO** Collaboration, C. Amole *et al.*, "Dark Matter Search Results from the PICO-2L C_3F_8 Bubble Chamber," *Phys. Rev. Lett.* **114** no. 23, (2015) 231302, `arXiv:1503.00008 [astro-ph.CO]`.

[22] **SuperCDMS** Collaboration, R. Agnese *et al.*, "New Results from the Search for Low-Mass Weakly Interacting Massive Particles with the CDMS Low Ionization Threshold Experiment," *Phys. Rev. Lett.* **116** no. 7, (2016) 071301, `arXiv:1509.02448 [astro-ph.CO]`.

[23] **CRESST** Collaboration, J. Schieck, "Direct Dark Matter Search with the CRESST-II Experiment," in *Proceedings, 50th Rencontres de Moriond Electroweak interactions and unified theories*, pp. 445–450. 2015. `arXiv:1505.03289 [astro-ph.CO]`.
`https://inspirehep.net/record/1369959/files/arXiv:1505.03289.pdf`.

[24] J. F. Beacom, "The diffuse supernova neutrino background," *Annual Review of Nuclear and Particle Science* **60** no. 1, (2010) 439–462.

[25] G. Bertone, D. Hooper, and J. Silk, "Particle dark matter: Evidence, candidates and constraints," *Phys. Rept.* **405** (2005) 279–390, `arXiv:hep-ph/0404175 [hep-ph]`.

[26] S. P. Martin, "A Supersymmetry primer," *Adv. Ser. Direct. High Energy Phys.* **18** (1998) 1–98, `arXiv:hep-ph/9709356`.

[27] K. Kowalska and E. M. Sessolo, "The discreet charm of higgsino dark matter: A pocket review," *Advances in High Energy Physics* **2018** (Jul, 2018) 1–15.
`https://doi.org/10.1155%2F2018%2F6828560`.

[28] C. F. Berger, J. S. Gainer, J. L. Hewett, and T. G. Rizzo, "Supersymmetry Without Prejudice," *JHEP* **02** (2009) 023, `arXiv:0812.0980 [hep-ph]`.

[29] **CMS** Collaboration, V. Khachatryan *et al.*, "Phenomenological MSSM interpretation of CMS searches in pp collisions at $\sqrt{s} = 7$ and 8 TeV," *JHEP* **10** (2016) 129, `arXiv:1606.03577 [hep-ex]`.

[30] M. Mrowietz, "Constraints on Supersymmetry from Collider Searches and Other Experiments," 2023. PhD thesis, University of Hamburg, to be published.

[31] **Super-Kamiokande** Collaboration, R. Matsumoto *et al.*, "Search for proton decay via $p \to \mu^+ K^0$ in 0.37 megaton-years exposure of Super-Kamiokande," *Phys. Rev. D* **106** no. 7, (2022) 072003, `arXiv:2208.13188 [hep-ex]`.

[32] B. Shuve, "Theory overview of long-lived particles," 2018. `https://indico.cern.ch/event/714087/contributions/2985914/attachments/1650488/2641192/LHC-LLP_Shuve.pdf`.

[33] J. Alimena *et al.*, "Searching for long-lived particles beyond the Standard Model at the Large Hadron Collider," *J. Phys. G* **47** no. 9, (2020) 090501, `arXiv:1903.04497 [hep-ex]`.

[34] **CMS** Collaboration, V. Kutzner, "Searches for long-lived particles with CMS," tech. rep., CERN, Geneva, Sep, 2018. `https://cds.cern.ch/record/2639964`.

[35] J. Antonelli, "LHC Long-Lived Particle Mini-Workshop," 2016. `https://indico.cern.ch/event/517268/contributions/2041293/attachments/1272363/`.

[36] **CMS** Collaboration, "Search for heavy stable charged particles with 12.9 fb^{-1} of 2016 data," Tech. Rep. CMS-PAS-EXO-16-036, `http://cds.cern.ch/record/2205281`, CERN, 2016.

[37] **CMS** Collaboration, "Search for long-lived particles with displaced vertices in multijet events in proton-proton collisions at $\sqrt{s}$ =13 TeV," Tech. Rep. CMS-PAS-EXO-17-018, `http://cds.cern.ch/record/2621291`, 2018. `arXiv:1808.03078 [hep-ex]`.

[38] **CMS** Collaboration, "Search for decays of stopped exotic long-lived particles produced in proton-proton collisions at $\sqrt{s} = 13$ TeV. *JHEP* 05 (2018) 127," *JHEP* **05** (2018) 127, `arXiv:1801.00359 [hep-ex]`.

[39] P. Mouche, "Overall view of the LHC. Vue d'ensemble du LHC,". `https://cds.cern.ch/record/1708847`. General Photo.

[40] **CMS** Collaboration, "The CMS experiment at the CERN LHC," *Journal of Instrumentation* **3** no. 08, (2008) S08004. `http://stacks.iop.org/1748-0221/3/i=08/a=S08004`.

[41] J. Nielsen, *Fundamentals of LHC Experiments*. 2011. `arXiv:1106.2516 [hep-ex]`. `https://inspirehep.net/record/913551/files/arXiv:1106.2516.pdf`.

[42] **CMS Tracker Group** Collaboration, W. Adam *et al.*, "The CMS Phase-1 Pixel Detector Upgrade," *JINST* **16** no. 02, (2021) P02027, `arXiv:2012.14304 [physics.ins-det]`.

[43] **CMS** Collaboration, "CMS Technical Design Report for the Pixel Detector Upgrade," Tech. Rep. CERN-LHCC-2012-016, `http://cds.cern.ch/record/1481838`, 2012. `http://cds.cern.ch/record/1481838`.

[44] **CMS** Collaboration, " CMS Tracker Detector Performance Results ," 2022. `https://twiki.cern.ch/twiki/bin/view/CMSPublic/DPGResultsTRK`. Accessed on Mar 25, 2023.

[45] E. James, Y. Maravin, M. Mulders, and N. Neumeister, "Muon identification in CMS," *CERN-CMS-NOTE-2006-010* (2006) . `http://cds.cern.ch/record/927392?ln=de`.

[46] **CMS** Collaboration, *The CMS muon project: Technical Design Report*. Technical Design Report CMS. CERN, Geneva, 1997. `https://cds.cern.ch/record/343814`.

[47] **CMS** Collaboration, A. M. Sirunyan *et al.*, "Precision luminosity measurement in proton-proton collisions at $\sqrt{s} = 13$ TeV in 2015 and 2016 at CMS," *Eur. Phys. J. C* **81** no. 9, (2021) 800, `arXiv:2104.01927 [hep-ex]`.

[48] **CMS** Collaboration, "Description and performance of track and primary-vertex reconstruction with the CMS tracker," *Journal of Instrumentation* **9** no. 10, (Oct, 2014) P10009–P10009. `https://doi.org/10.1088/1748-0221/9/10/p10009`.

[49] **CMS** Collaboration, A. M. Sirunyan *et al.*, "Particle-flow reconstruction and global event description with the CMS detector," *JINST* **12** no. 10, (2017) P10003, `arXiv:1706.04965 [physics.ins-det]`.

[50] M. Ibe, S. Matsumoto, and R. Sato, "Mass Splitting between Charged and Neutral Winos at Two-Loop Level," *Phys. Lett. B* **721** (2013) 252–260, `arXiv:1212.5989 [hep-ph]`.

[51] **CMS** Collaboration, S. Chatrchyan *et al.*, "Interpretation of Searches for Supersymmetry with Simplified Models," *Phys. Rev. D* **88** no. 5, (2013) 052017, `arXiv:1301.2175 [hep-ex]`.

[52] N. Nagata and S. Shirai, "Higgsino Dark Matter in High-Scale Supersymmetry," *JHEP* **01** (2015) 029, `arXiv:1410.4549 [hep-ph]`.

[53] H. Fukuda, N. Nagata, H. Otono, and S. Shirai, "Higgsino Dark Matter or Not: Role of Disappearing Track Searches at the LHC and Future Colliders," *Phys. Lett. B* **781** (2018) 306–311, `arXiv:1703.09675 [hep-ph]`.

[54] J. Alwall, M. Herquet, F. Maltoni, O. Mattelaer, and T. Stelzer, "MadGraph 5 : Going Beyond," *JHEP* **06** (2011) 128, `arXiv:1106.0522 [hep-ph]`.

[55] **CMS** Collaboration, " Run II Pixel Performance plots for data and simulation ," 2021. `https://twiki.cern.ch/twiki/bin/view/CMSPublic/PixelOfflinePlots2016`. Accessed on Jan 30, 2023.

[56] V. Khachatryan *et al.*, "The CMS trigger system," *Journal of Instrumentation* **12** no. 01, (Jan, 2017) P01020–P01020. `https://doi.org/10.1088/1748-0221/12/01/p01020`.

[57] J. Alwall *et al.*, "A Standard format for Les Houches event files," *Comput. Phys. Commun.* **176** (2007) 300–304, `arXiv:hep-ph/0609017`.

[58] C. Oleari, "The POWHEG-BOX," *Nucl. Phys. B Proc. Suppl.* **205-206** (2010) 36–41, `arXiv:1007.3893 [hep-ph]`.

[59] T. Sjöstrand, S. Ask, J. R. Christiansen, R. Corke, N. Desai, P. Ilten, S. Mrenna, S. Prestel, C. O. Rasmussen, and P. Z. Skands, "An introduction to PYTHIA 8.2" *Comput. Phys. Commun.* **191** (2015) 159–177, `arXiv:1410.3012 [hep-ph]`.

[60] S. Agostinelli *et al.*, "Geant4 — a simulation toolkit," *Nuclear Instruments and Methods in Physics Research Section A: Accelerators, Spectrometers, Detectors and Associated Equipment* **506** no. 3, (2003) 250–303. `https://www.sciencedirect.com/science/article/pii/S0168900203013688`.

[61] S. Abdullin, P. Azzi, F. Beaudette, P. Janot, and A. P. and, "The fast simulation of the CMS detector at LHC," *Journal of Physics: Conference Series* **331** no. 3, (Dec, 2011) 032049. `https://doi.org/10.1088/1742-6596/331/3/032049`.

[62] **CMS** Collaboration, S. Sekmen, "Recent Developments in CMS Fast Simulation," *PoS* **ICHEP2016** (2016) 181, `arXiv:1701.03850 [physics.ins-det]`.

[63] **CMS** Collaboration, A. M. Sirunyan *et al.*, "Electron and photon reconstruction and identification with the CMS experiment at the CERN LHC," *JINST* **16** no. 05, (2021) P05014, `arXiv:2012.06888 [hep-ex]`.

[64] **CMS** Collaboration, A. Sirunyan *et al.*, "Performance of the CMS muon detector and muon reconstruction with proton-proton collisions at $\sqrt{s} = 13$ TeV," *JINST* **13** (Jun, 2018) P06015. 53 p, `arXiv:1804.04528`. `http://cds.cern.ch/record/2313130`. Replaced with the published version. Added the journal reference and the DOI. All the figures and tables can be found at http://cms-results.web.cern.ch/cms-results/public-results/publications/MUO-16-001 (CMS Public Pages).

[65] M. Cacciari, G. P. Salam, and G. Soyez, "The anti-k_t jet clustering algorithm," *Journal of High Energy Physics* **2008** no. 04, (Apr, 2008) 063–063. `https://doi.org/10.1088%2F1126-6708%2F2008%2F04%2F063`.

[66] M. Cacciari, G. P. Salam, and G. Soyez, "FastJet User Manual," *Eur. Phys. J. C* **72** (2012) 1896, `arXiv:1111.6097 [hep-ph]`.

[67] **CMS** Collaboration, A. M. Sirunyan *et al.*, "Identification of heavy-flavour jets with the CMS detector in pp collisions at 13 TeV," *JINST* **13** no. 05, (2018) P05011, `arXiv:1712.07158 [physics.ins-det]`.

[68] **CMS** Collaboration, "The Phase-2 Upgrade of the CMS Tracker," tech. rep., CERN, Geneva, 2017. `https://cds.cern.ch/record/2272264`.

[69] E. Bulyak and N. Shul'ga, "Landau distribution of ionization losses: history, importance, extensions," `arXiv:2209.06387 [physics.plasm-ph]`.

[70] **CMS** Collaboration, Khachatryan *et al.*, "Search for heavy stable charged particles in pp collisions at $\sqrt{s}$ = 7 and 8 TeV," *JHEP* **03** (2011) 024, `arXiv:1101.1645 [hep-ex]`.

[71] **CMS** Collaboration, Khachatryan *et al.*, "Search for long-lived charged particles in proton-proton collisions at $\sqrt{s}$ = 13 TeV," *Phys. Rev. D* **94** (2016) 112004, `arXiv:1609.08382 [hep-ex]`.

[72] A. Hocker *et al.*, "TMVA - Toolkit for Multivariate Data Analysis," `arXiv:physics/0703039`. 2007.

[73] Y. Freund and R. E. Schapire, "A decision-theoretic generalization of on-line learning and an application to boosting," *Journal of Computer and System Sciences* **55** no. 1, (1997) 119–139. `https://www.sciencedirect.com/science/article/pii/S002200009791504X`.

[74] **CMS** Collaboration, S. Chatrchyan *et al.*, "Energy Calibration and Resolution of the CMS Electromagnetic Calorimeter in pp Collisions at $\sqrt{s} = 7$ TeV," *JINST* **8** (2013) 9009, `arXiv:1306.2016 [hep-ex]`.

[75] **CMS** Collaboration, A. M. Sirunyan *et al.*, "Searches for physics beyond the Standard Model with the M_{T2} variable in hadronic final states with and without disappearing tracks in proton-proton collisions at $\sqrt{s} = 13$ TeV," *Eur. Phys. J. C* **80** no. 1, (2020) 3, `arXiv:1909.03460 [hep-ex]`.

[76] **CMS** Collaboration, A. M. Sirunyan *et al.*, "Search for disappearing tracks in proton-proton collisions at $\sqrt{s} = 13$ TeV," *Phys. Lett. B* **806** (2020) 135502, `arXiv:2004.05153 [hep-ex]`.

[77] **CMS** Collaboration, V. Khachatryan *et al.*, "Search for new physics with the M_{T2} variable in all-jets final states produced in pp collisions at $\sqrt{s} = 13$ TeV," *JHEP* **10** (2016) 006, `arXiv:1603.04053 [hep-ex]`.

[78] **CMS** Collaboration, A. M. Sirunyan *et al.*, "Search for disappearing tracks as a signature of new long-lived particles in proton-proton collisions at $\sqrt{s} = 13$ TeV," *JHEP* **08** (2018) 016, `arXiv:1804.07321 [hep-ex]`.

[79] S. Pak, "Search for new long-lived particles with disappearing track signature in CMS experiment at LHC," 2022. `http://www.riss.kr/search/detail/DetailView.do?p_mat_type=be54d9b8bc7cdb09&control_no=89abe64c51e88349ffe0bdc3ef48d419`. PhD thesis, Kyungpook National University.

[80] H. Bichsel, "A method to improve tracking and particle identification in TPCs and silicon detectors," *Nuclear Instruments and Methods in Physics Research Section A: Accelerators, Spectrometers, Detectors and Associated Equipment* **562** no. 1, (2006) 154–197. `https://www.sciencedirect.com/science/article/pii/S0168900206005353`.

[81] **CMS** Collaboration, V. Khachatryan *et al.*, "Search for Heavy Stable Charged Particles in pp collisions at $\sqrt{s} = 7$ TeV," *JHEP* **03** (2011) 024, `arXiv:1101.1645 [hep-ex]`.

[82] **CMS** Collaboration, V. Khachatryan *et al.*, "Search for long-lived charged particles in proton-proton collisions at $\sqrt{s} = 13$ TeV," *Phys. Rev. D* **94** no. 11, (2016) 112004, `arXiv:1609.08382 [hep-ex]`.

[83] P. C. Bhat, H. B. Prosper, S. Sekmen, and C. Stewart, "Optimizing event selection with the random grid search," *Computer Physics Communications* **228** (2018) 245–257. `https://www.sciencedirect.com/science/article/pii/S001046551830047X`.

[84] A. Tews, "Track Reconstruction Performance for Semi-Stable Charged Particles at CMS," 2018. `https://www.physik.uni-hamburg.de/en/iexp/theses-pp-and-dd/pdfs/masterarbeit-alexandra-tews.pdf`. Master's thesis, University of Hamburg.

[85] **CMS** Collaboration, A. Giraldi, "Precision luminosity measurement with proton-proton collisions at the CMS experiment in Run 2," *PoS* **ICHEP2022** (2022) 638, `arXiv:2208.08214 [hep-ex]`.

[86] **CMS** Collaboration, G. Agarwal, "Jet Energy Scale and Resolution Measurements in CMS," *PoS* **ICHEP2022** (2022) 652, `arXiv:2301.02175 [hep-ex]`.

[87] D. E. Soper, "Parton distribution functions," *Nucl. Phys. B Proc. Suppl.* **53** (1997) 69–80, `arXiv:hep-lat/9609018`.

[88] J. Chyla, "Renormalization and factorization scale analysis of $\bar{b}b$ production in antiproton-proton collisions," *Journal of High Energy Physics* **7** (03, 2003) .

[89] **CMS** Collaboration, "Search for supersymmetry in proton-proton collisions at 13 TeV in final states with jets and missing transverse momentum," *JHEP* **10** (2019) 244, `arXiv:1908.04722 [hep-ex]`.

[90] A. Kalogeropoulos and J. Alwall, "The SysCalc code: A tool to derive theoretical systematic uncertainties," `arXiv:1801.08401 [hep-ph]`. 2018.

[91] S. Catani, D. de Florian, M. Grazzini, and P. Nason, "Soft gluon resummation for Higgs boson production at hadron colliders," *JHEP* **07** (2003) 028, `arXiv:hep-ph/0306211`.

[92] M. Cacciari, S. Frixione, M. L. Mangano, P. Nason, and G. Ridolfi, "The t anti-t cross-section at 1.8-TeV and 1.96-TeV: A Study of the systematics due to parton densities and scale dependence," *JHEP* **04** (2004) 068, `arXiv:hep-ph/0303085`.

[93] **CMS** Collaboration, A. M. Sirunyan *et al.*, "Pileup mitigation at CMS in 13 TeV data," *JINST* **15** no. 09, (2020) P09018, `arXiv:2003.00503 [hep-ex]`.

[94] S. Banerjee, A. Caner, S. Dutta, A. Khanov, F. Palla, and G. Tonelli, "Study of dE/dx Measurements with the CMS Tracker," tech. rep., CERN, Geneva, 1999. `http://cds.cern.ch/record/687166`.

[95] A. Harel, "Statistical methods in CMS searches," in *PHYSTAT 2011*, pp. 88–93. CERN, Geneva, 2011.

[96] **ATLAS** Collaboration, "The CLs method," 2011. Available at `https://www.pp.rhul.ac.uk/~cowan/stat/cls/CLsInfo.pdf`, accessed on Feb 9, 2023.

[97] **ATLAS** Collaboration, G. Aad *et al.*, "Search for the $\bar{b}b$-decay of the Standard Model higgs boson in associated (W/Z)H production with the atlas detector," *Journal of High Energy Physics* **2015** no. 1, (2015) 69. `https://doi.org/10.1007/JHEP01(2015)069`.

[98] B. Fuks, M. Klasen, D. R. Lamprea, and M. Rothering, "Gaugino production in proton-proton collisions at a center-of-mass energy of 8 TeV," *JHEP* **10** (2012) 081, `arXiv:1207.2159 [hep-ph]`.

[99] B. Fuks, M. Klasen, D. R. Lamprea, and M. Rothering, "Precision predictions for electroweak superpartner production at hadron colliders with RESUMMINO," *Eur. Phys. J. C* **73** (2013) 2480, `arXiv:1304.0790 [hep-ph]`.

[100] **CMS** Collaboration, A. Tumasyan *et al.*, "Combined searches for the production of supersymmetric top quark partners in proton–proton collisions at $\sqrt{s} = 13\,\text{TeV}$," *Eur. Phys. J. C* **81** no. 11, (2021) 970, `arXiv:2107.10892 [hep-ex]`.

[101] **ATLAS** Collaboration, M. Aaboud *et al.*, "Search for supersymmetry in events with b-tagged jets and missing transverse momentum in pp collisions at $\sqrt{s} = 13$ TeV with the ATLAS detector," *JHEP* **11** (2017) 195, `arXiv:1708.09266 [hep-ex]`.

[102] **ATLAS** Collaboration, M. Aaboud *et al.*, "Search for dark matter and other new phenomena in events with an energetic jet and large missing transverse momentum using the ATLAS detector," *JHEP* **01** (2018) 126, `arXiv:1711.03301 [hep-ex]`.

[103] **ATLAS** Collaboration, G. Aad *et al.*, "Search for squarks and gluinos in final states with same-sign leptons and jets using 139 fb^{-1} of data collected with the ATLAS detector," *JHEP* **06** (2020) 046, `arXiv:1909.08457 [hep-ex]`.

List of Figures

List of Tables

Eidesstattliche Versicherung
Declaration on oath

Hiermit versichere ich an Eides statt, die vorliegende Dissertationsschrift selbst verfasst und keine anderen als die angegebenen Hilfsmittel und Quellen benutzt zu haben.

Hamburg, den 27.4.2023

……………………………………………………………

Viktor Gerhard Kutzner